

N° d'ordre:



THÈSE

PRÉSENTÉE A

L'UNIVERSITÉ BORDEAUX 1

ÉCOLE DOCTORALE DES SCIENCES PHYSIQUES ET DE L'INGÉNIEUR

en cotutelle avec

**L'UNIVERSITÉ TECHNIQUE DE
CLUJ-NAPOCA**

(Roumanie)

Par **Cosmin LUDUȘAN**

POUR OBTENIR LE GRADE DE

DOCTEUR

SPÉCIALITÉ: Automatique, Productique, Signal et Image

DE LA RESTAURATION D'IMAGES AU

REHAUSSEMENT:

formalisme EDP pour la fusion d'images bruitées

Directeurs de recherche: Monica BORDA et Olivier LAVIALLE

Soutenue le: 28 novembre 2011

Devant la commission d'examen formée de:

Président

M. Gabriel OLTEAN Professeur – Université Technique de Cluj-Napoca (Roumanie)

Rapporteurs

MM. Philippe BOLON Professeur – Polytech Annecy-Chambéry

Ioan NAFORNIȚĂ Professeur – Université *Politehnica* Timișoara (Roumanie)

Examineurs

Mme. Monica BORDA Professeur – Université Technique de Cluj-Napoca (Roumanie)

MM. Olivier LAVIALLE Directeur – ENITA de Bordeaux

Christian GERMAIN Professeur – ENITA de Bordeaux

Romulus TEREBEȘ Maître de Conférences – Université Technique de Cluj-Napoca (Roumanie)

Université Bordeaux 1

Les Sciences et les Technologies au service de l'Homme et de l'environnement

Table des matières

Chapitre 1.

Introduction	1
1.1 Motivation	1
1.2 Conceptualisation	1
1.3 Organisation	2

Chapitre 2.

Restauration d’images en utilisant des équations aux dérivées partielles	3
2.1 Définitions	3
2.2 Le traitement d’images fondé sur les Équations aux Dérivées Partielles . . .	3
2.3 Le filtrage linéaire dans la restauration d’images	4
2.4 Filtrage non linéaire – diffusion anisotrope	5

Chapitre 3.

Restauration d’images par filtres de choc hybrides	6
3.1 Introduction	6
3.2 Le filtre de choc hybride	7
3.2.1 Le modèle mathématique	8
3.2.2 L’extension du modèle pour l’amélioration de cohérence	9
3.2.3 Analyse expérimentale	9
3.3 Conclusions	12

Chapitre 4.

La fusion d’images comme un processus d’amélioration d’images . . .	13
4.1 Introduction	13
4.2 Définitions et classifications	13

Chapitre 5.

La fusion d’images avec élimination du bruit	14
5.1 Motivation	14
5.2 Formulation mathématique	14
5.3 Analyse expérimentale	17

Chapitre 6.
 Conclusions, remarques, perspectives **20**

Bibliographie **21**

Table des figures

3.1	Exemple d'un processus de déconvolution pour un signal 1-D pour $I_0(x) = -\sin(x)$ défini sur l'intervalle $[-\pi, \pi]$. La ligne pointillée bleue représente le signal original, alors que la ligne continue illustre l'évolution temporelle de la fonction I . Les flèches indiquent la direction de propagation de l'effet de déconvolution.	7
3.2	Filtres de choc - analyse comparative : (a) Image de référence ; (b) Image initiale contaminée I_0 - flou gaussien ($\sigma_f = 3$) + bruit blanc gaussien additif ($\sigma_b = 10$) ; (c) Résultat du filtre Osher–Rudin ; (d) Résultat du filtre Alvarez–Mazorra [AM94] ; (e) Résultat du filtre Kornprobst <i>et al.</i> [KDA97] ; (f) Résultat du filtre Remaki–Cheriet [RC03] ; (g) Résultat du filtre Gilboa <i>et al.</i> ; (h) Résultat du filtre de choc hybride.	10
3.3	Filtres de choc hybride avec amélioration de cohérence – analyse comparative : (a) Image de référence ; (b) Image initiale contaminée I_0 flou gaussien ($\sigma_f = 10$) + bruit blanc gaussien additif ($\sigma_b = 25$) ; (c) Résultat du filtre Gilboa <i>et al.</i> ; (d) Résultat du filtre CESF de Weickert ; (e) Résultat du filtre de choc hybride avec amélioration de cohérence + détail.	11
5.1	Analyse comparative – résultats sélectives : (a) Image de référence I_1 ; (b) Image de référence I_2 ; (c) Résultat de la méthode MED ; (d) Résultat de la méthode SIDWT-hard ; (e) Résultat de la méthode Pop-2 ; (f) Résultat de la méthode méthode proposée	17
5.2	Scénario de fusion multi-luminance – modèle proposé : (a) I_1 et détail (d) ; (b) I_2 et détail (e) ; (c) \tilde{I} résultat de la fusion et détail (f).	19
5.3	Scénario de fusion d'images médicales – modèle proposé : (a) I_1 image CT et détail (d) ; (b) I_2 image RMN et détail (e) ; (c) \tilde{I} résultat de la fusion et détail (f).	19

Liste des tableaux

3.1	Résultats de l'analyse qualitative – cadre expérimental <i>Fig. 3.2</i>	11
3.2	Résultats de l'analyse qualitative – cadre expérimental <i>Fig. 3.3</i>	12
5.1	Analyse comparative – bruit blanc, gaussien additif - $\sigma_b = 13$	18

CHAPITRE 1

Introduction

1.1 Motivation

Les *objectifs* de cette thèse sont principalement axés sur la définition de nouveaux mécanismes de restauration et d'amélioration d'images s'appuyant sur une modélisation mathématique basée sur des Equations aux Dérivées Partielles. La question a d'emblée été abordée en évaluant la possibilité de définir des modèles unifiés, permettant la parallélisation des deux types de traitement d'images. Une fois définis ces nouveaux mécanismes, le but était d'en évaluer les performances et de les positionner parmi les méthodologies existantes, sur la base d'une analyse expérimentale comparative.

La fusion des deux approches (*restauration, amélioration*) en un seul processus parallélisé a été principalement motivée par l'existence de travaux sur le sujet qui, même en se situant à un stade préliminaire, ont montré un certain nombre d'avantages à gérer les tâches de traitement de manière simultanée. De plus, du point de vue théorique, les problèmes sont bien posés et peuvent aboutir à une solution unique.

Parmi les principaux arguments qui sont à la base du choix pour ces modèles combinés, une importance particulière est représentée par leur capacité à traiter une information corrélée. C'est notamment essentiel pour mener à bien des scénarios de fusion d'images pour lesquels l'information d'entrée (liée aux sources S) présente un certain degré de corrélation. Par suite, une approche parallèle permet l'utilisation de cette information corrélée comme information utile et facteur de décision dans le processus de restauration et amélioration d'images. Par ailleurs, dans les scénarios réels, les images ne sont jamais affectées par une seule source de contamination, comme le bruit ou le flou ; un traitement séquentiel conduisant à éliminer une source de contamination peut s'avérer désastreux pour la méthode suivante de la chaîne de traitement.

1.2 Conceptualisation

Pour approcher la solution générale proposée, la construction est fondée sur une approche progressive allant des concepts simples aux plus complexes. La solution finale est donc le résultat d'une analyse en étapes, le résultat intermédiaire de ce processus étant la première méthode proposée, *i.e.*, un nouveau modèle de *filtre de choc* pour simultanément éliminer les flous gaussiens et filtrer le bruit. Ce modèle est pour nous l'occasion d'étudier la faisabilité du concept de parallélisation des méthodes de restauration d'images, ouvrant la voie à un nouveau paradigme d'une complexité et applicabilité supérieure. Par ailleurs, une extension du modèle de filtre de choc proposé dans la première phase consiste à introduire la notion d'*amélioration de cohérence*, notion qui permet d'étendre les domaines d'application de la méthode.

Dans le même temps, le rajout de la caractéristique d'amélioration de cohérence au modèle proposé pour simultanément éliminer les flous gaussiens et filtrer le bruit est

une étape importante vers l'unification des concepts de restauration et d'amélioration des images, objectif final de cette thèse.

La deuxième méthode proposée, *la fusion des images avec élimination du bruit*, vise l'accomplissement d'un objectif double : **(a)** la validation, à la fois théorique et pratique, du concept de la fusion des tâches de traitement d'image ; **(b)** le positionnement en tant que méthode alternative dans le domaine de la fusion des images (au sens large) et dans le domaine de la fusion des images bruitées (au sens restreint), avec des résultats comparables ou supérieurs aux méthodes existantes.

1.3 Organisation

Pour des raisons de cohérence avec le manuscrit complet de la thèse, la structure générale du document a été conservée, en mettant cependant l'accent sur les contributions de la thèse, le fondement théorique étant largement disponible dans le manuscrit complet. Par conséquent, la structure du résumé est la suivante :

Chapitre 1 (section courante) représente la partie introductive de ce résumé, composé de trois parties : : **(i)** *la présentation de l'objet de cette thèse, i.e., la formulation du problème*, **(ii)** *la conceptualisation et l'approche pratique*, et **(iii)** *l'organisation du résumé*.

Chapitre 2 fournit une description des concepts théoriques fondamentaux concernant les approches de traitement d'images fondées sur les équations aux dérivées partielles et leur utilisation dans des formulations variationnelles.

Chapitre 3 présente le premier modèle proposé, *i.e.*, un filtre de choc pour éliminer le flou gaussien et filtrer le bruit simultanément, du point de vue de la formulation théorique, de la validation expérimentale et de l'analyse comparative.

Chapitre 4 est une vue d'ensemble de la terminologie et des définitions liées à la fusion d'images. Il permet de fixer les objectifs clés d'un processus de fusion et de mettre en évidence les lacunes de la méthodologie actuelle d'évaluation qualitative de la fusion dans des scénarios complexes, comme c'est le cas pour *la fusion d'images avec élimination du bruit*.

Chapitre 5 est consacré à décrire en détail le modèle proposé de fusion d'images avec élimination du bruit. Au-delà de la présentation théorique, une analyse expérimentale est proposée ainsi qu'une courte illustration des applications potentielles de la méthode.

Chapitre 6 permet de clore ce résumé en présentant les conclusions finales, les observations sur les modèles proposés ainsi que les perspectives offertes par ce travail de thèse.

CHAPITRE 2

Restauration d'images en utilisant des équations aux dérivées partielles

2.1 Définitions

Le sujet de cette thèse étant orienté vers des éléments spécifiques du traitement d'images, *i.e.*, la *restauration* et l'*amélioration* d'images, il est nécessaire de définir d'abord ces termes et de classer les principaux objectifs du traitement d'images¹.

Sous **DEX**, la *restauration* est définie comme l'action de « Réparer, pour rétablir la forme originale d'un monument architectural, une peinture, etc. ». L'action *d'amélioration* est elle définie comme « l'idée de réaliser une action pour augmenter la qualité ou la valeur d'un objet ».

Même si ces définitions n'expriment pas spécifiquement les concepts dans le contexte du traitement d'images, elles permettent de nous éclairer dans la détermination des différences fonctionnelles entre les deux processus. Ainsi, le processus de *restauration d'images* vise à ramener une image affectée par une contamination (par exemple : bruit, flou) à un état antérieur à la contamination en supposant que l'image était a priori intacte, ne contenant que l'information utile. D'autre part, le processus *d'amélioration des images* a comme point de départ une image a priori inaltérée et vise à augmenter et intensifier les caractéristiques utiles de l'image originale. Dans cette thèse, nous considérons l'amélioration d'images relativement à *l'amélioration de cohérence* d'une image d'une part et à *la fusion d'images* d'autre part.

2.2 Le traitement d'images fondé sur les Équations aux Dérivées Partielles

Dans la méthodologie actuelle, le formalisme EDP² ne représente qu'un des outils mathématiques possibles pour le traitement d'images, selon la classification établie dans [CS05] et au sein de laquelle nous retrouvons : les **méthodes morphologiques** ; l'**analyse de Fourier** et l'**analyse spectrale** ; l'**analyse en ondelettes** et les **espaces normalisés** ; la **modélisation stochastique** ; les **méthodes variationnelles** et donc ; les **méthodes EDP**.

Remarque En ce qui concerne la formulation mathématique, il faut noter que les méthodes variationnelles sont normalement exprimées par des EDP, mais toutes les méthodes fondées sur des EDP ne sont pas implicitement des méthodes variationnelles. Chan et

1. *n.b.* à travers cette thèse la notion de *traitement d'images* se réfère *stricto sensu* au traitement d'images par ordinateur, les images étant représentées par un signal numérique bi- ou tridimensionnel

2. Équations aux Dérivées Partielles

Shen ont montré cet aspect dans [CS05], en illustrant leurs propos à travers les équations *Navier-Stokes* pour la dynamique des fluides et celles de *Maxwell* pour l'électromagnétisme.

L'utilisation des EDP pour le traitement d'images est une des conséquences de leur utilisation en physique, où elles ont été utilisées pour modéliser certains phénomènes, parmi lesquels un bon exemple est la propagation de la chaleur. Koenderink a été le premier à établir dans [Koe84] l'équivalence entre la solution de l'équation de propagation de la chaleur au moment t (modélisée par une EDP) et le processus de convolution avec un noyau gaussien d'écart-type $\sqrt{2t}$. En traitement d'images, cette équation est connue comme *la diffusion isotrope* et a été formalisée initialement sur la base de trois principes [Koe84] : (i) *causalité*, (ii) *homogénéité* et (iii) *isotropie*.

2.3 Le filtrage linéaire dans la restauration d'images

Dans le domaine du traitement d'images, le bruit, facteur de contamination du signal utile, est considéré comme un signal à haute fréquence. Une solution immédiate au filtrage du bruit est donnée par *la diffusion isotrope*. Soit $I_0 : \mathbb{R}^2 \rightarrow \mathbb{R}$ la fonction luminance qui décrit l'image originale, contaminée, définie sur l'ensemble $\Omega = [0, a] \times [0, b]$. L'image filtrée, $I(x, y, \sigma)$, est mathématiquement exprimée comme :

$$I(x, y, \sigma) = I_0(x, y) * G_\sigma(x, y) = \int_{\Omega} G_\sigma(x - u, y - v) I_0(u, v) dudv \quad (2.1)$$

où σ représente l'écart-type de G , qui dans la plupart des cas représente un noyau gaussien. Basé sur l'équivalence établie par Koenderink dans [Koe84], le processus de filtrage peut être exprimé alternativement comme une EDP (*l'équation de diffusion isotrope*) :

$$\begin{cases} I(x, y, 0) = I_0(x, y) \\ \frac{\partial I}{\partial t} = \Delta I = I_{xx}(x, y, t) + I_{yy}(x, y, t) \end{cases} \quad (2.2)$$

Remarque Il faut souligner dès le départ que, à cause de son caractère isotrope, (2.2) a une applicabilité limitée, en raison de la complexité des images réelles. Cette complexité liée à la manière dont l'information utile est structurée dans les images numériques. Par exemple, l'œil humain est sensible aux changements de contraste qui se traduisent par la présence de contours et de bords, structures qui, au niveau du signal, représentent des composantes haute fréquence. Un processus isotrope filtrera une image sans prendre en compte sa structure et par conséquent filtrera sans discriminer à la fois le bruit et les bords et contours.

A partir des observations précédentes, les raisons pour lesquelles un filtrage isotrope ne peut être appliqué qu'aux images dotées d'une géométrie très simple sont faciles à comprendre. Dans ce cas, le temps d'évolution du modèle EDP isotrope doit être très limité pour empêcher le filtrage de l'information utile. Toutefois, l'équivalence établie par Koenderink entre le phénomène de diffusion de la chaleur, comme processus physique, et le processus de convolution, comme mécanisme de filtrage d'images, a été un précédent motivant, moteur du développement de la méthodologie EDP permettant de développer des méthodes plus en adéquation avec les besoins de l'analyse d'images.

2.4 Filtrage non linéaire – diffusion anisotrope

Partant des limitations du modèle isotrope, Perona et Malik ont proposé dans [PM90] le premier modèle de *diffusion anisotrope*, un modèle de diffusion sélective avec rehaussement des contours, exprimé par l'EDP suivante :

$$\frac{\partial I}{\partial t} = \operatorname{div} [c(x, y, t) \nabla I(x, y, t)] \quad (2.3)$$

où $I(x, y, 0) = I_0(x, y)$ est la condition initiale de (2.3), modèle qui peut être réécrit sous la forme :

$$\frac{\partial I}{\partial t} = c \Delta I + \nabla c \cdot \nabla I \quad (2.4)$$

et, en considérant le cas particulier $c(x, y, t) = \text{const.}$, l'équivalence de (2.4) et (2.2) est immédiate.

La fonction c , appelée par les auteurs *conductibilité*, est définie de façon à favoriser le filtrage intra-régions au détriment du filtrage inter-régions afin de donner au modèle proposé le caractère anisotrope, l'attribut clé de (2.3). Le contrôle du caractère anisotrope de (2.3), à travers de la fonction c , est obtenu en la rendant dépendante de la norme du gradient de la fonction image I :

$$c(x, y, t) = g(|\nabla I|)$$

Pour la fonction *conductibilité*, Perona et Malik [PM90] proposent des fonctions de base (2.4) de la forme :

$$g(|\nabla I|) = \exp \left[- \left(\frac{|\nabla I|}{K} \right)^2 \right] \quad (2.5)$$

et

$$g(|\nabla I|) = \frac{1}{1 + \left(\frac{|\nabla I|}{K} \right)^2} \quad (2.6)$$

où K est un paramètre de seuil, appelé la *barrière de diffusion*.

Le modèle de diffusion anisotrope de Perona et Malik proposé dans [PM90] marque le début de l'utilisation des EDP dans le traitement d'images et est le premier modèle formalisé par EDP avec des fonctionnalités complètes et une utilité immédiate. Il va sans dire que la diffusion anisotrope a représenté et représente toujours un point de départ dans le développement de nouveaux modèles mathématiques formulés par EDP. Parmi ces derniers, on peut mentionner ceux qui ont succédé au modèle de Perona et Malik, en apportant des améliorations à ce dernier ou en redéfinissant le concept de diffusion anisotrope : le modèle Catté *et al.* [CLMC92], le modèle Nitzberg et Shiota [NS92], le modèle Whitaker et Pizer [WP93], le modèle unificateur EDP-variationnel Deriche et Faugeras [DF95], les modèles tensoriels Weickert [Wei94], et d'autres.

Pour une description détaillée de la méthodologie EDP dans la restauration d'images, le lecteur est invité à consulter le manuscrit complet de la thèse, qui comprend entre autres, une section consacrée à la discrétisation des modèles mathématiques exprimées par EDP pour leur utilisation dans le traitement numérique des images.

CHAPITRE 3

Restauration d'images par filtres de choc hybrides

3.1 Introduction

Avant de détailler la première proposition de cette thèse (le *filtre de choc mixte pour l'élimination du flou gaussien avec filtrage de bruit*, i.e., le *filtre de choc hybride*), il est nécessaire de lier les concepts abordés dans le chapitre précédent avec les aspects théoriques caractéristiques des filtres de choc. Dans la problématique du filtrage du bruit, l'approche classique consiste à utiliser un processus de convolution pour filtrer les composantes isolées de haute fréquence du signal 2-D, réduisant ainsi l'entropie globale de l'image. La solution élémentaire dans le cas de l'utilisation d'un formalisme EDP consiste à utiliser un filtre décrit par l'équation de diffusion anisotrope proposée par Perona et Malik dans [PM90].

Dans le cas des filtres de choc, la contamination du signal utile est donnée par un processus indésirable de convolution, aussi appelé défocalisation. En tant que manifestation physique, la défocalisation est un effet commun dans la photographie et peut être causée par divers facteurs tels que les mouvements du sujet ou du dispositif d'acquisition des images, les conditions atmosphériques ou la focalisation incorrecte. Dans ce cas, la restauration de l'image défocalisée se traduit par l'application d'un processus inverse appelé déconvolution. L'inversion du processus de diffusion anisotrope peut être considéré comme une solution apparemment simple, le résultat étant une déconvolution en tant que processus de filtrage, au lieu de la convolution classique (diffusion). Mais du point de vue mathématique, une telle formulation est « mal posé », car elle représente un problème sans solution unique, qui, numériquement, se comporte de manière divergente.

Pour répondre de manière efficace à ce problème, Osher et Rudin ont proposé dans [OR90] une formulation mathématique basée sur une EDP, qui décrit un processus de déconvolution à solution unique, surmontant les problèmes posés par l'approche directe, celle de la diffusion inverse. Par exemple, considérons le cas particulier d'un signal unidimensionnel initialement décrit par la fonction $-\sin(x)$, le problème de traitement étant défini comme le processus de déconvolution décrit par une EDP à solution initiale $-\sin(x)$:

$$\begin{cases} \frac{\partial I}{\partial t} = -|I_x| \operatorname{sgn}(I_{xx}) \\ I(x, 0) = I_0(x) = -\sin(x) \end{cases} \quad (3.1)$$

La méthode décrite dans (3.1), connue dans la littérature comme le *filtre de choc*, représente une solution directe et relativement simple du problème de la convolution (flou) comme élément perturbateur dans le traitement d'images.

Remarque Il nous faut préciser que la validité de (3.1) n'est assurée que dans le domaine discret à travers d'une discrétisation explicite, proposée par les auteurs afin de s'assurer de la convergence et de l'unicité de la solution.

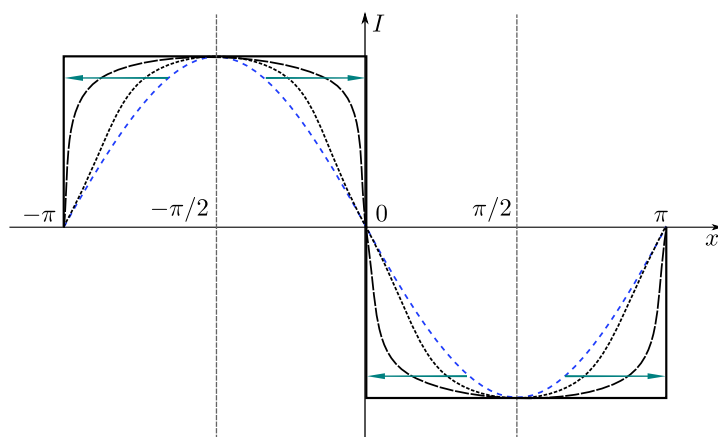


Figure 3.1 – Exemple d'un processus de déconvolution pour un signal 1-D pour $I_0(x) = -\sin(x)$ défini sur l'intervalle $[-\pi, \pi]$. La ligne pointillée bleue représente le signal original, alors que la ligne continue illustre l'évolution temporelle de la fonction I . Les flèches indiquent la direction de propagation de l'effet de déconvolution.

Le principe de fonctionnement d'un filtre de choc classique, pour un signal initial 1-D donné par la fonction $I_0(x) = -\sin(x)$, est illustré par *Fig. 3.1*. Dans ce cas, le signal d'origine I_0 est considéré comme affecté par une convolution gaussienne et le résultat du filtrage avec un filtre de choc est idéalement représenté par un signal *échelon unité*.

3.2 Le filtre de choc hybride

Les éléments présentés jusqu'à présent ont montré la manière dont on peut attaquer deux problèmes majeurs dans la restauration d'images, *i.e.*, le filtrage du bruit et la déconvolution. Du point de vue théorique, les deux processus sont modélisés par des procédés de caractéristique et effet inverses, par conséquent, leur résolution est obtenue à travers des méthodes d'effet contraire. Plus précisément, le filtrage du bruit nécessite un processus de convolution, alors que l'élimination des défocalisations exige un processus de déconvolution. Il est facile à comprendre que la définition d'un paradigme de restauration d'images qui puisse gérer les deux types de traitement (filtrage du bruit et déconvolution), impliquera un degré élevé de complexité devant gérer avec succès le caractère contradictoire de ces deux opérations.

Le filtre de choc hybride représente la première approche pour une problématique liée à la combinaison filtrage-déconvolution pour la restauration d'images. Les fondements de ce filtre se trouvent dans le filtre de choc complexe proposé par Gilboa *et al.* dans [GSZ02], qui propose une redéfinition radicale de la notion de filtre de choc par extension dans le domaine complexe. Ainsi, la fonction image I est considérée comme une fonction complexe, dont la partie réelle décrit la vraie image et la partie imaginaire se comporte comme un détecteur robuste de contours, détecteur qui permet la détection correcte des contours même en présence du bruit, performance qui manque au filtre de choc classique.

Bien que le filtre choc complexe proposé par Gilboa *et al.* possède plusieurs avantages qui lui permettent de gérer avec succès des scénarios complexes de restauration, tels que le bruit avec flou gaussien superposé, les résultats expérimentaux ont montré sa

divergence lorsque l'image d'entrée nécessite un degré de filtrage élevé. Lorsque le degré de contamination varie d'une image à une autre, il est difficile de fixer *a priori* le temps nécessaire pour un filtrage suffisant de chaque image.

Considérant les deux grandes classes de filtres de choc, c'est à dire, classique et complexe, et les avantages et inconvénients respectifs, le modèle hybride de filtre de choc a pour but de combiner les avantages des deux filtres, mais sans en conserver les inconvénients. Ainsi, le filtre de choc hybride possède la robustesse au bruit du filtre complexe et le caractère stable-convergent du filtre de choc classique.

3.2.1 Le modèle mathématique

Du point de vue mathématique, le filtre de choc hybride est défini sur un domaine complexe, de la même manière que le filtre de choc complexe, mais avec la différence qu'une de ses composantes est définie exclusivement de manière réelle en étant très similaire du point de vue fonctionnel au filtre de choc classique. Ainsi, soit $I: \Omega \rightarrow \mathbb{C}$, avec $\Omega \subset \mathbb{R}^2$ dans le cas où l'espace de l'image est considéré continu, et $\Omega \subset \mathbb{N}^2$ quand l'espace de l'image est un domaine discret.

Les conditions initiales pour l'EDP qui décrit le modèle du filtre de choc hybride sont exprimées pour l'image $I(x, y, t)$ avec $(x, y) \in \Omega$ comme : $I(x, y, 0) = I_0(x, y)$, $I_0(x, y) \in \mathbb{R}$ et $\frac{\partial I}{\partial n} = 0$, où n représente la direction orthogonale aux bords de l'image, exprimant ainsi des conditions au limite du type Neumann. Le modèle mathématique est exprimé comme suit :

$$\begin{cases} \operatorname{Re} \left(\frac{\partial I}{\partial t} \right) = -\frac{2}{\pi} \arctan \left(a \cdot \frac{\operatorname{Im}(I)}{\theta} \right) f_1(t) |\nabla I| - \operatorname{sgn}(\operatorname{Re}(I_{\eta\eta})) f_2(t) |\nabla I| \\ \quad + f_1(t) \left(\operatorname{Re}(\lambda) \operatorname{Re}(I_{\eta\eta}) - \operatorname{Im}(\lambda) \operatorname{Im}(I_{\eta\eta}) + \tilde{\lambda} \operatorname{Re}(I_{\xi\xi}) \right) \\ \operatorname{Im} \left(\frac{\partial I}{\partial t} \right) = \operatorname{Im}(\lambda) \operatorname{Re}(I_{\eta\eta}) - \operatorname{Re}(\lambda) \operatorname{Im}(I_{\eta\eta}) + \tilde{\lambda} \operatorname{Im}(I_{\xi\xi}) \end{cases} \quad (3.2)$$

Etant donné que le modèle du filtre de choc hybride est partiellement dérivé du filtre de choc complexe, les deux filtres partagent un certain nombre de paramètres d'entrée, lorsque le reste des paramètres sont spécifiques au filtre de choc hybride :

- a - le paramètre qui pilote la pente de la fonction signe *arctan*, permettant de gérer le fonctionnement du détecteur des contours.
- θ - l'argument complexe qui sert à calculer le paramètre complexe λ , où $\theta \in (-\pi/2, \pi/2)$. Quand $\theta \rightarrow 0$, $\frac{\operatorname{Im}(I)}{\theta}$ rapproche un laplacien lissé de la fonction image I , approximation mathématiquement démontrée en [GZS01], qui confère à la fonction un caractère de « détecteur de contour naturellement régularisé ».
- $|\nabla I|$ - la norme du gradient de la fonction I , approchée numériquement en utilisant la fonction *minmod*, de la manière dont elle a été initialement définie par Osher et Rudin dans [OR90].
- $\lambda = r \cdot e^{i\theta}$ - paramètre scalaire complexe, calculé en utilisant le paramètre θ .
- $\tilde{\lambda}$ - paramètre scalaire réel.
- $f_1(t)$ et $f_2(t)$ - les deux fonctions complémentaires de contrôle, propres au filtre de choc hybride. Leur rôle est de contrôler le comportement du filtre de choc hybride aux différents instants de son évolution temporelle. A travers ces fonctions de

contrôle, la transition d'un comportement exclusivement complexe à un comportement exclusivement réel est réalisée progressivement, les deux comportements coexistant pendant un nombre d'itérations paramétré.

L'ensemble des fonctions de contrôle est défini de la forme :

$$f_1(T_{1i}, T_{1s}) = \begin{cases} 1, & n < T_{1i} \\ 1 - \frac{n - T_{1i}}{T_{1s} - T_{1i}}, & T_{1i} \leq n < T_{1s} \\ 0, & n \geq T_{1s} \end{cases} \quad (3.3)$$

$$f_2(T_{2i}, T_{2s}) = \begin{cases} 0, & n < T_{2i} \\ \frac{n - T_{2i}}{T_{2s} - T_{2i}}, & T_{2i} \leq n < T_{2s} \\ 1, & n \geq T_{2s} \end{cases}$$

avec $n = 0 \dots N_n - 1$ et $T_{1i}, T_{1s}, T_{2i}, T_{2s} \in [0, N_n - 1]$, ou comme définition alternative :

$$\begin{cases} f_1(\omega) = \cos(\omega) \\ f_2(\omega) = \sin(\omega) \end{cases} \quad \omega = \frac{\pi}{2} \cdot \frac{n}{N_n - 1}, \quad n = 0 \dots N_n - 1 \quad (3.4)$$

3.2.2 L'extension du modèle pour l'amélioration de cohérence

Le rajout de la caractéristique *d'amélioration de cohérence* au filtre de choc hybride conduit à la combinaison de deux méthodes de traitement d'images, *i.e.*, le filtrage du bruit et l'élimination du flou, et par la même à la corrélation de deux domaines du traitement d'images, plus précisément, la restauration et le rehaussement d'images. De ce fait, le premier pas est fait vers la définition d'une méthode composée incluant la restauration et le rehaussement d'images dans un seul processus parallèle et indépendant. Le pas final afin d'atteindre cet objectif est représenté par *la méthode de fusion d'images avec élimination simultanée du bruit*, décrite dans le **Chapitre 5**.

Le modèle du filtre de choc hybride est donc reformulé pour inclure une composante d'amélioration de cohérence, de la façon dont elle est définie par Weickert [Wei03] :

$$\begin{cases} \operatorname{Re} \left(\frac{\partial I}{\partial t} \right) = -\frac{2}{\pi} \arctan \left(a \cdot \frac{\operatorname{Im}(I)}{\theta} \right) f_1(t) |\nabla I| - \operatorname{sgn} \left(\operatorname{Re}(I_{ww}^\sigma) \right) f_2(t) |\nabla I| \\ \quad + f_1(t) \left(\operatorname{Re}(\lambda) \operatorname{Re}(I_{\eta\eta}) - \operatorname{Im}(\lambda) \operatorname{Im}(I_{\eta\eta}) + \tilde{\lambda} \operatorname{Re}(I_{\xi\xi}) \right) \\ \operatorname{Im} \left(\frac{\partial I}{\partial t} \right) = \operatorname{Im}(\lambda) \operatorname{Re}(I_{\eta\eta}) - \operatorname{Re}(\lambda) \operatorname{Im}(I_{\eta\eta}) + \tilde{\lambda} \operatorname{Im}(I_{\xi\xi}) \end{cases} \quad (3.5)$$

où $I_{ww}^\sigma = (G_\sigma * I)_{ww}$, et w est le vecteur propre normalisé associé à la plus grande valeur propre du tenseur \mathbf{J}_ρ , valeur propre qui décrit la direction le long de laquelle le changement de contraste est maximum. Le tenseur \mathbf{J}_ρ représente la version lissé du *tenseur de structure* calculé pour chaque pixel de l'image I :

$$\mathbf{J}_\rho(\nabla I) = G_\rho * (\nabla I \cdot \nabla I^T) \quad (3.6)$$

3.2.3 Analyse expérimentale

Dans l'analyse expérimentale, les modèles de filtres de choc existantes, proposés dans [OR90, AM94, KDA97, GSZ02, RC03, BCM05, BCM06], vont être utilisés comme étalon.

Par ailleurs, une vaste gamme des métriques objectives pour l'évaluation qualitative des résultats est employée, par exemple RMSE (Root Mean Square Error - Erreur Quadratique Moyenne), PSNR (Peak Signal-to-Noise Ratio), SCC (Sample Correlation Coefficient), MI (Mutual Information - Information Mutuelle), SSIM (Structural SIMilarity index) proposé par Wang *et al.* dans [WBSS04], MSSIM (Multiscale Structural SIMilarity index), proposé aussi par Wang *et al.* et détaillé en [WSB03] et, sans oublier, VSNR (Visual Signal-to-Noise Ratio) [CH07] et VIF (Visual Information Fidelity) [SB06].

Pour assurer l'objectivité de l'évaluation et pour éliminer toute dépendance d'implantation des métriques de qualité, ces dernières ont été utilisées dans la forme incluse dans le paquet *MeTriX MuX Visual Quality Assessment Package*, disponible dans [Gau11].

La partie expérimentale est brièvement décrite dans ce résumé, l'analyse complète étant disponible dans le manuscrit de la thèse. L'image réelle *Bateau de pêche*, disponible dans la base d'images [Uni11], représente une scène réelle, en format numérique de 8 bits/pixel (en niveaux de gris) de dimension 512×512 pixels et va être utilisée pour illustrer les méthodes.

Le cadre expérimentale consiste à contaminer l'image de référence avec un flou gaussien d'écart-type $\sigma_f = 3$ et ensuite avec un bruit blanc gaussien additif d'écart-type $\sigma_b = 10$. L'image contaminée de cette façon va être considérée l'image I_0 à l'instant $t = 0$ et va représenter l'image d'entrée pour les filtres de choc testés dans la suite (Fig. 3.2 et Tableau 3.1).

L'analyse expérimentale du filtre de choc hybride est complétée par le test du modèle étendu, décrit par (3.6). En ce sens, le traitement des empreintes digitales est un scénar-

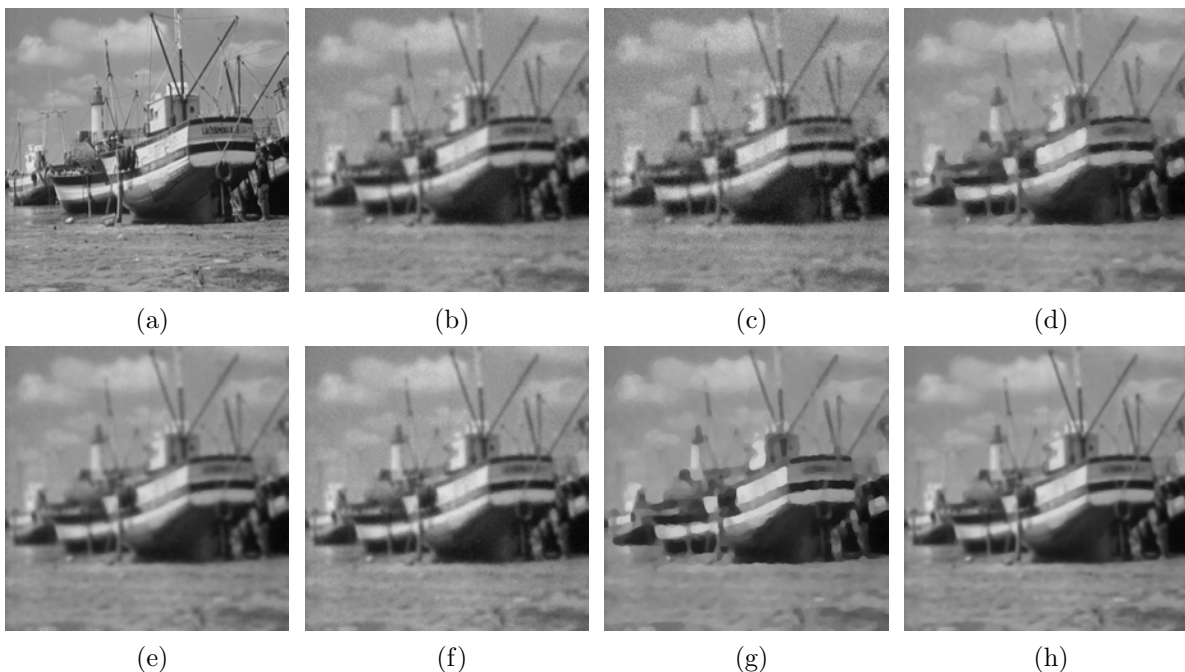


Figure 3.2 – *Filtres de choc - analyse comparative : (a) Image de référence ; (b) Image initiale contaminée I_0 - flou gaussien ($\sigma_f = 3$) + bruit blanc gaussien additif ($\sigma_b = 10$) ; (c) Résultat du filtre Osher–Rudin ; (d) Résultat du filtre Alvarez–Mazorra [AM94] ; (e) Résultat du filtre Kornprobst et al. [KDA97] ; (f) Résultat du filtre Remaki–Cheriet [RC03] ; (g) Résultat du filtre Gilboa et al. ; (h) Résultat du filtre de choc hybride.*

Table 3.1 – Résultats de l'analyse qualitative – cadre expérimental Fig. 3.2

Type de filtre de choc	Métriques de qualité							
	RMSE	PSNR	SCC	MI	SSIM	MSSIM	VSNR	VIF
Image initiale I_0	16,74	23,655	0,93	1,199	0,401	0,806	13,097	0,122
Osher–Rudin	19,96	22,127	0,901	1,041	0,292	0,764	12,901	0,1
Alvarez–Mazorra	15,072	24,567	0,944	1,38	0,653	0,82	11,455	0,101
Kornprobst <i>et al.</i>	14,669	24,802	0,948	1,453	0,678	0,831	11,473	0,128
Remaki–Cheriet	14,326	25,007	0,952	1,507	0,666	0,848	11,943	0,136
Gilboa <i>et al.</i>	14,812	24,718	0,946	1,425	0,671	0,824	11,62	0,104
Filtre de choc hybride	12,668	26,076	0,961	1,6	0,727	0,879	13,082	0,183

rio adapté pour souligner la caractéristique d'amélioration de cohérence. Le test repose, comme le précédent, sur une image de référence, soumise à une dégradation avec un flou gaussien, suivie par une contamination avec un bruit blanc, gaussien aditif. L'image résultante va représenter l'image initiale I_0 . En tant que méthodes comparatives, seuls deux filtres vont être utilisés : le filtre CESF proposé par Weickert, spécialement conçu pour ce type d'images, et le filtre de choc complexe. Ces deux filtres sont les plus représentatifs pour ce scénario de test, illustré à la Fig. 3.3 et qualitativement exprimé au Tableau 3.2.

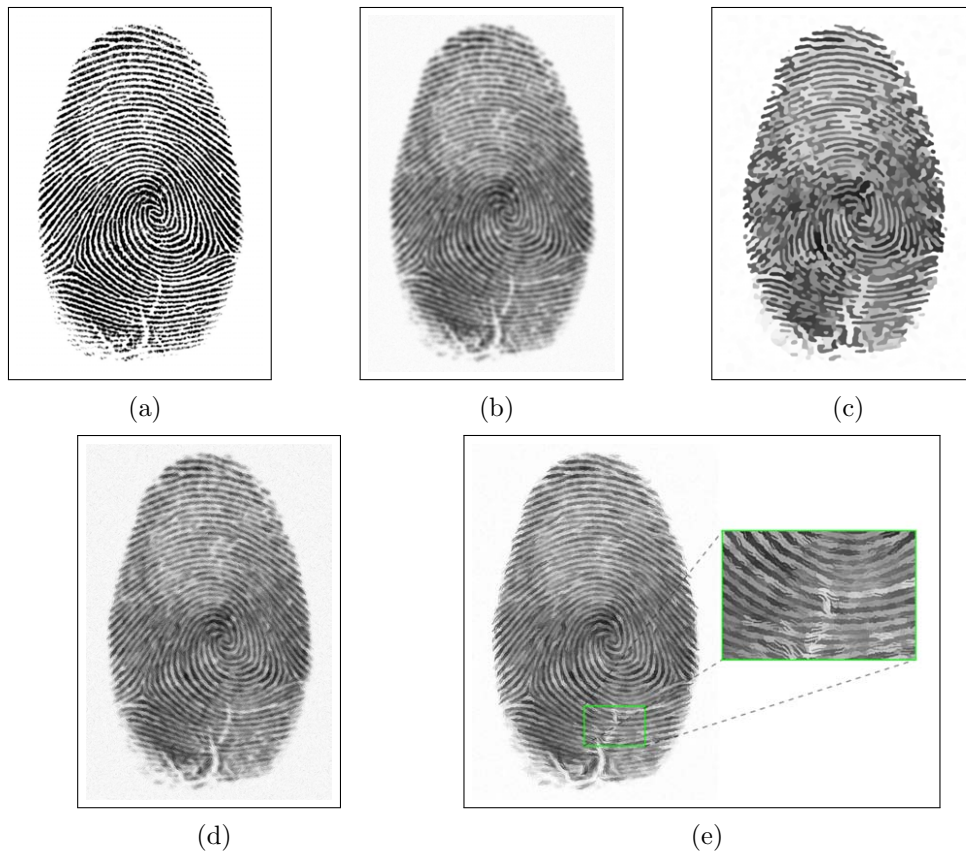


Figure 3.3 – Filtres de choc hybride avec amélioration de cohérence – analyse comparative : (a) Image de référence ; (b) Image initiale contaminée I_0 flou gaussien ($\sigma_f = 10$) + bruit blanc gaussien additif ($\sigma_b = 25$) ; (c) Résultat du filtre Gilboa *et al.* ; (d) Résultat du filtre CESF de Weickert ; (e) Résultat du filtre de choc hybride avec amélioration de cohérence + détail.

Table 3.2 – Résultats de l'analyse qualitative – cadre expérimental Fig. 3.3

Type de filtre de choc	Métriques de qualité						
	RMSE	PSNR	MI	SSIM	MSSIM	VSNR	VIF
Image initiale I_0	63,217	12,114	1,032	0,372	0,572	5,014	0,08
Gilboa <i>et al.</i>	65,471	11,809	0,84	0,519	0,561	5,167	0,04
Weickert CESF	62,394	12,227	0,935	0,289	0,577	5,857	0,059
Hybride avec amélioration de cohérence	61,203	12,395	0,995	0,486	0,627	5,576	0,059

3.3 Conclusions

Le modèle du filtre de choc est, comme précisé dans le **Chapitre 1**, une étape intermédiaire dans la démarche conduisant à définir un modèle EDP complexe, combinant la restauration et le rehaussement d'images. Néanmoins, il faut souligner le caractère original de cette méthode et son potentiel pour des applications concrètes en tant que méthode de restauration d'images. Par ailleurs, en rajoutant *l'amélioration de cohérence* au modèle initial, un paradigme de restauration-rehaussement d'images est obtenu, paradigme qui représente le pas intermédiaire dans la réalisation de l'objectif final : la définition d'un modèle pour la restauration et le rehaussement d'images.

Les résultats expérimentaux présentés en §3.2.3 ont démontré que le modèle proposé a atteint ses objectifs principaux : **(i)** gérer correctement les images bruitées et enlever le bruit de manière satisfaisante (spécificité du filtre de choc complexe); **(ii)** gérer le flou gaussien de façon adaptée tant du point de vue qualitatif que du point de vue de la stabilité et de la convergence (spécificité du filtre de choc classique); **(iii)** combiner avec succès des caractéristiques des filtres de choc classique et complexe et obtenir ainsi un nouveau modèle dont les caractéristiques combinent les avantages des deux filtres, sans en garder les inconvénients.

Les perspectives potentielles peuvent inclure les actions suivantes :

- définir des nouvelles fonctions de contrôle, directement dépendantes de la géométrie de l'image, pour mieux distinguer entre les zones homogènes et non-homogènes,
- redéfinir le détecteur de contours, afin de renforcer son caractère anisotrope,
- étudier la possibilité de rajouter un indicateur d'orientation, locale ou semi-locale, pour contrôler l'intensité du filtrage comme paramètre des fonctions de contrôle *et*
- utiliser des méthodes de discrétisation plus élaborées et une approche tensorielle afin d'augmenter la qualité du résultat filtré.

CHAPITRE 4

La fusion d'images comme un processus d'amélioration d'images

4.1 Introduction

En conformité avec [Mit10], les principaux avantages de la fusion d'images sont : (i) **une confiance accrue dans le résultat final**, (ii) **la réduction des incertitudes**, (iii) **la robustesse des performances**, (iv) **la représentation compacte de l'information**, (v) **le domaine étendu de l'applicabilité**, et (vi) **la couverture spatiale et temporelle étendue**.

4.2 Définitions et classifications

La fusion peut être définie dans beaucoup de domaines comme la combinaison d'informations ou de données multiples permettant d'en retirer l'essentiel en consolidant l'information utile. La fusion d'images exige une définition plus précise, adaptée aux rigueurs et aux réalités du traitement d'images. Par conséquent, au fil du temps, la fusion d'images a été définie dans divers contextes, comme partie de la fusion de données ou de la fusion d'informations. Parmi les définitions les plus pertinentes, on retrouve :

Abidi et Gonzalez [AG92] – « *La fusion de données* concerne la combinaison synergique de l'information mise à la disposition par diverses sources de connaissances, par exemple les capteurs, afin de mieux comprendre une scène réelle donnée. »

Hall [Hal92] – « *La fusion de données multi-sensoriale* cherche à combiner l'information issue de plusieurs capteurs pour formuler des déductions autrement impossible à formuler en s'appuyant sur un seul capteur. »

Bloch et Maître [BM08] – « *La fusion d'information* consiste à combiner l'information issue de sources multiples afin d'améliorer le processus de prise de décision. »

En ce qui concerne la classification des processus de fusion, plusieurs critères peuvent être employés. Parmi les plus utilisés, nous retrouvons celui de la nature et de la complexité de l'information fusionnée, plus précisément la complexité d'intégration de l'information pendant la fusion. Ainsi, quatre niveaux de complexité peuvent être distingués :

- *niveau du signal*
- *niveau de l'image*, aussi appelé *niveau de pixel*
- *niveau de la caractéristique* ou autrement dit *niveau de symbole*
- *niveau de décision*

Une autre classification assez souvent rencontrée dans la littérature, répartit les méthodes de fusion en : (a) *des méthodes basées sur des décompositions multi-échelle* et (b) *des méthodes basées sur des décompositions non-multi-échelle*.

CHAPITRE 5

La fusion d'images avec élimination du bruit

5.1 Motivation

L'idée de réunir plusieurs processus dans un seul prend sa source dans la nécessité de réaliser le traitement d'images d'une manière réaliste, les cas réels de perturbation d'image n'étant jamais causés par un seul facteur perturbateur. Le modèle proposé et analysé dans ce chapitre est basé sur la remise en cause de l'a priori que les images sont « parfaites » ; en réalité, les images sont affectées par diverses sources perturbantes, une des plus communes étant le bruit.

Par conséquent, en considérant un scénario proche de la réalité (les images à fusionner ne sont pas idéales), la nécessité de la formulation d'un modèle qui puisse combiner la fusion d'images avec des éléments de restauration d'images est évidente. Etant donné que parmi les facteurs perturbateurs les plus souvent rencontrés il y a le bruit, le modèle proposé est représenté par un paradigme de fusion d'images avec filtrage simultané du bruit, défini en utilisant un formalisme variationnel, exprimé théoriquement par des EDP. La méthode s'inscrit ainsi dans la catégorie d'autres propositions, relativement récentes, [Pha01, PLTB07, PTB⁺07, MS08, Pop08, WSF08], qui abordent également le processus de fusion d'images d'une manière complexe, tenant compte de la réalité des problèmes posés.

Une des questions posées dans le cas de ce scénario est « quels sont les avantages d'un traitement parallèle par rapport à un traitement séquentiel ? ». La réponse est en partie donnée par la complexité et la corrélation de l'information dans les processus de fusion d'images. Dans le cas d'un scénario réel de fusion pour lequel les images d'entrée sont contaminées par du bruit, le traitement séquentiel éliminerait une partie de la corrélation préexistante entre les sources à travers le préfiltrage du bruit. Le filtrage réalisé pour chaque image de manière indépendante ne permettrait pas la prise en compte des connexions au niveau informationnel entre l'image courante et le reste des images d'entrée (voir le chapitre 5 de la thèse pour plusieurs détails et des approches expérimentales).

En opérant simultanément les deux processus, *i.e.*, fusion et élimination du bruit, nous proposons une méthode qui non seulement filtre le bruit d'une manière plus efficace (par la corrélation et le traitement simultané des images d'entrée), mais aussi conduit à un résultat final de qualité équivalente ou supérieure aux processus séquentiels.

5.2 Formulation mathématique

Le modèle mathématique de la méthode de *fusion d'images avec élimination simultanée du bruit* a ses racines dans le modèle variationnel de fusion d'images proposé par John

et Vorontsov dans [JV05]. Ce modèle est basé sur la théorie de l'estimation de l'erreur, théorie qui suppose l'existence d'une image dégradée observée $I: \Omega \rightarrow \mathbb{R}$ et de sa version restaurée $I_r(x, y)$, où (x, y) représente les coordonnées du pixel dans l'espace de l'image $\Omega \subset \mathbb{R}^2$.

L'image restaurée $I_r(x, y)$ peut être estimée en utilisant la théorie de l'estimation de l'erreur, à travers une fonctionnelle d'erreur $E(I_r)$ qui exprime la différence entre l'image originale, observée, et l'image estimée, comme fonction de I_r :

$$E(I_r) = \int_{\Omega} \rho((x, y), I_r(x, y), |\nabla I_r(x, y)|) dx dy \quad (5.1)$$

où Ω est le support de l'image et $\nabla I_r(x, y)$ est le vecteur gradient de l'image au pixel (x, y) .

La norme de l'erreur ρ est définie en concordance avec les exigences de l'application mais également avec le type de contamination à filtrer. Par exemple, dans le cas de l'élimination de bruit sur une image dégradée, un choix possible pour ρ est le minimum de la norme de l'erreur quadratique moyenne, exprimé par :

$$\rho((x, y), |\nabla I_r(x, y)|) = \frac{1}{2} |\nabla I_r(x, y)|^2 \quad (5.2)$$

Il faut préciser qu'un tel choix n'est pas adapté pour des applications pratiques, parce que du point de vue du filtrage son comportement est isotrope ce qui conduit à des effets indésirables dans le cas du traitement d'images (fait déjà commenté dans le **Chapitre 2**). Pour les détails concernant la théorie de l'estimation de l'erreur, le lecteur est invité à consulter le manuscrit complet de la thèse.

L'alternative utilisée dans les méthodes variationnelles de fusion basées sur cette formalisation, e.g., [JV05, WSF08, MS08], est une norme d'erreur avec une composante de diffusion isotrope et rehaussement des contours, définie comme suit :

$$\begin{aligned} \rho((x, y), I_r(x, y, t), |\nabla I_r(x, y, t)|) &= \frac{\alpha}{2} |\nabla I_r(x, y, t)|^2 \\ &+ \frac{\beta}{2} J_I(x, y) [I_r(x, y, t) - I(x, y)]^2 \end{aligned} \quad (5.3)$$

où α et β sont les paramètres utilisés pour le contrôle du niveau de filtrage du bruit et du rehaussement des contours, tandis que J_I est une carte de contours avec un pre-filtrage gaussien de la forme :

$$J_I(x, y) = \int |\nabla I(x', y')|^2 G(x - x', y - y', \sigma) dx' dy' \quad (5.4)$$

où G est une fonction gaussienne de moyenne nulle et d'écart-type σ .

L'inconvénient de (5.3) est le fait que, même s'il permet d'ajouter une composante de rehaussement de contours contenant également un mécanisme d'attache aux données initiales (différence entre l'image estimée et l'image dégradée), le filtrage du bruit est toujours réalisé de manière isotrope. Ainsi définie, la méthode de fusion ne peut être appelée méthode combinée de restauration-rehaussement, étant du point de vue fonctionnel exclusivement une méthode de fusion d'images.

En conséquence, pour définir une méthode complexe de restauration et rehaussement d'images, plus précisément de *fusion d'images avec élimination simultanée du bruit*, il est

nécessaire de définir une norme d'erreur appropriée, permettant un filtrage anisotrope efficace du bruit, de la forme :

$$\begin{aligned} \rho((x, y), I_r(x, y, t), |\nabla I_r(x, y, t)|) = & -\frac{\alpha}{2} \frac{|\nabla I_r(x, y, t)|^2}{\nabla I_r(x, y, t)} \nabla^{-1} [\mathfrak{D}_a(I_r(x, y, t))] \\ & - \frac{\beta}{2} J(x, y, t) [I_r(x, y, t) - I(x, y)]^2 \end{aligned} \quad (5.5)$$

où ∇^{-1} est l'inverse de l'opérateur ∇ et $J(x, y, t) = J_I(x, y) - J_{I_r}(x, y, t)$ la fonction de control du rehaussement des contours, initialement définie dans [JV05], et redéfinie pour le modèle proposé comme suit :

$$\begin{aligned} J(x, y, t) = & \int |\dot{\nabla} I(x', y')| G(x - x', y - y', \sigma_{em}) dx' dy' \\ & - \int |\dot{\nabla} I_r(x', y', t)| G(x - x', y - y', \sigma_{em}) dx' dy' \end{aligned} \quad (5.6)$$

avec $\dot{\nabla}$ représentant le vecteur gradient calculé exclusivement sur la direction η , $\vec{\eta} = \nabla I_r / |\nabla I_r|$.

En remplaçant la norme d'erreur proposée, *i.e.*, (5.6), dans la solution (5.1) pour plusieurs détails, voir la version intégrale de la thèse), l'expression suivante est obtenue pour l'image restaurée I_r :

$$\frac{\partial I_r(x, y, t)}{\partial t} = -\alpha \mathfrak{D}_a(I_r(x, y, t)) + \beta \Theta(J(x, y, t)) J(x, y, t) [I_r(x, y, t) - I(x, y)] \quad (5.7)$$

où

$$\mathfrak{D}_a(I_r) = c_\xi I_{r\xi\xi} + c_\eta I_{r\eta\eta} \quad (5.8)$$

représente un opérateur différentiel de diffusion anisotrope, initialement définie dans [TLBB02, TBB⁺04], tandis que $\Theta(J)$ est définie de façon à permettre seulement le transfert d'information pertinente dans I_r :

$$\Theta(J) = \begin{cases} 1, & \text{si } J \geq 0 \\ 0, & \text{si } J < 0 \end{cases} \quad (5.9)$$

Ayant ainsi défini le cadre théorique de l'estimation de l'erreur, la transposition du modèle mathématique en formalisme de fusion d'images avec filtrage simultané du bruit est immédiate. En utilisant l'interprétation de [MS08], où le processus de fusion est vu comme une combinaison pondérée linéaire de ses entrées I_s , et l'évolution temporelle de ce processus peut être translatée à l'évolution des poids de chaque entrée $w_s(x, y, t)$, l'image fusionnée \tilde{I} est ainsi exprimée :

$$\tilde{I}(x, y, t) = \sum_{s=1}^S w_s(x, y, t) \cdot I_s(x, y) \quad (5.10)$$

Dans ce cas, l'image fusionnée représente l'image restaurée I_r de la théorie de l'estimation de l'erreur, tandis que les images d'entrée I_s représentent les images dégradées, à la base desquelles l'estimation I_r est faite. Chaque fonction de poids est itérativement estimée d'après la règle :

$$w_s(x, y, t + 1) \leftarrow w_s(x, y, t) - \tau \frac{\partial w_s(x, y, t)}{\partial t} \quad (5.11)$$

où

$$\frac{\partial w_s(x, y, t)}{\partial t} = \frac{1}{I_s(x, y)} \left\{ -\alpha \mathfrak{D}_a(\tilde{I}(x, y, t)) + \beta \Theta(J_s(x, y, t)) J_s(x, y, t) [\tilde{I}(x, y, t) - I_s(x, y)] \right\} \quad (5.12)$$

Pour chaque itération, à la fin du processus d'estimation des poids, l'image fusionnée \tilde{I} est obtenue par la réintégration des poids $w_s(x, y, t)$ en (5.10). Une composante importante de la méthode proposée est l'approximation numérique, basée sur l'estimation de l'orientation par L'Analyse en Composantes Principales (ACP) [Don99], afin de calculer le système relatif des coordonnées (ξ, η) , nécessaire pour le schéma d'interpolation de précision sub-pixel, utilisée parmi d'autres dans le calcul de \mathfrak{D}_a par Terebes [Ter04]. Tous ces détails concernant la manière dont le modèle mathématique est transposé en pratique sont décrits dans le manuscrit complet de la thèse.

5.3 Analyse expérimentale

Etant donné le caractère de ce document, et implicitement les limites imposées concernant sa taille, l'analyse expérimentale va être réduite à un seul exemple de fusion d'images bruitées, les méthodes comparatives étant préalablement optimisées afin de permettre une évaluation qualitative la plus pertinente. L'optimisation du choix des paramètres a été largement traitée dans [Pop08] pour l'ensemble des images utilisées et un

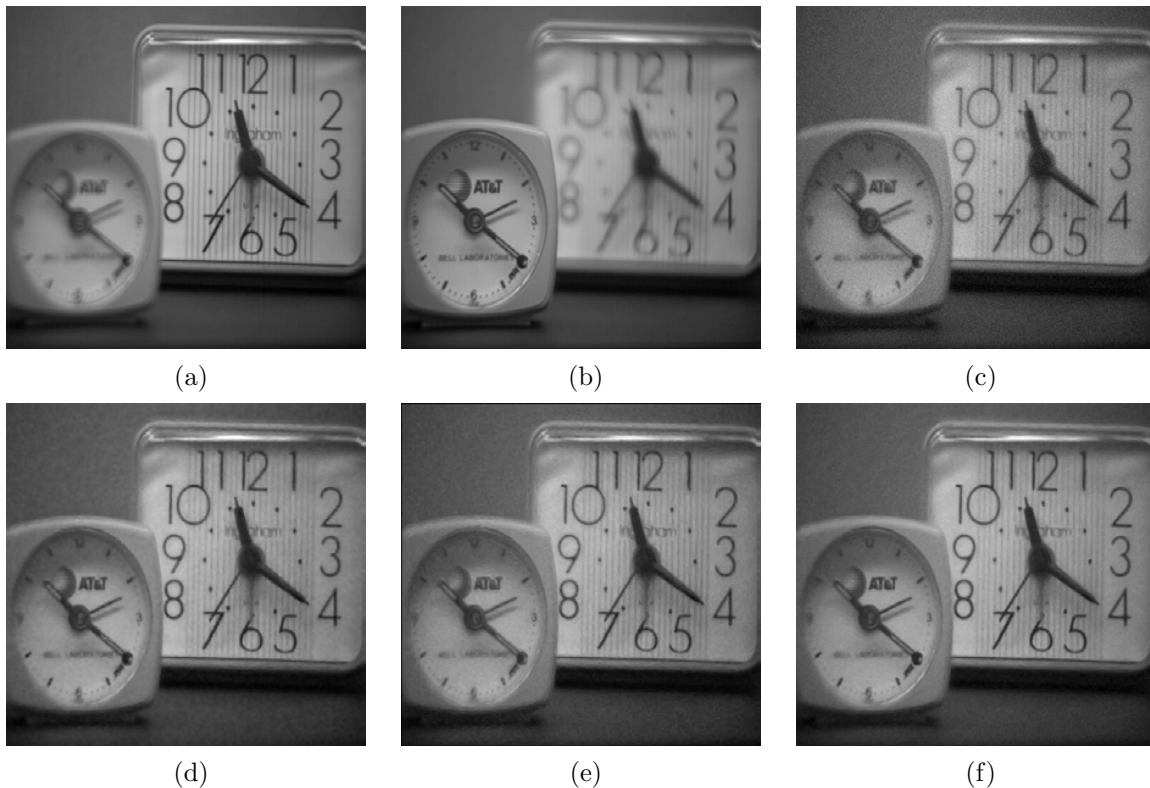


Figure 5.1 – Analyse comparative – résultats sélectives : (a) Image de référence I_1 ; (b) Image de référence I_2 ; (c) Résultat de la méthode **MED**; (d) Résultat de la méthode **SIDWT-hard**; (e) Résultat de la méthode **Pop-2**; (f) Résultat de la méthode **méthode proposée**.

Table 5.1 – Analyse comparative – bruit blanc, gaussien additif - $\sigma_b = 13$

Méthode de fusion	Ensemble de paramètres optimaux	Métriques de qualité dédiée			Métriques de qualité classiques						
		Q_W	$rSFe$	$Q^{AB/F}$	RMSE	PSNR	SSIM	MSSIM	VSNR	VIF	MI
MED		0,833	0,726	0,295	10,913	27,371	0,557	0,904	21,485	0,354	1,981
DWT	$L=7$ $H=mar$	0,79	2,103	0,257	17,427	23,305	0,358	0,823	19,276	0,336	1,502
SIDWT	$L=5$ $H=mar$	0,821	1,854	0,292	15,461	24,345	0,395	0,861	21,852	0,383	1,618
DWT-soft	$L=7$ $L_n=1$ $H=mar$	0,885	0,439	0,335	10,112	28,033	0,637	0,89	19,568	0,352	2,209
DWT-hard	$L=7$ $L_n=2$ $H=mar$	0,877	0,503	0,356	9,948	28,175	0,674	0,892	19,853	0,333	2,284
SIDWT-soft	$L=5$ $L_n=1$ $H=mar$	0,929	0,021	0,425	6,837	31,433	0,798	0,932	21,448	0,432	2,726
SIDWT-hard	$L=5$ $L_n=2$ $H=mar$	0,931	-0,082	0,477	5,771	32,905	0,911	0,965	23,275	0,455	3,055
JoV	$IT=339$ $dt=0,0001$ $\sigma=5$ $\alpha=2500$ $\beta=0,9$	0,855	1,197	0,328	11,585	26,852	0,524	0,906	24,569	0,418	1,961
Pop-1	$IT=35$ $dt=0,1$ $\alpha=0,7$ $\beta=0,3$ $\gamma=1,5$ $K_\xi=5$ $K_\eta=2$	0,864	-0,25	0,424	9,557	28,523	0,878	0,94	18,489	0,391	2,657
Pop-2		0,925	-0,161	0,485	7,904	30,173	0,902	0,959	21,517	0,436	2,976
Modèle proposé-Q_W	$IT=18$ $dt=0,1$ $\alpha=1,6$ $\beta=0,3$ $W_{PCA}=5 \times 5$ $K_\xi=15$ $K_\eta=1,5$ $\sigma_{em}=5$	0,936	-0,046	0,524	5,162	33,874	0,879	0,965	26,029	0,482	3,027
Modèle proposé	$IT=16$ $dt=0,1$ $\alpha=1,7$ $\beta=0,4$ $W_{PCA}=5 \times 5$ $K_\xi=10$ $K_\eta=5$ $\sigma_{em}=5$	0,932	-0,048	0,478	5,219	33,777	0,885	0,965	25,993	0,48	3,04

bruit blanc gaussien, additif d'écart-type $\sigma_b = 13$. Pour plus de détails concernant les paramètres de chaque modèle analysé et concernant l'optimisation de la méthode proposée, voir le manuscrit complet de la thèse.

Le scénario expérimentale présenté est construit pour le set *Réveils* [Ima11], qui contient deux images d'entrée (le scénario minimal de fusion) avec des focalisations différentes (Fig. 5.1a et Fig. 5.1b). Il faut aussi préciser que, même si les deux images sont considérées comme références et, implicitement idéales du point de vue du bruit, le bruit estimé pour les deux entrées est de $\sigma_{b_1} = 0,53$ et $\sigma_{b_2} = 0,51$, représentant en fait un cas réel avec du bruit. L'analyse expérimentale comparative est construite en rajoutant du bruit blanc, gaussien additif d'écart-type $\sigma_b = 13$.

Les modèles comparés dans ce cas sont les suivantes : **MED** représente la moyenne arithmétique des deux entrées et, au même temps, le plus simple mécanisme de fusion ; il est présenté dans le *Tableau 5.1* avec rôle d'approche étalon ; **DWT** et **SIDWT** sont deux modèles de fusion basés sur des ondelettes [Roc97, RF98], leurs versions *hard* et *soft* étant adaptées au filtrage du bruit (voir la thèse) ; les méthodes **JoV** et **Pop** représentent des modèles de fusion EDP, le premier étant le modèle proposé par John et Vorontsov dans [JV05] et le deuxième étant un modèle de fusion d'images avec du filtrage de bruit, amplement décrit dans [Pop08].

Dans le cadre de l'analyse comparative, l'évaluation qualitative (*Tableau 5.1*) a été réalisée en utilisant à la fois des métriques de qualité dédiées à la fusion d'images, *i.e.*, $Q^{AB/F}$ [XP00, Pet01], Q_W [Pie04] et $rSFe$ [ZEHH07], et les métriques classiques, mentionnées dans le **Chapitre 3**. Afin de ne pas influencer l'évaluation, dans le cas des métriques classiques avec image de référence unique, le résultat de la fusion des images de référence sans bruit a été choisi. Ce résultat a été obtenu en utilisant la méthode de la pyramide laplacienne, méthode non-adaptée au filtrage du bruit, et, par conséquent, non-incluse dans le scénario illustré dans la Fig. 5.1.

Les résultats expérimentaux décrits dans le *Tableau 5.1* indiquent, à travers des métriques de qualité, les performances supérieures du modèle proposé. Les valeurs des métriques classiques, *e.g.*, RMSE, PSNR, VSNR, confirment la capacité de la méthode de fusion proposée à filtrer le bruit de manière efficace simultanément avec le processus de fusion. La qualité du processus de fusion a été de son côté confirmée à la fois par les métriques de qualité dédiées, et par celles classiques, *i.e.*, SSIM, MSSIM, VIF.

La méthode proposée conduit à de bonnes performances y compris dans les scénarios

simples, de fusion, ou un filtrage explicite du bruit n'est pas nécessaire. Dans ces cas, comme démontré par l'analyse expérimentale décrite en détail dans le chapitre 5 de la thèse, les résultats obtenus sont comparables ou supérieurs aux meilleurs résultats des méthodes existantes.

Pour illustrer les applications potentielles, deux scénarios réels de fusion d'images sont décrits, plus précisément, *la fusion multi-luminance* et *la fusion d'images médicales*. Dans les deux cas, les images d'entrée, disponibles à [ECE11], sont fusionnées en l'état, sans altération artificielle.

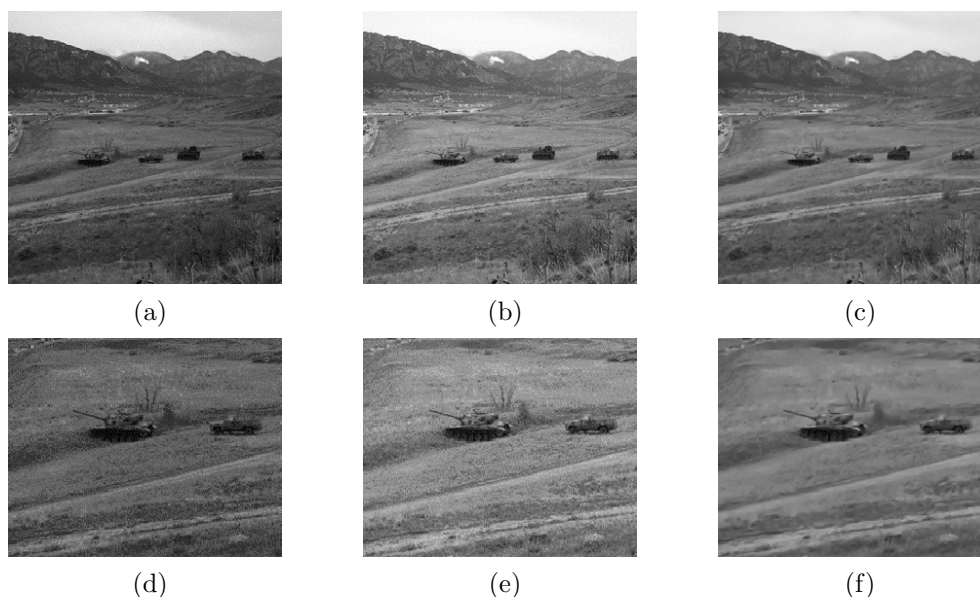


Figure 5.2 – Scénario de fusion multi-luminance – modèle proposé : (a) I_1 et détail (d); (b) I_2 et détail (e); (c) \tilde{I} résultat de la fusion et détail (f).

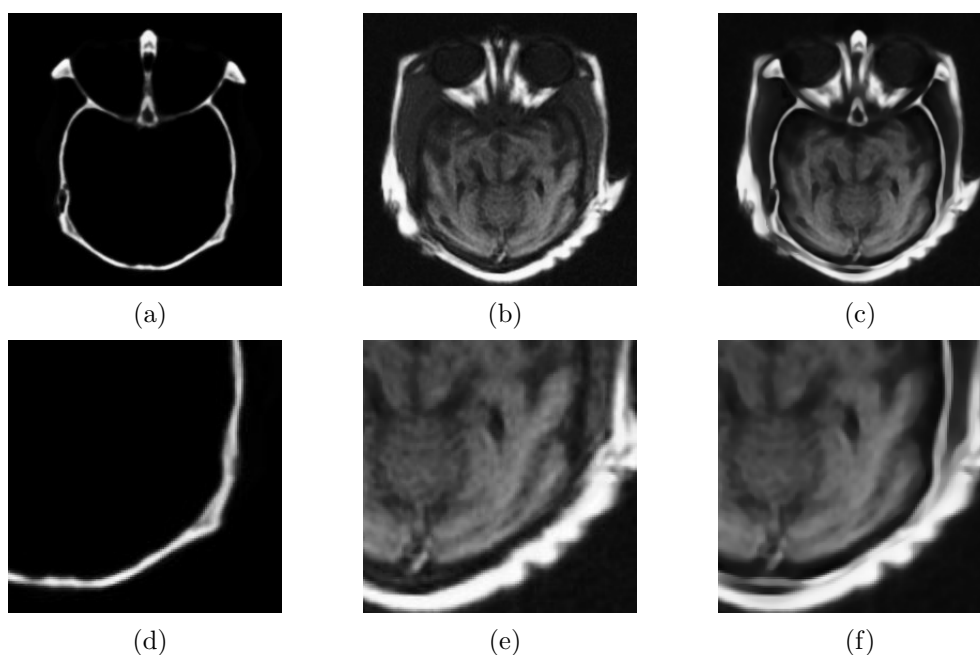


Figure 5.3 – Scénario de fusion d'images médicales – modèle proposé : (a) I_1 image CT et détail (d); (b) I_2 image RMN et détail (e); (c) \tilde{I} résultat de la fusion et détail (f).

CHAPITRE 6

Conclusions, remarques, perspectives

La problématique traitée dans cette thèse se positionne autour de l'étude et de la définition d'un cadre théorique permettant d'unir des concepts de restauration et rehaussement d'images. Dès le début, les objectifs sont poursuivis à travers un formalisme EDP du fait de sa flexibilité, sa polyvalence et, bien entendu, son efficacité en tant qu'outil mathématique dans le traitement d'images.

Ce cadre théorique permet au final d'unifier de manière naturelle une série de méthodes essentielles pour le traitement d'images comme le filtrage du bruit, l'élimination du flou gaussien, le rehaussement de cohérence et de contours ou la fusion d'images. Les aspects de restauration et de rehaussement d'images sont étudiés progressivement pour mieux évaluer les résultats et pour analyser plus facilement la façon dont les divers processus interagissent lorsqu'ils sont utilisés simultanément.

La première contribution de la thèse est *le filtre de choc hybride*, à propos duquel les remarques suivantes peuvent être faites :

- Ce modèle est tout à la fois l'occasion de réaliser une étude de faisabilité de la combinaison de deux processus en restauration d'images et une approche indépendante et finalisée ayant des applications potentiels en traitement d'images.
- A travers son extension (l'amélioration de cohérence), il représente la première liaison entre restauration et rehaussement d'images, à travers un mécanisme parallèle qui unifie les deux processus.
- Même si les performances obtenues sont satisfaisantes, étant comparables ou supérieures aux méthodes alternatives existantes, la formulation actuelle peut être encore améliorée.

Concernant le deuxième modèle proposé, *i.e.*, *la fusion d'images avec élimination simultanée du bruit*, il faut préciser que :

- Dans la forme courante, le modèle est limité par la manière dont est faite l'initialisation de la fonction image fusionnée \tilde{I} à l'instant $t = 0$, plus spécifiquement, par un processus de fusion élémentaire (MED).
- Bien que les résultats obtenus positionnent la méthode proposée en haut du classement des procédés de fusion comparés dans **Chapitre 5** la caractéristique anisotrope du modèle pourrait être encore améliorée aussi bien du point de vue du filtrage du bruit que du point de vue du rehaussement des contours.
- Sachant que la méthode dans sa forme courante peut être appliquée de manière assez générique, une amélioration des performances est possible pour des applications spécifiques, par une adaptation préalable de la méthode aux caractéristiques des images traitées.

Serial no.

BORDEAUX 1 UNIVERSITY

**TECHNICAL UNIVERSITY OF
CLUJ-NAPOCA**
– Joint PhD Thesis –

Date:

WE HEREBY RECOMMEND THAT THE THESIS PREPARED UNDER
OUR SUPERVISION BY

Cosmin Ludusan

ENTITLED

**FROM IMAGE RESTORATION TO IMAGE
ENHANCEMENT:**

*using Partial Differential Equations for concurrent
image fusion and denoising*

BE ACCEPTED IN PARTIAL FULFILLMENT OF THE REQUIREMENTS

FOR THE DEGREE OF

DOCTOR OF PHILOSOPHY IN ELECTRICAL ENGINEERING

Acknowledgments

I would like to start by extending my sincerest thanks and gratitude to my two thesis co-advisers, Prof. Monica Borda and Prof. Olivier Laviaille, for their continuous support and guidance and for helping me discover my passion for image processing. I am also grateful for their effort in continuing and consolidating the academic collaboration between the *Technical University of Cluj-Napoca, Romania* and *Bordeaux 1 University, France*, this joint PhD thesis being the fourth of its kind between the two universities. I would also like to thank Prof. Monica Borda for her confidence in me and in my academic abilities when selecting my candidacy for an Erasmus student mobility program that ultimately paved the way for this thesis. On the same note I would like to also thank Prof. Olivier Laviaille for believing in me and for his decision to start a fourth joint PhD thesis.

My sincerest thanks and appreciation also go to Assoc. Prof. Romulus Terebeș with the *Technical University of Cluj-Napoca, Romania*, which through his *CNCSIS – PNI-IDEI* research grant has supported my thesis, both by providing mobility funding as well as general research funding. Without his initial support, both moral and financial, I would not have been able to embark on this journey. He has always been a personal and a professional role model to me, his advice and guidance being pivotal in shaping the researcher I am today.

I would also like to thank Prof. Philippe Bolon with the *Polytech Annecy-Chambéry, France* and Prof. Ioan Nafornită with the “*Politehnica*” *University of Timișoara, Romania* for having accepted to be my thesis referees. I greatly appreciate and value their pertinent remarks and observations, which helped shape this manuscript into its final form.

Sincerest thanks also go to Prof. Gabriel Oltean with the *Technical University of Cluj-Napoca, Romania* for accepting to preside the thesis defense committee and to Prof. Christian Germain with *ENITA de Bordeaux, France* for accepting to be a member of my thesis defense committee.

My appreciation and thanks also go to my colleagues and professors with the two research groups that I have been part of during my thesis, the *Technical University of Cluj-Napoca* group and the *Signal and Image* group within the *IMS - CNRS UMR5218*. Their constant support and guidance as well as their friendship and kindness always made me feel at home, whether I was in France or in Romania.

Without forgetting the moral support of my friends and family, I would like to extend my sincerest thanks and gratitude to them for believing in me and always being by my side.

Last but certainly not least, I would like to thank a very special someone in my life, *Cornelia*, for her constant support and patience, for always believing in me, for her love and friendship and also for making the last two and a half years of my thesis and my life, exciting, adventurous and filled with so many beautiful memories.

I would like to conclude by adding that this thesis would not have been possible without the financial support of the following funding agencies and programs: the *TUCN doctoral program* – through a 3-year doctoral scholarship, the *CNCSIS (the Romanian national research council)* – through a 3-year research grant (PNII-IDEI 908/2007) under the supervision of Assoc. Prof. Romulus Terebes (grant director) and through a 3-year research scholarship for young researchers (type BD), the *EGIDE scholarship program* – through a 2-year doctoral scholarship and a 1-year *Eiffel excellence* doctoral scholarship, and last but not least *ENITA Bordeaux* – for funding the final months of my thesis. On the same note, I would like to mention the 3-month *Socrates/Erasmus* student mobility scholarship that initially paved the way for this joint PhD thesis.

In loving memory of my grandfather, Emil Ludusan

Abstract

This thesis addresses key issues of current image restoration and enhancement methodology, and through a progressive approach introduces two new image processing paradigms, *i.e.*, concurrent image deblurring and denoising with coherence enhancement, and joint image fusion and denoising, defined within a Partial Differential Equation – variational theoretical setting.

The first image processing paradigm represents an intermediary step in validating and testing the concept of compound image restoration and enhancement, while the second proposition, *i.e.*, the joint fusion-denoising model fully illustrates the advantages of using concurrent image processing as opposed to sequential approaches.

Both propositions are theoretically formalized and experimentally analyzed and compared with the similar existing methodology, proving thus their validity and emphasizing their characteristics and advantages when considered an alternative to a sequential image processing chain.

Résumé

Cette thèse aborde les principaux aspects applicatifs en matière de restauration et amélioration d'images. A travers une approche progressive, deux nouveaux paradigmes sont introduits : la mise en place d'une déconvolution et d'un débruitage simultanés avec une amélioration de cohérence, et la fusion avec débruitage. Ces paradigmes sont définis dans un cadre théorique d'approches EDP – variationnelles.

Le premier paradigme représente une étape intermédiaire dans la validation et l'analyse du concept de restauration et d'amélioration combinées, tandis que la deuxième proposition traitant du modèle conjoint fusion-débruitage illustre les avantages de l'utilisation d'une approche parallèle en traitement d'images, par opposition aux approches séquentielles.

Ces deux propositions sont théoriquement et expérimentalement formalisées, analysées et comparées avec les approches les plus classiques, démontrant ainsi leur validité et soulignant leurs caractéristiques et avantages.

Rezumat

Prezenta teză abordează aspecte cheie ale metodologiei actuale în restaurarea și îmbunătățirea de imagini, tratând aceste aspecte de o manieră progresivă prin propunerea a două noi paradigme de procesare de imagini. Cele două modele, *i.e.*, *deconvoluție cu eliminare simultană de zgomot și ameliorare de coerență* și *fuziune de imagini cu eliminare concomitentă de zgomot*, fiind formalizate într-un cadru teoretic comun, și anume *Ecuatii cu Derivate Parțiale*.

Din punct de vedere funcțional, cel dintâi model de procesare de imagini propus reprezintă un pas intermediar în validarea și testarea conceptului de *restaurare și îmbunătățire simultană de imagini*, în timp ce al doilea model, *i.e.*, *fuziune de imagini cu eliminare concomitentă de zgomot*, ilustrează pe deplin avantajele unei abordări simultane (paralelizate) în procesarea de imagini, comparativ cu abordarea oarecum clasică a procesării secvențiale de imagini în vederea restaurării și îmbunătățirii acestora.

În ceea ce privește metodologia de lucru, cele două modele propuse sunt formalizate atât din punct de vedere teoretic precum și experimental, fiind analizate și comparate cu modelele similare existente, în conformitate cu rigorile științifice actuale. Analiza experimentală evidențiază caracteristicile și particularitățile celor două modele propuse, în timp ce studiul comparativ reiterează avantajele ce derivă din paralelizarea, și implicit comasarea, celor două procese (restaurare și îmbunătățire de imagini) în raport cu abordarea standard, secvențială.

Table of Contents

Chapter 1.

- Introduction 1**
- 1.1 Overall motivation 1
- 1.2 Conceptualization 2
- 1.3 Contents layout 3

Chapter 2.

- Image restoration using Partial Differential Equations 7**
- 2.1 Motivation 7
- 2.2 A short introduction to image processing 8
 - 2.2.1 Variational methods 9
 - 2.2.2 Partial Differential Equations 9
- 2.3 Multiscale image processing and PDEs 11
- 2.4 Linear filtering 12
- 2.5 Nonlinear filtering 15
 - 2.5.1 The Perona–Malik model 15
 - 2.5.1.1 The anisotropic diffusion equation 15
 - 2.5.1.2 Model limitations 18
 - 2.5.2 The Catté *et al.* model 19
 - 2.5.3 The Forward-and-Backward diffusion model 20
- 2.6 The variational approach 21
 - 2.6.1 Total variation minimization 21
 - 2.6.2 A unifying PDE–variational approach 25
- 2.7 Tensor-based filtering 27
 - 2.7.1 The Weickert tensor-based diffusion models 27
 - 2.7.1.1 The Weickert CED model 28
- 2.8 Level-set and curvature-based filtering 29
 - 2.8.1 The Euclidean Morphological Scale Space analysis 30
 - 2.8.2 The Affine Morphological Scale Space analysis 31
- 2.9 Numerical approximations 32
 - 2.9.1 Finite difference approximations 32
 - 2.9.1.1 Approximating partial derivatives 33

2.9.1.2	Approximating differential geometry operators	35
2.9.1.3	Multiscale approximations	37
2.10	Conclusion	38
Chapter 3.		
	Hybrid shock filters: an image restoration paradigm	41
3.1	Motivation	41
3.2	Deblurring as an image restoration concept	42
3.3	Concurrent denoising and deblurring: an image restoration approach	43
3.4	Shock filters	44
3.4.1	The Osher–Rudin shock filter	45
3.4.2	The Alvarez–Mazorra shock filter	48
3.4.3	The Kornprobst <i>et al.</i> shock filter	50
3.4.4	The Remaki–Cheriet shock filter	50
3.4.5	Weickert’s CESF model	52
3.4.6	The Gilboa <i>et al.</i> complex shock filter	54
3.4.7	Shock filters: afterword	55
3.5	The hybrid shock filter paradigm	55
3.5.1	Mathematical model	56
3.5.2	The small θ approximation	58
3.5.3	The f_1 and f_2 control functions	59
3.5.4	Adding coherence enhancement to the hybrid shock filter formalism	60
3.6	Experimental analysis	61
3.6.1	Image quality assessment	62
3.6.2	Hybrid shock filter parameter and stability analysis	63
3.6.3	Shock filters: a comparative analysis	66
3.6.4	The coherence-enhancing hybrid shock filter: experimental analysis	71
3.7	Conclusion	73
Chapter 4.		
	Image fusion: an image enhancement paradigm	75
4.1	Motivation	75
4.2	Image fusion: a short introduction	76
4.3	Definitions and classifications	77
4.4	Methodology in image fusion: an overview	79
4.4.1	Non-multiscale-decomposition-based fusion techniques	80
4.4.1.1	Addition as a fusion paradigm	80
4.4.2	Multiscale-decomposition-based fusion techniques	81
4.4.2.1	Pyramid-decomposition-based methods	82
4.4.2.2	Wavelet-based methods	82
4.4.2.3	Fusion criteria in multiscale image fusion	83

4.5	Variational and PDE-based approaches to image fusion	85
4.5.1	Socolinsky’s variational image fusion model	85
4.5.2	The John–Vorontsov variational fusion model	87
4.5.3	The Wang <i>et al.</i> variational fusion model	88
4.5.4	The Pop <i>et al.</i> variational fusion model	90
4.5.5	The Piella variational fusion model	90
4.5.6	Other variational or quasi-variational fusion models	91
4.6	Quality assessment in image fusion	93
4.6.1	The Xydeas–Petrovic quality assessment metric	94
4.6.2	The Piella quality assessment metrics	94
4.6.3	The <i>rSFe</i> quality assessment metric	95
4.7	Properly choosing a reference in image fusion quality assessment	96
4.7.1	Experimental setting	96
4.7.2	Quality evaluation when a ground truth image is available	97
4.7.3	Image fusion quality assessment in the presence of noise	98
4.7.4	Image fusion quality assessment for joint fusion–restoration scenarios	102
4.8	Conclusion	104

Chapter 5.

	A variational approach for concurrent image fusion and denoising . .	107
5.1	Motivation	107
5.2	Theoretical prerequisites	108
5.2.1	Error estimation theory: an overview	108
5.2.2	Vector orientation estimation using Principal Component Analysis	110
5.3	Mathematical model	112
5.3.1	Concurrent image fusion and denoising: a variational approach	113
5.3.2	Fusion algorithm and model discretization	117
5.4	Experimental analysis	122
5.4.1	Sequential denoising and fusion vs. concurrent fusion and denoising	122
5.4.2	Experimental validation and noise robustness assessment	124
5.4.3	Model parametrization	132
5.4.4	Concurrent fusion and denoising: a comparative analysis	135
5.5	Potential application areas	143
5.6	Conclusion	148

Chapter 6.

	Conclusions, remarks, perspectives	151
6.1	Conclusions	151
6.2	Remarks	154
6.3	Perspectives	155

Appendix A	
Concurrent fusion and denoising – model optimization	157
Bibliography	161
List of Publications	175

List of Figures

1.1	Covered research areas.	3
1.2	Thesis contents.	6
2.1	Isotropic diffusion results: (a) Initial noisy image I_0 contaminated with an AWGN of $\sigma_n = 25$; (b) Diffusion result for $t = 5$; (c) Diffusion result for $t = 50$; (d) Diffusion result for $t = 500$; (e)-(h) Corresponding gradient norm maps.	14
2.2	The $(\vec{\xi}, \vec{\eta})$ frame of reference.	17
2.3	Isotropic diffusion (b) and anisotropic diffusion (c) filtering of the Paolina image (a); $t = 4$, $K = 7$	18
2.4	The Catté <i>et al.</i> anisotropic diffusion: (a) Synthetic starting image 128×128 pixels; (b) Blurred initial image I_0 ; (c) Edge-enhanced result.	19
2.5	FAB diffusion functions: $K_f = 8$, $K_b = 25$, $w = 5 \bullet g_1: n = 4, m = 1, \alpha = 0.15 \bullet g_2: n = 4, m = 2, \alpha = 0.2$	21
2.6	TV-based denoising methods: (a) Initial image; (b) Noisy image – AWGN of $\sigma_n = 20$; (c) TV Diffusion result; (d) Digital TV filter result.	24
3.1	1-D blurring–deblurring example.	43
3.2	1-D deblurring principle for $I_0(x) = -\sin(x)$ represented on $[-\pi, \pi]$	46
3.3	Time evolution of I , the solution of (3.5) at different time scales t	46
3.4	The Osher–Rudin shock filter – time evolution example: (a) The initial Airplane [<i>Uni11</i>] blurred image – Gaussian PSF of $\sigma = 2$; (b) Shock filtered image at time scale $t = 1$; (c) Shock filtered image at time scale $t = 10$	48
3.5	Alvarez–Mazorra shock filter example: (a) GB($\sigma_b = 2$)+AWGN($\sigma_n = 10$) contaminated image – true color original available at [<i>Kod11</i>]; (b) Filtered image for $t = 1$, $C = 2$ and $\sigma = 1$	49
3.6	Kornprobst <i>et al.</i> shock filter example: (a) GB($\sigma_b = 2$)+AWGN($\sigma_n = 10$) contaminated image; (b) Filtered image for $t = 0.5$, $\sigma = 1$, $\tau = 15$ and $\alpha_f = \alpha_r = \alpha_e = 1$	50

3.7	Remaki–Cheriet shock filter example: (a) $\text{GB}(\sigma_b = 2) + \text{AWGN}(\sigma_n = 10)$ contaminated image; (b) Filtered image for $t = 1$, using a Gaussian mollifier of $\sigma = 1$	52
3.8	Weickert’s CESF example: (a) Original fingerprint image [<i>Bio11</i>]; (b) Filtered image: $t = 20$, $\sigma = 2$ and $\rho = 6$	53
3.9	Gilboa <i>et al.</i> complex shock filter example: (a) $\text{GB}(\sigma_b = 2) + \text{AWGN}(\sigma_n = 10)$ contaminated image; (b) Filtered image for $t = 2$, $ \lambda = 0.1$, $\tilde{\lambda} = 0.5$, $a = 0.5$ and $\theta = 0.01$	54
3.10	Hybrid shock filter example for $t = 2$: (a) $\text{GB}(\sigma_b = 1) + \text{AWGN}(\sigma_n = 5)$ contaminated image – true color original available at [<i>Kod11</i>]; (b) Hybrid shock filter result – real part $\text{Re}(I)$, <i>i.e.</i> , the filtered output; (c) Hybrid shock filter – imaginary part $\text{Im}(I)$, <i>i.e.</i> , the edge detector.	57
3.11	The small θ approximation and its influence on the stability of the hybrid shock filter.	58
3.12	Hybrid shock filter control functions examples for $N_n = 1000$: (a) The (3.26) control function set for $T_{1i} = 200$, $T_{1s} = 500$, $T_{2i} = 100$, $T_{2s} = 700$; (b) The alternative control function set (3.27): $f_1(t) = \cos(t)$ and $f_2(t) = \sin(t)$	59
3.13	Hybrid shock filter control functions GB+AWGN comparison for $t = 2$: (a) Filtered result using the (3.26) control function set for $T_{1i} = 5$, $T_{1s} = 15$, $T_{2i} = 5$, $T_{2s} = 15$; (b) Filtered result using the (3.27) control function set.	60
3.14	Coherence-enhancing hybrid shock filter example: (a) Original fingerprint image [<i>Bio11</i>]; (b) Filtered image: $t = 5$, $\sigma = 1$ and $\rho = 5$	61
3.15	Hybrid shock filter parameter analysis experimental setting: (a) Reference synthetic image; (b) $\text{GB}(\sigma_b = 5) + \text{AWGN}(\sigma_n = 40)$ contaminated initial image I_0	64
3.16	Hybrid shock filter parameter analysis: behavior of the parameter \mathbf{a}	64
3.17	Hybrid shock filter parameter analysis: control function sets behavior.	65
3.18	Hybrid shock filter stability analysis.	66
3.19	Comparative analysis based on the first experimental setting – <i>Fig. 3.15</i>	67
3.20	Shock filters – comparative analysis: (a) Reference House image; (b) $\text{GB}(\sigma_b = 1) + \text{AWGN}(\sigma_n = 10)$ contaminated initial image I_0 ; (c) Osher–Rudin result; (d) Alvarez–Mazorra result; (e) Gilboa <i>et al.</i> result; (f) Hybrid shock filter result.	68
3.21	Shock filters – comparative analysis: (a) Reference Fishing Boat image; (b) $\text{GB}(\sigma_b = 1.5) + \text{AWGN}(\sigma_n = 5)$ contaminated initial image I_0 ; (c) Osher–Rudin result; (d) Alvarez–Mazorra result; (e) Remaki–Cheriet result; (f) Gilboa <i>et al.</i> result; (g) Hybrid shock filter result.	69

3.22	Shock filters – comparative analysis: (a) Reference Fishing Boat image; (b) $GB(\sigma_b = 3)+AWGN(\sigma_n = 10)$ contaminated initial image I_0 ; (c) Osher–Rudin result; (d) Alvarez–Mazorra result; (e) Remaki–Cheriet result; (f) Gilboa <i>et al.</i> result; (g) Hybrid shock filter result.	70
3.23	Coherence enhancement and shock filters – comparative analysis: (a) Reference fingerprint image; (b) $GB(\sigma_b = 10)+AWGN(\sigma_n = 25)$ contaminated initial image I_0 ; (c) Gilboa <i>et al.</i> result; (d) Weickert’s CESF result; (e) Coherence-enhancing hybrid shock filter result and detailed view of the coherence-enhancing effect.	71
4.1	<i>[Mit10]</i> – The pyramid representation of the multiscale analysis of an input image I	82
4.2	Initial experimental setting: (a) Ground truth image; (b) I_1 input image; (c) I_2 input image; (d) \tilde{I} fused image.	97
4.3	$(I_1^{\sigma_n}, I_2^{\sigma_n}) \tilde{I}^{\sigma_n}$ fusion quality assessment, using $Q^{AB/F}$, Q_W and $rSFe$	99
4.4	$(I_1^{\sigma_n=0}, I_2^{\sigma_n=0}) \tilde{I}^{\sigma_n}$ fusion quality assessment, using $Q^{AB/F}$, Q_W and $rSFe$	100
4.5	Q_W and $Q^{AB/F}$ relative error between assessing the image quality for $(I_1^{\sigma_n}, I_2^{\sigma_n}) \tilde{I}^{\sigma_n}$ as opposed to assessing the quality for $(I_1^{\sigma_n=0}, I_2^{\sigma_n=0}) \tilde{I}^{\sigma_n}$	101
4.6	Quality assessment for a joint fusion–restoration process.	102
4.7	Q_W and $Q^{AB/F}$ relative error for a joint fusion–restoration scenario $(I_1^{\sigma_n=0}, I_2^{\sigma_n=0}) \tilde{I}^{\sigma_n=0}$	103
5.1	Vector orientation estimation using a PCA of rectangular support and fixed size $W_{PCA} = 5$: (a) Grayscale concentric circles synthetic image; (b) Orientation color map; (c) θ_η orientation map; (d) θ_ξ orientation map.	110
5.2	Vector orientation estimation using a PCA of rectangular support – multiscale characteristic example: θ_ξ orientation map for (a) $W_{PCA} = 3$, (b) $W_{PCA} = 11$ and (c) $W_{PCA} = 21$	111
5.3	Vector orientation estimation using a multiscale PCA: (a) Grayscale concentric circles synthetic image; (b) θ_ξ – the result of a multiscale PCA.	112
5.4	(ξ, η) frame of reference approximation example for a given contour, in pixel $I_{i,j}$: (a) <i>[Ter04]</i> – The $\vec{\xi}$ direction approximation frame; (b) The $\vec{\eta}$ direction approximation frame.	118
5.5	<i>[Ter04]</i> – $\vec{\xi}$ direction sub-pixel approximations: (a) V_1, V_2 and V_3 approximation points for computing $I(\xi + d\xi, \eta)$; (b) V'_1, V'_2 and V'_3 approximation points for computing $I(\xi - d\xi, \eta)$	119
5.6	<i>[Ter04]</i> – $\vec{\eta}$ direction sub-pixel approximations: (a) Z_1, Z_2 and Z_3 approximation points for computing $I(\xi, \eta + d\eta)$; (b) Z'_1, Z'_2 and Z'_3 approximation points for computing $I(\xi, \eta - d\eta)$	120

5.7	Concurrent fusion and denoising – advantages. The Book image set test scenario: (a) Book 1 original input image and detail (b); (c) Book 2 original input image and detail (d).	122
5.7	<i>(continued)</i> : (e) <i>SIDWT with Haar</i> fusion method result and detail (f); (g) Anisotropic noise filtering of the inputs followed by <i>SIDWT with Haar</i> fusion result and detail (h); (i) <i>Proposed</i> fusion method result and detail (j).	123
5.8	Multifocus image fusion test setting: (a) First input image I_1 ; (b) Second input image I_2 ; (c) <i>Simple average</i> reference image R_{avg} ; (d) Fusion reference image R_{fus} ; (e) I_1 – detail; (f) I_2 – detail; (g) R_{avg} – detail; (h) R_{fus} – detail.	125
5.9	Multifocus image fusion test scenario (ES1) - quality metrics: (a) $RSME/\sigma_{noise}$ evolution; (b) $PSNR/\sigma_{noise}$ evolution; (c) VIF/σ_{noise} evolution; (d) $SSIM/\sigma_{noise}$ evolution.	126
5.10	Noise robustness test scenario: (a) $RSME/\sigma_{noise}$ coarse optimization; (b) $PSNR/\sigma_{noise}$ coarse optimization; (c) VIF/σ_{noise} coarse optimization; (d) $SSIM/\sigma_{noise}$ coarse optimization.	128
5.11	Noise robustness test scenario – dedicated fusion quality metrics evaluation: (a) $Q^{AB/F}/\sigma_{noise}$ coarse optimization; (b) Q_W/σ_{noise} coarse optimization.	129
5.12	Noise robustness test scenario – pre-smoothing example: (a) $\tilde{I}^{\sigma_n=30}$ fused result; (b) $\tilde{I}^{\sigma_n=30}_{\sigma_{ps}=0.5}$ fused result.	130
5.13	Office image set – multi-exposure fusion scenario: (a) I_1 input image – with an estimated noise of $\sigma_{noise-bias} = 2.62$ and detail (d); (b) I_2 input image – with an estimated noise of $\sigma_{noise-bias} = 2.55$ and detail (e); (c) Proposed fusion model fused result \tilde{I} and detail (f).	131
5.14	Clock image set – multifocus fusion scenario: (a) Clock 1 original image – with an estimated noise of $\sigma_{noise-bias} = 0.53$; (b) Clock 2 original image – with an estimated noise of $\sigma_{noise-bias} = 0.51$; (c) I_1 reference input image; (d) I_2 reference input image; (e) Reference fused image – used in the noise stress analysis.	132
5.15	Proposed fusion method – noise stress behavior: (a) $RMSE/\text{noise}$ evolution – α ; (b) $PSNR/\text{noise}$ evolution – α ; (c) $SSIM/\text{noise}$ evolution – α ; (d) $RMSE/\text{noise}$ evolution – β	133
5.15	<i>(continued)</i> : (e) $PSNR/\text{noise}$ evolution – β ; (f) $SSIM/\text{noise}$ evolution – β ; (g) $RMSE/\text{noise}$ evolution – σ_{em} ; (h) $PSNR/\text{noise}$ evolution – σ_{em} ; (i) $SSIM/\text{noise}$ evolution – σ_{em}	134
5.16	I_1 and I_2 's variance maps – used in computing the Q_W fusion quality metric: (a) I_1 's variance map; (b) I_2 's variance map.	138
5.17	Comparative analysis – Table 5.4: (a) AVG fused result; (b) PCA fused result; (c) LAP fused result; (d) FSD fused result; (e) RAT fused result; (f) CON fused result; (g) GRA fused result; (h) DWT fused result; (i) SIDWT fused result.	139

5.17	<i>(continued)</i> : (j) Soc fused result; (k) WaY fused result; (l) JoV fused result; (m) Pop-out2 fused result; (n) Proposed-Q_W fused result; (o) Proposed-$rSFe$ fused result.	140
5.18	Comparative analysis – <i>Table 5.5</i> : AWGN of $\sigma_n = 13$ – (a) AVG fused result; (b) SIDWT-hard fused result; (c) Pop-out2 fused result; (d) Proposed-Q_W fused result; (e) Proposed fused result.	142
5.19	Multifocus image fusion application example: Lab image set – (a) I_1 and detail (d); (b) I_2 and detail (e); (c) \tilde{I} fused result and detail (f).	144
5.20	Multifocus image fusion application example: Pepsi image set – (a) I_1 ; (b) I_2 ; (c) \tilde{I} fused result.	144
5.20	<i>(continued)</i> : (d) I_1 detail; (e) I_2 detail; (f) \tilde{I} fused result detail.	145
5.21	Multi-exposure image fusion application example: Battlefield image set – (a) I_1 and detail (d); (b) I_2 and detail (e); (c) \tilde{I} fused result and detail (f).	145
5.22	Medical image fusion application example: (a) I_1 CT image and detail (d); (b) I_2 MRI image and detail (e); (c) \tilde{I} fused result and detail (f).	146
5.23	Remote sensing fusion application example: (a) I_1 and detail (d); (b) I_2 and detail (e); (c) \tilde{I} fused result and detail (f).	147
5.24	Enhanced vision application example: (a) I_1 LLTV image; (b) I_2 FLIR image; (c) \tilde{I} fused result.	147

List of Tables

2.1	Regularization functions studied by Deriche and Faugeras [<i>DF95</i>]	26
3.1	$f_1(t)$ and $f_2(t)$ test parameters – <i>Fig. 3.17</i>	65
3.2	Qualitative analysis results for the “ <i>Fig. 3.20</i> ” experimental setting	67
3.3	Qualitative analysis results for the “ <i>Fig. 3.21</i> ” experimental setting	68
3.4	Qualitative analysis results for the “ <i>Fig. 3.22</i> ” experimental setting	69
3.5	Qualitative analysis results – <i>Fig. 3.23</i> experimental setting	72
4.1	Standard qualitative analysis (when a reference image is available) results .	98
4.2	Image fusion qualitative analysis results for the $(I_1^{\sigma_n}, I_2^{\sigma_n}) \tilde{I}^{\sigma_n}$ scenario . . .	99
4.3	Image fusion qualitative analysis results for the $(I_1^{\sigma_n=0}, I_2^{\sigma_n=0}) \tilde{I}^{\sigma_n}$ scenario	100
4.4	Quality assessment for a joint fusion–restoration process - experimental data	103
5.1	Noise robustness assessment – experimental settings	127
5.2	Noise robustness assessment of the pre-smoothing example – quality evaluation	130
5.3	Compared fusion methods and their input parameters	136
5.4	Comparative analysis – AWGN of $\sigma_n = 0$	138
5.5	Comparative analysis – AWGN of $\sigma_n = 13$	141
5.6	Comparative analysis – AWGN of $\sigma_n = 30$	141
5.7	Potential application areas – model parametrization	148
A.1	Q_W optimization – concurrent fusion and denoising: comparative analysis for an AWGN of $\sigma_n = 13$ – <i>Table 5.5</i>	157
A.1	(continued) Q_W optimization – concurrent fusion and denoising: comparative analysis for an AWGN of $\sigma_n = 13$ – <i>Table 5.5</i>	158
A.2	Q_W optimization – concurrent fusion and denoising: comparative analysis for an AWGN of $\sigma_n = 30$ – <i>Table 5.6</i>	158
A.2	(continued) Q_W optimization – concurrent fusion and denoising: comparative analysis for an AWGN of $\sigma_n = 30$ – <i>Table 5.6</i>	159

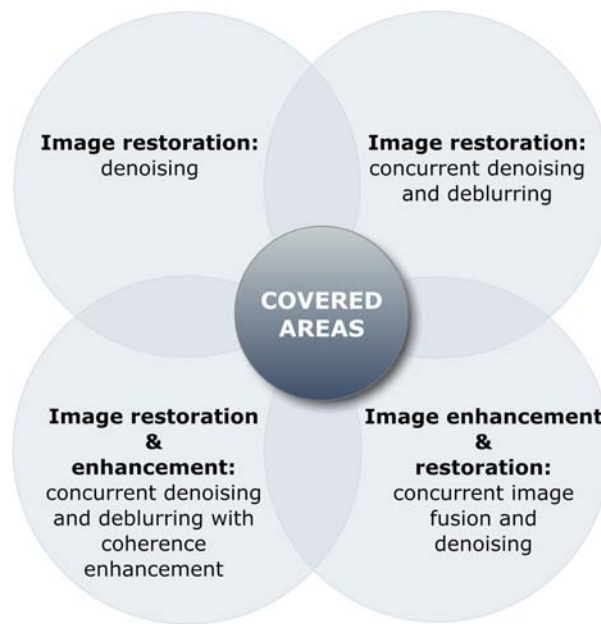


Fig. 1.1 – *Covered research areas.*

the next and final step was to define, analyze and experimentally validate the proposed concurrent image fusion and denoising model. The proposed fusion–denoising model fulfills the initial desideratum of defining a PDE-based model that synergistically combines elements from image restoration (*i.e.*, denoising) with elements from image enhancement (*i.e.*, image fusion).

Since this thesis is about *image processing*, and consequently about *images*, and since “*a picture is worth a thousand words*”, the previous discussion about how the general problem statement of the thesis was progressively addressed can be eloquently synthesized by a single “picture” (*Fig. 1.1*).

1.3 Contents layout

In terms of manuscript contents, it is only logical to follow the same progressive approach in order to ensure a required descriptive consistency and also to provide the reader with a clear picture of how the worked described within was carried out. In its general layout the manuscript is divided into six chapters and three appendices that provide additional information, where needed, in order to clarify, supplement or reinforce the existing notions already addressed within a given chapter.

Each of the six chapters can be briefly described as follows:

Chapter 1 , also the current chapter, provides an overall description of the thesis from three different perspectives: **(i)** *general problem statement and initial desiderata*, **(ii)** *practical approach or conceptualization*, and **(iii)** *thesis layout*.

Chapter 2 establishes a preliminary foothold in the image restoration realm by providing a comprehensive analysis of the fundamental variational and PDE-based models for image restoration, more specifically image denoising. Moreover, the beginning of the chapter also provides a brief incursion into image processing as a whole, in

generic terms, with emphasis on variational and PDE-based techniques in image processing. As already mentioned, this manuscript follows a functional layout rather than a traditional one, being organized so as to best describe the progressive line of reasoning behind defining the new concurrent image processing paradigms, thus being able to provide an intrinsic walk-through of the thesis in its entirety.

Chapter 3 addresses the other core image restoration concept, *i.e.*, image deblurring. Due to its importance and to the fact that the first major proposition, *i.e.*, joint image deblurring and denoising, is at its core a deblurring model, the issue of image deblurring as an image restoration process is analyzed separately from image denoising. The proposed joint image deblurring and denoising model is in essence a *shock filter* with added denoising capabilities and, as a further additional feature, coherence-enhancing characteristics. The proposed joint image deblurring and denoising model is defined using two counteracting filtering paradigms, image sharpening (deblurring) and image denoising. The filtering process is divided between the filter's two main components, *i.e.*, complex and real, which leads to a robust noise filtering with edge preservation and enhancement. Thus, the proposed model possesses increased filtering capabilities, especially in high *Gaussian Blur+Additive White Gaussian Noise* scenarios, while exhibiting a stable-convergent time behavior. The experimental results unequivocally show that the proposed model can be successfully employed for sharpening as well as for denoising tasks, and that through its complex framework allows tackling with high contamination values, while yielding superior results to the existing shock filter models.

Chapter 4 provides a preliminary analytical incursion into the area of image enhancement, more precisely image fusion. Since this thesis covers multiple topics, albeit interconnected, it was necessary to provide a theoretical background for each stand-alone concept in order to ensure a proper understanding of the area of research on the one hand and of the proposed models on the other. Once again, this layout follows the practical progressive manner in which each part of the problem statement has been addressed in terms of preliminary study, analysis and solution. That is why, the first part of the chapter covers fundamental notions of data fusion in general and image fusion in particular, from definitions to classifications and a quick overview of existing methodology in image fusion, without loss of generality. In order to establish a proper starting point for the joint image restoration and enhancement model, this chapter also analyzes the most relevant existing³ variational and PDE-based approaches to image fusion, since these methods provide a direct comparison reference base. The chapter concludes by addressing yet another crucial issue in image fusion, especially in compound scenarios such as joint fusion and denoising, *i.e.*, quality assessment. The topic is subjected both to theoretical and experimental analysis, with emphasis on the differences between using the existing dedicated quality metrics in simple image fusion scenarios as opposed to employing the same quality metrics in compound scenarios. By providing this analysis and underlining the inherent shortcomings of quality assessment in the special case of joint restoration and enhancement, two important objectives are reached, *i.e.*, (1) it is shown that the current methodology in image fusion quality assessment is

³to date

incomplete and in some cases detrimental to the objective evaluation, since it under-evaluates the quality of the output results, and (2) it establishes the initial quality evaluation framework for the proposed joint fusion–denoising model, by showing that the assessed results may in some cases be under-evaluated.

Chapter 5 defines, experimentally validates and compares the proposed concurrent fusion and denoising model. The proposed model is methodologically established on robust error estimation theory and expressed as a *Total Variation* minimization problem, *i.e.*, representing a variational model with PDE-expressed functional components. The proposed joint fusion–denoising model, although based on an existing formalism, is fundamentally different from the original formalism in the following ways:

- it employs an “intelligent” diffusion component in the form of geometry-driven anisotropic diffusion as opposed to a Total Variation-based isotropic diffusion that was not explicitly designed for denoising (the original model has limited denoising capabilities),
- its edge-enhancing component is also defined anisotropically, as opposed to the original formalism that is based on a classic Gaussian-smoothed gradient map.

These key aspects of the proposed joint fusion–denoising model allow for a truly anisotropic fusion with concurrent denoising, an image processing paradigm with numerous advantages both in terms of computational effort and complexity as well as in terms of quality of the processed result. The first part of the chapter deals with the necessary theoretical prerequisites, from continuous domain definition to numerical approximation and the discrete interpolation scheme for approximating the first and second order partial derivatives with sub-pixel accuracy. The second part of the chapter experimentally underlines the difference between a sequential approach to the combined fusion–denoising problem and a concurrent one, and further continues with experimentally validating the proposed model as functional and efficient joint image restoration and enhancement processing tool. The final part of this chapter provides a required comparative analysis using a wide range of existing fusion models as well as an extensive set of quality metrics, in order to provide an objective and thorough qualitative assessment, [Appendix A](#) detailing the optimization of the proposed fusion–denoising model. After thoroughly proving the validity and the advantages of the proposed model, in multifocus and multi-exposure fusion scenarios, the chapter concludes by providing a short glimpse into the potential practical application areas and the immediate benefits of using a joint fusion–denoising model instead of a standard fusion approach.

Chapter 6 closes this manuscript by providing the necessary overall conclusions concerning the initial problem statement and how each point of the thesis requirements has been addressed and solved. Furthermore, it provides a series of remarks that point out the advantages and disadvantages, if any, of the proposed methods and the overall approach towards the development of this thesis and implicitly towards writing and organizing the corresponding manuscript. The concluding part of this chapter consists of a list of perspectives, in specific terms of future work and possible improvements of the proposed models, while in more general terms further work us-

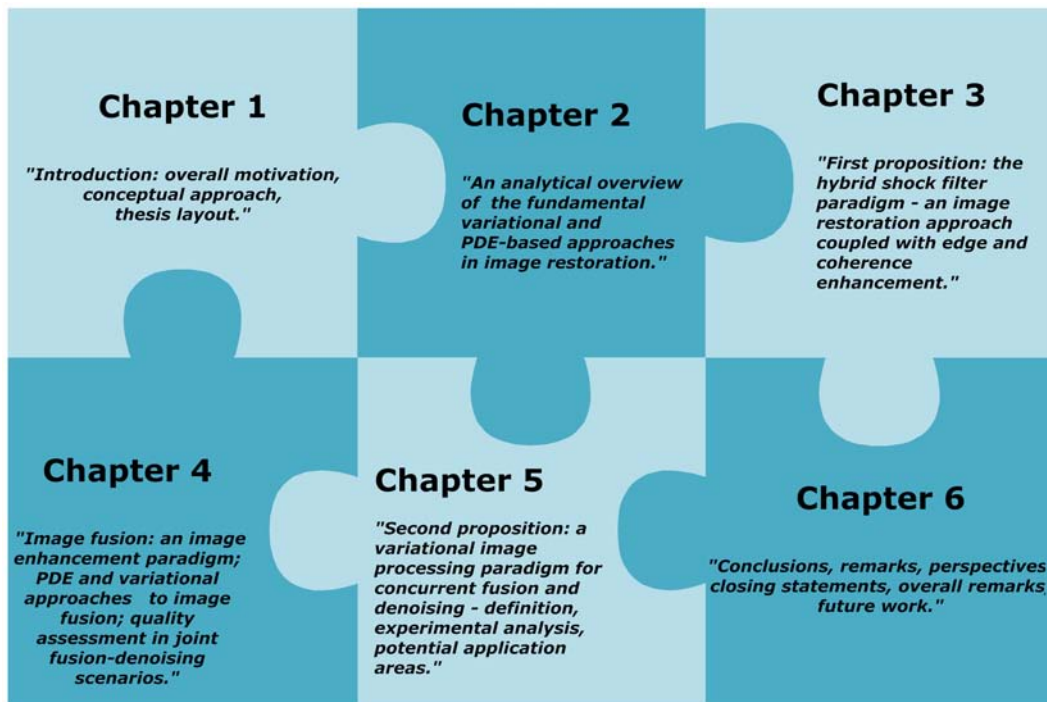


Fig. 1.2 – *Thesis contents.*

ing the variational and PDE frameworks, potential new image processing paradigms and their advantages over the other existing methodologies.

As before, the contents layout of this manuscript can be easily and eloquently synthesized by a single “picture”, as illustrated in *Fig. 1.2*.

Final remarks

1. Given the intricate nature of this thesis, in terms of approached topics (*i.e.*, image denoising, deblurring and fusion), a challenge in itself was also to find the best way of writing it. Since the discussed topics range from PDE-based denoising and deblurring to variational image fusion, it was difficult to construct the manuscript in the classic fashion, that is, by providing a first chapter of theoretical prerequisites, with all subsequent chapters describing the original contribution of the thesis. Although, image restoration and image enhancement share a considerable common framework they also differ in just as many ways. Therefore, accommodating the necessary theoretical prerequisites for each topic was considered best handled through a functional approach, rather than a classic one. In this way, the manuscript is effectively organized both in terms of functionality and logic, as well as in terms of facilitating its reading and understanding.
2. On a related note, given the functional construction of the manuscript, at the end of each chapter a “*Contents to Context*” (C2C) section is provided in order to properly explain the relevance of each section and of the topics within.

CHAPTER 2

Image restoration using Partial Differential Equations

Main Contents

2.1	Motivation	7
2.2	A short introduction to image processing	8
2.3	Multiscale image processing and PDEs	11
2.4	Linear filtering	12
2.5	Nonlinear filtering	15
2.6	The variational approach	21
2.7	Tensor-based filtering	27
2.8	Level-set and curvature-based filtering	29
2.9	Numerical approximations	32
2.10	Conclusion	38

2.1 Motivation

The purpose of this chapter is divided between providing a basic understanding of notions such as *image restoration*, *image enhancement*, *diffusion*, *denoising*, etc., and establishing the general framework not only for the theoretical concepts discussed in this chapter but also for all the topics covered throughout this thesis.

The general layout of the chapter comprises a short introduction that deals with basic image processing notions and definitions, followed by a brief presentation of the current trends in image processing, methodology-wise, continues with an overview of PDE¹ and variational-based image processing techniques and their evolution since their emergence as mathematical frameworks for image (signal) processing. The chapter concludes by analyzing the proper means of approximating continuous domain models and thus adapting them for numerical use.

From a functional point of view **Chapter 2** serves both as theoretical background and as the first building block of the *image restoration–image enhancement* paradigm, providing the starting point for the following chapters. The understanding of the fundamental principles behind image restoration and its evolution from basic approaches to complex, more sophisticated ones is of paramount importance in defining, implementing and validating new models, such as the ones described in **Chapter 3** and **Chapter 5**. The study and understanding of the basic principles associated with PDE- and variational-based image restoration is a prerequisite in further defining new concepts both from a theoretical standpoint as well as a practical, experimental one required for validating newly proposed image processing paradigms.

¹Partial Differential Equation

2.2 A short introduction to image processing

Image processing transforms visual information in order to:

- improve it – e.g., restoration, enhancement;
- extract pertinent features – e.g., analysis, recognition;
- or*
- change its structure – e.g., composition, editing.

Although images can be processed either by optical, photographic or electronic means, this thesis focuses on digital image processing since it is the method of choice for visual information analysis, being fast, flexible and precise.

Visual information improvement plays a crucial role in image processing, since all subsequent processing tasks rely on the quality of the input images. The aim of image improvement is to deliver the best possible result given an initial, degraded image. Although image restoration and image enhancement are both visual information improvement tasks, their definitions are not equivalent, at most, they partially overlap. According to the **Oxford** dictionary, *restoration* is defined as “*the process of restoring a building, work of art, etc. to its original condition*”, while the **Merriam-Webster** dictionary defines it as “*something that is restored; especially: a representation or reconstruction of the original form (as of a fossil or a building)*”. Similarly, *enhancement* is defined by the **Oxford** dictionary as “*an increase or improvement in quality, value, or extent*”.

In a narrower sense, the purpose of image restoration is to *compensate for* or *undo* defects which degrade an image, e.g., motion blur, noise, camera misfocus. Image enhancement, on the other hand, aims to improve the interpretability or perception of visual information in images for human viewers, or to provide “better” input for other automated image processing techniques.

Historically, the first image processing techniques were derived from 1-D signal processing and relied on filter theory (linear or nonlinear), spectral analysis, or on some basic concepts of probability and statistics, as noted by Aubert and Kornprobst [AK06].

Nowadays, more sophisticated, more evolved tools have been developed to tackle the complex task of digital image processing. The current major approaches in image processing can be classified, according to Chan and Shen [CS05], into:

- **Morphological**
- **Fourier and Spectral Analysis**
- **Wavelet and Scale-Space Analysis**
- **Stochastic Modeling**
- **Variational**
- **PDE-based**

Since not all existing approaches directly relate to the topics addressed by this thesis, only the relevant ones, i.e., *variational methods* and *PDE-based techniques*, are detailed in the following.

2.2.1 Variational methods

According to Chan and Shen [CS05], a variational approach can be viewed as the deterministic reflection of the Bayesian framework in the mirror of Gibbs' equation in statistical mechanics [Gib02, Cha87]:

$$p(F) = \frac{1}{Z} e^{-\beta E[F]}$$

with $\beta = 1/(kT)$ being the reciprocal of temperature T multiplied by the Boltzmann constant k , and $Z = Z_\beta$ representing the partition function for probability normalization.

Thus, $p(F)$ expresses the likelihood of a feature configuration F in terms of its energy $E[F]$ [CS05]. For the sake of example, the following additive noise model can be considered:

$$I_0(x) = I(x) + n(x), \quad x \in \Omega$$

The following assumptions are made [CS05]:

- n is a homogeneous field of Gaussian white noise of zero mean, and
- ∇I is a homogeneous random field of isotropic Gaussian white vectors with zero means.

Using a variational formulation, the estimation of $F = I$ from I_0 is achieved by:

$$\hat{I} = \operatorname{argmin} E[I|I_0] = \operatorname{argmin} \frac{\alpha}{2} \int_{\Omega} |\nabla I|^2 dx + \frac{\lambda}{2} \int_{\Omega} (I - I_0)^2 dx \quad (2.1)$$

with the two weights being inversely proportional to the variances [CS05].

2.2.2 Partial Differential Equations

The effective use of PDEs in image processing can be credited to the following factors [CS05]:

- first, many variational problems or their regularized approximations can be effectively computed from their Euler–Lagrange equations, *and*
- second, PDEs belong to one of the most important parts of mathematical analysis and are closely related to the physical world.

Moreover, PDEs are powerful tools to describe, model, and simulate many dynamic as well as equilibrium phenomena, including diffusion, advection or transport, reaction, etc. [CS05].

The use of PDEs in applied sciences was initially limited to physics, describing phenomena like heat and sound propagation (*the heat equation*) or modeling physical processes in electromagnetics or fluid dynamics (*the wave equation*). The most recognizable names associated with the notion of PDEs are the ones of great mathematicians such as Isaac Newton, Gottfried Leibniz, Leonhard Euler, Pierre-Simon Laplace or John Forbes Nash, Jr., and although PDEs were initially used in physics and mechanics, nowadays they can be encountered more and more in other fields such as biology, finance, artificial intelligence, engineering and last but not least, image analysis.

The ease of use of PDEs in image analysis, since this is the field of interest in this case, is mainly given by their well-established status in mathematical theory. Hence,

the rigorous mathematical way to define PDEs is in a continuous setting, and once the existence and uniqueness of the solution is proven, the functional algorithm is obtained by means of discretization, thus arriving at a numerical solution [AK06].

Revisiting the denoising model (2.1) and using calculus of variations, this can be alternatively described within a PDE framework, and its solution amounts to solving an elliptic boundary value problem [CS05]:

$$-\alpha\Delta I + \lambda I = \lambda I_0, \quad x \in \Omega; \quad \partial I / \partial \nu = 0 \text{ along } \partial\Omega \quad (2.2)$$

An alternative way of solving (2.1) is dynamically, via gradient descent marching [CS05]:

$$I_t = \alpha\Delta I + \lambda(I_0 - I), \quad x \in \Omega; \quad \partial I / \partial \nu = 0 \text{ along } \partial\Omega \quad (2.3)$$

with a suitable initial condition $I(x, t = 0)$.

Remark As noted by [CS05], PDE modeling in image processing is not necessarily linked to expressing variational models, such being the case in physics, e.g., the Navier-Stokes equations in fluid dynamics, Schrödinger equations in quantum mechanics or the Maxwell equations in electromagnetics.

Image restoration and image enhancement form the setting and represent the main topics of this thesis, while the PDE-based approach employed in accomplishing these tasks constitutes the chosen mathematical tool.

Special emphasis will be placed throughout this thesis on PDE-based methods in conjunction with variational approaches, since these two main image processing techniques coexist from a mathematical point of view.

In image processing, an *image* is usually a digital representation of a scene, hence its definition domain is represented by a discrete plane of points, called *pixels*² in 2-D or *voxels*³ in 3-D. Therefore, a gray-level digital image will be equivalent to a function of spatial coordinates (x, y) and time t , and value the luminance in each of the points belonging to the 2-D lattice \mathbb{Z}^2 . Obtaining a restored or enhanced image via PDE modeling is achieved by means of a PDE function which has as arguments the luminance function and its partial derivatives; the solution of this PDE at any given instant of time t represents the restored (enhanced) image.

Let $I_0 : \mathbb{R}^2 \rightarrow \mathbb{R}$ be the initial gray-level image that requires processing, with $I_0(x, y)$ the luminance level associated to a pixel of coordinates (x, y) . The general image evolution model can be expressed as follows [CMST98]:

$$\begin{cases} \frac{\partial I}{\partial t} = F(I(x, y, t)) \\ I(x, y, 0) = I_0(x, y) \end{cases} \quad (2.4)$$

where F represents a given image processing algorithm, being a function of the original image I_0 and its first and second order spatial derivatives.

The solution of (2.4) at a given time t is none other than the processed image at a scale t , that is why certain PDE techniques are used, and are consequently considered, as multiscale analysis tools. The following section of this chapter will detail this connection.

²or **pel** (*picture element*) is a single point in a raster image, or the smallest addressable screen element in a display device.

³*volumetric pixel* or, more correctly, *volumetric picture element* is a volume element, representing a value on a regular grid in three dimensional space.

2.3 Multiscale image processing and PDEs

The notion of *scale*, and implicitly that of *multiscale*, is widely employed in image processing and computer vision, the scale parameter being used to express and define a wide range of processes. The notion of scale is particularly important when talking about objects or details that exist as significant entities only at certain observation scales. A complete visual system should allow for the analysis, extraction and characterization of objects of different sizes by controlling the observation scale through an independent parameter: *the scale* t [Ter04].

A multiscale analysis is defined by a family of transforms $(T_t)_{t \geq 0}$, which, applied to an initial image I_0 , yields a family of images dependent on the scale parameter t . The initial image I_0 corresponds to a scale $t = 0$, while for scales $t > 0$ the resulting image is a simplified version of the initial one, where the goal is to not have any false structures or details. Thus, the family of images obtained by varying the scale parameter t allows having a multiscale representation of the initial image I_0 .

The fundamental properties that need to be satisfied by a multiscale analysis were stipulated by Morel and Solimini in [MS95]:

1. Fidelity – $T_t(I_0) = I_0$, $t \rightarrow 0$;
2. Causality – $T_t(I_0)$ depends only on $T_{t'}$ with $t' < t$;
3. Euclidean invariance – if A is an isometry $T_t(I_0 \circ A) = T_t(I_0) \circ A$;
4. Strong causality (for edge/contour detection) – let K_t be the set of contours at scale $t \implies K_t \subset K_{t'}$ for $t' < t$.

The notion of image representation as a multiscale smoothing was first formalized by Marr and Hildreth [MH80] and further formalized by Witkin [Wit84] through a model that allows obtaining images of increasingly coarse scale by convoluting the initial image I_0 with Gaussian kernels of increasing standard deviation σ . By varying the scale parameter σ in a continuous manner the method can be successfully employed as an edge detector [Wit84]. The method works by using larger scale versions of the initial image to coarsely identify structures, while the smallest scales follow the initial identification and refine the search in order to accurately pinpoint them.

The same functionality, of an edge detector using a multiscale approach, can be obtained with the Marr and Hildreth's [MH80] method by considering a pixel (x, y) at a scale t as belonging to an edge if the Laplacian $\Delta I(x, y, t)$ of the convolved image I changes the sign, and the gradient $\nabla I(x, y, t)$ is “large enough”. This approach yields a dendriform representation of the image, thus allowing the identification of pertinent structures within the initial image I_0 .

It should be noted that Koenderink [Koe84] was the first to underline the equivalence between the convolution with a Gaussian kernel of standard deviation $\sqrt{2t}$ and the solution of the PDE describing the heat diffusion, at a time t . He also formalized the principles of:

- *causality* – stipulates that every image detail at a coarser scale is caused by details at a smaller scale;
- *homogeneity* and *isotropy* – are related to the presence or the absence of a spatial invariance within a given space.

The main limitation of Koenderink’s model consists in not complying with the principle of *strong causality*, in the sense that isotropic diffusion does not ensure spatial edge preservation [Ter04].

In overcoming the limitations of the isotropic diffusion model and abiding by the *strong causality* principle, Perona and Malik [PM90] proposed an adaptive smoothing model with edge enhancement. The Perona–Malik anisotropic diffusion model can be considered seminal to the theory of edge detection and anisotropic filtering as it represents a stepping stone in PDE-based image filtering, marking the beginning of an entire family of PDE-based methods dedicated to image processing and analysis. By employing a nonlinear diffusion function, the Perona–Malik model also allows the interaction between different scales of the initial image I_0 . The anisotropic diffusion model allows for a stronger smoothing in regions of weak luminance variations (small gradients, indicative of homogeneous or quasi-homogeneous surfaces) while it inhibits, partially or totally, the smoothing process near edges or contours, *i.e.*, regions of strong luminance variations – large gradients. Thus, the filtered contours are stable across the different scales of representation, meaning that this nonlinear multiscale method is in complete accordance with the *strong causality* principle.

Of extreme importance to what is now called in image processing *anisotropic diffusion* are also the contributions of Alvarez *et al.* [ALM92] and Catté *et al.* [CLMC92] based on the notion of MCM⁴. The proposed models were defined using a family of parabolic equations for diffusion filtering, with emphasis on selective smoothing using the orthogonal vector to the gradient vector as the main filtering direction.

Further on, the approaches proposed in [AGLM93] and [ST94] introduced the EMSS⁵ and the AMSS⁶ nonlinear multiscale spaces, with the latter describing the affine evolution of *level curves* employed in anisotropic filtering.

A different multiscale approach is that of Weickert [Wei94], employing a diffusion PDE model for matrix-based diffusion functions.

The approaches mentioned so far represent only the cornerstone of PDE-based image processing, their analysis, together with the analysis of more recent methods – derived or evolved from them – will be the topics of the following sections.

2.4 Linear filtering

In image and signal processing, noise is usually considered to be a high frequency contamination. A classic approach in image restoration is to employ a linear convolution process in order to reduce the effects of this contamination. Let $I_0 : \mathbb{R}^2 \rightarrow \mathbb{R}$ be the initial contaminated luminance function defined on $\Omega = [0, a] \times [0, b]$. The restored version, $I(x, y, \sigma)$ is expressed as follows:

$$I(x, y, \sigma) = I_0(x, y) * G_\sigma(x, y) = \int_{\Omega} G_\sigma(x - u, y - v) I_0(u, v) dudv \quad (2.5)$$

σ is the parameter that controls the intensity of G , which is often a Gaussian-type operator. The convolution product from (2.5) describes the smoothing process of I_0 that

⁴Mean Curvature Motion

⁵Euclidean Morphological Scale Space

⁶Affine Morphological Scale Space

suppresses spatial variations at scales inferior to σ , which acts as a scale parameter.

Remark The same convolution product (2.5) can be extended to functions defined on $\mathbb{R}^n \rightarrow \mathbb{R}$, hence a pixel becomes $x = (x_1, x_2, \dots, x_n) \in \mathbb{R}^n$ and the Gaussian distribution of standard deviation σ and zero mean is defined accordingly:

$$G_\sigma(x_1, x_2, \dots, x_n) = \frac{1}{(\sqrt{2\pi}\sigma)^n} \exp\left(-\frac{x_1^2 + x_2^2 + \dots + x_n^2}{2\sigma^2}\right) \quad (2.6)$$

As already mentioned in §2.3, Koenderink [Koe84] was the first to point out the equivalence between the convolution product (2.5) and the evolution of the heat propagation equation at a scale $t = \sigma^2/2$:

$$\begin{cases} I(x, y, 0) = I_0(x, y) \\ \frac{\partial I}{\partial t} = \Delta I = I_{xx}(x, y, t) + I_{yy}(x, y, t) \end{cases} \quad (2.7)$$

The heat equation can also be written as a divergence:

$$\begin{cases} I(x, y, 0) = I_0(x, y) \\ \frac{\partial I}{\partial t} = \operatorname{div} [\nabla I(x, y, t)] \end{cases} \quad (2.8)$$

The well-posedness of (2.8) and the properties of its solution strongly depend on the chosen boundary conditions – the notion of *well-posedness* being classically defined as:

Definition 2.4.1 [AK06]: *well-posed* – “When a minimization problem or a PDE admits a unique solution that depends continuously on the data, it is said that the minimization problem or the PDE is **well-posed** in the sense of Hadamard⁷. Conversely, if existence, uniqueness, or continuity fails, it is said that the minimization problem or the PDE is **ill-posed**.”

In this case, the proper boundary conditions are the Neumann boundary conditions, expressed as follows:

$$\nabla I(x, y, 0)|_{(x,y) \in \partial\Omega, t \in (0, \infty)} = 0 \quad (2.9)$$

Given the image space boundary $\partial\Omega$ and its outward oriented normal \vec{n} , in conjunction with the divergence theorem, the image evolution can be expressed as:

$$\int_{\Omega} \frac{\partial I}{\partial t} d\Omega = \int_{\Omega} \operatorname{div} [\nabla I(x, y, t)] d\Omega = \int_{\mathfrak{B}=\partial\Omega} \nabla I(x, y, t) \cdot \vec{n} d\mathfrak{B} = 0 \quad (2.10)$$

By defining the mean intensity of the image as $\mu(t) = \frac{1}{|\Omega|} \int_{\Omega} I(x, y, t) d\Omega$ and using (2.10) it can be shown that the multiscale time evolution process is $\mu(t)$ preserving, complying with the principle of *conservation of average value*:

$$\frac{\partial}{\partial t} [\mu(t)] = \frac{1}{|\Omega|} \frac{\partial}{\partial t} \left[\int_{\Omega} I(x, y, t) d\Omega \right] = \int_{\Omega} \frac{\partial I}{\partial t} d\Omega \stackrel{(2.10)}{=} 0 \quad (2.11)$$

⁷Jacques Salomon Hadamard

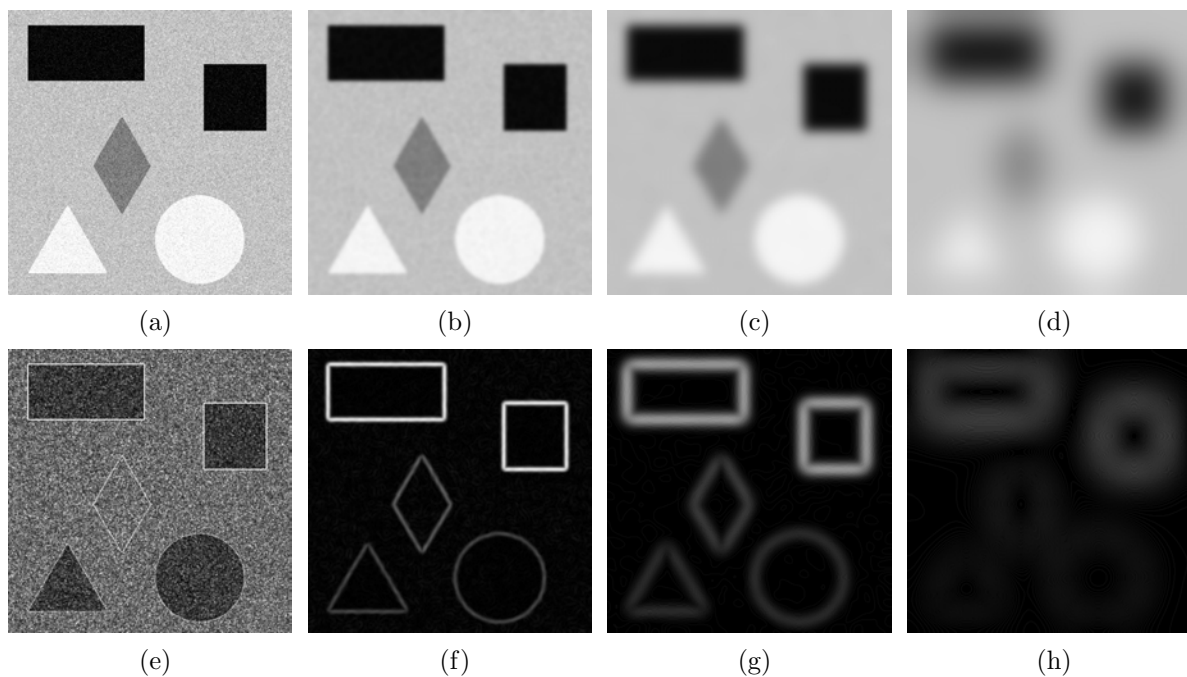


Fig. 2.1 – *Isotropic diffusion results: (a) Initial noisy image I_0 contaminated with an AWGN of $\sigma_n = 25$; (b) Diffusion result for $t = 5$; (c) Diffusion result for $t = 50$; (d) Diffusion result for $t = 500$; (e)-(h) Corresponding gradient norm maps.*

The downside of the isotropic diffusion approach described by the linear parabolic equation (2.7) is that the filtering is performed in all directions, indiscriminately, leading to contour smoothing and edge filtering. This unwanted effect is illustrated in Fig. 2.1 for an initial image I_0 contaminated by an AWGN⁸ of standard deviation $\sigma_n = 25$.

Fig. 2.1a illustrates a synthetic image containing various geometrical objects with an overlaid unwanted AWGN contamination. The goal is to use a filtering method so as to filter out the noise whilst preserving salient information. In the context of image processing and analysis, salient information is often considered to be edge and contour information. A simple, yet efficient, tool in detecting and quantifying this information is the gradient norm $|\nabla I|$, as illustrated in Fig. 2.1e – 2.1h. The most simple approach – based on edge detection and noise smoothing – is the isotropic diffusion method (2.7) expressed by means of a linear parabolic equation. Fig. 2.1b – 2.1h illustrate the isotropic diffusion solutions at different scales, *i.e.*, $t = 5$, $t = 50$ and $t = 500$. As the scale t increases, the AWGN is filtered out and the gradient norm maps are more coherent, but at the same time the spatial accuracy of the edges and contours diminishes. For a scale $t \rightarrow \infty$ the solution of the diffusion equation equals the mean intensity $\mu(t)$ of the initial noisy image (Fig. 2.1a).

Remark Isotropic diffusion or, equivalently, the convolution with a Gaussian kernel is not directly applicable in noise filtering since it cannot properly filter edge information. Nevertheless, when employed, it can lead to a progressively simplified version of the noisy image, making it ideal for preprocessing tasks.

⁸Additive White Gaussian Noise

2.5 Nonlinear filtering

Although, as previously discussed in §2.4, the isotropic diffusion model is not directly usable in noise filtering due to its nondiscriminatory filtering nature, it also possesses some desired characteristics, such as efficient noise filtering and image simplification. Adding to these characteristics one of the main objectives in image restoration, *i.e.*, edge enhancement, a viable image filtering method can be envisaged. Such seminal methods, that combine these three characteristics, were proposed by Perona and Malik [PM90] for anisotropic noise filtering or by Osher and Rudin [Rud87, OR90] for edge enhancement of blurry images, also known as *shock filters*.

Remark Since *shock filters* represent a special case of image restoration coupled with edge enhancement (partly an image enhancement paradigm), their overall characteristics, theoretical definition and practical use are to be analyzed in detail in **Chapter 3**, a chapter intended to bridge the two fundamental notions of image processing, *i.e.*, restoration and enhancement, in the context of PDE-based image processing.

2.5.1 The Perona–Malik model

Any comprehensive discussion about PDEs in image processing should cover the Perona–Malik anisotropic diffusion model since this approach represents the first attempt to overcome the isotropic diffusion’s drawbacks. Due to the fact that the linear multiscale analysis (*i.e.*, isotropic diffusion) has its inherent problem of edge delocalization, the Perona–Malik approach employs a nonlinear multiscale analysis that ensures proper noise filtering with edge preservation. It represents, at the same time, the first directly applicable PDE-based filtering method, fulfilling the following principles [PM90]:

- causality,
- immediate localization – at any scale the edges should be sharp and preserve their spatial position,
- the intra-region smoothing is preferred to the inter-region smoothing.

The selective smoothing with edge enhancement translates into performing a conditional diffusion: a strong smoothing within the homogeneous regions of the image and a weak, selective smoothing across non-homogeneous ones.

2.5.1.1 The anisotropic diffusion equation

The method for selective smoothing with edge enhancement proposed by Perona and Malik in [PM90] is described by the following PDE:

$$\frac{\partial I}{\partial t} = \operatorname{div} [c(x, y, t) \nabla I(x, y, t)] \quad (2.12)$$

with initial conditions $I(x, y, 0) = I_0(x, y)$. In order to simplify the notations, from now on for a given scale parameter t , $I(x, y, t) = I$ and $\nabla I(x, y, t) = \nabla I$.

Remark As likewise noted by [Ter04], the Perona–Malik model, often referred to as *anisotropic diffusion* is a name also used by Weickert *et al.* in [Wei94, WtHRV96, Wei97a,

[WtHRV98] to describe a series of tensor-based diffusion approaches. For the sake of clarity, only the Perona–Malik method will be further referred to as the *anisotropic diffusion model*, since it has chronological precedence.

By rewriting (2.12) as:

$$\frac{\partial I}{\partial t} = c\Delta I + \nabla c \cdot \nabla I \quad (2.13)$$

and considering the particular case $c(x, y, t) = \text{const.}$ the equivalence with (2.7) is immediate.

The function c is called the *conductivity* and it is defined so as to favor intra-region smoothing while diminishing the inter-region one by means of a gradient norm-dependent function of generic form:

$$c(x, y, t) = g(|\nabla I|)$$

If $c(s)$ is a decreasing function satisfying $c(0) = 1$ and $\lim_{s \rightarrow +\infty} c(s) = 0$ the following behaviors can be distinguished:

- Within the regions where $|\nabla I|$ is small, (2.12) has a heat equation-like behavior, resulting in isotropic smoothing.
- Near edges, where $|\nabla I|$ is large, the regularization process is attenuated, thus the salient information (edges) is preserved.

In [PM90] the authors propose two alternatives for $g(s)$:

$$g(|\nabla I|) = \exp \left[- \left(\frac{|\nabla I|}{K} \right)^2 \right] \quad (2.14)$$

and

$$g(|\nabla I|) = \frac{1}{1 + \left(\frac{|\nabla I|}{K} \right)^2} \quad (2.15)$$

where K is a threshold parameter, while $\phi(s) = s \cdot g(s)$ is called the *flux function* and controls the diffusion process along the gradient direction.

The anisotropic diffusion equation (2.12) can also be expressed in terms of second order directional derivatives, in order to facilitate its understanding and to help differentiate it from the isotropic formulation. The directional derivatives are computed along the gradient direction $\vec{\eta} = \left(\frac{I_x}{|\nabla I|}, \frac{I_y}{|\nabla I|} \right)^T$ and its orthogonal $\vec{\xi} = \left(-\frac{I_y}{|\nabla I|}, \frac{I_x}{|\nabla I|} \right)^T$ (Fig. 2.2). Many PDE-based approaches employ the same frame of reference, making it an almost standardized approach in PDE image analysis paradigms.

Before further discussing about the notion of edge enhancement, in the context of the Perona–Malik model as well as in any future reference to this concept, the generic term *edge* should receive a proper definition, from a mathematical point of view, in the context of the anisotropic diffusion model:

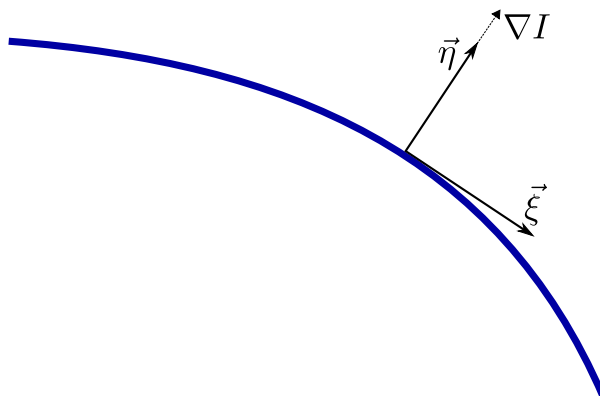


Fig. 2.2 – The $(\vec{\xi}, \vec{\eta})$ frame of reference.

Definition 2.5.1 [AK06]: *edge* – “For a fixed time t , $(\widehat{x}, \widehat{y})$ is called an edge of a function $I(x, y, t)$ if $I'(\widehat{x}, \widehat{y}, t) = \max_{(x,y)} I'(x, y, t)$. If I is smooth enough, at $(\widehat{x}, \widehat{y})$, $I''(\widehat{x}, \widehat{y}, t)$ is necessarily equal to 0 and $I'''(\widehat{x}, \widehat{y}, t) \leq 0$. An edge $(\widehat{x}, \widehat{y})$ is said to be blurred by a PDE if in a neighborhood of $(\widehat{x}, \widehat{y})$, $I'(\widehat{x}, \widehat{y}, t)$ decreases as t increases, or in other words, if $\frac{\partial}{\partial t} (I'(\widehat{x}, \widehat{y}, t)) \leq 0$.”

“It is said that an edge $(\widehat{x}, \widehat{y})$ is enhanced by a PDE if in a neighborhood of $(\widehat{x}, \widehat{y})$, $I'(\widehat{x}, \widehat{y}, t)$ increases as t increases, i.e., $\frac{\partial}{\partial t} (I'(\widehat{x}, \widehat{y}, t)) \geq 0$.”

The intrinsic edge-enhancing characteristic of the anisotropic diffusion model that allows for the diffusion filter to simultaneously behave as a low-pass and a high-pass filter, was also underlined by Perona and Malik for the 1-D case, by rewriting the diffusion equation:

$$\frac{\partial I}{\partial t} = \phi'(I_x) I_{xx} \quad (2.16)$$

and the slope’s variation with respect to time is expressed as [PM90]:

$$\frac{\partial I_x}{\partial t} = \phi''(I_x) I_{xx}^2 + \phi'(I_x) I_{xxx} \quad (2.17)$$

Although this intrinsic edge-enhancing characteristic of the Perona–Malik model is a desired filtering component, the presence of the same characteristic impedes simultaneously proving the existence and uniqueness of solution. Without claiming that such a solution exists, Perona and Malik introduce a maximum principle for their numerical model in order to guarantee the causality principle and avoid unbounded oscillations. For twice differentiable functions $I(x, y, t)$ defined on $\Omega \times (0, T)$ that respect the conditions imposed in [PM90]:

$$\frac{\partial I}{\partial t} - c\Delta I - \nabla c \nabla I = 0 \quad (2.18)$$

with Neumann boundary conditions, the maxima and minima belong to the initial image I_0 :

$$\inf_{\Omega} I_0 \leq I \leq \sup_{\Omega} I_0 \quad (2.19)$$

In the discrete setting, this principle extends to:

$$I_{\min}^t|(i,j) = \min_{(k,l) \in N(i,j)} I_{k,l}(x, y, t) \text{ then } I_{\max}^t|(i,j) = \max_{(k,l) \in N(i,j)} I_{k,l}(x, y, t)$$

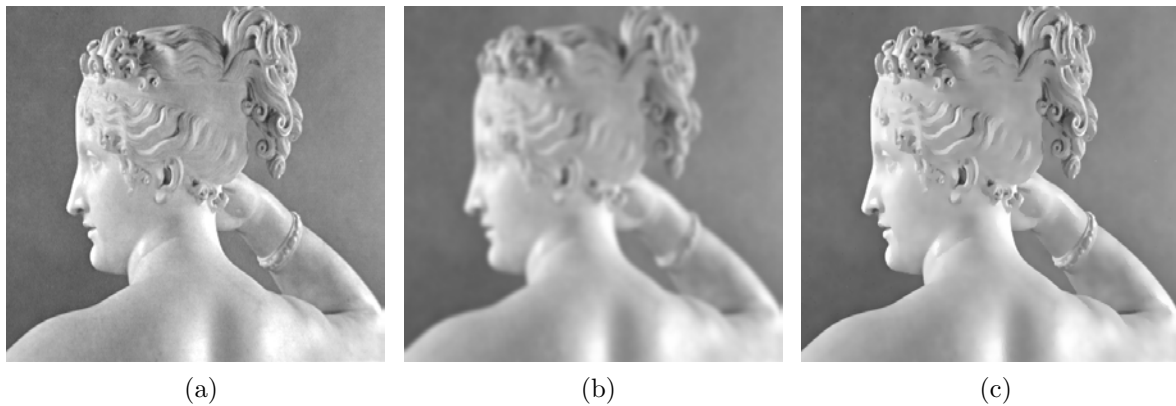


Fig. 2.3 – Isotropic diffusion (b) and anisotropic diffusion (c) filtering of the *Paolina* image (a); $t = 4$, $K = 7$.

where $N(i, j)$ represents the (i, j) pixel's 4⁹ or 8-neighborhood¹⁰ and if the numerical scheme is stable:

$$I_{\min|(i,j)}^t \leq I_{(i,j)}^{t+1} \leq I_{\max|(i,j)}^t \quad (2.20)$$

The two important principles of multiscale analysis, *i.e.*, *causality* and *strong causality*, are only experimentally validated, despite the maximum principle introduced for the numerical model by Perona and Malik. The edge-enhancing characteristic may also create new maxima and minima [PM90].

The difference between isotropic and anisotropic diffusion filtering is illustrated in Fig. 2.3. As compared to the isotropic diffusion model (Fig. 2.3b), the anisotropic diffusion approach (Fig. 2.3c) successfully restores the original image *Paolina* [Com11] (Fig. 2.3a) by filtering out the unwanted noise and preserving the salient information (edges) from the original image.

2.5.1.2 Model limitations

A first drawback of the Perona–Malik model is tied to the inherent edge-enhancing characteristic of the model: for high and very high noise levels within the initial image, the anisotropic diffusion will enhance edges and noise alike, indiscriminately. A simple solution to overcome this effect was proposed with the initial model, by Perona and Malik: nowadays a common practice in image restoration as well as in other image processing-related tasks, the input image of the diffusion process will be a slightly smoothed version of the initial image I_0 and not the initial image itself.

Despite the impressive¹¹ anisotropic filtering capabilities of the Perona–Malik model, as illustrated in Fig. 2.3 the model also exhibits a series of shortcomings, namely the *pinhole effect*, latter corrected by the approach of Monteil and Beghdadi [MB98, MB99], and the *staircase effect*, highlighted and overcome by the Whitaker–Pizer [WP93] model.

⁹4-neighborhood = (N, E, S, W)

¹⁰8-neighborhood = 4-neighborhood + (NE, SE, SW, NW)

¹¹*n.b.* Then, *i.e.*, 1990, more than now, but still a generally valid statement by today's standards.

2.5.2 The Catté *et al.* model

As already discussed, the anisotropic diffusion equation (2.12) with its diffusion functions (2.14) and (2.15), where the flux functions are non-monotone, lacks the mathematical rationale that simultaneously guarantees the existence and uniqueness of its solution [CLMC92]. Catté *et al.* [CLMC92] have highlighted this problem, showing that for gradient values greater than the threshold parameter K , the anisotropic diffusion equation behaves locally like an inverse diffusion equation, susceptible to developing singularities at any given time t . Finding a unique solution which respects the regularity theorem and ensures the stability of (2.12) can prove difficult, if not impossible.

Catté *et al.* argue that for the Perona–Malik maximum principle, at scale t , the continuity hypothesis of the solution I and of its derivatives does not hold since the model’s stability cannot be theoretically justified, being strongly dependent of its numerical discretization. To this end, the authors propose the following diffusion equation:

$$\begin{cases} \frac{\partial I}{\partial t} = \operatorname{div} [g(|\nabla(G_\sigma * I)|)|\nabla I|] = 0, & \text{defined on } \Omega \times (0, T) \\ I(x, y, 0) = I_0(x, y) \end{cases} \quad (2.21)$$

with:

$$G_\sigma(x, y) = \frac{1}{4\pi\sigma^2} \exp \left[-\frac{(x^2 + y^2)}{4\sigma^2} \right] \quad (2.22)$$

Using a smoothed version $I_\sigma = G_\sigma * I$ of the image I together with Neumann boundary conditions, (2.21) yields a unique solution. In terms of model parametrization, the threshold parameter K is selected similarly to the original Perona–Malik model, while the inferior limit for the scale parameter t is of order σ . Properly choosing an “optimal” stopping criterion is linked to σ since the convolution product $G_\sigma * I$ yields a smoothed version of the image for estimating the diffusion coefficients, which in the Fourier domain can be interpreted as a selective smoothing according to different spatial frequencies. This translates to a selective smoothing that favors large homogeneous regions to small nonhomogeneous ones, *i.e.*, details like edges and structures. Hence, in order to use this selective smoothing to an advantage and thus preserve small details within the initial image I_0 , the

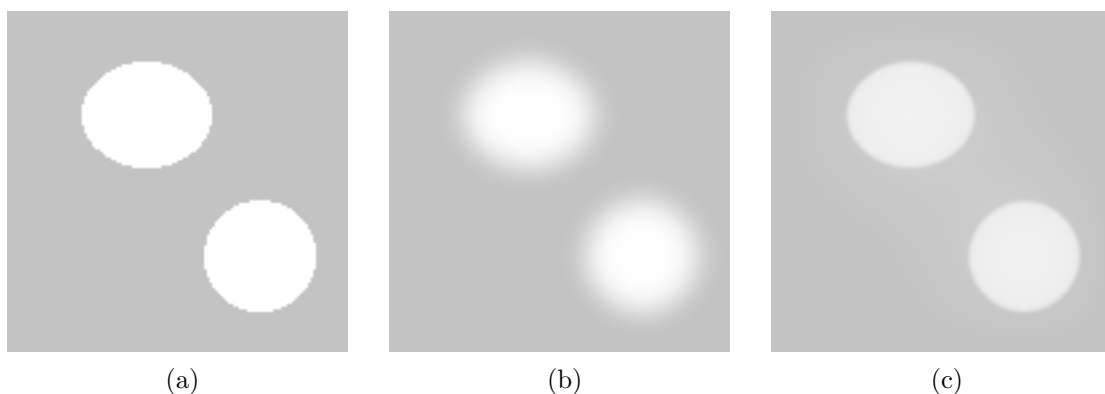


Fig. 2.4 – *The Catté et al. anisotropic diffusion: (a) Synthetic starting image 128×128 pixels; (b) Blurred initial image I_0 ; (c) Edge-enhanced result.*

PDE evolution time will be chosen as short as possible, while fulfilling at the same time the inferior limit condition for the scale parameter.

Remark For Gaussian kernels of relatively small standard deviation, the Catté *et al.* filter can lead to edge enhancement, making the model's PDE an inverse diffusion equation, where the solution's stability and uniqueness cannot be theoretically guaranteed.

The edge-enhancing characteristic of the Catté *et al.* model is illustrated in Fig. 2.4 where the original synthetic image (Fig. 2.4a) has been blurred using a Gaussian kernel of standard deviation $\sigma_b = 5$ (Fig. 2.4b). The parameters for the Catté *et al.* anisotropic diffusion filter are as follows: $\sigma = 0.5$, $K = 3$ and $t = 200$ (Fig. 2.4c).

2.5.3 The Forward-and-Backward diffusion model

Another approach emanating from the classic Perona–Malik model, is the FAB¹² diffusion model, proposed by Gilboa *et al.* in [GZS00, GSZ02a]. The model behaves in a selective manner: the *forward* diffusion is the equivalent of the anisotropic diffusion, for gradient norms less than K while the *backward* diffusion is a diffusion process with a negative diffusion coefficient.

$$\frac{\partial I}{\partial t} = \operatorname{div} [-c\nabla I], \quad c > 0 \quad (2.23)$$

The FAB mechanism is controlled using the following diffusion functions:

$$g_1(|\nabla I|) = \begin{cases} 1 - \left(\frac{|\nabla I|}{K_f}\right)^n & \text{if } 0 \leq |\nabla I| \leq K_f \\ \alpha \left[\left(\frac{|\nabla I| - K_b}{w}\right)^{2m} - 1 \right] & \text{if } K_b - w \leq |\nabla I| \leq K_b + w \\ 0 & \text{otherwise} \end{cases} \quad (2.24)$$

or

$$g_2(|\nabla I|) = \frac{1}{1 + \left(\frac{|\nabla I|}{K_f}\right)^n} - \frac{\alpha}{1 + \left(\frac{|\nabla I| - K_b}{w}\right)^{2m}} \quad (2.25)$$

The diffusion functions (2.24) and (2.25) depend on several parameters that control their behavior: K_f is the equivalent of the classic threshold parameter K , K_b is the backward threshold parameter, w represents the width of the inverse diffusion domain and α denotes the ration between forward and backward diffusion. In conclusion, K_f represents the upper limit of the gradients that will be smoothed, while K_b and w determine the gradients that will be enhanced. The pair (n, m) controls the variation speed of the diffusion functions g_1 or g_2 . The two diffusion functions are very similar, with the remark that g_2 produces better results since it is less sensitive to noise and has a more natural description. The two diffusion functions used by the FAB model are illustrated in Fig. 2.5.

By introducing a negative diffusion behavior for gradients $\in [K_b - w, K_b + w]$ the FAB model does not respect the Perona–Malik maximum principle (2.19), therefore, for gradients belonging to this interval, maxima and minima may occur during the PDE time evolution. Furthermore, this provides a more effective contrast enhancement than the one obtained using the classic Perona–Malik model.

¹²Forward-and-Backward

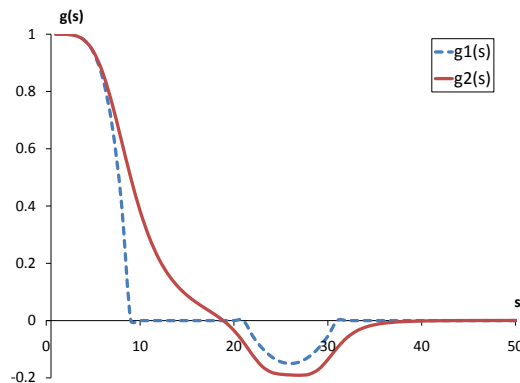


Fig. 2.5 – FAB diffusion functions: $K_f = 8$, $K_b = 25$, $w = 5$ • g_1 : $n = 4$, $m = 1$, $\alpha = 0.15$
 • g_2 : $n = 4$, $m = 2$, $\alpha = 0.2$.

In order to avoid uncontrolled oscillations caused by the backward diffusion, the forward flux needs to be greater than the backward flux according to the inequality: $\alpha \leq K_f/2K_b$ for (2.24) and $\alpha \leq K_f/2(K_b + w)$ with $0 < w < K_b - K_f$ for (2.25) [GZS00, GSZ02a]. These conditions were stated for the 1-D case in order to limit the formation of extrema, for the 2-D case no such conditions were given by Gilboa *et al.*.

2.6 The variational approach

PDEs, as discussed in §2.5, can be successfully employed as stand-alone image processing tools, or in conjunction with other methods. Variational methods in themselves represent an alternative approach to image processing, providing the necessary framework for various image processing tasks. What makes the synergy between PDEs and variational methods so appealing is the way in which variational methods are naturally expressed using PDEs. In the simplest sense, a given PDE describing the evolution of an image can be regarded as the solution of a variational problem. Among all interconnected methods (Fig. ??), PDEs and variational methods share the most extensive theoretical common ground.

This common ground was explored by Morel and Solimini [MS95], underlining the link between PDEs and the general segmentation model of Mumford and Shah [MS89]. The same synergy between the two approaches was highlighted by Deriche and Faugeras [DF95] with the introduction of a variational method that unifies the most important classic diffusion paradigms.

2.6.1 Total variation minimization

The TV¹³ denoising model was first introduced in 1992 by Rudin *et al.* [ROF92] and further developed in [RO94]. Since its first appearance as an image processing tool, there have been numerous contributions based on the original TV denoising and restoration model, e.g., [AV97, CL97, CM99, CS00, CKS01, TD01, Ves01, CS02, TD02, VO02, CS03, BCRS03].

¹³Total Variation

The original TV denoising model is expressed as follows:

$$E(I) = \iint_{\Omega} |\nabla I| dx dy \quad (2.26)$$

with the following constraints:

$$\iint_{\Omega} I dx dy = \iint_{\Omega} I_0 dx dy \quad - \text{mean value preservation} \quad (2.27a)$$

$$\iint_{\Omega} \frac{1}{2} (I - I_0)^2 dx dy = \sigma^2 \quad - \text{noise distribution knowledge} \quad (2.27b)$$

The noise of standard deviation σ is also assumed white of zero mean.

If I is a differentiable function, (2.26) represents the TV of I :

$$TV(I) = \iint_{\Omega} |\nabla I| dx dy \quad (2.28)$$

Remark As noted in [ROF92], the use of the L^1 norm in the minimization process, instead of the L^2 norm, provides an essential advantage: the minimum of the energy function in the BV^{14} space can be a monotone function, not necessarily continuous, thus allowing for an efficient noise removal with edge preservation.

Using Lagrange multipliers, $E(I)$ can be expressed as a minimization problem without constraints since (2.27a) is implicitly fulfilled [ROF92]:

$$E'(I) = E(I) + \lambda \left[\iint_{\Omega} \frac{1}{2} (I - I_0)^2 dx dy - \sigma^2 \right] \quad (2.29)$$

Imposing Neumann boundary conditions, the minimum of (2.26) is the result of the following parabolic equation:

$$\begin{cases} \frac{\partial I}{\partial t} = \operatorname{div} \left(\frac{\nabla I}{|\nabla I|} \right) - \lambda (I - I_0) \\ \frac{\partial I}{\partial n} = 0, \text{ on } \partial\Omega \end{cases} \quad (2.30)$$

Since (2.29) is not a diffusion equation, (2.10) does not hold, hence (2.27a) is implicitly fulfilled only for an initial condition of the type:

$$I(x, y, 0) = I_0(x, y) + \sigma \frac{I_0(x, y) - \bar{I}_0}{\sigma(I_0)} \quad (2.31)$$

and a time-dependent Lagrange multiplier:

$$\lambda = \lambda(t) = -\frac{1}{2\sigma} \iint_{\Omega} \left(|\nabla I| - \frac{\nabla I \cdot \nabla I_0}{|\nabla I|} \right) dx dy \quad (2.32)$$

The removal of all constraints of (2.30) leads to a *diffusion equation through TV minimization*, also called the *weighted mean curvature motion* defined as:

$$\frac{\partial I}{\partial t} = \operatorname{div} \left(\frac{\nabla I}{|\nabla I|} \right) \quad (2.33)$$

¹⁴Bounded Variation

The parallel between the Perona–Malik model and (2.33) is straightforward, the latter being a particular case of the former, employing a diffusion function of the form:

$$g(|\nabla I|) = \frac{1}{|\nabla I|} \quad (2.34)$$

directionally expressed as:

$$\begin{cases} \frac{\partial I}{\partial t} = c_\xi I_{\xi\xi} \\ c_\xi = \frac{1}{|\nabla I|} \end{cases} \quad (2.35)$$

From a theoretical point of view, (2.33) is a parabolic equation, with provable existence and uniqueness of solution [ALM92]. The anisotropic diffusion through TV minimization acts along edges, while canceling out along the gradients direction, acting in every point of the image.

The TV minimization problem can also be expressed in a strictly numerical manner, without a prior definition on a continuous domain, such a proposition being made by Chan *et al.* in [COS01]. The digital TV filter thus obtained, can be regarded as a simplified version of the continuous model, using finite differences computed on a 4-neighborhood. Denoting the current pixel with α and its four neighboring pixels with β , thus the 4-neighborhood being defined as N_α , the local TV is expressed as

$$|\nabla_\alpha I| = \sqrt{\sum_{\beta \in N_\alpha} (I_\beta - I_\alpha)^2}$$

and its regularized version as:

$$|\nabla_\alpha I|_a = \sqrt{|\nabla_\alpha I|^2 + a^2}$$

By introducing the following weights:

$$\omega_{\alpha,\beta}(I) = \frac{1}{|\nabla_\alpha I|_a} + \frac{1}{|\nabla_\beta I|_a}$$

Chan *et al.* show that (2.30) can be replaced by:

$$\sum_{\beta \in N_\alpha} \omega_{\alpha,\beta}(I_\beta - I_\alpha) + \lambda(I - I_0) = 0$$

The digital TV filter $F : I \rightarrow J$ is an iteratively low-pass filter of the form:

$$\begin{cases} J_{\alpha,t-1} = F_\alpha(I_{t-1}) = \sum_{\beta \in N_\alpha} \frac{\omega_{\alpha,\beta}}{\lambda + \sum_{\gamma \in N_\alpha} \omega_{\alpha,\gamma}} I_{\beta,t-1} + \sum_{\beta \in N_\alpha} \frac{\lambda}{\lambda + \sum_{\gamma \in N_\alpha} \omega_{\alpha,\gamma}} I_{\beta,0} \\ I_t = F(J_{t-1}) \end{cases} \quad (2.36)$$

with the following parameters:

- the small positive parameter a called the regularization parameter – avoids division by zero for regions containing null gradients;

- the positive parameter λ called the fitting parameter – plays the role of the Lagrange multiplier from (2.30).

For illustrative purposes, the two major TV-based denoising methods, *i.e.*, *TV diffusion* (2.33) and the *digital TV filter* (2.36), are compared (Fig. 2.6) using a standard AWGN test scenario. An initial, noise free image (Fig. 2.6a), available at [Ima11b] and also found in [GW06], is contaminated with an AWGN of $\sigma = 20$ (Fig. 2.6b). The TV diffusion result (Fig. 2.6c) is obtained for $t = 15$, while the two extra parameters of the digital TV filter (Fig. 2.6d) are $\lambda = 10$ and $\alpha = 0.0001$, respectively.

Due to the existence of an attachment to the initial data I_0 , the digital TV filter (Fig. 2.6d) is less sensitive to the stopping time, conversely, since the filtered result is tightly linked to I_0 , the noise filtering is weaker. On the other hand, the TV diffusion result (Fig. 2.6c) shows that the TV diffusion method is more efficient at filtering out the noise, sometimes at the expense of small details, erased because of gradient estimation errors – directly proportional to noise.

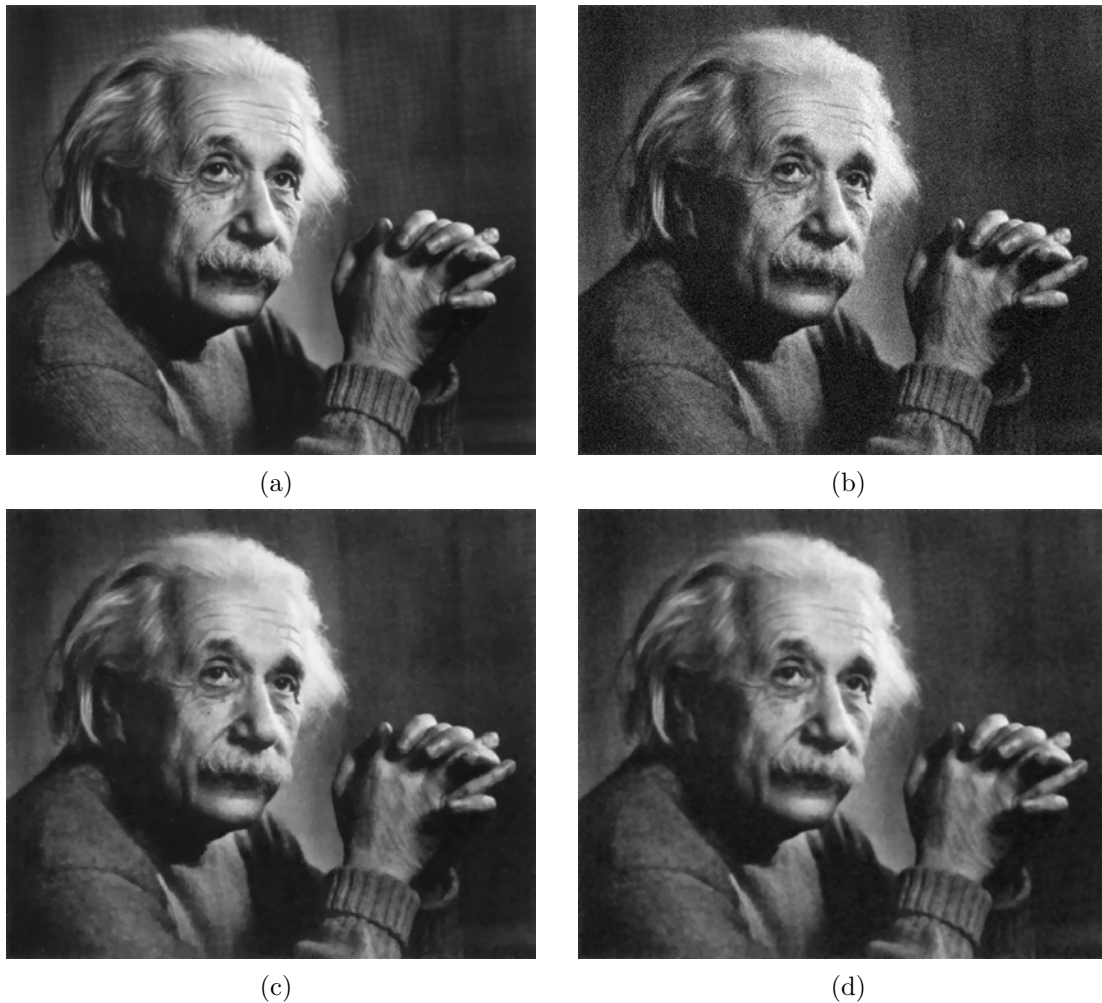


Fig. 2.6 – TV-based denoising methods: (a) Initial image; (b) Noisy image – AWGN of $\sigma_n = 20$; (c) TV Diffusion result; (d) Digital TV filter result.

2.6.2 A unifying PDE–variational approach

Since the two distinct image processing methods, *i.e.*, *PDEs* and *variational approaches*, share a common ground, Deriche and Faugeras [DF95] have shown that classic PDE models can be expressed using a unifying variational approach, thus bridging the two image processing frameworks. The classically expressed PDE methods can be reinterpreted as standard TV minimization problems, as the ones discussed in §2.6.1.

The unifying approach of Deriche and Faugeras is based on the initial assumption of a linear noisy model of the form:

$$I_0 = P \cdot I + N \quad (2.37)$$

where P is a linear operator – *e.g.*, the identity operator (when working only with noisy images) or the convolution operator (when working in a more generalized scenario of blur + additive noise) – and N is considered to be additive Gaussian in nature, of standard deviation σ and zero mean.

Obtaining the solution I from I_0 under a unifying framework, amounts to solving (2.37) using a TV minimization approach:

$$E(I) = \frac{1}{2} \underbrace{\|I_0 - P \cdot I\|^2}_{E_1(I)} + \underbrace{\iint_{\Omega} \varphi(|\nabla I|) dx dy}_{E_2(I)} \quad (2.38)$$

The TV minimization energy $E(I)$ comprises two energy terms: an energy term $E_1(I)$ linking the solution I to the initial data I_0 and a regularization term $E_2(I)$. Properly solving (2.38), and thus finding the solution I , revolves around the set of requirements that need to be fulfilled by the regularization function φ , with the following associated Euler–Lagrange equation:

$$\begin{cases} P^* \cdot (I_0 - P \cdot I) + \lambda \operatorname{div} \left[\varphi'(|\nabla I|) \frac{\nabla I}{|\nabla I|} \right] = 0, & (x, y) \in \Omega \\ \frac{\varphi'(|\nabla I|)}{|\nabla I|} \nabla I \cdot \vec{n} = 0, & (x, y) \in \partial\Omega \end{cases} \quad (2.39)$$

where P^* is the adjoint of P , \vec{n} is the unit vector normal to the image boundary and λ is the regularization term.

The steady-state solution of (2.39) is expressed using the following PDE:

$$\frac{\partial I}{\partial t} = \varphi''(|\nabla I|) I_{\eta\eta} + \frac{\varphi'(|\nabla I|)}{|\nabla I|} I_{\xi\xi} \quad (2.40)$$

The regularization function $\varphi(s)$ should fulfill the following conditions [DF95]:

- $\varphi''(|\nabla I|) \geq 0$ and $\varphi'(|\nabla I|) \geq 0$ – ensures the convexity of the energy function $E_2(I)$ and implicitly the stability of the minimization process.
- $\lim_{|\nabla I| \rightarrow 0} \frac{\varphi'(|\nabla I|)}{|\nabla I|} = \lim_{|\nabla I| \rightarrow 0} \varphi''(|\nabla I|) = \varphi''(0) \geq 0$ – ensures an isotropic smoothing for small gradient norms.

Table 2.1 – Regularization functions studied by Deriche and Faugeras [DF95]

Model/author	$\varphi(s)$	$\varphi'(s)/s$	$\varphi''(s)$
Perona–Malik	$-\frac{K^2}{2} \left[e^{-\left(\frac{s}{K}\right)^2} - 1 \right]$	$e^{-\left(\frac{s}{K}\right)^2}$	$e^{-\left(\frac{s}{K}\right)^2} \left[1 - 2 \left(\frac{s}{K}\right)^2 \right]$
	$\frac{K^2}{2} \log \left[1 + \left(\frac{s}{K}\right)^2 \right]$	$\frac{1}{1+\left(\frac{s}{K}\right)^2}$	$\frac{K^2(K^2-s^2)}{(K^2+s^2)^2}$
Rudin	s	$\frac{1}{s}$	0
Charbonnier <i>et al.</i>	$\sqrt{1 + \left(\frac{s}{K}\right)^2} - 1$	$\frac{K^{-2}}{\sqrt{\frac{K^2+s^2}{K^2}}}$	$\frac{ K }{\sqrt{(K^2+s^2)^3}}$
Green	$\log \cosh\left(\frac{s}{K}\right)$	$\tanh\left(\frac{s}{K}\right)$	$K^2 \left[\cosh\left(\frac{s}{K}\right) \right]^{-2}$

- $\lim_{|\nabla I| \rightarrow \infty} \frac{\varphi'(|\nabla I|)}{|\nabla I|} = \text{const.} \geq 0$, $\lim_{|\nabla I| \rightarrow \infty} \varphi''(|\nabla I|) = 0$ – ensures a unidirectional smoothing, orthogonally to the gradient direction, for large gradient norms.

Table 2.1 synthesizes the more notable functions studied by Deriche and Faugeras [DF95], i.e., the classic Perona–Malik diffusion functions, Rudin’s diffusion function and two nondecreasing flux functions: proposed by Charbonnier *et al.* [CBFAB94] and by Green [Gre90], respectively. The equivalence between the diffusion functions g – flux functions ϕ of the Perona–Malik model and the regularization functions φ is readily obtainable by defining:

$$g(s) = \frac{\varphi'(s)}{s} \text{ and}$$

$$\phi'(s) = \varphi''(s).$$

Thus the precondition $\phi''(|\nabla I|) \geq 0$ meant to ensure the minimization process’ stability, is reduced to imposing that the flux function be monotonous. Within this framework, the Perona–Malik functions exhibit an unstable behavior when applied over edge (nonhomogeneous) regions, while the Rudin function is not isotropic across homogeneous regions (where the gradient norms are small).

On the other hand, the functions proposed by Charbonnier *et al.* and by Green do not bestow a physical meaning to the diffusion threshold parameter K , while it remains a weighting coefficient, it no longer determines which gradients will be preserved and which will be smoothed out.

The initial unifying approach of Deriche and Faugeras was revisited by Kornprobst *et al.* in [KDA96, KDA97b, KDA99] with the initial assumption that P from (2.37) is the identity operator, resulting the following energy minimization functional:

$$E(I) = \iint_{\Omega} [(I - I_0)^2 + \lambda \varphi(|\nabla I|)] \, dx dy \quad (2.41)$$

with its respective associated Euler–Lagrange equation:

$$2(I - I_0) - \lambda \operatorname{div} \left[\varphi'(|\nabla I|) \frac{\nabla I}{|\nabla I|} \right] = 0 \quad (2.42)$$

The minimization problem (2.41) with its necessary condition (2.42) can be solved implicitly or explicitly, as indicated by Kornprobst *et al.* [KDA96, KDA97b, KDA99], the best results being obtained using a *half quadratic minimization* approach.

Remark The authors indicate that the best results are obtained when using Perona–Malik-type diffusion and flux functions.

2.7 Tensor-based filtering

The use of diffusion functions in defining PDE-based filtering models can sometimes prove restrictive and show its implicit limitations when trying to define complex 2-D or 3-D structures. Tackling junctions or complex edges simply using a 1-D control function approach, can prove inefficient if the desired results need to fulfill a high fidelity standard. 1-D diffusion functions of gradient norm arguments do not always suffice for properly describing the image geometry, thus the diffusion process is inherently limited by its control functions.

An alternative way of describing image structures and overall image geometry, rather than using scalar diffusion functions, is through diffusion matrices, yielding a PDE-based model of the form:

$$\frac{\partial I}{\partial t} = \operatorname{div}(\mathbf{D}\nabla I) \quad (2.43)$$

with initial conditions: $I(x, y, 0) = I_0(x, y) \in \Omega$ and $I(x, y) = 0$ or $\mathbf{D}\nabla I \cdot \vec{n} = 0$ on the boundary of $\partial\Omega$ where \vec{n} is the outward normal to the boundary.

The diffusion matrices, hereinafter called diffusion tensors, are symmetric matrices with the corresponding set of eigenvalues (λ_1, λ_2) that allow a decomposition within the orthonormal vectors (\vec{v}_1, \vec{v}_2) basis [Str05]:

$$\mathbf{D} = (\vec{v}_1 | \vec{v}_2) \begin{pmatrix} \lambda_1 & 0 \\ 0 & \lambda_2 \end{pmatrix} \begin{pmatrix} \vec{v}_1^T \\ \vec{v}_2^T \end{pmatrix} \quad (2.44)$$

Properly choosing \mathbf{D} strongly influences the filtered result, since the diffusion process is steered along the diffusion matrix eigenvectors' directions. Furthermore, \mathbf{D} describes the local variations of the gradient orientation, thus, a smoothed gradient map or orientation coherence-dependent functions are used in constructing the diffusion matrix.

2.7.1 The Weickert tensor-based diffusion models

The Weickert tensor-based diffusion model family, initially proposed in [Wei94], relies on a steered diffusion mechanism that uses directional information computed either based on the gradient vector's norm or based on a notion of spatial coherence. The two main types of filters derived from these principles are:

- Edge Enhancing Diffusion (EED) – performs an image smoothing with selective edge enhancement [Wei94, WtHRV96];
- Coherence Enhancing Diffusion (CED) – specifically designed for edge reconstruction – e.g., fingerprint ridges, in fingerprint images – or fault detection [Wei95, Wei97b, Wei99].

2.7.1.1 The Weickert CED model

The CED model was initially introduced by Weickert in [Wei95] for enhancing the coherence of 1-D textures and further developed in [Wei97b, Wei99], being centered on the notion of *structure tensor*. The structure tensor had been previously used in [KW87, Rao90, RS91] for orientation estimation purposes. The CED tensor-based diffusion model shares a common framework with the previously discussed models, being described by the same diffusion equation (2.43). What fundamentally differs is the way in which the diffusion matrix \mathbf{D} is constructed: starting from the symmetric matrix $\mathbf{J}_0(\nabla I_\sigma)$ that corresponds to the smoothed gradient vectors tensor product, at a scale σ ($\nabla I_\sigma = G_\sigma * \nabla I$):

$$\mathbf{J}_0(\nabla I_\sigma) = \nabla I_\sigma \cdot \nabla I_\sigma^T = \begin{pmatrix} \frac{\partial^2 I_\sigma}{\partial x^2} & \frac{\partial I_\sigma}{\partial x} \frac{\partial I_\sigma}{\partial y} \\ \frac{\partial I_\sigma}{\partial x} \frac{\partial I_\sigma}{\partial y} & \frac{\partial^2 I_\sigma}{\partial y^2} \end{pmatrix} \quad (2.45)$$

The structure tensor is defined by performing a convolution product on each of the components of (2.45) using a Gaussian kernel G_ρ of standard deviation ρ :

$$\mathbf{J}_\rho(\nabla I_\sigma) = G_\rho * \mathbf{J}_0(\nabla I_\sigma) = \begin{pmatrix} G_\rho * \frac{\partial^2 I_\sigma}{\partial x^2} & G_\rho * \frac{\partial I_\sigma}{\partial x} \frac{\partial I_\sigma}{\partial y} \\ G_\rho * \frac{\partial I_\sigma}{\partial x} \frac{\partial I_\sigma}{\partial y} & G_\rho * \frac{\partial^2 I_\sigma}{\partial y^2} \end{pmatrix} \quad (2.46)$$

Hence, the eigenvectors of the symmetric matrix $\mathbf{J}_\rho(\nabla I_\sigma)$ yield the gradient vectors' mean orientation (\vec{w}_1) and the structures' mean orientation (\vec{w}_2), corresponding to a scale ρ , while the associated eigenvalues represent the mean contrast value along the \vec{w}_1 direction. The scale parameter σ , also called by Weickert the *local scale* parameter, establishes the minimum size of the structures that will be preserved during the smoothing process, its interpretation being similar in nature to the one of the anisotropic diffusion model. Finally, the second scale parameter, ρ , also called the *integration scale* parameter, indicates the size of structures of interest, within the processed image.

By using the simplified notation:

$$\mathbf{J} = \begin{pmatrix} j_{11} & j_{12} \\ j_{12} & j_{22} \end{pmatrix}$$

the eigenvalues are expressed as [Ter04]:

$$\begin{cases} \mu_1 = \frac{1}{2} \left(j_{11} + j_{22} + \sqrt{(j_{11} - j_{22})^2 + 4j_{12}^2} \right) \\ \mu_2 = \frac{1}{2} \left(j_{11} + j_{22} - \sqrt{(j_{11} - j_{22})^2 + 4j_{12}^2} \right) \end{cases} \quad (2.47)$$

The CED model uses the difference between the two eigenvalues:

$$\mu_1 - \mu_2 = \sqrt{(j_{11} - j_{22})^2 + 4j_{12}^2} \quad (2.48)$$

as a coherence indicator, *i.e.*, the homogeneous regions are characterized by $\mu_1 = \mu_2 = 0$, the linear structures by $\mu_1 \gg \mu_2 = 0$ and the junctions by $\mu_1 \geq \mu_2 \gg 0$.

In order to ensure a directional diffusion process along \vec{w}_2 , the eigenvalues are chosen as follows [Wei95]:

$$\begin{cases} \lambda_1 = \alpha \\ \lambda_2 = \begin{cases} \alpha & \text{if } j_{11} = j_{22} \text{ and } j_{12} = 0 \\ \alpha + (1 - \alpha) \exp \left[-\frac{1}{(j_{11} - j_{22})^2 + 4j_{12}^2} \right] & \text{otherwise} \end{cases} \end{cases} \quad (2.49)$$

Parameter-wise, α controls the diffusion along the smoothed gradients' direction: for small values it induces an anisotropic behavior, while for values close to 1 the behavior is almost isotropic in nature.

The resulting diffusion matrix having the following form:

$$\mathbf{D} = (\vec{w}_1 \mid \vec{w}_2) \begin{pmatrix} \lambda_1 & 0 \\ 0 & \lambda_2 \end{pmatrix} \begin{pmatrix} \vec{w}_1^T \\ \vec{w}_2^T \end{pmatrix} \quad (2.50)$$

Deducing the behavior of the CED model, based on (2.49) is straightforward: for homogeneous regions, the diffusion process is isotropic with a diffusion speed indicated by α ; for elongated structures, like edges or textures, the diffusion is strongly anisotropic, characterized by the ratio λ_1/λ_2 .

The importance of tensor fields and tensor-based image processing is further underlined by dedicated books, e.g., [WH06, LW09]¹⁵, showing the existing interest in these methods even after more than a decade and a half since their first use in PDE-based image processing and analysis.

2.8 Level-set and curvature-based filtering

This class of filters was motivated by the need of defining a nonlinear diffusion operator that exhibits a strong anisotropic behavior, acting along edges and contours. Thus the resulting diffusion operator is curvature-dependent, driving the diffusion process along isolines, luminance-wise.

By revisiting the isotropic diffusion equation (2.8) and rewriting it using its second order directional derivatives, the following expression is obtained:

$$\frac{\partial I}{\partial t} = \text{div}(\nabla I) = \Delta I = I_{\xi\xi} + I_{\eta\eta} \quad (2.51)$$

The proposition of Alvarez *et al.* [ALM92] is to replace (2.51) with a PDE model that acts orthogonally to the gradient vector's direction:

$$\begin{cases} \frac{\partial I}{\partial t} = I_{\xi\xi} = \Delta I - I_{\eta\eta} = I_{xx} + I_{yy} - \frac{I_{xx}I_x^2 + 2I_{xy}I_xI_y + I_{yy}I_y^2}{|\nabla I|^2} \\ \quad = \frac{I_{xx}I_y^2 - 2I_{xy}I_xI_y + I_{yy}I_x^2}{|\nabla I|^2} \\ I(x, y, 0) = I_0(x, y) \end{cases} \quad (2.52)$$

¹⁵Recommended reading for further understanding various key tensor-related topics

The relevance of (2.52) is reinforced by the extensive study of its geometrical interpretation and its connection with the Euclidean geometric diffusion equation, covered in [KS96, Sap01].

2.8.1 The Euclidean Morphological Scale Space analysis

In [AGLM93], Alvarez *et al.* lay down the fundamental principles of multiscale image processing, stating that the only continuous domain analysis that abides by those principles (§2.3, §2.4) is obtained at scale t by the following PDE:

$$\begin{cases} \frac{\partial I}{\partial t} = |\nabla I| F(\kappa, t) \\ I(x, y, 0) = I_0(x, y) \end{cases} \quad (2.53)$$

where $\kappa = \operatorname{div} \left(\frac{\nabla I}{|\nabla I|} \right)$ describes the isolines' curvature and $F(\kappa, t)$ is a nondecreasing function with respect to κ .

In practice, the initial condition $I(x, y, 0) = I_0(x, y)$ is replaced with a smoothed version of the initial image, $I(x, y, 0) = G_\sigma * I_0(x, y)$ in order to ensure the continuity and differentiation of the image function I , thus ensuring a robust mathematical framework.

For the particular case $F(\kappa, t) = \kappa \cdot t$, (2.53) can be rewritten as:

$$\begin{aligned} \frac{\partial I}{\partial t} &= t|\nabla I|\kappa = t|\nabla I| \operatorname{div} \left(\frac{\nabla I}{|\nabla I|} \right) = t|\nabla I| \left[\frac{\partial}{\partial x} \left(\frac{I_x}{|\nabla I|} \right) + \frac{\partial}{\partial y} \left(\frac{I_y}{|\nabla I|} \right) \right] \\ &= t|\nabla I| \frac{I_{xx}(I_x^2 + I_y^2) - I_x(I_x I_{xx} + I_y I_{xy}) + I_{yy}(I_x^2 + I_y^2) - I_y(I_x I_{xy} + I_y I_{yy})}{|\nabla I|^{3/2}} \\ &= t|\nabla I| \frac{I_x^2 I_{yy} - 2I_x I_y I_{xy} + I_y^2 I_{xx}}{|\nabla I|^{3/2}} = t \frac{I_x^2 I_{yy} - 2I_x I_y I_{xy} + I_y^2 I_{xx}}{|\nabla I|^2} \end{aligned} \quad (2.54)$$

Remark By changing the scale parameter t to $t' = 0.5t^2$ (2.54) becomes (2.52).

Equation (2.54) exhibits a unidirectional smoothing, being similar in this respect with the anisotropic diffusion model, but missing the contrast parameter, thus ensuring the morphological invariance. On the other hand, (2.54) is also similar to the TV diffusion model (2.32), having a directional interpretation of the following form:

$$\begin{cases} \frac{\partial I}{\partial t} = c_\xi I_{\xi\xi} \\ c_\xi = 1 \end{cases} \quad (2.55)$$

The same equation, *i.e.*, (2.54) can be obtained geometrically [Ter04]: let $C(x, y, t)$ be a closed plane curve defined through its position vector \vec{C} and let, by convention, $\vec{n} = -\frac{\nabla I}{|\nabla I|}$ be the normal unity vector. Then, the deformation of C for the Euclidean geometric diffusion equation corresponds to the deformation of this curve in every point along the normal direction with a speed proportional to the curvature κ :

$$\frac{\partial \vec{C}}{\partial t} = \kappa \vec{n} \text{ with initial condition: } C(x, y, 0) \quad (2.56)$$

An important property of (2.56) consists in its ability to transform any non-convex curve into a convex one [Gra87] without developing junctions as a byproduct, while exhibiting a finite time evanescent behavior [GH86]. The rest of the properties of (2.56) are detailed in [GH86, Gra87, KS96].

Since the EMSS model is linked to the theory of curve deformation, (2.52) has a geometrical interpretation: all the image's isocontours deform along their orthogonal direction with a speed proportional to the mean curvature¹⁶.

Remark As noted in [Ter04], the EMSS model is capable of efficiently eliminating the unwanted noise contamination: since the noisy areas are characterized by strong curves, the model exhibits a strong smoothing behavior within those areas. Conversely, the use of this model is limited, especially for large values of the scale parameter t : in this case the structures are reduced to convex curves, which in time become more and more rounded at the edges. The model ensures edge preservation only for small values of t .

2.8.2 The Affine Morphological Scale Space analysis

The AMSS analysis was first introduced, as an image analysis tool, by Alvarez *et al.* in [AGLM93] and later explained independently from the image analysis framework, using curve deformation theory by Sapiro and Tannenbaum in [ST94, Sap01].

Similarly to the EMSS, by replacing the Euclidean invariance axiom with an affine invariance axiom, Alvarez *et al.* show that the only multiscale analysis that obeys the required axioms [AGLM93] is expressed using the following PDE:

$$\begin{cases} \frac{\partial I}{\partial t} = |\nabla I| \left[t \cdot \operatorname{div} \left(\frac{\nabla I}{|\nabla I|} \right) \right]^{1/3} \\ I(x, y, 0) = I_0(x, y) \end{cases} \quad (2.57)$$

Rewriting (2.57) yields:

$$\frac{\partial I}{\partial t} = |\nabla I| \left(t \cdot \frac{I_x^2 I_{yy} - 2I_x I_y I_{xy} + I_y^2 I_{xx}}{(I_x^2 + I_y^2)^{3/2}} \right)^{1/3} = t^{1/3} (I_x^2 I_{yy} - 2I_x I_y I_{xy} + I_y^2 I_{xx})^{1/3} \quad (2.58)$$

By analogy with the EMSS model, changing the scale parameter t with $t' = 3/4 \cdot t^{4/3}$, (2.58) can be rewritten as:

$$\frac{\partial I}{\partial t'} = (I_x^2 I_{yy} - 2I_x I_y I_{xy} + I_y^2 I_{xx})^{1/3} \quad (2.59)$$

The AMSS model can be also viewed from a directional point of view, being expressed according to its second order directional derivatives as follows:

$$\begin{cases} \frac{\partial I}{\partial t} = c_\xi I_{\xi\xi} \\ c_\xi = |\nabla I|^{2/3} I_{\xi\xi} \end{cases} \quad (2.60)$$

¹⁶The equation describing this process is commonly known as MCM – Mean Curvature Motion

Remark As also noted by [Ter04], the properties of (2.60) are identical to its EMSS counterpart: a non-convex curve evolves in time into a convex one; the closed curves evolve toward elliptical points, while ellipses preserve their eccentricity. The AMSS analysis, just as the EMSS analysis, ensures edge preservation only for small values of the scale parameter t .

2.9 Numerical approximations

Since PDEs are naturally defined in a continuous setting and conversely, the ones employed in image processing model discrete processes, the discrete PDEs do not naturally yield a straightforward solution. In order to successfully use PDEs as digital image processing tools, their continuous solution needs to be approximated.

The existing numerical approximation techniques cover a wide spectrum of approaches, from finite difference schemes to convolution masks, and due to the extensive nature of these techniques, a complete reference to approximating PDEs can be found in [Ort87, Fun92, Dzy95, Tho95, BDH06, Chi08, QV08]. This section covers only the topics directly relevant to the work presented in the following chapters, leaving the other approximation methods as a further recommended reading. Other useful resources that extensively cover the topic of PDEs in image processing are [AK06, Mar06, TLCO07, Eva10].

Among the existing approximation techniques, a widely used method is that of *finite difference approximation*, mainly because digital images are defined on discrete lattices and thus, a finite difference approach is best suited for their numerical analysis.

2.9.1 Finite difference approximations

For every PDE describing an image processing model, there exists a set of *a priori* requirements: the existence of an image definition domain, e.g., $\Omega = [0, a] \times [0, b]$, initial conditions and boundary conditions.

For the numerical approximation part, a series of preconditioning assumptions need to be made: the discrete lattices, on which a digital image is usually defined, will be considered as having an equal spacing h between two lattice points (nodes) on the horizontal direction x and the vertical direction y , respectively. Since digital image processing inherently deals with discrete quantities, the image definition domain is considered implicitly discretized, thus the values of the image function are samples (pixels) of a theoretically continuous function, expressed within the (x, y) frame of reference. In conclusion, the image size (in pixels) can be expressed as $M \times N$, where: $M = a/h$ and $N = b/h$.

Hence, the continuous function $I : \Omega \times (0, \infty) \rightarrow \mathbb{R}$ is replaced by:

$$I(x, y, t) \rightarrow I(ih, jh, t) = I(i, j, t) \text{ with } i = \{0, 1, \dots, N\} \text{ and } j = \{0, 1, \dots, M\} \quad (2.61)$$

Every PDE describing the models discussed so far is expressed numerically as a discrete recursive process. The discretization of this process is done three dimensionally for 2-D images or four dimensionally for 3-D images, the extra dimension being the theoretical evolution time. The discrete time domain is expressed using uniformly distributed time samples, multiples of a discretization time step dt . The numerical representation of a time-evolving digital image at instant t is expressed as:

$$I(i, j, t) \rightarrow I(i, j, n \cdot dt) = I_{i,j}^n \quad (2.62)$$

where n represents the number of iterations required to reach the discrete time t .

The initial condition image function will be similarly expressed as:

$$I(i, j, 0) \rightarrow I_{i,j}^0 \quad (2.63)$$

Remark From a practical point of view, in digital image processing, the boundary conditions do not influence the final result, save for the image margins. For the sake of consistency with the rigorous mathematical definitions, Neumann and(or) Dirichlet boundary conditions will be imposed for the numerical models, whenever needed.

2.9.1.1 Approximating partial derivatives

In order to preserve the localized characteristics of PDEs, the first order derivatives are replaced by first and second order approximations, furthermore, the spatial and temporal derivatives are approximated based on Taylor series expansions using the $(x+k, y+l, t+m)$ set of points. The *central difference* approximation is expressed using symmetrical approximations:

$$\frac{\partial}{\partial x}[I(x, y, t)] = D_x^0[I(x, y, t)] = \frac{I(x+k, y, t) - I(x-k, y, t)}{2|k|} \quad (2.64)$$

The (2.64) approximation is similarly computed for $\frac{\partial}{\partial y}[I(x, y, t)]$ and $\frac{\partial}{\partial t}[I(x, y, t)]$.

By considering $x = ih$, $y = jh$, $t = n \cdot dt$ and displacements of the type $k = \pm h$, $l = \pm h$, $m = \pm dt$, the spatial approximations using central differences can be rewritten as:

$$D_x^0(I_{i,j}^n) = \frac{I_{i+1,j}^n - I_{i-1,j}^n}{2h}, \quad D_y^0(I_{i,j}^n) = \frac{I_{i,j+1}^n - I_{i,j-1}^n}{2h} \quad (2.65)$$

First order derivatives can be also approximated using *forward* or *backward differences* of order one:

$$\begin{aligned} D_x^+(I_{i,j}^n) &= \frac{I_{i+1,j}^n - I_{i,j}^n}{h}, & D_x^-(I_{i,j}^n) &= \frac{I_{i,j}^n - I_{i-1,j}^n}{h} \\ D_y^+(I_{i,j}^n) &= \frac{I_{i,j+1}^n - I_{i,j}^n}{h}, & D_y^-(I_{i,j}^n) &= \frac{I_{i,j}^n - I_{i,j-1}^n}{h} \end{aligned} \quad (2.66)$$

Alternative approaches, like the one of Scharf and Weickert [SW00] tackle the PDE approximation problem differently, by estimating first order derivatives using optimized convolution masks. More specifically, 3×3 (F_x and F_y respectively) rotation-optimized masks:

$$\frac{\partial I_{i,j}^n}{\partial x} = \mathbf{F}_x * I_{i,j}^n, \quad \frac{\partial I_{i,j}^n}{\partial y} = \mathbf{F}_y * I_{i,j}^n \quad (2.67)$$

The derivative with respect to time is always estimated using a forward difference approximation of order one of the form:

$$D_t^+(I_{i,j}^n) = \frac{I_{i,j}^{n+1} - I_{i,j}^n}{dt} \quad (2.68)$$

The finite difference approximations can be also computed along directions other than the ones of the standard (x, y) frame of reference. An example of such directions is

the diagonal axes approximation: let $\vec{d}x$ and $\vec{d}y$ be h -norm vectors along the horizontal and vertical direction, respectively. Hence, the diagonal vectors are expressed as:

$$\begin{cases} \vec{d}u = \vec{d}x + \vec{d}y \\ \vec{d}v = \vec{d}x - \vec{d}y \\ \text{with } |\vec{d}u| = |\vec{d}v| = \sqrt{2}h \end{cases}$$

yielding:

$$D_u^0(I_{i,j}^n) = \frac{I_{i+1,j+1}^n - I_{i-1,j-1}^n}{2\sqrt{2}h}, \quad D_v^0(I_{i,j}^n) = \frac{I_{i+1,j-1}^n - I_{i-1,j+1}^n}{2\sqrt{2}h} \quad (2.69)$$

and

$$\begin{aligned} D_u^+(I_{i,j}^n) &= \frac{I_{i+1,j+1}^n - I_{i,j}^n}{\sqrt{2}h}, & D_u^-(I_{i,j}^n) &= \frac{I_{i,j}^n - I_{i-1,j-1}^n}{\sqrt{2}h} \\ D_v^+(I_{i,j}^n) &= \frac{I_{i+1,j-1}^n - I_{i,j}^n}{\sqrt{2}h}, & D_v^-(I_{i,j}^n) &= \frac{I_{i,j}^n - I_{i-1,j+1}^n}{\sqrt{2}h} \end{aligned} \quad (2.70)$$

The second order derivatives along the x and y directions are expressed using the corresponding finite difference approximations of order two:

$$\begin{cases} \frac{\partial^2 I_{i,j}^n}{\partial x^2} = \frac{I_{i+1,j}^n + I_{i-1,j}^n - 2I_{i,j}^n}{h^2} = D_x^-[D_x^+(I_{i,j}^n)] \\ \frac{\partial^2 I_{i,j}^n}{\partial y^2} = \frac{I_{i,j+1}^n + I_{i,j-1}^n - 2I_{i,j}^n}{h^2} = D_y^-[D_y^+(I_{i,j}^n)] \\ \frac{\partial^2 I_{i,j}^n}{\partial x \partial y} = \frac{I_{i+1,j+1}^n + I_{i-1,j-1}^n - I_{i+1,j-1}^n - I_{i-1,j+1}^n}{4h^2} \end{cases} \quad (2.71)$$

Remark Similarly, $\frac{\partial^2 I_{i,j}^n}{\partial u^2}$, $\frac{\partial^2 I_{i,j}^n}{\partial v^2}$ and $\frac{\partial^2 I_{i,j}^n}{\partial u \partial v}$ can be numerically expressed using finite difference approximations of order two.

Another important set of derivatives that often needs to be approximated is the $(I_{\eta\eta}, I_{\xi\xi})$ pair. A straightforward way of numerically expressing $I_{\eta\eta}$ and $I_{\xi\xi}$ is using (2.71), since they are mathematically expressed as:

$$\begin{cases} I_{\eta\eta} = \eta_x^2 I_{xx} + 2\eta_x \eta_y I_{xy} + \eta_y^2 I_{yy} \\ I_{\xi\xi} = \xi_x^2 I_{xx} + 2\xi_x \xi_y I_{xy} + \xi_y^2 I_{yy} \end{cases} \quad (2.72)$$

where:

$$\vec{\eta} = \begin{pmatrix} \eta_x \\ \eta_y \end{pmatrix} = \begin{pmatrix} \frac{I_x}{|\nabla I|} \\ \frac{I_y}{|\nabla I|} \end{pmatrix} \quad \text{and} \quad \vec{\xi} = \begin{pmatrix} \xi_x \\ \xi_y \end{pmatrix} = \begin{pmatrix} \frac{-I_y}{|\nabla I|} \\ \frac{I_x}{|\nabla I|} \end{pmatrix} \quad (2.73)$$

Remark The (2.72) approximation is not rotation-invariant and may lead to instabilities within quasi-homogeneous regions. An immediate solution is to approximate these derivatives using more robust, rotation-invariant approaches, e.g., 4, 6 or 8-neighborhood convolution masks.

2.9.1.2 Approximating differential geometry operators

Numerically expressing classic differential geometry operators like the gradient vector or the Laplacian operator requires using the numerical approximations previously defined in §2.9.1.1.

Based on those approximations, one way of expressing the gradient vector is:

$$\nabla I_{i,j}^n = \frac{\partial I_{i,j}^n}{\partial x} \vec{d}x + \frac{\partial I_{i,j}^n}{\partial y} \vec{d}y = \frac{\partial I_{i,j}^n}{\partial u} \vec{d}u + \frac{\partial I_{i,j}^n}{\partial v} \vec{d}v \quad (2.74)$$

Using (2.65) and (2.69) the gradient norm can be further expressed as:

$$|\nabla I|_{i,j}^n = \sqrt{(D_x^0(I_{i,j}^n))^2 + (D_y^0(I_{i,j}^n))^2} = \sqrt{(D_u^0(I_{i,j}^n))^2 + (D_v^0(I_{i,j}^n))^2} \quad (2.75)$$

or, alternatively, using the (2.67) convolution mask approach:

$$|\nabla I|_{i,j}^n = \sqrt{(\mathbf{F}_x * I_{i,j}^n)^2 + (\mathbf{F}_y * I_{i,j}^n)^2} \quad (2.76)$$

The gradient vector, more precisely the gradient norm, numerically expressed either as (2.75) or as (2.76), is usually employed in expressing diffusion equations or MCM image processing models.

Another basic differential geometry operator, the Laplacian operator, is most commonly approximated as:

$$\Delta I(i, j, n) = \Delta I_{i,j}^n = \frac{\partial^2 I_{i,j}^n}{\partial x^2} + \frac{\partial^2 I_{i,j}^n}{\partial y^2} = D_x^- [D_x^+ (I_{i,j}^n)] + D_y^- [D_y^+ (I_{i,j}^n)] \quad (2.77)$$

Since the Laplacian operator is inherently rotation-invariant, alternative approximations are readily available, simply by replacing the (x, y) frame of reference with the (u, v) or (ξ, η) .

Another important differential operator, widely used in defining PDE-based models, is the divergence operator. One possible approximation such as the one employed by the Perona–Malik model is obtained from the 1-D diffusion equation at a given scale t :

$$\begin{aligned} \frac{\partial I_i^n}{\partial t} &= \frac{\partial}{\partial x} \left[g \left(\left| \frac{\partial I_i^n}{\partial x} \right| \right) \cdot \frac{\partial I_i^n}{\partial x} \right] \approx \frac{\partial}{\partial x} \left[g \left(\left| \frac{\partial I_i^n}{\partial x} \right| \right) \cdot \frac{I_{i+h/2}^n - I_{i-h/2}^n}{h} \right] \\ &= \frac{1}{h} \left[g \left(\left| \frac{\partial I_i^n}{\partial x} \right| \right) \Big|_{i+h/2} \cdot \frac{I_{i+h/2+h/2}^n - I_{i-h/2+h/2}^n}{h} \right. \\ &\quad \left. - g \left(\left| \frac{\partial I_i^n}{\partial x} \right| \right) \Big|_{i-h/2} \cdot \frac{I_{i+h/2-h/2}^n - I_{i-h/2-h/2}^n}{h} \right] \\ &= \frac{1}{h} \left[g \left(\left| \frac{\partial I_i^n}{\partial x} \right| \right) \Big|_{i+h/2} \cdot D_x^+ I_i^n - g \left(\left| \frac{\partial I_i^n}{\partial x} \right| \right) \Big|_{i-h/2} \cdot \frac{I_i^n - I_{i-h}^n}{h} \right] \end{aligned} \quad (2.78)$$

Where the value of the diffusion function for the $i \pm h/2$ pixels is replaced with a backward or forward first order finite difference approximation [Ter04]:

$$\begin{cases} g \left(\left| \frac{\partial I_i^n}{\partial x} \right| \right) \Big|_{i+h/2} \approx g \left(\left| \frac{\partial I_i^n}{\partial x} \right| \Big|_{i+h/2} \right) = g[|D_x^+(I_i^n)|] \\ g \left(\left| \frac{\partial I_i^n}{\partial x} \right| \right) \Big|_{i-h/2} \approx g \left(\left| \frac{\partial I_i^n}{\partial x} \right| \Big|_{i-h/2} \right) = g[|D_x^-(I_i^n)|] \end{cases} \quad (2.79)$$

Equation (2.79) leads to the simplified form of (2.78):

$$\begin{aligned}\frac{\partial I_i^n}{\partial t} &= \frac{1}{h} \{g[|D_x^+(I_i^n)|]D_x^+(I_i^n) - g[|D_x^-(I_i^n)|]D_x^-(I_i^n)\} \\ &= D_x^- \{g[|D_x^+(I_i^n)|]D_x^+(I_i^n)\} = \phi_{right} - \phi_{left}\end{aligned}\quad (2.80)$$

where ϕ_{right} and ϕ_{left} represent the flux functions belonging to neighboring pixels, with respect to the current pixel i .

The 2-D extension of (2.78) is straightforward and amounts to adding another dimension and writing the diffusion function as a diagonal matrix [Ter04]:

$$c(\nabla I_{i,j}^n) = \begin{bmatrix} g\left(\left|\frac{\partial I_{i,j}^n}{\partial x}\right|\right) & 0 \\ 0 & g\left(\left|\frac{\partial I_{i,j}^n}{\partial y}\right|\right) \end{bmatrix}$$

thus resulting:

$$\begin{aligned}\frac{\partial I_{i,j}^n}{\partial t} &= \frac{\partial}{\partial x} \left[g\left(\left|\frac{\partial I_{i,j}^n}{\partial x}\right|\right) \cdot \frac{\partial I_{i,j}^n}{\partial x} \right] + \frac{\partial}{\partial y} \left[g\left(\left|\frac{\partial I_{i,j}^n}{\partial y}\right|\right) \cdot \frac{\partial I_{i,j}^n}{\partial y} \right] \\ &= D_x^- \{g[|D_x^+(I_{i,j}^n)|]D_x^+(I_{i,j}^n)\} + D_y^- \{g[|D_y^+(I_{i,j}^n)|]D_y^+(I_{i,j}^n)\} \\ &= \phi_{east} - \phi_{west} + \phi_{south} - \phi_{north}\end{aligned}\quad (2.81)$$

Remark (2.81) represents the standard 4-neighborhood approximation, an 8-neighborhood approximation being proposed in [Kor98].

Weickert *et al.* note in [WtHRV98] that the classic (2.81) approximation lacks the property of rotation invariance and, based on the work of Catté *et al.* [CLMC92], propose a more robust approximation:

$$\begin{aligned}\frac{\partial I_{i,j}^n}{\partial t} &= \frac{1}{h} \left\{ \frac{[g(|\nabla I_\sigma|)|_{i+h,j} + g(|\nabla I_\sigma|)|_{i,j}]}{2} D_x^+ I_{i,j}^n - \frac{[g(|\nabla I_\sigma|)|_{i-h,j} + g(|\nabla I_\sigma|)|_{i,j}]}{2} D_x^- I_{i,j}^n \right\} \\ &\quad + \frac{1}{h} \left\{ \frac{[g(|\nabla I_\sigma|)|_{i,j+h} + g(|\nabla I_\sigma|)|_{i,j}]}{2} D_y^+ I_{i,j}^n - \frac{[g(|\nabla I_\sigma|)|_{i,j-h} + g(|\nabla I_\sigma|)|_{i,j}]}{2} D_y^- I_{i,j}^n \right\}\end{aligned}\quad (2.82)$$

Another possible way of approximating the divergence operator is using a matrix form. This is especially useful when dealing with matrix-based diffusion models, resulting a 3×3 local diffusion kernel discretization of the $\text{div}(\mathbf{D} \cdot \nabla I_{i,j}^n)$ operator:

$$\begin{aligned}\frac{\partial I_{i,j}^n}{\partial t} &= \text{div}(\mathbf{D} \cdot \nabla I_{i,j}^n) = \text{div} \left[\begin{pmatrix} a & b \\ b & c \end{pmatrix} \begin{pmatrix} \frac{\partial I_{i,j}^n}{\partial x} \\ \frac{\partial I_{i,j}^n}{\partial y} \end{pmatrix} \right] \\ &= \frac{\partial}{\partial x} \left(a \frac{\partial I_{i,j}^n}{\partial x} + b \frac{\partial I_{i,j}^n}{\partial y} \right) + \frac{\partial}{\partial y} \left(b \frac{\partial I_{i,j}^n}{\partial x} + c \frac{\partial I_{i,j}^n}{\partial y} \right) \\ &\approx \frac{1}{2} \{ D_x^+ [a D_x^-(I_{i,j}^n)] + D_x^- [a D_x^+(I_{i,j}^n)] \} + D_x^0 [b D_y^0(I_{i,j}^n)] \\ &\quad + D_y^0 [b D_x^0(I_{i,j}^n)] + \frac{1}{2} \{ D_y^+ [c D_y^-(I_{i,j}^n)] + D_y^- [c D_y^+(I_{i,j}^n)] \}\end{aligned}\quad (2.83)$$

which in turn leads to a convolution kernel of the form:

$$\mathbf{L} = \begin{pmatrix} -\frac{b_{i-1,j} + b_{i,j+1}}{4h^2} & \frac{c_{i,j+1} + c_{i,j}}{2h^2} & \frac{b_{i+1,j} + b_{i,j+1}}{4h^2} \\ \frac{a_{i-1,j} + a_{i,j}}{2h^2} & -\frac{a_{i-1,j} + 2a_{i,j} + a_{i+1,j}}{2h^2} & \frac{a_{i+1,j} + a_{i,j}}{2h^2} \\ \frac{b_{i-1,j} + b_{i,j-1}}{4h^2} & \frac{c_{i,j-1} + c_{i,j}}{2h^2} & -\frac{b_{i+1,j} + b_{i,j-1}}{4h^2} \end{pmatrix} \quad (2.84)$$

For a given scale n , the diffusion equation is expressed as:

$$\frac{\partial I_{i,j}^n}{\partial t} = \mathbf{L} * I_{i,j}^n$$

Given the generic definition of a diffusion tensor (2.44), and the eigenvectors:

$$\begin{cases} \vec{v}_1 = (\cos \alpha, \sin \alpha)^T \\ \vec{v}_2 = (-\sin \alpha, \cos \alpha)^T \end{cases}$$

the coefficients of the convolution kernel (2.84) are expressed as:

$$\begin{cases} a = \lambda_1 \cos^2 \alpha + \lambda_2 \sin^2 \alpha \\ b = (\lambda_1 - \lambda_2) \cos \alpha \sin \alpha \\ c = \lambda_2 \cos^2 \alpha + \lambda_1 \sin^2 \alpha \end{cases} \quad (2.85)$$

Remark Due to stability problems, Weickert [Wei95] proposes an alternative to (2.84) that ensures increased stability and nonnegative diagonal coefficients.

2.9.1.3 Multiscale approximations

Multiscale approximations mainly refer to the methods employed in the numerical modeling of the PDE solution at a given scale t . A widely used approach consists in a progressive time discretization:

$$\frac{\partial I_{i,j}^n}{\partial t} = \frac{I_{i,j}^{n+1} - I_{i,j}^n}{dt} \quad (2.86)$$

where dt is the time discretization step.

The PDE solution is numerically described as an iterative process, where the solution at the time instant $n \cdot dt$ is used in determining the solution at $(n + 1) \cdot dt$.

Remark For the discretization of (2.86), result accuracy may vary according to the way in which the spatial derivatives are approximated.

The 1-D Perona–Malik diffusion equation is a perfect way of exemplifying this remark. Using a forward difference time approximation, (2.12) is numerically expressed as:

$$\frac{\partial I}{\partial t} \approx \frac{I_{i,j}^{n+1} - I_{i,j}^n}{dt} = \frac{\partial}{\partial x} \left[g \left(\left| \frac{\partial I}{\partial x} \right| \right) \frac{\partial I}{\partial x} \right] \quad (2.87)$$

If the spatial derivatives are expressed at scale $n \cdot dt$, the approximation is explicit in time:

$$\frac{\partial I}{\partial t} \approx \frac{I_{i,j}^{n+1} - I_{i,j}^n}{dt} = \frac{\partial}{\partial x} \left[g \left(\left| \frac{\partial I^n}{\partial x} \right| \right) \frac{\partial I^n}{\partial x} \right] \quad (2.88)$$

The $(n+1) \cdot dt$ solution is readily computed based on the $n \cdot dt$ one, using the following discretization scheme:

$$I^{n+1} = I^n + dt \cdot \frac{\partial}{\partial x} \left[g \left(\left| \frac{\partial I^n}{\partial x} \right| \right) \frac{\partial I^n}{\partial x} \right] \quad (2.89)$$

Although (2.89) requires a large number of iterations to ensure a proper convergence, its advantage consists in its simplicity and ease of implementation.

Over the years, more complex and efficient discretization schemes have been proposed, both *semi-implicit* and *explicit*, each of them having its advantages and disadvantages. A comparison between the two categories can be found in [WtHRV98], concluding that given a predefined set of stability constraints, the explicit scheme yields better results.

2.10 Conclusion

From a functional point of view, this chapter was aimed at discussing and analyzing the prerequisite concepts in PDE and variational-based image processing, each approached topic relating to the general context of this thesis.

The basic notions presented in **Chapter 2** are comprised even in today's more evolved, more complex PDE-based image processing models. Some of the newest trends in PDE-based image processing, relating to the original contributions that are the subject of this thesis, will be briefly analyzed when needed, while others that are outside the scope of this work will be referenced only as recommended reading material.

It should also be stressed that one of the main tasks, and at the same challenges, of this thesis was to ultimately propose (a) new paradigm(s) that synergistically combines image restoration and enhancement into a single paradigm. Therefore, in order to accomplish this, the present manuscript describes a step-by-step approach, starting from image restoration, passing through image restoration coupled with edge enhancement and finally, defining a processing paradigm for joint image restoration and image enhancement.

The image restoration part, since it has seen extensive development over the last decade, required only a thorough analysis and understanding (this being the intended purpose of **Chapter 2**), the remaining parts, *i.e.*, image restoration coupled with edge enhancement and joint image restoration and enhancement, being detailed in the following chapters.

In the following, a “C 2 C”¹⁷ section will provide a brief overview of **Chapter 2** and of the relevance of the topics discussed within this chapter with respect to the overall context of the thesis.

C 2 C

A short introduction to image processing – §2.2 – provided a quick overview of existing image processing techniques, emphasizing the particularities of those directly

¹⁷ *Contents to Context* – relevance of chapter contents to overall thesis context

relevant to the present thesis, *i.e.*, PDE- and variational-based image processing, while at the same time it defined in general terms the two main topics of this thesis: *image restoration* and *image enhancement*.

Multiscale image processing and PDEs – §2.3 – explained the basic concepts of *scale* and *multiscale* in the context of image processing, as well as the properties and principles of multiscale image analysis and processing, the cornerstone of PDE-based image processing.

Linear filtering – §2.4 – the most basic form of PDE-based image processing, embodied by the *isotropic diffusion model*. A classic example of PDE-based image restoration, with limited practical functionality but of paramount theoretical importance in the sense of representing the starting point of image processing via PDE modeling. It was also relevant to the general context of this thesis because it underlines through negative example the importance of *anisotropic diffusion* in image restoration, *i.e.*, noise filtering.

Nonlinear filtering – §2.5 – introduced the notion of *anisotropic diffusion* for image denoising (the Perona–Malik model) and analyzed the major differences between anisotropic and isotropic filtering. The subsequent anisotropic models, *i.e.*, Catté *et al.*, FAB, were chosen to reinforce two important notions directly relating to this thesis:

- The Catté *et al.* model as an example of the well-posedness of using pre-smoothing either for the input I image or for its gradient map – an approach also employed by the second proposition of this thesis, discussed at length in **Chapter 5**.
- The FAB diffusion model, as a perfect example of combining diffusion with inverse (negative) diffusion in order to obtain a processing paradigm suitable for both denoising and deblurring. This approach directly relates to the first proposition of this thesis, discussed in **Chapter 3**.

It should be stressed that all discussed methods were studied both theoretically and experimentally, as a prerequisite for designing and testing the proposed methods, hence their presence within this manuscript.

The variational approach – §2.6 – was extremely relevant from a second proposition (**Chapter 5**) point of view, since it provides the theoretical background for notions such as TV minimization and unifying PDE–variational problems (the second proposition of this thesis relying on such a combined formulation, *i.e.*, PDE–variational).

Tensor-based filtering – §2.7 – provided the theoretical understanding of Weickert’s CED model in the context of image denoising, directly relating to the extension of the model for concurrent image restoration and enhancement proposed in **Chapter 3**.

Level-set and curvature-based filtering – §2.8 – described the fundamental notions of “*intelligent anisotropic diffusion*”, *i.e.*, image geometry-based and structure-guided anisotropic filtering, employing the $\vec{\eta}$ and ξ filtering directions. This approach to anisotropic diffusion is fundamental in understanding the theoretical principles and reasoning behind the denoising component of the proposed variational model for concurrent fusion and denoising (**Chapter 5**).

Numerical approximations – §2.9 – a mandatory discussion topic in *digital* image processing.

CHAPTER 3

Hybrid shock filters: an image restoration paradigm

Main Contents

3.1	Motivation	41
3.2	Deblurring as an image restoration concept	42
3.3	Concurrent denoising and deblurring: an image restoration approach	43
3.4	Shock filters	44
3.5	The hybrid shock filter paradigm	55
3.6	Experimental analysis	61
3.7	Conclusion	73

3.1 Motivation

This chapter presents the first major contribution of this thesis, related to image restoration, *i.e.*, a novel image deblurring filter, defined for the generalized restoration scenario of concurrently filtering blur and overlaid noise.

Although the two processing tasks, *i.e.*, deblurring and denoising, are implicitly image restoration paradigms, *shock filters*, through their intrinsic edge enhancement bridge the domains of image restoration and image enhancement, especially if they possess coherence enhancement properties (§3.4.5). The theoretical aspects of shock filter theory, along with a detailed discussion of the most representative shock filter models will be covered in §3.4.

Since the proposed shock filter model combines the two important restoration tasks of deblurring and denoising into a single approach, and moreover, as a further extension of the proposed shock filter model, adds a coherence-enhancing component to the initial proposition, it can be regarded as a complex image restoration–image enhancement paradigm. The duality of the proposed model arises from two distinct perspectives:

- the intrinsic edge enhancement characteristic of the shock filter formalism, as an image restoration tool, which partly extends the concept of edge enhancement from image restoration into the image enhancement realm;
- the coherence-enhancing property, first defined by Weickert in [Wei03] (detailed in §3.4.5), which is a purely image enhancement paradigm.

Reiterating the overall desideratum of this thesis, its aim is to study, analyze and develop image restoration and image enhancement approaches, and if possible define a unifying paradigm that synergistically combines the two processing tasks, all this to be achieved by means of PDEs. In following this main guideline, the *hybrid shock filter* embodies the first proposition to unify the two processing tasks, in this case starting from a restoration perspective and moving toward an image enhancement perspective.

Since the first chapter dealt exclusively with the image restoration issue, and since the proposed *hybrid shock filter* is an approach originating from image restoration paradigms, combined with image enhancement elements, it is only fitting to have a chapter that follows in a functional sense, from simple to complex, the overall layout of the thesis.

The general structure of this chapter comprises an introductory part, describing some basic notions related to the subject at hand, most notable existing approaches and of course, the proposed model analyzed both from a theoretical and an experimental point of view.

The first part of this chapter focuses on the key aspects of image deblurring: proper definition of this image restoration process, theoretical understanding of its underlying contaminant, *i.e.*, blur, concluding with the motivation behind further improving existing approaches. The proposed improvement consists in the introduction of a new approach, capable of filtering complex contamination in the form of blur with overlaid additive noise.

3.2 Deblurring as an image restoration concept

Image deblurring, also known as image sharpening or image deconvolution is, in simple terms, the process of removing (filtering out) unwanted blur. *Blur*, as an unwanted contaminant is defined as “*the process of obscuring or blemishing by smearing, or making dim, indistinct, or vague in outline or character*”, conversely, the inverse process, of removing blur, can be defined in a more restrictive sense, *i.e.*, *image sharpening*, as “*putting an image into focus*”.

In essence, the problem of image deblurring amounts to recovering a sharp image from its blurry observation. It is often a crucial image restoration step in numerous image processing fields, such as industrial processes, military applications, astronomy, medical image processing, computer vision, just to name a few. In layman’s terms, image deblurring is an edge enhancement process that is performed under the assumption of the sole presence of blur as an image contaminant, defined as an unwanted convolution, behaviorally similar to a diffusion process – discussed at length in **Chapter 2**.

Thus, mathematically, image deblurring is closely related to the process of inverse diffusion or deconvolution. At first, the deconvolution problem was approached in a rather simplistic way, by assuming a linear degrading convolution with an *a priori* known blurring kernel, as noted by Gilboa in [Gil04]. The purpose, and at the same time the filtering effect, of deblurring models is to enhance (sharp) edges since, as already mentioned, salient information is primarily represented by the edges and contours within an image.

Remark It should be stressed right from the beginning that there exists a subtle difference between image enhancement and edge enhancement, difference that is not always sufficiently underlined in some papers, books, etc. Image enhancement deals, as mentioned in the beginning of **Chapter 2** – §2.2, with increasing or improving the quality of an input image, while restoration is defined as the process of restoring an image to its initial condition, or at least close to that initial condition. In this respect, the process of deblurring with its edge-enhancing component is aimed at restoring a blurred image to its initial, non-blurred state. In conclusion, throughout this thesis, the particular process of edge enhancement is considered to be a subcomponent of the general image restoration framework.

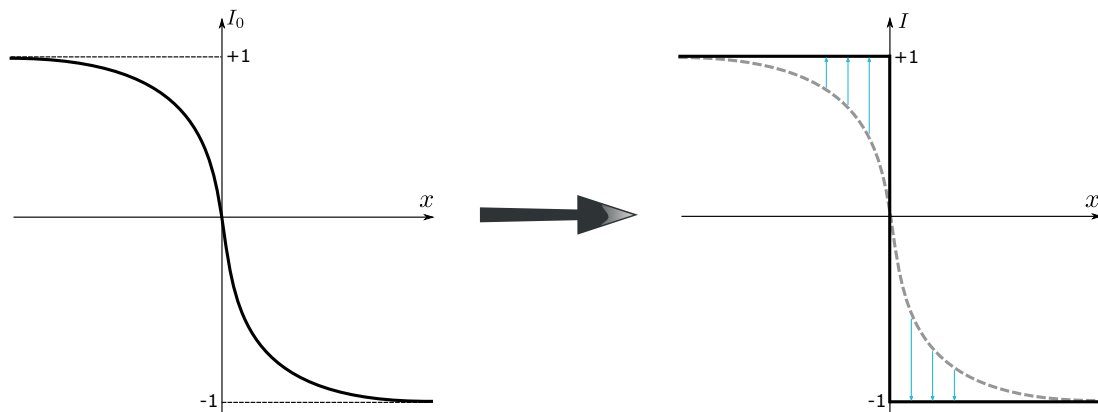


Fig. 3.1 – 1-D blurring–deblurring example.

The simplest way of describing a deblurring process, assuming that it mainly refers to edge enhancement, is to employ a trivial 1-D example: ideally, an edge can be modeled by a simple step function of the form:

$$I(x) = \begin{cases} 1 & \text{if } x < 0 \\ -1 & \text{if } x > 0 \end{cases}$$

This ideal edge $I(x)$ is further subjected to a convolution process, as part of adding a contaminant to the original signal. The resulting image, I_0 will represent a smoothed version of I , where the initial condition is expressed as:

$$I_0(x) = -\sin(x)$$

Thus, the deblurring process represents an inverse problem of deconvolution, with initial condition I_0 , as illustrated in *Fig. 3.1*. Mathematically, the convolution–deconvolution process is an initial value problem, convolution-wise and an inverse problem, deconvolution-wise: obtaining $I \rightarrow I_0$ is straightforward, while solving $I_0 \rightarrow I$ relates to all the difficulties of an ill-posed problem.

Since deblurring is considered to some extent the inverse of a smoothing process, in a PDE framework the process can be modeled by an inverse diffusion paradigm. The simplest example of an inverse diffusion process, would be the isotropic *inverse heat equation*, which is in essence an inverse problem, thus inherently unstable. Inverse problems, as noted by Chan and Shen [CS05], are crucially dependent on proper regularizers or conditioners that ensure stability, often at the expense of losing high frequency details, belonging to ideal (non-blurred) images. The regularization of inverse problems guarantees the existence and uniqueness of solution.

3.3 Concurrent denoising and deblurring: an image restoration approach

The motivation for further exploring the concept of deblurring is partly due to the limitations presented by the *classic shock filter* model proposed by Osher and Rudin in [OR90]

as well as by the ones of its subsequent evolutions – e.g., [AM94, KDA97a, GSZ02b, RC03, Wei03].

The main drawback of the classic model consists in the fact that in the presence of AWGN, the filtering is at best minimal – this minimal filtering effect is mainly due to the numerical scheme employed in its implementation. The aforementioned numerical scheme is based on the *minmod* function defined in [OR90] and used in computing the gradient norm in each point of the image function – restricting large value variations in neighboring pixels, such being the case of noise-corrupted images.

Another important drawback of the classic shock filter model resides in its edge detector based on the second order directional derivative that, in generalized GB+AWGN¹ scenarios, fails to correctly detect edges and contours, thus blocking the shock filter’s natural time evolution.

By knowing these *a priori* limitations of the classic model, a series of steps toward improving its overall performance were taken over time. Noteworthy results were described in [AM94, RC03, Wei03], the edge detector and its robustness being their main focus, somehow neglecting the global GB+AWGN scenario. This generalized scenario was approached in [KDA97a] and [GSZ02b] where the useful signal affected by both GB and AWGN was part of the problem’s statement.

Handling both contamination sources at the same time implies a series of compromises either processing quality-wise, noise removal-wise or edge enhancement-wise. In the case of the model described in [GSZ02b], in order to surpass the inherent classic edge detector’s limitations, a new approach is proposed: an approximation of the second order directional derivative given by the imaginary part of the image function.

In order to accomplish this, the image definition domain needs to be changed from the real one to the more general domain, the complex one, thus adding a new dimension to the work space. The major improvement brought by this edge detector consists in its robustness to noise even when dealing with low SNR images.

On the other hand, this edge detector presents also a noticeable disadvantage due to the fact that it will continuously evolve over time, leading to a divergent effect of the filtered result, instead of reaching a steady-state solution, as in the case of the classic shock filter model.

More on the PDE-based shock filter formalism for image deblurring, in the forthcoming sections of this chapter, which will cover: the theoretical framework of shock filters, most notable propositions within the formalism and their characteristics, advantages and shortcomings, concluding with the proposed method, the *hybrid shock filter*.

3.4 Shock filters

In the ever expanding field of image processing, image enhancement plays an important role either as an intermediary step of a processing chain or as a stand-alone processing task. Since its beginnings, image processing has relied on PDEs to help solve complex problems, e.g., filter modeling, image segmentation, analysis or fusion.

The advantages of using PDEs in image processing arise from their well-established theoretical basis and extensive use in mathematics, hence allow for a straightforward

¹Gaussian Blur with overlaid Additive White Gaussian Noise

extension to image processing tasks. Such an important task, a fundamental component of image restoration, is edge enhancement.

3.4.1 The Osher–Rudin shock filter

Revisiting previous statements, in a more restrictive sense, edge enhancement can be regarded as a technique of improving or recovering a signal degraded by an unwanted convolution process, defined in [OR90] as *blurring*. A process of deconvolution, also known as *deblurring*, is required in order to recover the original image. Performing a direct deconvolution of a discrete signal is not a well-posed problem, since discrete signals are only piecewise continuous.

As previously discussed, edge enhancement or more generally, deblurring, is the opposite process of image smoothing: the former process is aimed at creating discontinuities at points in space where they ideally should be, while the latter process removes superfluous features and false discontinuities [AK06].

A PDE-based approach to image deblurring was first proposed by Osher and Rudin [OR90] using a so-called *shock filter*, based on hyperbolic equation theory and an explicit monotone scheme which preserves the TV and the size and location of local extrema.

Recalling the most simple 1-D deblurring example, an edge can be ideally modeled by a step function of the form:

$$I(x) = \begin{cases} 1 & \text{if } x < 0 \\ -1 & \text{if } x > 0 \end{cases} \quad (3.1)$$

The ideal edge, $I(x)$ is subjected to a convolution process, as part of adding a contaminant to the ideal signal. The resulting image, I_0 will represent a smoothed version of I , where the initial condition for the previous 1-D deblurring example is expressed as:

$$I_0(x) = -\sin(x) \quad (3.2)$$

The deblurring process consists in defining a family of evolving curves $\{I(x, t)\}_{t>0}$ in order to achieve image sharpening. Following this line of reasoning, Osher and Rudin [OR90] propose to solve:

$$\begin{cases} \frac{\partial I}{\partial t} = -|I_x| \operatorname{sgn}(I_{xx}) \\ I(x, 0) = I_0(x) = -\sin(x) \end{cases} \quad (3.3)$$

where:

$$\operatorname{sgn}(I) = \begin{cases} 1 & \text{if } I > 0 \\ -1 & \text{if } I < 0 \\ 0 & \text{if } I = 0 \end{cases} \quad (3.4)$$

The advection characteristic of (3.3) can be easily verified by examining $\frac{\partial I}{\partial t}$ at points where $I_x > 0$ and $I_{xx} > 0$, with:

$$\frac{\partial I}{\partial t} + I_x = 0$$

a transport equation with speed “+1”, as also illustrated in Fig. 3.2.

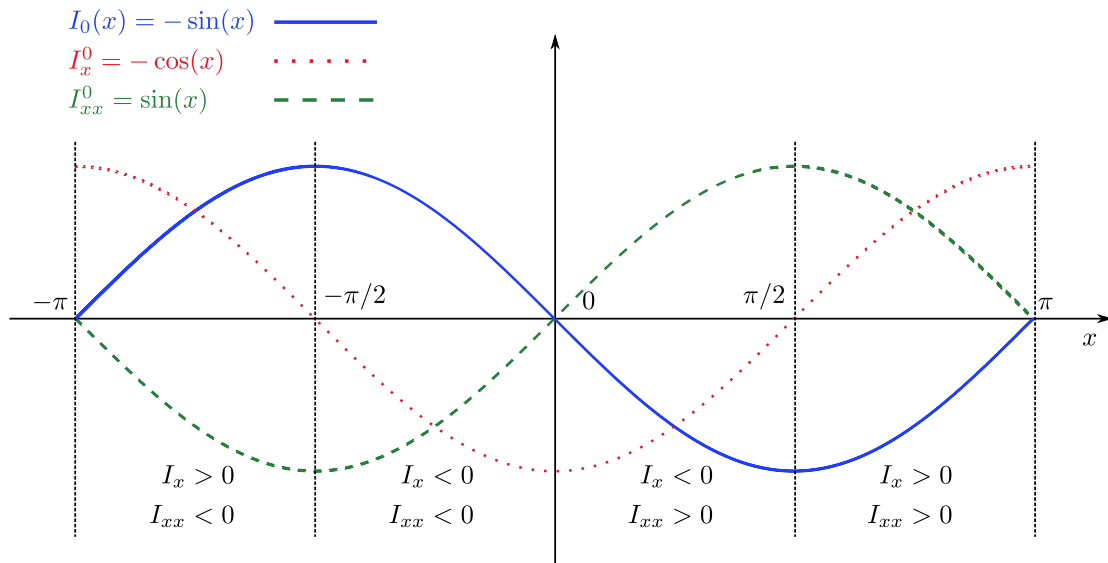


Fig. 3.2 – 1-D deblurring principle for $I_0(x) = -\sin(x)$ represented on $[-\pi, \pi]$.

According to [AK06], a simplified version of (3.3) can be expressed as:

$$\begin{cases} \frac{\partial I}{\partial t} = -|I_x| \operatorname{sgn}((I_0)_{xx}) \\ I(x, 0) = I_0(x) = -\sin(x) \end{cases} \quad (3.5)$$

with an explicit solution determined using the *method of characteristics* [AK06]. The time evolution of I from (3.5) at different times scales t is illustrated in Fig. 3.3.

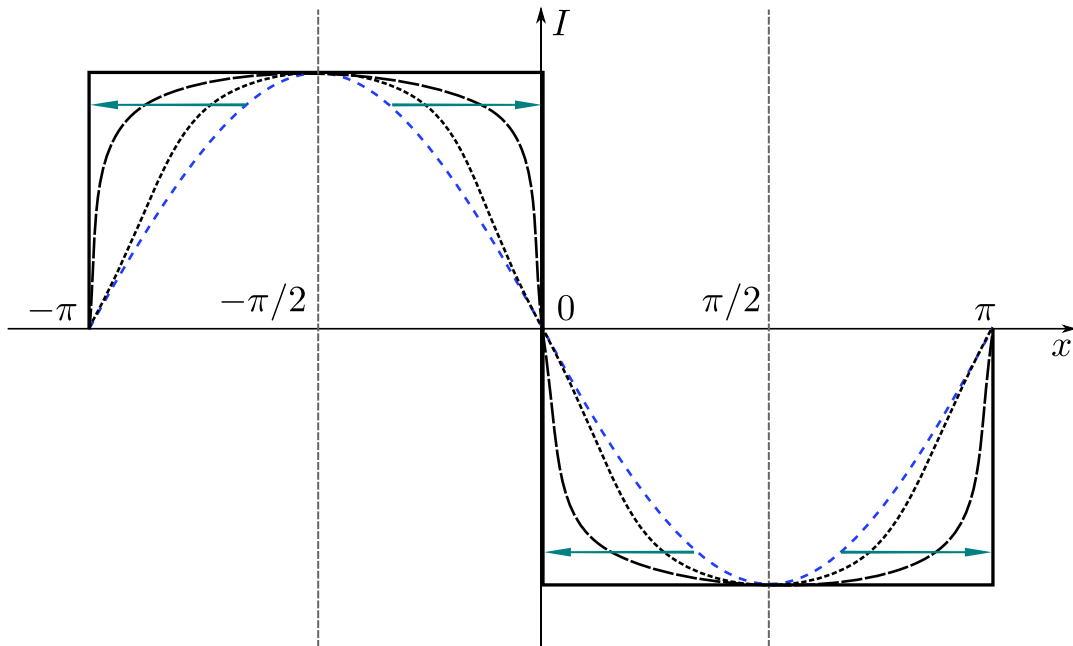


Fig. 3.3 – Time evolution of I , the solution of (3.5) at different time scales t .

The 1-D general expression of the shock filter proposed by Osher and Rudin [OR90] is the following:

$$\begin{cases} \frac{\partial I}{\partial t} = -F(I_{xx}) \cdot |I_x|, & x \in \mathbb{R}, t > 0 \\ I(x, 0) = I_0(x) \end{cases} \quad (3.6)$$

with F satisfying the following constraints:

$$\begin{cases} F(0) = 0 \\ F(s) \cdot \text{sgn}(s) \geq 0, \quad s \neq 0 \end{cases} \quad (3.7)$$

Although in the continuous domain, the shock filter problem seems ill-posed, the numerical simulations of Osher and Rudin yield generally good results that contradict the continuous domain ill-posedness. To this end, the two authors conjecture their results as follows:

Conjecture 3.4.1 [OR90]: “The evolution equation (3.6), with $I_0(x)$ continuous, has a unique solution that has jumps only at inflection points of $I_0(x)$ and for which the TV in x of $I(x, t)$ is invariant in time, as well as in the locations and values of local extrema.”

For the 2D case the shock filter’s expression becomes:

$$\frac{\partial I}{\partial t} = -F(I_{\eta\eta}) \cdot |\nabla I| \quad (3.8)$$

with $\eta = \frac{\nabla I}{|\nabla I|}$ and $\xi \perp \eta$. Thus, shock filtering translates into the filtered signal developing shocks at the positions of the zero crossings of $I_{\eta\eta}$, hence producing an enhancement of the edges.

A direct approach to numerically discretizing the classic shock filter model using, for example, finite difference schemes (§2.9.1) for numerically approximating partial derivatives is not suitable since in essence the shock filter model is an inverse diffusion equation, well known for its inherent instability. In overcoming this problem, Osher and Rudin propose an explicit discretization scheme that preserves TV and local extrema.

Recalling the notations used in §2.9, the time evolution of I is expressed in terms of finite differences and the *minmod* function as follows:

$$|\nabla I|_{i,j}^n = \sqrt{\{m[D_x^+(I_{i,j}^n), D_x^-(I_{i,j}^n)]\}^2 + \{m[D_y^+(I_{i,j}^n), D_y^-(I_{i,j}^n)]\}^2} \quad (3.9)$$

where:

$$m(x, y) = \begin{cases} \text{sgn}(x) \min(|x|, |y|) & \text{if } xy > 0 \\ 0 & \text{if } xy \leq 0 \end{cases} \quad (3.10)$$

The *minmod* function allows to select in every pixel the filtering direction according to the minimal variation in order to avoid oscillations and produce a constant image with jumps only at inflection points.

Although the Osher–Rudin shock filter is efficient at removing unwanted blur, there are also extreme situations, e.g., the patch effect (Fig. 3.4c) as underlined in [AK06], when the filter shows its limitations. Another major shortcoming of the classic shock filter, from an image restoration point of view, is that when dealing with noise, the filtering process

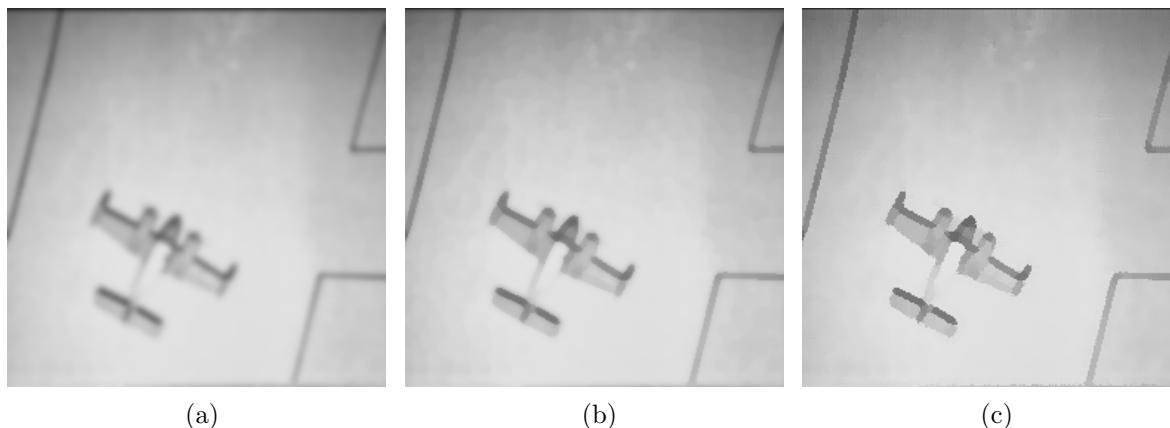


Fig. 3.4 – *The Osher–Rudin shock filter – time evolution example: (a) The initial **Airplane** [Uni11] blurred image – Gaussian PSF of $\sigma = 2$; (b) Shock filtered image at time scale $t = 1$; (c) Shock filtered image at time scale $t = 10$.*

can behave erratic, introducing an infinite number of inflexion points, thus perturbing the deblurring process.

This sensitivity to noise limits the practical application of the classic shock filter to simple deblurring scenarios. Several subsequent approaches, e.g., [AM94] or [KDA97a], have studied this problem, initially proposing a basic solution to it: using a convolution for stabilizing the edge detector, since, in the presence of noise it is the one which is responsible for false detections that lead to an infinite number of inflexion points. The slightly improved shock filter model has the following expression:

$$\frac{\partial I}{\partial t} = -\operatorname{sgn}[(G * I)_{\eta\eta}] \cdot |\nabla I| \quad (3.11)$$

Remark As noted by [Ter04], even if (3.11) manages to overcome the edge detector’s instability in generalized GB+AWGN scenarios, the new issue is the size of the Gaussian kernel G : if σ is too small, the noise filtering of the second order directional derivative is only partially achieved, while a value too large, could produce an isotropic diffusion-like effect, leading in turn to false edge detection.

3.4.2 The Alvarez–Mazorra shock filter

Following the discussion about the seminal work of Osher and Rudin [Rud87, OR90] and their proposition of a PDE-based approach to image deblurring – the first major PDE-based contribution to image deblurring theory – this section will analyze the first of many evolutions of the initial proposition, that of Alvarez and Mazorra [AM94].

The proposition of Alvarez and Mazorra emanates from the classic shock filter model, but at the same time tries to integrate a denoising component into the existing deblurring model, in order to achieve a complete image restoration paradigm. The proposed approach is modeled in 1-D by the following hyperbolic PDE:

$$\frac{\partial I}{\partial t} + F(G_\sigma * I_{xx}, G_\sigma * I_x)I_x = 0 \quad \text{in } \mathbb{R} \times \mathbb{R}^+ \quad (3.12)$$

where G_σ is a family of smoothing kernels, e.g., a family of Gaussian functions and F a function that satisfies:

$$F(x, y) \cdot xy \geq 0, \quad \forall x, y \in \mathbb{R} \quad (3.13)$$

A simple choice for F , proposed by the authors is:

$$F(x, y) = \text{sgn}(x) \text{sgn}(y)$$

where the *signum* function is defined as in (3.4).

The proposed filter will develop shocks in the position of the zero crossings of $G_\sigma * I_{xx}$ which will lead to edge enhancement, as it is typically the behavior of all shock filters. The discretization of (3.12) is done using an unconditionally stable recursive scheme, dissipative only within homogeneous regions, and nonoscillatory. The smoothing kernel $G_\sigma(\cdot)$ is defined as an approximation of a Gaussian convolution using a fast recursive discretization of the heat equation, i.e., $I_t - I_{xx} = 0$.

For the two dimensional case, the authors propose a shock filter modeled by the following PDE:

$$\frac{\partial I}{\partial t} = C \mathfrak{L}(I) - F(G_\sigma * I_{\eta\eta}, G_\sigma * I_\eta) I_\eta \quad \text{in } \mathbb{R}^2 \times \mathbb{R}^+ \quad (3.14)$$

where η is the direction of ∇I , F verifies (3.13), G_σ is a family of 2-D smoothing kernels, C a strictly positive constant and $\mathfrak{L}(I)$ a directional smoothing operator, e.g., $\mathfrak{L}(I) = I_{\xi\xi}$, where ξ is the normal to the gradient vector.

Summarizing the behavior of (3.14), the Alvarez–Mazorra shock filter model diffuses the initial image $I(x, y, 0)$ along the directions parallel to the edges, for noise filtering purposes, while it develops shocks along the perpendicular directions to the edges, thus achieving concurrent edge enhancement and denoising.

The 2-D model (3.14) is discretized using a fast, unconditionally stable recursive scheme, following the same lines as the 1-D model.

Fig. 3.5 illustrates a typical example of image restoration using the Alvarez–Mazorra shock filter: the test scenario is the generalized GB+AWGN contamination, while the filter has an evolution time $t = 1s$ for a discretization step $dt = 0.1$ with $C = 2$ and $\sigma = 1$.



Fig. 3.5 – Alvarez–Mazorra shock filter example: (a) GB($\sigma_b = 2$)+AWGN($\sigma_n = 10$) contaminated image – true color original available at [Kod11]; (b) Filtered image for $t = 1$, $C = 2$ and $\sigma = 1$.



Fig. 3.6 – Kornprobst *et al.* shock filter example: (a) $GB(\sigma_b = 2) + AWGN(\sigma_n = 10)$ contaminated image; (b) Filtered image for $t = 0.5$, $\sigma = 1$, $\tau = 15$ and $\alpha_f = \alpha_r = \alpha_e = 1$.

3.4.3 The Kornprobst *et al.* shock filter

Another proposition, subsequent in time to both the Osher–Rudin and Alvarez–Mazorra models, following the same line of reasoning, *i.e.*, coupling the deblurring process with the denoising one, is proposed by Kornprobst *et al.* in [KDA97a]. For this model, a third term is added with the purpose of coupling the evolving signal to the contaminated one in order to maintain signal similarity, *i.e.*, an attachment to the initial data:

$$\begin{aligned} \frac{\partial I}{\partial t} = & \underbrace{\alpha_f(I - I_0)}_{\text{Coupling}} + \underbrace{\alpha_r[h_\tau(|G_\sigma * \nabla I|)I_{\eta\eta} + I_{\xi\xi}]}_{\text{Denoising}} \\ & - \underbrace{\alpha_e[1 - h_\tau(|G_\sigma * \nabla I|)] \operatorname{sgn}(G_{\tilde{\sigma}} * I_{\eta\eta})|\nabla I|}_{\text{Deblurring}} \end{aligned} \quad (3.15)$$

where:

$$h_\tau(x) = \begin{cases} 1 & \text{if } x < \tau \\ 0 & \text{otherwise} \end{cases}$$

For sake of consistency, the Kornprobst *et al.* model is illustrated using the previous GB+AWGN contaminated initial image (Fig. 3.6a). The filtered result (Fig. 3.6b) was obtained for a theoretical evolution time $t = 0.5s$ with $\sigma = 1$, $\alpha_f = \alpha_r = \alpha_e = 1$ and $\tau = 15$.

3.4.4 The Remaki–Cheriet shock filter

Remaki and Cheriet [RC03] approach the classic shock filter shortcomings in a slightly different way, by proposing an alternative numerical scheme following a space-split strategy and normalized inputs. The resulting filter exhibits increased robustness to noise and high frequency details and is mathematically described as follows:

For the x direction the shock filter is defined as:

$$\frac{\partial I}{\partial t} + a_1(I) \cdot F_1(I_{xx}^0, I_x^0) \frac{\partial}{\partial x} f_1(I) = 0 \quad (3.16)$$

where:

$$F_1(u, v) = \operatorname{sgn}(u) \operatorname{sgn}(v)$$

$$f_1(u) = \begin{cases} u & \text{or} \\ \frac{1}{2} \operatorname{sgn}(u) u^2 \end{cases}$$

$$a_1(u) = \begin{cases} 1 & \text{or} \\ 1 + (1 - u_0)(1 + u_0) \end{cases}$$

The approximation of I is computed at the point $(x, y, (n + \frac{1}{2}) dt)$, where $x = ih_1$ and $y = jh_2$ – revisit §2.9 if necessary. Thus resulting the simplified notation:

$$I \left[x, y, \left(n + \frac{1}{2} \right) dt \right] = I_{i,j}^{n+\frac{1}{2}}$$

The x -direction discretization is thus expressed:

$$I_{i,j}^{n+\frac{1}{2}} = I_{i,j}^n$$

$$- \frac{1}{2} r_1 \max \left[0, a_1(I_{i,j}) F_1 \left(\frac{I_{i+1,j}^0 - 2I_{i,j}^0 + I_{i-1,j}^0}{h_1^2}, \frac{I_{i+1,j}^0 - I_{i,j}^0}{h_1} \right) f_1'(I_{i,j}^n) \right] (I_{i,j}^n - I_{i-1,j}^n) \quad (3.17)$$

$$- \frac{1}{2} r_1 \min \left[0, a_1(I_{i,j}) F_1 \left(\frac{I_{i+1,j}^0 - 2I_{i,j}^0 + I_{i-1,j}^0}{h_1^2}, \frac{I_{i+1,j}^0 - I_{i,j}^0}{h_1} \right) f_1'(I_{i,j}^n) \right] (I_{i+1,j}^n - I_{i,j}^n)$$

where $I_i^0 = I^0(ih_1, jh_2)$.

For the y direction the shock filter is similarly defined:

$$\frac{\partial I}{\partial t} + a_2(I) \cdot F_2(I_{yy}^0, I_y^0) \frac{\partial}{\partial y} f_2(I) = 0 \quad (3.18)$$

with a_2 , F_2 and f_2 defined as their x -direction counterparts.

The approximation of I is computed at the point $(x, y, (n + 1)dt)$, the y -direction discretization being expressed as:

$$I_{i,j}^{n+1} = I_{i,j}^{n+\frac{1}{2}}$$

$$- \frac{1}{2} r_2 \max \left[0, a_2(I_{i,j}) F_2 \left(\frac{I_{i,j+1}^0 - 2I_{i,j}^0 + I_{i,j-1}^0}{h_2^2}, \frac{I_{i,j+1}^0 - I_{i,j}^0}{h_2} \right) f_2'(I_{i,j}^{n+\frac{1}{2}}) \right] (I_{i,j}^{n+\frac{1}{2}} - I_{i,j-1}^{n+\frac{1}{2}}) \quad (3.19)$$

$$- \frac{1}{2} r_2 \min \left[0, a_2(I_{i,j}) F_2 \left(\frac{I_{i,j+1}^0 - 2I_{i,j}^0 + I_{i,j-1}^0}{h_2^2}, \frac{I_{i,j+1}^0 - I_{i,j}^0}{h_2} \right) f_2'(I_{i,j}^{n+\frac{1}{2}}) \right] (I_{i,j+1}^{n+\frac{1}{2}} - I_{i,j}^{n+\frac{1}{2}})$$

The stability of the filter is summarized by the authors with the following proposition:

Proposition 3.4.1 [RC03]: “Assume that a_1 , F_1 , f_1' and a_2 , F_2 , f_2' belong in $L^\infty(\mathbb{R})$ and I_0 belongs in $BV(\mathbb{R}) \cap L^\infty(\mathbb{R})$. Under the CFL conditions $r_1 |a_1 F_1 f_1'| < \frac{1}{2}$ and $r_2 |a_2 F_2 f_2'| < \frac{1}{2}$ the 2-D numerical scheme is stable for the L^∞ norm and spatiotemporally TV bounded with the following properties:”

$$(i) |I_{i,j}^n| \leq \|I_0\|_{L^\infty(\mathbb{R})}, \quad \forall i, j \in \mathbb{Z}, \forall n \in \mathbb{N}.$$

$$(ii) \sum_{i,j \in \mathbb{Z}} |I_{i+1,j}^n - I_{i,j}^n| + |I_{i,j+1}^n - I_{i,j}^n| \leq \operatorname{TV}(I_0), \quad \forall n \in \mathbb{N}.$$



Fig. 3.7 – Remaki–Cheriet shock filter example: (a) $GB(\sigma_b = 2) + AWGN(\sigma_n = 10)$ contaminated image; (b) Filtered image for $t = 1$, using a Gaussian mollifier of $\sigma = 1$.

$$(iii) \sum_{i,j \in \mathbb{Z}} |I_{i,j}^{n+1} - I_{i,j}^n| \leq \text{TV}(I_0), \quad \forall n \in \mathbb{N}.$$

Remark The Remaki–Cheriet shock filter can be numerically modeled with or without a regularizer for the initial image I_0 , as stated by the authors.

If a mollifying kernel is used to smooth the input image I_0 , the authors suggest either a standard Gaussian kernel or a compact support smoothing kernel, defined as:

$$\rho_\varepsilon(x) = \begin{cases} \frac{1}{\varepsilon} e^{\left(\frac{3\varepsilon^2}{x^2 - \varepsilon^2} + 3\right)} & \text{if } x^2 < \varepsilon^2 \\ \varepsilon & \\ 0 & \text{otherwise} \end{cases} \quad (3.20)$$

Fig. 3.7 illustrates an example of image restoration using the Remaki–Cheriet filter for $t = 1s$: a Gaussian smoothing kernel of $\sigma = 1$ was used for regularization, $a_1(u) = a_2(u) = 1 + (1 - u_0)(1 + u_0)$ and $f_1(u) = f_2(u) = \frac{1}{2} \text{sgn}(u)u^2$.

3.4.5 Weickert’s CESF model

Following the CED model first proposed in [Wei95] and discussed in §2.7.1.1, Weickert proposes in [Wei03] the corresponding counterpart pertaining to shock filter theory. As for the CED denoising paradigm, the CESF² is developed on the notion of structure tensor and coherence enhancement in order to better respond to the need of shock filtering by combining the classic shock filter’s stability with enhancement of coherent flow-like structures. The coherence enhancement effect is achieved by steering the shock filtering along the directions yielded by a structure tensor [KW87, Rao90, RS91]. Thus resulting a deblurring model that acts like a contrast enhancing shock filter, normal to the flow direction, while along the flow direction it creates a constant signal by applying either a dilation or an erosion process.

The author motivates his proposition by stressing that the shock filter’s performance strongly depends on the direction η and that in the presence of flow-like structures, e.g., fingerprints, the gradient of a Gaussian-smoothed image $G * I$ does not supply reliable orientation information, since parallel lines lead to patterns with opposite gradients [Wei99].

²Coherence Enhancing Shock Filter

If these gradients are smoothed using a Gaussian kernel approach, cancellation effects may occur that further cause very large fluctuations of the resulting gradient direction. In order to circumvent this cancellation problem, Weickert proposes a more reliable local structure descriptor in the form of the *structure tensor*, replacing ∇I with its tensor product:

$$\mathbf{J}_0(\nabla I) = \nabla I \cdot \nabla I^T \quad (3.21)$$

Thus the cancellation effect is circumvented, since $\mathbf{J}_0(-\nabla I) = \mathbf{J}_0(\nabla I)$. The structure tensor is obtained through an averaging of the gradient directions by smoothing (3.21) component-wise using a Gaussian kernel of standard deviation ρ :

$$\mathbf{J}_\rho(\nabla I) = G_\rho * (\nabla I \cdot \nabla I^T) \quad (3.22)$$

The resulting positive semidefinite 2×2 matrix is known as the structure tensor, second moment matrix, scatter matrix or the Förstner interest operator [Wei03]. Its orthogonal system of eigenvectors describes the direction of local minimal and maximal contrast, while the contrast intensity is a measure of its eigenvalues.

Let w be the normalized eigenvector corresponding to the largest eigenvalue, w being also called the dominant eigenvector of \mathbf{J}_ρ that describes the direction where the contrast change is maximal. Using w , the CESF is defined as follows [Wei03]:

$$\frac{\partial I}{\partial t} = -\text{sgn}(I_{ww}^\sigma) |\nabla I| \quad (3.23)$$

where $I_{ww}^\sigma = (G_\sigma * I)_{ww}$.

The *structure scale* σ determines the size of the resulting flow-like patterns, while the *integration scale* ρ averages orientation information.

Remark As noted by [Wei03], it is possible to close interrupted lines if ρ is equal or larger than the gap size. Moreover, in order to enhance coherent structures, the integration scale should be larger than the structure scale.



Fig. 3.8 – Weickert's CESF example: (a) Original fingerprint image [Bio11]; (b) Filtered image: $t = 20$, $\sigma = 2$ and $\rho = 6$.

Since one of the main applications of the CESF is digital fingerprint restoration, a suitable filtering example would be on such an image, breaking the continuity of the previous examples. Hence, *Fig. 3.8a* illustrates an original fingerprint image, part of the *FVC2000* fingerprint database [Bio11], while *Fig. 3.8b* shows the filtered result for $t = 20s$ and $\sigma = 2$, $\rho = 6$. The dual edge enhancing – coherence enhancing characteristic of the filter is clearly discernable in *Fig. 3.8b*, underlining the unique capabilities of the CESF.

3.4.6 The Gilboa *et al.* complex shock filter

The necessity of fundamentally rethinking shock filters, as a whole, arose from the specific problem of accurately detecting zero crossings required in correctly performing edge enhancement. Such an approach was first proposed in [GZS01] where the term of *complex diffusion* was introduced, followed by the definition of the complex shock filter framework in [GSZ02b]:

$$\frac{\partial I}{\partial t} = -\frac{2}{\pi} \arctan\left(a \cdot \frac{\text{Im}(I)}{\theta}\right) |\nabla I| + \lambda I_{\eta\eta} + \tilde{\lambda} I_{\xi\xi} \quad (3.24)$$

The novelty of the complex filter resides in its edge detector, which is no longer defined using the *signum* function, being defined instead by a construction of the form $F(s) = \frac{2}{\pi} \arctan(a \cdot s)$, where a controls the steepness of the second order derivative's slope near 0 and the *arctan* function allows taking into account not only the second order derivative's sign but also its magnitude. Defining the edge detector in this way, also ensures an implicit anisotropic characteristic of the edge detector [GSZ02b], partially replacing the role of the anisotropic diffusion filter.

The second major improvement brought by the complex shock filter formalism is represented by the replacement of the real definition domain of the image function with the complex one. This allowed to completely redefine the edge detector's frame of reference, augmenting its robustness to AWGN and ensuring increased performance in image restoration scenarios.

Summarizing, the complex shock filter is a viable alternative to classic shock filtering and a valuable image restoration tool because [GSZ02b]:

- It represents an elegant way to avoid the need of convolving the signal at each



Fig. 3.9 – Gilboa *et al.* complex shock filter example: (a) $GB(\sigma_b = 2) + AWGN(\sigma_n = 10)$ contaminated image; (b) Filtered image for $t = 2$, $|\lambda| = 0.1$, $\tilde{\lambda} = 0.5$, $a = 0.5$ and $\theta = 0.01$.

iteration, and still get smoothed estimations.

- The time dependency of the process is inherent, without the need to explicitly use a time evolution parameter t .
- Moreover, the imaginary part receives feedback – it is smoothed by the diffusion component and enhanced at sharp transitions by the shock filtering component, thus it is more suitable for controlling the process than a simple second derivative.

3.4.7 Shock filters: afterword

As it can be concluded from the previous sections, image deblurring is an important part of image restoration as a generalized processing tool and, in particular, the shock filter formalism represents a seminal contribution to the field of PDE-based image deblurring. Numerous contributions to the field of PDE-based deblurring, *e.g.*, [Bar01, Che03, WTBW05, BW06, WWG07, BS08, RC08], underline the importance and continuous study of this image processing problem.

The current trend in image deblurring is to attempt to unify the two opposite in nature image restoration components, *i.e.*, denoising and deblurring, and bring them under a complementary framework, thus working in synergy as a complete image restoration tool.

Since variational approaches are closely related to PDE-based ones, it is worth mentioning some of the contributions to image deblurring, more specifically blind deconvolution, that have been proposed over the years: [CW98, KSZ05, BKS06, BDF06, BBSK07, OBDF09]. The ultimate goal of unifying denoising with deblurring under a single image restoration paradigm is also tackled by some of the aforementioned variational approaches.

Within these prerequisites, the first major contribution of this thesis, the *hybrid shock filter* was developed in the spirit and based on the study of previous deblurring and denoising models and with the intent of bringing together denoising and deblurring under a common PDE-based framework. The general theoretical support is derived from the Gilboa *et al.* complex shock filter and classic shock filter theory, relying on the strengths of each while discarding their weaknesses.

Even though subsequent shock filter developments, like the Alvarez–Mazorra [AM94] model, the Kornprobst *et al.* [KDA97a] model or the Gilboa *et al.* [GSZ02b] complex shock filter successfully deal with the AWGN, there still persists the issue of stability and convergence for high AWGN values. Therefore, the problem of finding a proper balance between effective noise filtering on the one hand, and stability and convergence on the other, still remains an open subject of research. The *hybrid shock filter* establishes its premise on finding this balance and achieving all desiderata for robust and reliable image restoration, within the PDE-based shock filter framework.

3.5 The hybrid shock filter paradigm

As previously discussed in §3.4, the classic shock filter design is not entirely suited for noise filtering, and more generally, for image restoration. Subsequent developments have thus addressed this task, distinguishing themselves into two main classes:

- The first class, tackles the problem by adding diffusion filters to the classic shock filter model and working on pre-smoothed versions of the input signal,

- While the second class redefines the edge detector, allowing for a robust and accurate edge detection without the need of additional noise filtering.

Both classes possess a series of advantages and disadvantages: the first class inherits the stability and convergent behavior of the classic shock filter, defined in [OR90], while it behaves less efficiently in AWGN filtering, especially in high noise scenarios. The second class, on the other hand, successfully filters out AWGN, even for high standard deviation values, however, lacks the stability and convergent behavior of the classic shock filter.

The ultimate goal in shock filter design is to conceive a filter that is both able to perform properly in generalized GB+AWGN scenarios and to exhibit a stable-convergent time behavior. The stability of the filter is of paramount importance since the final result's accuracy strongly depends on the filter's capacity to converge, from a qualitatively point of view, toward the reference signal.

3.5.1 Mathematical model

Although the complex shock filter proposed by Gilboa *et al.* in [GSZ02b] proves to be a viable alternative to the classic model in circumventing the noise problem in the generalized scenario of GB+AWGN contamination, it presents at the same time a series of shortcomings. The most important of them being its numerical implementation, making the filter unstable after a sufficiently large number of iterations. This translates into the method's dependency on the human supervised control, the algorithm's stopping criterion being tied to its input parameters and sensitive to the nature of the input image.

These shortcomings along with the ones presented by the classic shock filter represent the premise for the *hybrid shock filter* model. The main goal is to combine the advantages of both models without preserving any of their disadvantages. So far the hybrid model solves the inability to efficiently process AWGN of the classic shock filter as well as the divergent behavior of the complex one, thus resulting a shock filter capable of image restoration in GB+AWGN scenarios that is both efficient and stable.

Another advantage of this method resides in its modularity, allowing the use of multiple sets of control functions, useful in the filter's behavioral analysis over a large variety of input images.

The general mathematical model of the hybrid shock filter is defined for $I: \Omega \rightarrow \mathbb{C}$, with $\Omega \subset \mathbb{R}^2$ when the image space is considered to be continuous and $\Omega \subset \mathbb{N}^2$ when the image space is viewed as a discrete domain.

The initial conditions for the PDE describing the filtering process of an image $I(x, y, t)$, with $(x, y) \in \Omega$, are the following: $I(x, y, 0) = I_0(x, y)$, $I_0(x, y) \in \mathbb{R}$ and $\frac{\partial I}{\partial n} = 0$, where n is the direction orthogonal to the image boundary, *i.e.*, Neumann boundary conditions.

Thus, the hybrid shock filter is mathematically expressed as:

$$\begin{cases} \operatorname{Re} \left(\frac{\partial I}{\partial t} \right) = -\frac{2}{\pi} \arctan \left(a \cdot \frac{\operatorname{Im}(I)}{\theta} \right) f_1(t) |\nabla I| - \operatorname{sgn}(\operatorname{Re}(I_{\eta\eta})) f_2(t) |\nabla I| \\ \quad + f_1(t) \left(\operatorname{Re}(\lambda) \operatorname{Re}(I_{\eta\eta}) - \operatorname{Im}(\lambda) \operatorname{Im}(I_{\eta\eta}) + \tilde{\lambda} \operatorname{Re}(I_{\xi\xi}) \right) \\ \operatorname{Im} \left(\frac{\partial I}{\partial t} \right) = \operatorname{Im}(\lambda) \operatorname{Re}(I_{\eta\eta}) - \operatorname{Re}(\lambda) \operatorname{Im}(I_{\eta\eta}) + \tilde{\lambda} \operatorname{Im}(I_{\xi\xi}) \end{cases} \quad (3.25)$$

Since the hybrid shock filter is partly derived from the complex shock filter [GSZ02b], it naturally shares some of its parameters, while others belong exclusively to the former:

- a is the parameter controlling the slope of the edge detector's sign function \arctan .
- θ is the complex argument input parameter, with $\theta \in (-\pi/2, \pi/2)$. When $\theta \rightarrow 0$, $\frac{\text{Im}(I)}{\theta}$ is an approximation of the smoothed Laplacian of the image function I , as mathematically proven in [GZS01] and revisited in §3.5.2, making the imaginary part “a natural regularized edge detector”.
- $|\nabla I|$ represents the gradient norm of the image function I , computed using the slope limiter minmod function, as defined in [OR90].
- $\lambda = r \cdot e^{i\theta}$ is a complex scalar parameter, computed based on the θ input parameter.
- $\tilde{\lambda}$ is a real scalar input parameter.
- $f_1(t)$ and $f_2(t)$ – discussed at length in §3.5.3 – are two complementary control functions. Their purpose is to control the nature of the hybrid shock filter, *i.e.*, to control the transition rate of the filter's behavior from an exclusively complex one to an exclusively real one.

A typical example of how the hybrid shock filter works and how its constituent components interact, *i.e.*, the real and imaginary part of the complex image function I , is illustrated in Fig. 3.10 for $t = 2s$, $|\lambda| = 0.1$, $\tilde{\lambda} = 0.5$, $a = 0.5$ and $\theta = 0.01$, using the (3.27) control function set.

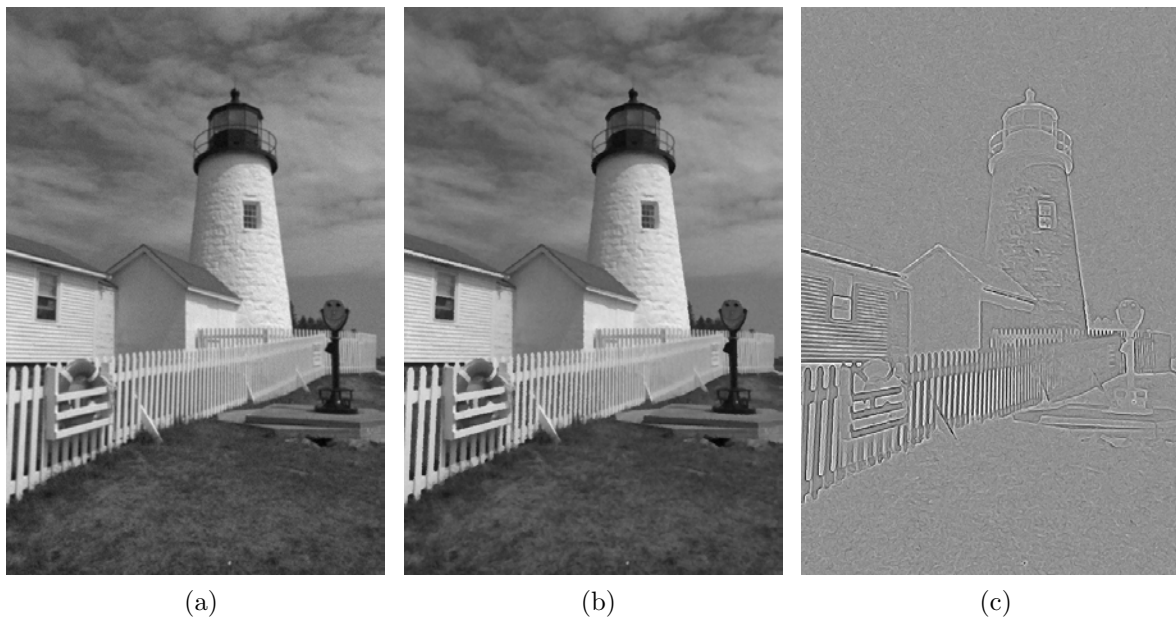


Fig. 3.10 – Hybrid shock filter example for $t = 2$: (a) $GB(\sigma_b = 1) + AWGN(\sigma_n = 5)$ contaminated image – true color original available at [Kod11]; (b) Hybrid shock filter result – real part $\text{Re}(I)$, *i.e.*, the filtered output; (c) Hybrid shock filter – imaginary part $\text{Im}(I)$, *i.e.*, the edge detector.

3.5.2 The small θ approximation

A fundamental component of both the original complex shock filter and the subsequent hybrid shock filter, the θ parameter is a common parameter of the two filters, first defined and analyzed by Gilboa *et al.* in [GZS01] in the context of complex diffusion. Later, this context was extended to encompass the notion of complex shock filtering, [GSZ02b], completely redefining this notion and fundamentally changing the core aspect of the formalism.

This alternative approach defines the image function as a complex function, where the real part is the actual time evolving filtered image, while the imaginary part is the edge detector based on which the complex shock filtering is performed. Due to this natural parallel evolution of the two key components of shock filtering, the complex shock filter successfully deals with noise as an input contaminant, thus allowing for a complete deblurring–denoising image restoration approach.

In a standardized mathematical framework, the complex formulation does not naturally behaves as a shock filter–edge detector tandem, hence the necessity of adjusting the initial definition in order to describe this desired behavior. The small θ approximation, as advocated in [GZS01] and at length in [Gil04] is the necessary and sufficient condition for having the imaginary part of the image function behave like a robust edge detector.

The importance of the small θ approximation is illustrated in Fig. 3.11 for the generalized GB+AWGN scenario, with the RMSE³ used as a control similarity measure, measuring the divergent behavior of the filter according to the different values of θ . The RMSE is computed between the “ideal” image I and the time evolving version $\frac{\partial I}{\partial t}$ of the contaminated initial image I_0 . As θ moves farther and farther away from 0, the hybrid shock filter exhibits an increasingly divergent behavior, showing that the complex framework approximates the filter–edge detector paradigm only if θ is small enough. The filter evolution is illustrated for $t = 100s$, where $t = n \cdot dt$ with $n = 0 \dots N_n$ ⁴ the n^{th} time iteration and dt the time discretization step size.

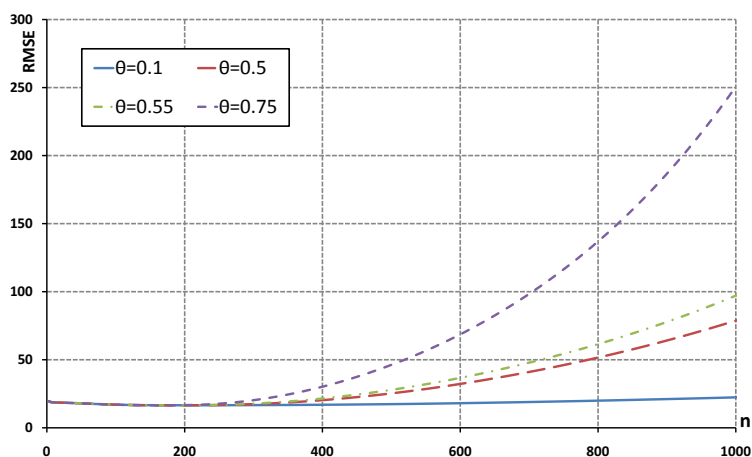


Fig. 3.11 – The small θ approximation and its influence on the stability of the hybrid shock filter.

³Root Mean Square Error

⁴Disambiguation: in other cases n denotes the normal to the image space Ω , the distinction is always made by clearly defining the meaning of n according to its current use.

3.5.3 The f_1 and f_2 control functions

A key component of the hybrid shock filter formulation, the $f_1(t)$ and $f_2(t)$ control functions are responsible, as previously mentioned, with controlling the nature of the filter, *i.e.*, controlling the transition of the filter's behavior from an exclusively complex one to an exclusively real one.

The current set of control functions employed by the hybrid shock filter is defined as follows:

$$f_1(T_{1i}, T_{1s}) = \begin{cases} 1, & n < T_{1i} \\ 1 - \frac{n - T_{1i}}{T_{1s} - T_{1i}}, & T_{1i} \leq n < T_{1s} \\ 0, & n \geq T_{1s} \end{cases} \quad (3.26)$$

$$f_2(T_{2i}, T_{2s}) = \begin{cases} 0, & n < T_{2i} \\ \frac{n - T_{2i}}{T_{2s} - T_{2i}}, & T_{2i} \leq n < T_{2s} \\ 1, & n \geq T_{2s} \end{cases}$$

with $n = 0 \dots N_n - 1$ and $T_{1i}, T_{1s}, T_{2i}, T_{2s} \in [0, N_n - 1]$.

The hybrid shock filter's overall behavior, weighted by its control functions f_1 and f_2 , can be summarized as follows:

- (i) $f_1 = 1$ and $f_2 = 0$ – the filter behaves predominantly as a denoising filter. This behavior is required in order to effectively deal with the AWGN. Thus, the hybrid shock filter relies on its edge detector (imaginary part of the image function I) in correctly detecting edges and contours in GB+AWGN scenarios.
- (ii) $f_1, f_2 \in (0, 1)$ – following the filter's time evolution, after a certain number of iterations the AWGN is properly filtered. Thus, focusing the filtering process on concurrent denoising and deblurring, which translates into a simultaneous evolution of the two hybrid shock filter's components, *i.e.*, real and complex.
- (iii) $f_1 = 0$ and $f_2 = 1$ – at the end of the filtering process, the hybrid shock filter acts as an edge enhancement filter, filtering the GB through its real component.

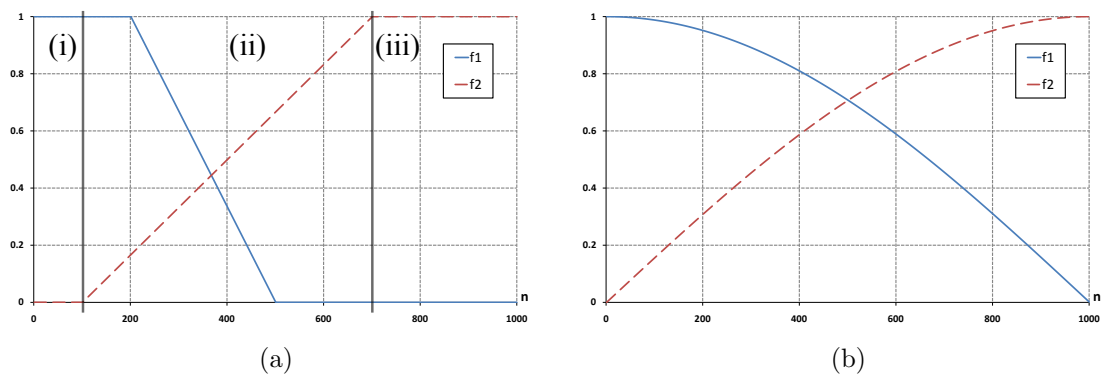


Fig. 3.12 – Hybrid shock filter control functions examples for $N_n = 1000$: (a) The (3.26) control function set for $T_{1i} = 200$, $T_{1s} = 500$, $T_{2i} = 100$, $T_{2s} = 700$; (b) The alternative control function set (3.27): $f_1(t) = \cos(t)$ and $f_2(t) = \sin(t)$.



Fig. 3.13 – Hybrid shock filter control functions GB+AWGN comparison for $t = 2$: (a) Filtered result using the (3.26) control function set for $T_{1i} = 5$, $T_{1s} = 15$, $T_{2i} = 5$, $T_{2s} = 15$; (b) Filtered result using the (3.27) control function set.

Depending on the choice of the threshold parameters for f_1 and f_2 from (3.26), other sub-behaviors can be obtained, some of them useful in specific test scenarios, others, simply prolonging the filter's time evolution without additional signal filtering.

Although the control function set (3.26) is adequate in defining and modeling the desired behavior of the hybrid shock filter, for mild GB+AWGN contamination an alternative can be:

$$\begin{cases} f_1(\omega) = \cos(\omega) \\ f_2(\omega) = \sin(\omega) \end{cases} \quad \omega = \frac{\pi}{2} \cdot \frac{n}{N_n - 1}, \quad n = 0 \dots N_n - 1 \quad (3.27)$$

since it requires less parameters, yielding at the same time similar results to the (3.26) set, as experimental tests have shown.

Fig. 3.12 illustrates the graphical representation of the two control function sets, while Fig. 3.13 shows a comparative example of the hybrid shock filter employing the aforementioned control function sets (3.26) and (3.27), respectively. In order to produce an objective comparison, the same same of input parameters was used, i.e., $t = 2s$, $|\lambda| = 0.1$, $\tilde{\lambda} = 0.5$, $a = 0.5$ and $\theta = 0.001$ and the same input image I_0 (Fig. 3.5a) as for the previously discussed shock filter models.

3.5.4 Adding coherence enhancement to the hybrid shock filter formalism

Using the same reasoning and mathematical approach as Weickert in [Wei03] that lead to the development of the CESF, the initial hybrid shock filter model (3.25) can be further extended so as to possess coherence-enhancing properties. Employing the same structure tensor construction (3.22) as the CESF and using a smoothed version of the input image



Fig. 3.14 – Coherence-enhancing hybrid shock filter example: (a) Original fingerprint image [Bio11]; (b) Filtered image: $t = 5$, $\sigma = 1$ and $\rho = 5$.

$I_\sigma = G_\sigma * I$, the hybrid shock filter can be rewritten as:

$$\begin{cases} \operatorname{Re}\left(\frac{\partial I}{\partial t}\right) = -\frac{2}{\pi} \arctan\left(a \cdot \frac{\operatorname{Im}(I)}{\theta}\right) f_1(t) |\nabla I| - \operatorname{sgn}(\operatorname{Re}(I_{ww}^\sigma)) f_2(t) |\nabla I| \\ \quad + f_1(t) \left(\operatorname{Re}(\lambda) \operatorname{Re}(I_{\eta\eta}) - \operatorname{Im}(\lambda) \operatorname{Im}(I_{\eta\eta}) + \tilde{\lambda} \operatorname{Re}(I_{\xi\xi}) \right) \\ \operatorname{Im}\left(\frac{\partial I}{\partial t}\right) = \operatorname{Im}(\lambda) \operatorname{Re}(I_{\eta\eta}) - \operatorname{Re}(\lambda) \operatorname{Im}(I_{\eta\eta}) + \tilde{\lambda} \operatorname{Im}(I_{\xi\xi}) \end{cases} \quad (3.28)$$

For illustrating the coherence-enhancing property of the hybrid shock filter (3.28) an original fingerprint image from the *FVC2000* fingerprint database [Bio11] (Fig. 3.14a) is used, resulting a filtered image (Fig. 3.14b) for $t = 5s$ with $|\lambda| = 0.1$, $\tilde{\lambda} = 0.5$, $a = 0.5$, $\theta = 0.01$ and the control function set (3.27).

3.6 Experimental analysis

The experimental analysis will be divided from a functional point of view into the following parts:

- Parameter and stability analysis – with focus on testing the model's key parameters and their behavior in generalized GB+AWGN test scenarios.
- Comparative analysis – using existing models, the hybrid shock filter will be tested against those models and its performances qualitatively assessed from an objective perspective.
- Coherence-enhancing capability assessment – testing the coherence-enhancing version of the hybrid shock filter (3.28) from a comparative point of view against similar filters.

3.6.1 Image quality assessment

In performing an unbiased experimental analysis, objective image quality assessment is of paramount importance in image processing, dedicated research being conducted in order to improve and diversify quality metrics and measurement protocols. Quality metrics can be classified into two main categories:

- Objective evaluation metrics that require a reference image
- Objective evaluation metrics that do not require a reference image

Since this chapter has been dedicated to an image restoration paradigm, it is implied by the definition of image restoration itself, that the process *restores* a real image I_0 to its previously “ideal” state I . Therefore, the most appropriate evaluation metrics for this particular case are the ones that use a reference image, since in a controlled test environment the “ideal” image can be *a priori* known or generated – when dealing with synthetic test images.

Among the objective quality metrics that require a reference image, there are the classic ones, such as the RMSE, mathematically defined as:

$$\text{RMSE}(I_R, I_T) = \sqrt{\frac{\sum_{i=0}^{N-1} \sum_{j=0}^{M-1} [I_R(i, j) - I_T(i, j)]^2}{M \times N}} \quad (3.29)$$

where the discrete image space is defined as in (2.61) for $M \times N$ images and I_R is the reference image, while I_T is the test image.

A closely related quality metric to the RMSE is the PSNR⁵, defined as:

$$\text{PSNR}(I_R, I_T) = 20 \lg \left(\frac{L}{\text{RMSE}(I_R, I_T)} \right) \quad (3.30)$$

where $L = 2^{\text{bits per pixel}} - 1$ is the the dynamic range of I , e.g., for grayscale images $L = 255$.

Another standard quality metric is the SCC⁶, mathematically expressed as:

$$\text{SCC}(I_R, I_T) = \frac{\sum_{i=0}^{N-1} \sum_{j=0}^{M-1} [I_R(i, j) - \bar{I}_R] \cdot [I_T(i, j) - \bar{I}_T]}{\sqrt{\sum_{i=0}^{N-1} \sum_{j=0}^{M-1} [I_R(i, j) - \bar{I}_R]^2 \cdot \sum_{i=0}^{N-1} \sum_{j=0}^{M-1} [I_T(i, j) - \bar{I}_T]^2}} \quad (3.31)$$

with \bar{I}_R and \bar{I}_T the mean values of the reference image and the test image, respectively.

A statistical measure, emerged as an alternative to the RMSE, the MI⁷ measures the degree of dependence between two random variables and it is defined as:

$$\text{MI}_{RT}(I_R, I_T) = \sum_{I_R, I_T} p_{RT}(I_R, I_T) \cdot \lg \frac{p_{RT}(I_R, I_T)}{p_R(I_R) \cdot p_T(I_T)} \quad (3.32)$$

⁵Peak Signal-to-Noise Ratio

⁶Sample Correlation Coefficient

⁷Mutual Information

where I_R and I_T are the two random variables, $p_{RT}(I_R, I_T)$ is the joint distribution and $p_R(I_R) \cdot p_T(I_T)$ is the distribution associated with the case of complete independence between the two random variables.

The quality metrics presented so far have one thing in common, they are all computed using a per-pixel approach, measuring the differences between any two pixels, one being the reference and the other the test sample. In image processing this is often insufficient, since the aforementioned metrics are unable to account for visual perception or structural information [WB09]. This topic, of thoroughly and precisely measuring visual perception and other complex image data as a quality metric quantity is a research subject on its own and will not be detailed in this thesis.

Among the most relevant quality metrics belonging to the new wave of dedicated image quality assessment tools is the SSIM⁸ developed by Wang *et al.* [WBSS04], a further development of the original *Universal Image Quality Index* [WB02]:

$$\text{SSIM}(I_R, I_T) = \frac{(2\mu_R\mu_T + c_1)(2\sigma_{RT} + c_2)}{(\mu_R^2 + \mu_T^2 + c_1)(\sigma_R^2 + \sigma_T^2 + c_2)} \quad (3.33)$$

with μ_R the average of I_R , μ_T the average of I_T , σ_R^2 the variance of I_R , σ_T^2 the variance of I_T , σ_{RT} the covariance of I_R and I_T , and $c_1 = (k_1L)^2$, $c_2 = (k_2L)^2$ two variables that stabilize the division with weak denominator. L is the dynamic range of the image functions and $k_1 = 0.01$ and $k_2 = 0.03$ by default.

Another important quality metric is the multiscale version of the SSIM, the MSSIM⁹, also proposed by Wang *et al.* and detailed in [WSB03].

From the recently proposed image-dedicated quality metrics, worth mentioning are the VSNR¹⁰ [CH07] and the VIF¹¹ [SB06]. For additional information concerning these quality metrics, *i.e.*, the recently proposed ones, both from a theoretical and a numerical implementation point of view, please refer to [Lab11].

In order to ensure an objective, unbiased quality assessment, all of the previously mentioned quality metrics will be used under a third-party implementation, *i.e.*, the *MeTriX MuX Visual Quality Assessment Package*, available at [Gau11].

3.6.2 Hybrid shock filter parameter and stability analysis

Based on the initial parameter and stability analysis [LLT⁺10], the hybrid shock filter will be experimentally tested in generalized GB+AWGN initial conditions using a synthetic test image.

In carrying out the parameter analysis, as well as the stability and convergence study of the hybrid shock filter, an experimental setting is defined, based on an initial synthetic reference image (*Fig. 3.15a*) contaminated with a GB+AWGN-type contamination of $\sigma_b = 5$ and $\sigma_n = 40$, respectively (*Fig. 3.15b*).

Since the small θ parameter has been already illustrated (*Fig. 3.11*) for the same experimental setting (*Fig. 3.15*), the parameter analysis will focus on testing the behavior

⁸Structural SIMilarity index

⁹Multiscale Structural SIMilarity index

¹⁰Visual Signal-to-Noise Ratio

¹¹Visual Information Fidelity

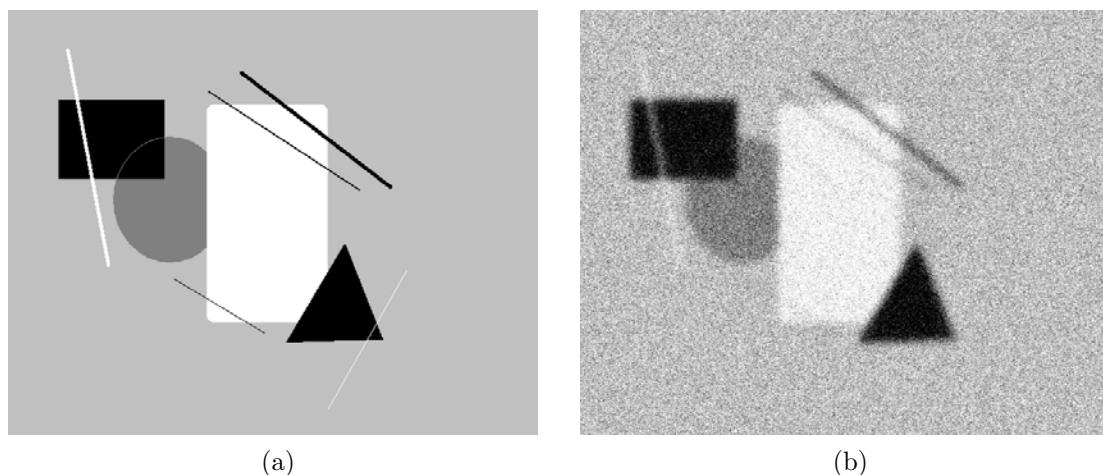


Fig. 3.15 – Hybrid shock filter parameter analysis experimental setting: (a) Reference synthetic image; (b) $GB(\sigma_b = 5) + AWGN(\sigma_n = 40)$ contaminated initial image I_0 .

of the parameter a controlling the slope of the edge detector's sign function \arctan , detector which is none other than the imaginary part of the image function itself.

Based on the evolution of a , illustrated in *Fig. 3.16*, where the real component of the hybrid shock filter is set to zero, it can be easily seen how the size of a influences the filter's behavior and, moreover, how the filter diverges, irrespective of a if parameterized exclusively based on its imaginary component, *i.e.*, using only its imaginary part as edge detector.

Since the control function set can be defined either as (3.26) or as (3.27) it is interesting to see how each set behaves under strong GB+AWGN conditions, with emphasis on the former since it is more flexible due to its increased parametrization. The parameter analysis is illustrated in *Fig. 3.17*, the filter's parameters being the following: $|\lambda| = 0.5$, $\tilde{\lambda} = 0.5$, $a = 0.55$, $dt = 0.1$ and $\theta = 0.00001$ for $t = 100s$ with the control functions' parameters detailed in *Table 3.1*.

Analyzing the test results from *Fig. 3.17* the following conclusion can be drawn:

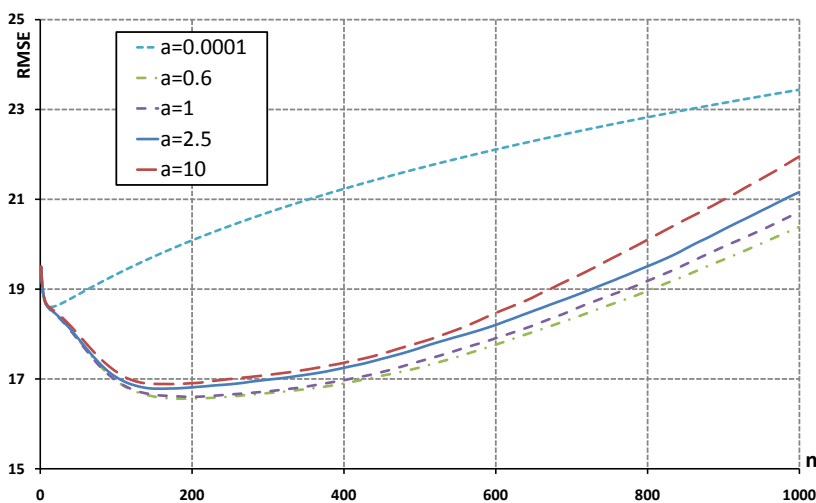


Fig. 3.16 – Hybrid shock filter parameter analysis: behavior of the parameter a .

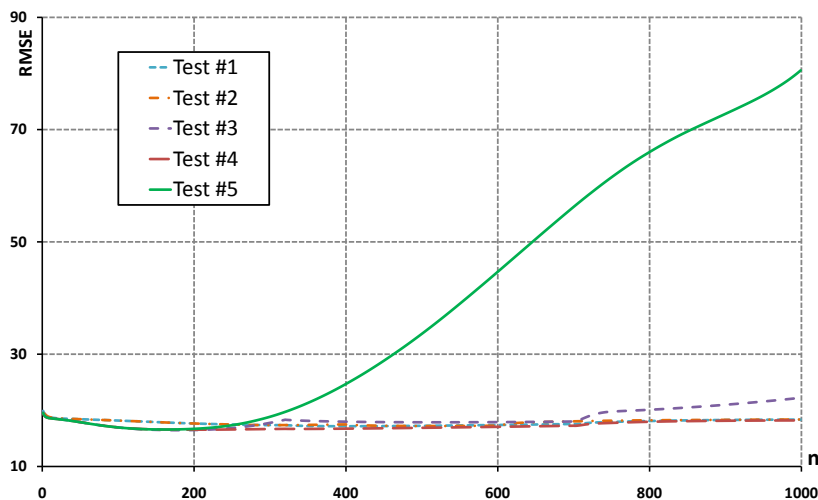


Fig. 3.17 – Hybrid shock filter parameter analysis: control function sets behavior.

the hybrid shock filter performs better in the generalized GB+AWGN scenario when f_1 has a short transient evolution from values different from 0, followed by a decreasing characteristic to its inferior limit, *i.e.*, 0; the f_2 control function on the other hand, having a complementary time characteristic, will exclusively control the filter's real part without affecting the imaginary part (which remains unchanged) that acts as an edge detector.

Another important remark that needs to be made is that for low SNR scenarios, the control function set (3.26) is better suited than the (3.27) set since it allows for better control, irrespective of the time parameter t .

Recalling the statement from §3.4.7, even if the Gilboa *et al.* [GSZ02b] complex shock filter successfully deals with the AWGN contamination, there still persists the issue of stability and convergence for high AWGN values. Hence, finding a proper balance between effective noise filtering on the one hand, and stability and convergence on the other remained an open issue for the previously discussed shock filters (§3.4).

The following test scenario is designed to demonstrate the stable time evolution of the hybrid shock filter compared to the highly divergent behavior of the complex shock filter [LLTB10b]. Fig. 3.18 illustrates the core principle behind the development of the hybrid shock filter, which establishes its premise on finding the balance between robust denoising and stability, thus achieving all desiderata for robust and reliable image restoration, within the PDE-based shock filter framework.

The test results illustrated in Fig. 3.18 were obtained under the same experimental

Table 3.1 – $f_1(t)$ and $f_2(t)$ test parameters – Fig. 3.17

Test no.	Parameters			
	T_{1i}	T_{1s}	T_{2i}	T_{2s}
Test 1	150	250	200	1000
Test 2	50	100	100	900
Test 3	300	400	300	900
Test 4	300	320	300	1000
Test 5	<i>cosine-sine</i> control function set (3.27)			

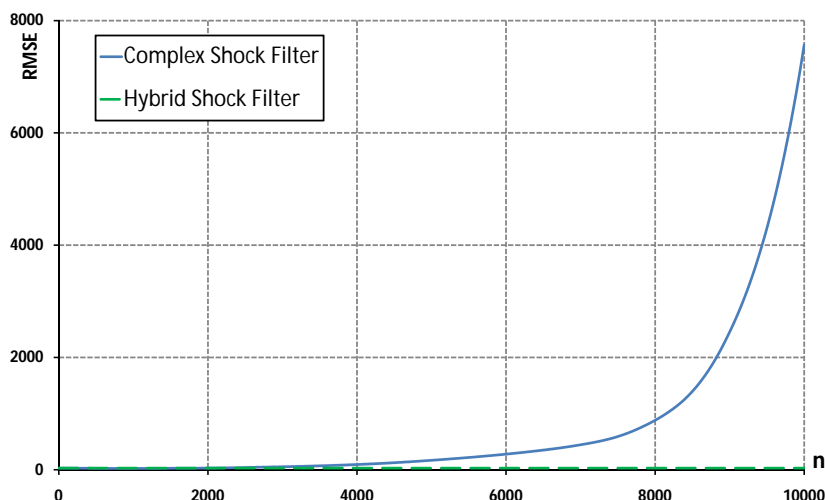


Fig. 3.18 – Hybrid shock filter stability analysis.

setting, *i.e.*, Fig. 3.15 for $t = 1000s$ with $|\lambda| = 0.5$, $\tilde{\lambda} = 0.5$, $a = 0.55$, $dt = 0.1$, $\theta = 0.00001$, $T_{1i} = T_{1s} = 60$ and $T_{2i} = 60$, $T_{2s} = 500$. The divergent behavior of the complex shock filter can be explained through its edge detector: although, redefining the image space as a complex quantity and using the imaginary part of the image function as an edge detector – under certain constraints (§3.5.2) – is an innovative approach and allowed for a shock filter paradigm that was efficient at both denoising and deblurring, the same edge detector is the cause of the complex filter’s long-term instability.

In other words, since the edge detector, *i.e.*, imaginary part, is closely linked to the image function itself, having a parallel time evolution of its own, every edge misalignment from one iteration to the next will be exponentially amplified over time by the edge detector, causing edge shifting up to a point where they no longer, even remotely, correspond to the initial image geometry.

3.6.3 Shock filters: a comparative analysis

This section will focus on presenting a comparative analysis between the hybrid shock filter model and previously-developed, well-established ones, *e.g.*, [OR90, AM94, KDA97a, GSZ02b, RC03].

Using, for the last time the experimental setting illustrated in Fig. 3.15, the motivation for developing the hybrid shock filter, *i.e.*, finding a proper balance between effective noise filtering on the one hand, and stability and convergence on the other, is illustrated in Fig. 3.19, describing the RMSE/time evolution of three filters, *i.e.*, the classic shock filter [OR90], the complex shock filter [GSZ02b] and the hybrid shock filter (3.25). The RMSE computation was performed between the reference image Fig. 3.15a and each of the three filtered results.

As it can be visually observed, the hybrid shock filter possesses the advantages of both the classic shock filter – stable time evolution, steady-state solution – and the complex shock filter, *i.e.*, efficient AWGN filtering with concurrent GB deblurring.

Since any output image is considered to be information and according to the definition of information, it represents an entity about which no prior knowledge is possessed, it is

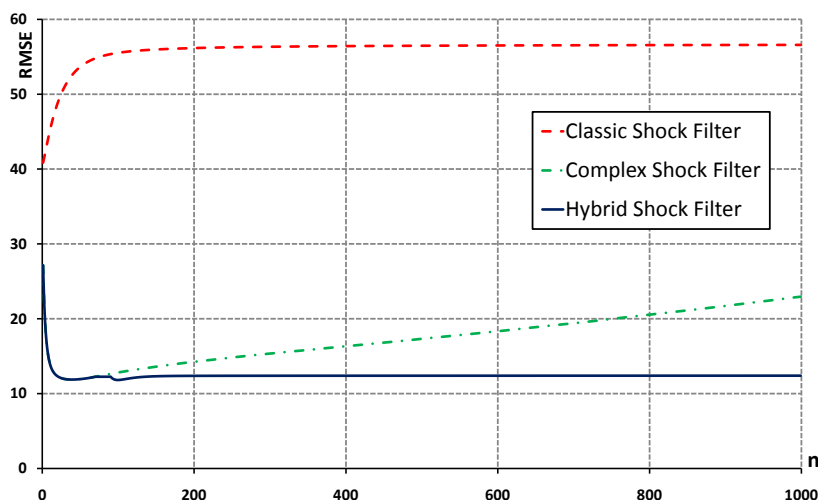


Fig. 3.19 – Comparative analysis based on the first experimental setting – Fig. 3.15.

impossible to *a priori* know the minimum value of the RMSE obtained by filtering. Thus, the complex shock filter lacks the ability of maintaining a stable behavior – that leads to a steady-state solution – long enough to ensure that its time evolution has reached the minimum RMSE value before diverging.

So far the experimental analysis has focused on synthetic images, since they implicitly provide the reference image and because certain particularities, like edges or junctions at specific angles can be created as part of the synthetic image’s geometry. What synthetic images lack is the complexity and stochastic nature of natural images.

To this end, the first experimental setting of the comparative analysis is based on the *House* “natural” image, part of the *USC-SIPI Image Database* [Uni11]. The original image (Fig. 3.20a) is subjected to a generalized GB+AWGN contamination with $\sigma_b = 1$ and $\sigma_n = 10$, resulting the initial image I_0 (Fig. 3.20b). The evolution time of the four filters is $t = 50s$ and the parameter set is the following: $\sigma = 1$, $c = 1$, $|\lambda| = 0.1$, $\tilde{\lambda} = 0.5$, $a = 0.5$, $dt = 0.1$, $\theta = 0.00001$, $T_{1i} = 40$, $T_{1s} = 300$ and $T_{2i} = 30$, $T_{2s} = 350$.

Even after a simple visual analysis, the differences in the filtered results are obvious, the dual characteristic of the hybrid shock filter, *i.e.*, efficient denoising coupled with a stable-convergent behavior, being once again underlined. In order to ensure an objective comparative analysis, the experimental results are qualitatively assessed using the previously described metrics (§3.6.1) as shown in Table 3.2.

The next experimental setting will test a progressive GB+AWGN contamination

Table 3.2 – Qualitative analysis results for the “Fig. 3.20” experimental setting

Filtered result	Quality metrics						
	RMSE	PSNR	MI	SSIM	MSSIM	VSNR	VIF
GB+AWGN	12.186	26.413	1.512	0.583	0.928	33.302	0.339
Osher–Rudin	17.676	23.182	1.37	0.446	0.883	20.184	0.248
Alvarez–Mazorra	18.176	22.94	1.374	0.689	0.837	14.458	0.173
Gilboa <i>et al.</i>	20.036	22.094	1.485	0.681	0.852	13.147	0.125
Hybrid shock filter	9.264	28.794	1.633	0.785	0.951	21.767	0.33

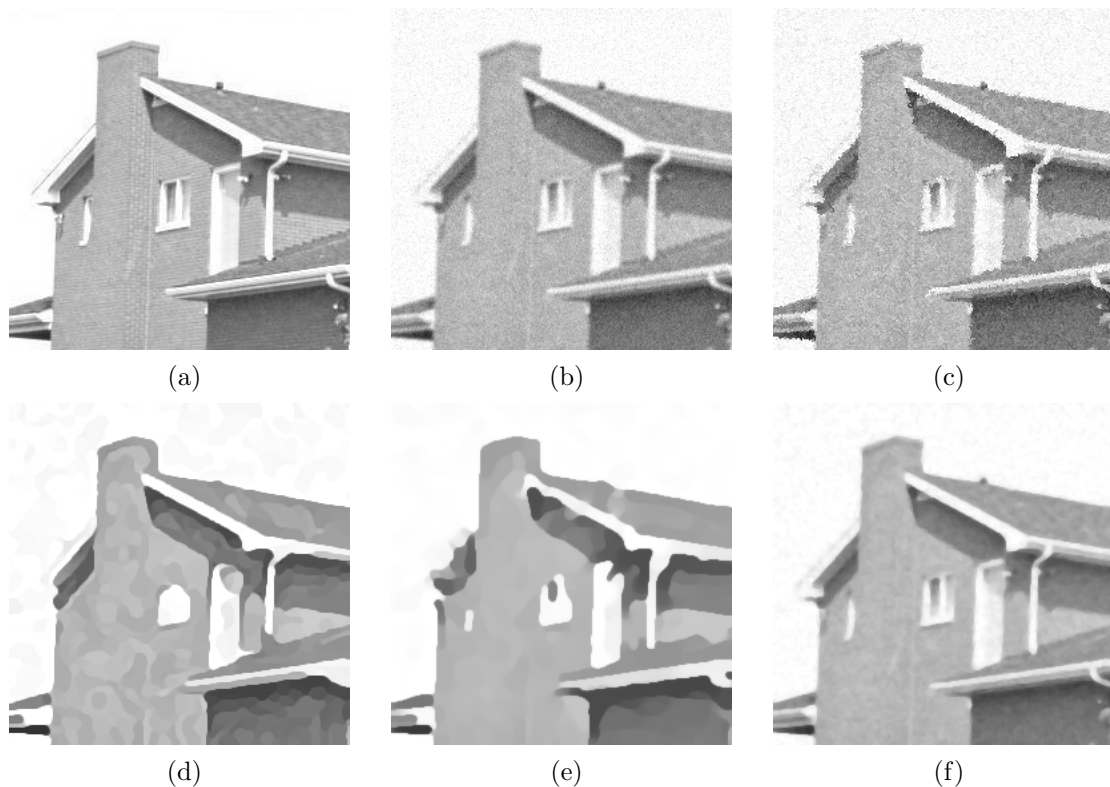


Fig. 3.20 – *Shock filters – comparative analysis: (a) Reference **House** image; (b) $GB(\sigma_b = 1) + AWGN(\sigma_n = 10)$ contaminated initial image I_0 ; (c) Osher–Rudin result; (d) Alvarez–Mazorra result; (e) Gilboa *et al.* result; (f) Hybrid shock filter result.*

scenario, where the reference test image (Fig. 3.21a) is a Gaussian pre-smoothed ($\sigma = 0.6$) version of the 512×512 pixels, 8 bits/pixel gray scale *Fishing Boat* image from [Uni11], as the original contained an unknown noise degradation. Since shock filters are implicitly designed to filter only Gaussian-type interference it was important to work with a unknown noise-free reference image.

All tested filters were implemented according to their original description, while the hybrid shock filter’s numerical model was discretized using finite differences approximation schemes.

For the first part of this experimental setting (Fig. 3.21) a GB of $\sigma_b = 1.5$ with an overlaid AWGN of $\sigma_n = 5$ contaminant has been chosen, which is considered to be a mild

Table 3.3 – *Qualitative analysis results for the “Fig. 3.21” experimental setting*

Filtered result	Quality metrics							
	RMSE	PSNR	SCC	MI	SSIM	MSSIM	VSNR	VIF
GB+AWGN	9.502	28.573	0.978	1.824	0.729	0.943	18.96	0.349
Osher–Rudin	11.017	27.289	0.97	1.661	0.66	0.936	19.898	0.322
Alvarez–Mazorra	9.041	29.006	0.98	2.021	0.822	0.945	18.097	0.309
Remaki–Cheriet	12.434	26.237	0.979	2.103	0.828	0.947	16.454	0.331
Gilboa <i>et al.</i>	9.084	28.965	0.98	2.032	0.828	0.944	17.266	0.329
Hybrid shock filter	8.399	29.645	0.983	2.094	0.844	0.952	18.246	0.358

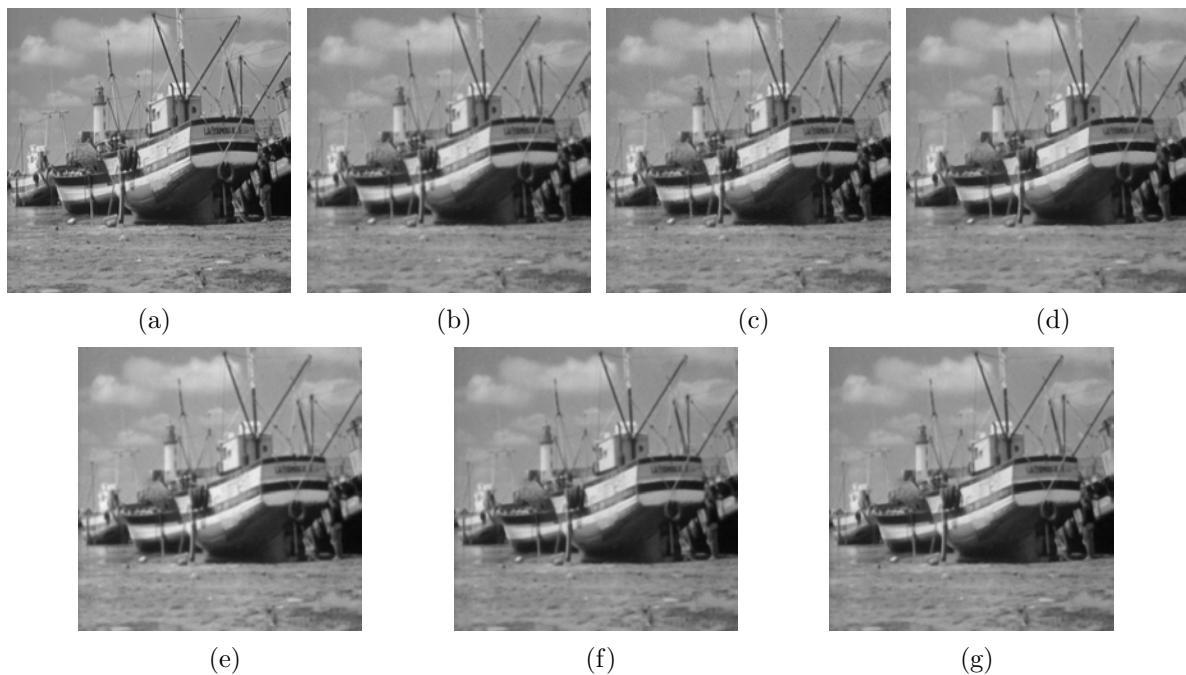


Fig. 3.21 – *Shock filters – comparative analysis: (a) Reference **Fishing Boat** image; (b) $GB(\sigma_b = 1.5)+AWGN(\sigma_n = 5)$ contaminated initial image I_0 ; (c) Osher–Rudin result; (d) Alvarez–Mazorra result; (e) Remaki–Cheriet result; (f) Gilboa et al. result; (g) Hybrid shock filter result.*

GB+AWGN signal contamination.

The filter parametrization can be summarized as follows: $t = 2s$, $dt = 0.1$, $\sigma = 0.5$, $c = 1$, $\tau = 1$, $|\lambda| = 0.1$, $\tilde{\lambda} = 0.5$, $a = 0.5$, $\theta = 0.01$ and $T_{1i} = 16$, $T_{1s} = 19$, $T_{2i} = 17$, $T_{2s} = 18$. All previous parameters comprise the combined parameter pool common to all aforementioned filters and were empirically chosen to ensure a minimum difference in filter parametrization, where applicable. From a qualitative point of view, the test results are summarized in *Table 3.3*.

For the second part of the experimental setting (*Fig. 3.22*) a GB of $\sigma_b = 3$ with an overlaid AWGN of $\sigma_n = 10$ contaminant has been chosen, regarded as a strong GB+AWGN signal contamination. *Fig. 3.22* illustrates the filtered results, while the qualitative analysis is summarized in *Table 3.4*.

For this part of the experimental setting, the only input parameters that have changed

Table 3.4 – *Qualitative analysis results for the “Fig. 3.22” experimental setting*

Filtered result	Quality metrics							
	RMSE	PSNR	SCC	MI	SSIM	MSSIM	VSNR	VIF
GB+AWGN	16.74	23.655	0.93	1.199	0.401	0.806	13.097	0.122
Osher–Rudin	19.96	22.127	0.901	1.041	0.292	0.764	12.901	0.1
Alvarez–Mazorra	15.072	24.567	0.944	1.38	0.653	0.82	11.455	0.101
Remaki–Cheriet	14.326	25.007	0.952	1.507	0.666	0.848	11.943	0.136
Gilboa <i>et al.</i>	14.812	24.718	0.946	1.425	0.671	0.824	11.62	0.104
Hybrid shock filter	12.668	26.076	0.961	1.6	0.727	0.879	13.082	0.183

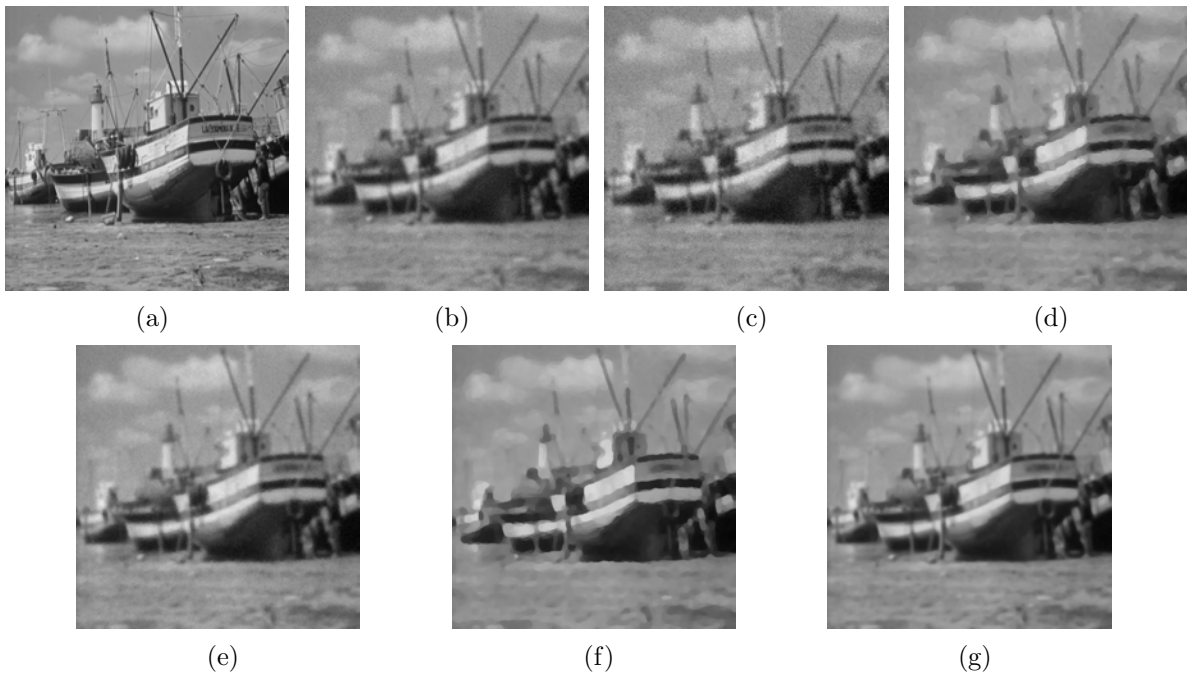


Fig. 3.22 – *Shock filters – comparative analysis: (a) Reference **Fishing Boat** image; (b) $GB(\sigma_b = 3) + AWGN(\sigma_n = 10)$ contaminated initial image I_0 ; (c) Osher–Rudin result; (d) Alvarez–Mazorra result; (e) Remaki–Cheriet result; (f) Gilboa et al. result; (g) Hybrid shock filter result.*

are: $t = 20s$ and the empirically chosen threshold parameters of the hybrid shock filter, $T_{1i} = 50$, $T_{1s} = 70$, $T_{2i} = 60$ and $T_{2s} = 180$.

After reviewing the data from the two main experimental settings, *i.e.*, Fig. 3.20 and Fig. 3.21 & Fig. 3.22, and analyzing the quality metrics measurements from Table 3.2 - Table 3.4 the following remarks need to be made:

- As already mentioned in §3.6.1, the quality metrics used for the experimental analysis cover a wide range of image properties, measuring denoising capabilities (RMSE, PSNR), image fidelity (MI, SCC, VIF) or edge enhancement and structure preservation (SSIM, MSSIM). By analyzing the measured data using these indicators, conclusions regarding how each filter works and how well it performs in a complete image restoration scenario, such as the GB+AWGN filtering, can be formulated.
- In both experimental settings, the measured data indicates that the hybrid shock filter effectively behaves as any standard shock filter would, that is properly enhancing edges as indicated by the highest SSIM and MSSIM values in both scenarios.
- On the other hand, the hybrid shock filter also performs well as a denoising filter, as indicated by the highest measured RMSE and PSNR, a task which traditionally is outside the scope of shock filters. This is an important feature since denoising is performed in this case simultaneously with edge enhancement, making the hybrid shock filter a complex and versatile image restoration tool.
- Achieving these performances concurrently, while providing a result that converges toward the reference image, as indicated by the MI, VIF or the SCC was the underlying reason to further study shock filter theory, which ultimately led to the development of the hybrid shock filter model.

3.6.4 The coherence-enhancing hybrid shock filter: experimental analysis

As stated in the beginning of §3.6 another interesting concept surrounding shock filters is coherence enhancement, introduced for the first time as part of the general shock filter formalism by Weickert [Wei03]. Weickert's CESF, discussed in §3.4.5 proves that shock filters can perform additional tasks to that of edge enhancement if properly conditioned an model, a proof to that statement being the proposed hybrid shock filter itself. Since the CESF model is assumed to perform concurrent deblurring and coherence enhancement, *i.e.*, edge completion, it is just as natural to assume a broader application, where the initial image is also contaminated by an AWGN source.

Having this generalized scenario as prerequisite, the coherence-enhancing hybrid

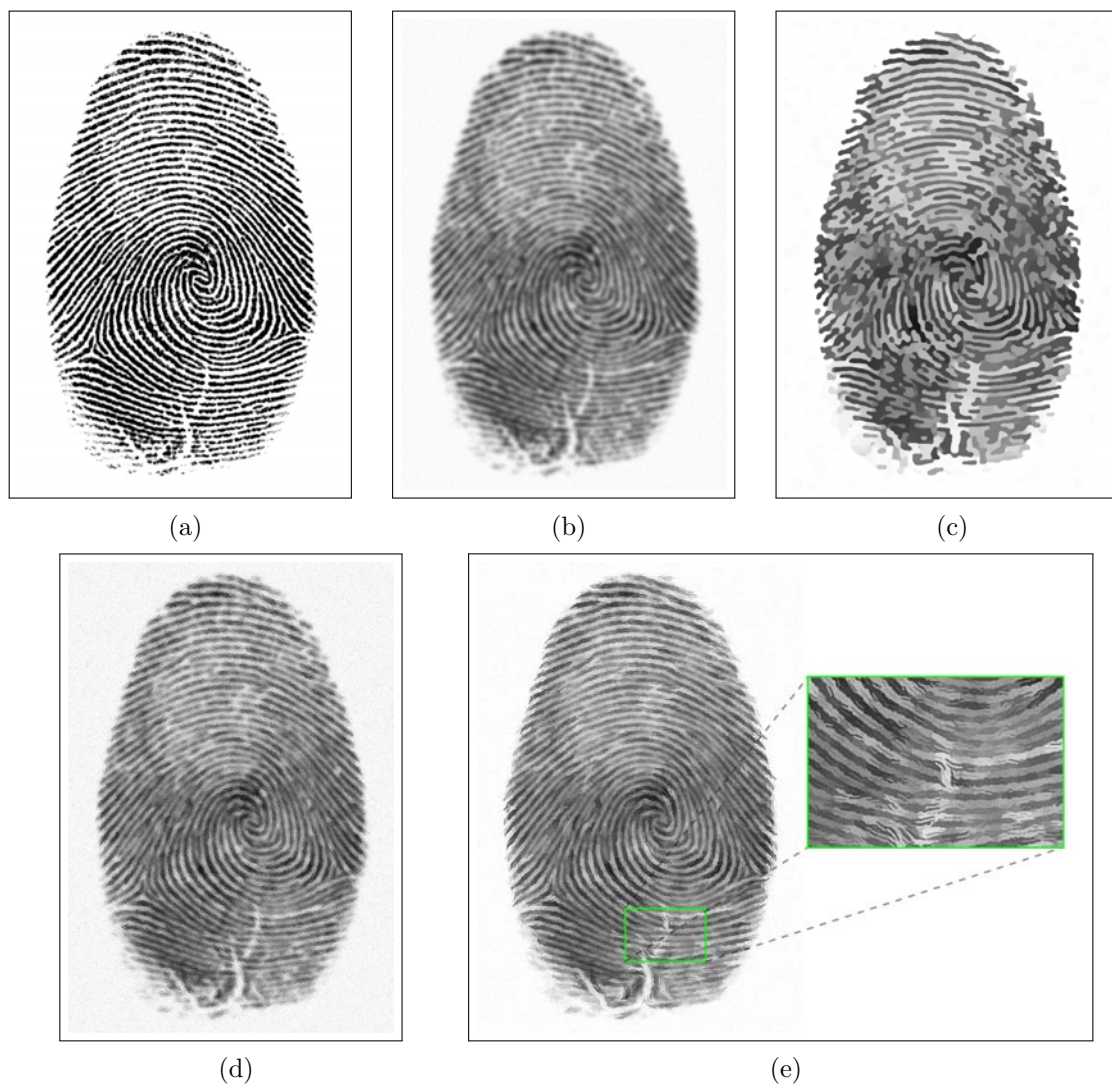


Fig. 3.23 – *Coherence enhancement and shock filters – comparative analysis: (a) Reference fingerprint image; (b) $GB(\sigma_b = 10) + AWGN(\sigma_n = 25)$ contaminated initial image I_0 ; (c) Gilboa et al. result; (d) Weickert's CESF result; (e) Coherence-enhancing hybrid shock filter result and detailed view of the coherence-enhancing effect.*

Table 3.5 – Qualitative analysis results – Fig. 3.23 experimental setting

Filtered result	Quality metrics						
	RMSE	PSNR	MI	SSIM	MSSIM	VSNR	VIF
GB+AWGN	63.217	12.114	1.032	0.372	0.572	5.014	0.08
Gilboa <i>et al.</i>	65.471	11.809	0.84	0.519	0.561	5.167	0.04
Weickert CESF	62.394	12.227	0.935	0.289	0.577	5.857	0.059
Hybrid shock filter	61.203	12.395	0.995	0.486	0.627	5.576	0.059

shock filter (3.28) [LLTB10a, LLBT11] is intended to fulfill a triple task: denoising, deblurring and coherence enhancement, simultaneously. It is an empirically proven fact that when attempting to develop too generalized tools, they tend to perform a multitude of tasks, but none of them particularly well. In order to refute this rule, or more accurately to provide the exception to it, the following test scenario is set in place: an “incomplete” fingerprint image, in the sense that it requires ridge completion, thus suited for an edge-enhancing-like processing is first blurred with a Gaussian kernel of $\sigma_b = 10$ and then contaminated with an AWGN of $\sigma_n = 25$.

Since the main purpose of this experimental setting is to test the shock filters’ coherence-enhancing ability in GB+AWGN scenarios, only the more relevant filters are tested, *i.e.*, Weickert’s CESF, naturally, the Gilboa *et al.* complex shock filter, due to its dual denoising–deblurring nature, and last but not least, the hybrid shock filter, redefined as described by (3.28). Due to the image size and the nature of the process, the evolution time is set to $t = 100s$. The results are illustrated in Fig. 3.23 and qualitatively synthesized in Table 3.5.

Since this test scenario is different from the others in the sense that it introduces and tests the notion of coherence enhancement, the classic approach of assessing the results’ quality is only partly suitable, due to the nature of the performed processing. In other words, coherence enhancement is a process best defined as image enhancement, like image inpainting or image fusion, since it brings additional information to the processed result, thus enhancing its quality. The additional information is built using existing information and a given decision criterion, with a set of rules based on which the process evolves over time.

It is a well established fact that for image enhancement tasks, determining the quality of the processed result is not straightforward since the reference is not known *a priori*, an ideal initial image, defeating the purpose of image enhancement. The enhanced result represents an improved version of the initial image, not only a restored one, hence directly comparing it with its references is not entirely accurate in assessing its quality.

The quality metrics used so far, reveal only in part the qualitative differences between reference image and filtered result. Even so, the denoising capability is expressed in terms of RMSE and PSNR, with the hybrid shock filter yielding the best result for both, while the edge enhancement and to some extent the coherence-enhancing property is quantified by the SSIM and its multiscale version, the MSSIM. As it can be seen in Table 3.5, the highest values belong, once again to the hybrid shock filter.

Thus, the previous experimental setting confirms that the hybrid shock filter model (3.25) can be successfully extended to include coherence-enhancing capabilities (3.28) without any tradeoff between range of application and filtering performance.

3.7 Conclusion

The development of the hybrid shock filter has managed to establish a balance between robust image restoration prerequisites and stability and convergence. The experimental results in §3.6 clearly indicate, not only that the hybrid shock filter performs well for noise filtering, as shown by the highest RMSE and PSNR values in all proposed experimental settings, but also that it surpasses compared filters in edge enhancement, as indicated by the SSIM and MSSIM values – specifically defined to measure edge enhancement quality.

The most important quality of the hybrid shock filter is that it achieves image denoising with edge enhancement simultaneously, making it a versatile and useful image processing tool. Its versatility can be further extended by adding a coherence-enhancing component to the initial mathematical model (3.25), thus making possible the successful use of the *extended hybrid shock filter model* (3.28) in coherence enhancing scenarios, like the ones experimentally analyzed in §3.6.4. In this case, the initial GB+AWGN is kept, adding to the image restoration scenario the requirement of coherence enhancement.

Potential further work will concentrate on improving the current hybrid shock filter formulation by:

- experimenting with alternative types of control functions, making them to be image dependent, discriminating between homogeneous and nonhomogeneous regions within the image.
- inserting into the initial model an explicit more sophisticated anisotropic steering component.
- studying the potential of a localized or semi-localized orientation indicator, that can be used as argument for the strength of the filtering process and the definition of the control function set.

and

- using more sophisticated discretization schemes and tensor-driven image restoration.

All of the aforementioned ideas would help improving the filter’s performance, but to what extent remains to be determined by experimental analysis.

In conclusion, the modular character of the hybrid shock filter allows not only to define different sets of control functions, to best suit various image restoration tasks – according to the nature of the processed images, but also to extend its use to coherence-enhancing practical tasks, such as fingerprint restoration.

Albeit, not the first unifying approach in terms of concurrent deblurring and denoising, the *hybrid shock filter* helps consolidate the principle of a combined image restoration process, reiterating at the same time the versatility and effectiveness of PDEs as image processing tools. Furthermore, the proposed model provides a glimpse at the feasibility of tackling complex problems in a structured, simultaneous manner, paving the way for the joint restoration–enhancement proposed approach, detailed in **Chapter 5**.

In essence, the proposed *hybrid shock filter* is an intermediary step toward validating the even more general concept, of a coalescent image restoration and enhancement paradigm, emphasizing at the same time, the ubiquitous nature of PDEs in image processing.

In this context, the *hybrid shock filter* as a processing tool, and **Chapter 3** as a constituent part of this thesis, represent an essential intermediary stage both in terms

of formalism and thesis composition, bridging image restoration (**Chapter 2**) to image enhancement (**Chapter 4**) and ultimately to joint image restoration and enhancement (**Chapter 5**).

C 2 C

Deblurring as an image restoration concept – §3.2 – provided a quick overview of *deblurring* in the context of image restoration (in general) and addressed and viewed as inverse diffusion (in particular), in the context of PDE-based image processing, in particular. Even though the notions of *denoising* and *deblurring* represent to facets of image restoration, the many differences between them, from contamination source to filtering, required a separate discussion, hence the inclusion of PDE-based deblurring fundamentals in **Chapter 3** and not in **Chapter 2**.

Concurrent denoising and deblurring – §3.3 – before discussing the first proposition of this thesis, *i.e.*, the *hybrid shock filter* is was necessary to provide a *problem statement* in the context of image restoration and of what was expected from the proposed model in terms of practical behavior and filtering performance.

Shock filters – §3.4 – since PDE-based deblurring as an image restoration paradigm already comprises a series of existing proposition, starting with the *classic shock filter*, it was necessary to provide a short overview of the existing approaches, serving for both problem assessment as well as for experimental comparison and analysis.

The hybrid shock filter – §3.5 – introduced the first proposition of this thesis, *i.e.*, the *hybrid shock filter*, a PDE-based image restoration paradigm for image deblurring with simultaneous denoising. The analysis of the proposed model was carried out along the following lines:

- mathematical definition,
- parameter discussion,
- extended model (adding coherence enhancement to the initial definition).

Experimental analysis – §3.6 – provided the practical analysis of the proposed hybrid shock filter, experimentally assessing the following:

- parameter and stability analysis,
- comparative analysis, using as filtering reference existing shock filter models, described in §3.4,
- experimental analysis of the extended model on a particular type of input images, *i.e.*, fingerprint images, to properly assess coherence enhancement.

In order to properly analyze and compare the proposed model, it was also *a priori* required to present the employed *objective quality metrics*.

Conclusion – §3.7 – presented the conclusions derived from the experimental analysis for the proposed *hybrid shock filter* while at the same time offering several pointers in the direction of further improving and extending the proposed model.

CHAPTER 4

Image fusion: an image enhancement paradigm

Main Contents

4.1	Motivation	75
4.2	Image fusion: a short introduction	76
4.3	Definitions and classifications	77
4.4	Methodology in image fusion: an overview	79
4.5	Variational and PDE-based approaches to image fusion	85
4.6	Quality assessment in image fusion	93
4.7	Properly choosing a reference in image fusion quality assessment	96
4.8	Conclusion	104

4.1 Motivation

This chapter represents the transition in terms of topic, from image restoration to image enhancement. Its intended purpose is to lay down the fundamentals required for a basic understanding of the key notions and concepts describing image fusion, and thus answer the basic questions of:

- *What is fusion in general and image fusion in particular?*
- *Why use fusion in image processing?*
- *When is image fusion necessary?*
- *How does it work?*

Naturally, the contents of this chapter go beyond answering these basic questions, and further address more complex issues in the area of image fusion, like concurrent image fusion and denoising, truly bridging the two image processing tasks, *i.e.*, restoration and enhancement. This new paradigm (detailed in **Chapter 5**) also brings new difficulties in properly assessing the quality of the results produced by such methods, and, in part, the purpose of this chapter is to underline the complexity of not only the task itself but of quantifying its results as well, raising the intricate questions of *how to properly assess the image quality in concurrent fusion and denoising scenarios?* and *how much of the actual quality of the results from such scenarios is lost in the quality assessment process, on account of not having a truly dedicated quality metric?*

In terms of contents, this chapter is organized as follows: the first part presents the main definitions, fusion vocabulary and classifications required for having a basic knowledge of this particular image processing paradigm, followed by a brief analysis of the current image fusion methodology, *i.e.*, image fusion formalisms. Afterward, the discussion is further narrowed in scope to existing variational approaches in image fusion,

a direct link to the proposed paradigm, discussed in **Chapter 5**. Before concluding this chapter, two interconnected aspects of image fusion will be discussed: quality assessment, covering dedicated quality metrics and their particular properties, and the related subject of properly choosing a reference image when assessing the quality of a fused image.

4.2 Image fusion: a short introduction

As an integral component of image processing, image fusion is, according to the definitions discussed in §2.2, an image enhancement paradigm with wide spread applicability both in terms of image types (image acquisition-wise) and in terms of application domain, e.g., image classification, computer vision, remote sensing, medical imaging, concealed weapon detection, multifocus image fusion, digital camera application, battlefield monitoring, etc. As an image enhancement paradigm, image fusion can be approached in terms of theoretical formalization using any of the general image processing techniques, briefly analyzed in §2.2.

Image fusion first emerged as a distinct image processing tool in the attempt to emulate the practice of image interpretation experts, as noted by Bloch and Maître in [BM08]. Images, as an additional source of information, are also integrated more general fusion processes, such as multi-sensor fusion or data (information) fusion, concepts that will be properly defined and classified in §4.3.

In very simplistic terms, serving the purpose of an interim definition, image fusion can be defined as the process of combining multiple input images into a single composite image, often referred to as *fused image*. According to Mitchell [Mit10], the aim of image fusion is to create from this collection of input images a single output image which contains a better description of the scene than the one provided by any of the individual input images. The basic problem of image fusion is to determine what is the best procedure of combining the input images so as to maximize the useful information contained by the fused image [Mit10].

In a strictly image processing context, image fusion represents a key decision making component in complex and usually poorly formalized situations, in which each input image provides an element of “truth” that contributes, in collaboration and in opposition with the rest of the input images to the overall interpretation of the scene described by these input images [BM08].

According to Mitchell [Mit10], the main benefits of image fusion are: (i) **increased reliability**, (ii) **reduced uncertainty**, (iii) **robust system performance**, (iv) **compact information representation**, (v) **extended range of operation**, and (vi) **extended spatial and temporal coverage**.

Nowadays, image fusion is not restricted to the rather traditional sense of the word “image”, since today’s imaging sensors comprise optical cameras, MMW¹ cameras, IR² cameras, x-ray and radar devices. Therefore, the broader definitions that previously applied only to multisensor fusion are now applicable to image fusion, when dealing with different image acquisition techniques, e.g., an optical image fused with an IR image.

¹millimeter wave

²infrared

4.3 Definitions and classifications

In acquiring a basic understanding of image fusion both as a process and as a theoretical concept, it is helpful to analyze the notion from a broader perspective, *i.e.*, *data fusion*. In the scientific community the fusion process is often referred to using different names, *e.g.*, *sensor fusion*, *information fusion*, and although they may seem synonymous, they only partly overlap, application-wise, as pointed out by Steinberg *et al.* in [SBW99].

According to the **Oxford** dictionary, the term ***fusion*** refers to “*the process or result of joining two or more things together to form a single entity*”. Similarly, the **Merriam-Webster** dictionary defines ***fusion*** as “*a merging of diverse, distinct, or separate elements into a unified whole*”. In terms of a comprehensive approach to understanding fusion both as a process and as a research field, these definitions are inadequate since they do not convey the full meaning of *fusion* as an image processing technique, this, of course being outside their scope.

Over the years, numerous researchers have tried to define both in terms of purpose and of meaning, the concept of fusion, linking it to various application domains, according to their specific field of research. A review of the most pertinent definitions should necessarily include the following ones:

Hall [Hal92] – “*Multisensor data fusion* seeks to combine data from multiple sensors to perform inferences that may not be possible from a single sensor alone.”

Wald [Wal98] – “*Data fusion* is a formal framework in which are expressed means and tools for the alliance of data of the same scene originating from different sources. It aims at obtaining information of greater quality; the exact definition of greater quality will depend upon the application.”

Gonsalves *et al.* [GCTO00] – “The overall goal of *data fusion* is to combine data from multiple sources into information that has greater benefit than what would have been derived from each of the contributing parts.”

From a complexity point of view, image fusion is classified using the following levels of representation [Sam03, Sam04]:

signal-level

image-level, also known as ***pixel-level*** – is defined as the combination of the raw data from multiple source images into a single fused image. This level consists in combining the signals provided by different sensors without any preprocessing performed on the input images. For the fusion process to be robust the sensors must be similar and, consequently, the signals must be commensurate. The way in which the signals are combined depends on the relationships that exist between the sensors. A fused image is obtained by “summing” the input images, fused result that can be further used for feature extraction purposes either as a preprocessing stage or as an intermediary image fusion stage.

feature or symbol-level – relies on the extracted features from each sensor and an identity declaration based on those extracted features. The identity declaration process comprises several methods, such as knowledge-based approaches (*e.g.*, expert system, fuzzy logic) or training based approaches (*e.g.*, discriminant analysis,

neural networks, Bayesian techniques, K-nearest neighbor methods, center mobile algorithms).

decision-level – the highest level of complexity in image fusion; uses the identity declaration provided by each sensor, further processed by means of: e.g., heuristic methods, Bayesian techniques, or the Dempster-Shafer approach – a generalization of Bayesian techniques applied to data with a high level of uncertainty.

In other words, image fusion produces a single fused image by combining information from a set of source images, using one of the previously described fusion levels. The purpose of image fusion is to obtain a fused image that possesses a greater information content than any of the individual sources alone. Due to the addition of redundant and complementary information the reliability and overall detail of the image is increased.

In a multisensor environment, for example, pixel-level fusion can generate a fused image that provides the best description of a scene. In this case, each sensor provides complementary information that is combined into a fused image. The obtained fused image can be used by other algorithms for further processing or by human end-users – who cannot easily visualize and combine the results from multiple sensors without the aid of digital image processing tools.

The processed data, the basis of every fusion scenario, can be classified into:

- multisensor data
- multi-temporal data
- multiresolution data
- multi-parameter data

Since its emergence as a stand-alone research field, image fusion has seen a rapid expansion, encompassing numerous fusion models based on various mathematical formalisms, thus requiring a classification according to complexity, employed formalism and purpose. Such a classification is proposed by Blum *et al.* in [BXZ06]:

- **Multiscale-decomposition-based** image fusion
 - *Pyramid Transform* (PT), e.g., Laplacian pyramid, contrast pyramid, gradient pyramid, steerable pyramid
 - *Discrete Wavelet Transform* (DWT)
 - *Discrete Wavelet Frame* (DWF)
- **Non-multiscale-decomposition-based** image fusion
 - *pixel-level weighted averaging*, e.g., Addition, Robust Addition, Subtraction, Division, Multiplication, Adaptive Weight Averaging(AWA)
 - *image subspace techniques*, e.g., Principal Component Analysis (PCA), Independent Component Analysis (ICA), nonnegative matrix factorization (NMF), Canonical Correlation Analysis (CCA), Linear Discriminant Analysis (LDA)
 - *nonlinear methods*
 - *estimation theory-based methods*
 - *color composite fusion*
 - *artificial neural networks*

The intended purpose of all previous definitions and classifications is to properly define and position the proposed fusion method, detailed in **Chapter 5**, in order to correctly juxtapose it against the existing fusion methodology. This is an extremely important factor in the comparative analysis since comparing methods of different levels of complexity, e.g., pixel-level with decision-level, does not provide an adequate amount of relevancy, since it would be like comparing *apples and oranges* (different comparison criteria apply to each fusion level and thus, comparison between different levels is not straightforward).

Therefore, in the context of the previously discussed definitions and classification, the proposed fusion model (detailed in **Chapter 5**) can be defined as: *a pixel-level, non-multiscale-decomposition-based, nonlinear method*, which can be applied to multi-sensor or multi-temporal data. Furthermore, the definitions of *data fusion* were provided to: clearly delineate the purpose of image fusion, underline the general expectations in terms of fused result and last but not least to provide the basic quality assessment guidelines.

This section has covered so far the most pertinent definitions, classifications and objectives pertaining to data fusion in general and image fusion in particular, and in order to attain its intended purpose it cannot close without any reference to the requirements of image fusion. In image fusion, the fused result is usually a single image \tilde{I} , on which the following requirements are imposed [Mit10]:

- *Pattern conservation* – The fusion process should preserve all relevant information of the input images in the composite image.
- *Artifact free* – The fusion scheme should not introduce any artifacts or inconsistencies that would distract the human observer or alter subsequent image processing stages.
- *Invariance* – The fusion scheme should be shift and rotational invariant, i.e., the fused result should not depend on the location or orientation of an object in the input image.

For time-evolving fusion paradigms, where the fusion data is a set of input images $I_s(t)$, $t \in [T_1, T_2]$, $s \in \{1, 2, \dots, S\}$, the fused result is an image $\tilde{I}(t)$. In this case the following additional requirements are imposed [Mit10]:

- *Temporal stability* – The fusion output should be temporally stable, that is, gray level changes in $\tilde{I}(t)$ should be present in at least one of the input images $I_s(t)$.
- *Temporal consistency* – Gray level changes which occur in the input images $I_s(t)$ must be also present in the fused image $\tilde{I}(t)$.

4.4 Methodology in image fusion: an overview

Since image fusion is nowadays a complex, stand-alone research field with fusion techniques covering a large variety of mathematical formalisms and being classified into different levels of complexity (§4.3), and considering the characteristics of the proposed image fusion model, this section will not exhaustively cover the existing image fusion methodology. In fact, it is meant to describe only the methods of relevance in acquiring a basic understanding of image fusion, and which have a similar application range as the proposed model, described in detail in **Chapter 5**. As a last remark of this paragraph, in order to provide a structured analysis the selected image fusion methodology will be discussed according to the Blum *et al.* [BXZ06] classification (§4.3).

4.4.1 Non-multiscale-decomposition-based fusion techniques

From a complexity point of view, the most basic fusion techniques within this class are pixel-level fusion methods that rely on simple pixel operations performed on the input image's values. In order to simplify the discussion and focus the interest on the fusion methods themselves, it is assumed that the input images are spatially and temporally aligned (where applicable), semantically equivalent and that the general image fusion scenario is formulated using S input images I_1, I_2, \dots, I_S .

4.4.1.1 Addition as a fusion paradigm

From an intuitive and mathematical point of view, the addition operation can be considered as the simplest image fusion example, where the fused image \tilde{I} represents the average intensity value of the input images I_s , with $s \in \{1, 2, \dots, S\}$, on a per-pixel basis. For a pixel (m, n) the fused image \tilde{I} is expressed as:

$$\tilde{I}(m, n) = \frac{1}{S} \sum_{s=1}^S I_s(m, n) \quad (4.1)$$

Despite its simplicity, addition as a fusion technique is widely used if the input images are of the same modality [Mit10]. Although, this fusion method assumes semantic alignment and requires very accurate spatial alignment, as pointed out by Mitchell [Mit10], it also has the advantage of suppressing any noise, present in the input images. This advantage relies on the theoretical property of certain types of noise, modeled by a uniform random distribution, property that for a large enough number of input images – ideally $S \rightarrow \infty$ – ensures noise cancelation, as a byproduct of the addition process.

Remark As noted in [Mit10], the pixel average technique has the disadvantage that it tends to suppress salient image features producing a low contrast image with a “washed-out” appearance. This effect can be alleviated, to some extent, by using a linear weighted average of the input images.

Such an approach can be expressed as:

$$\tilde{I}(m, n) = \frac{\sum_{s=1}^S w_s I_s(m, n)}{\sum_{s=1}^S w_s} \quad (4.2)$$

where w_s are preselected scalars, chosen so that each input image contributes to the fused result with an amount *a priori* specified by some fusion criterion, defined according to application requirements. A more efficient approach to selecting the w_s weights is by using the AWA technique in order to allow the weights to vary dynamically, according to the amount of information contained in each input image I_s .

An alternative altogether to the addition method (4.1) are robust averaging methods such as the *median operator*:

$$\tilde{I}(m, n) = \text{median}_s (I_s(m, n)) \quad (4.3)$$

or the *trimmed mean operator*:

$$\tilde{I}(m, n) = \frac{1}{S - 2\alpha} \sum_{s=\alpha+1}^{S-\alpha} I_{(s)}(m, n) \quad (4.4)$$

where $I_{(s)}(m, n) = I_l(m, n)$, if $I_l(m, n)$ is the l^{th} largest gray level value for pixel (m, n) , while α is a small constant, often set to $\alpha = \lfloor S/20 \rfloor$.

Remark As previously mentioned, without going into detail, *non-multiscale-decomposition-based fusion techniques* also include: **fusion by means of subtraction, color space image fusion, image subspace fusion, et al.**

4.4.2 Multiscale-decomposition-based fusion techniques

Multiscale (multiresolution) techniques are the basis of a wide range of image processing tools, from image compression to image coding, segmentation or filtering, and last but not least, image fusion. This versatility resides in the fact that multiscale techniques closely approximate the HVS³ in terms of perception and interpretation, since the HVS relies on multiscale decomposition in order to completely assess a scene.

For instance, when analyzing a landscape, at first glance, only the coarser elements are visible providing the first level of analysis, or in other words the first scale of representation. If that landscape is further analyzed, from a more detailed perspective, by taking into account only parts of it, smaller and smaller representation scales are obtained, each providing a new set of details, not visible before at larger scales. In essence, the same image can be viewed at different scales, each of them with its own unique set of details that cannot be seen at any other scale.

It is thus obvious how such a representational format could provide, in terms of information output, an exhaustive perspective of the analyzed image. Therefore, multiscale techniques applied to image fusion problems, integrate the entire detail spectrum of a multiscale representation into a single fused image, an immediate application as image fusion tools being in satellite imagery. Although, their use in satellite imagery usually deals with input images of different resolutions, multiscale fusion techniques perform just as well on input images of the same resolution [Pop08].

According to Piella [Pie03], signals often contain physically relevant features at different scales of representation. Thus, for a comprehensive understanding of a signal, an analysis over a broad range of resolutions is required, although, sometimes signals behave in a similar way across different scales, *i.e.*, scale-invariant signals. For signals that are not scale-invariant, it cannot be *a priori* asserted at which scales the signal contains the more relevant information, thus all representation scales are of equal importance, meaning that the signal is uniformly analyzed across all representation scales.

In image fusion, multiscale techniques comprise three processing stages:

- I. The decomposition (analysis) stage of each input image, which produces an *approximation* image and one or more *detail* images.
- II. The fusion stage, where for each decomposition scale a fusion criterion is applied.
- III. The reciprocal of the decomposition operation, the recomposition (synthesis) stage, which yields the fused image.

³Human Visual System

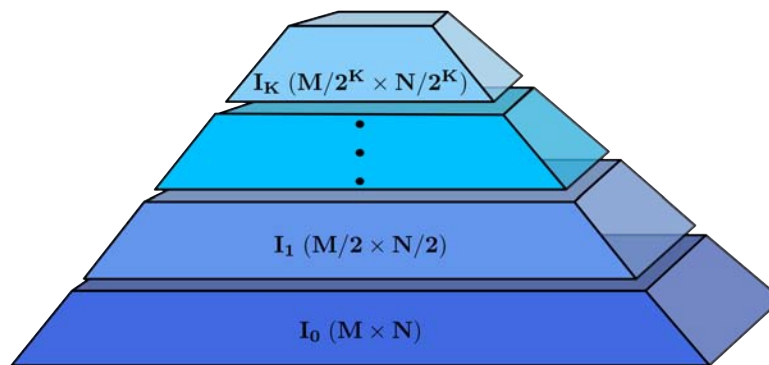


Fig. 4.1 – [Mit10] – *The pyramid representation of the multiscale analysis of an input image I .*

4.4.2.1 Pyramid-decomposition-based methods

According to Mitchell [Mit10], in pyramid-based multiscale analysis an input image I is decomposed into a sequence of images I_k , $k \in \{1, 2, \dots, K\}$ each of which captures the information from I corresponding to the scale k . In the pyramid decomposition scheme, as illustrated in Fig. 4.1⁴, at the bottom of the pyramid is the image I_0 – the original input image I – followed at each successive level k by the image I_k . Each image I_k is recursively constructed by low-pass filtering and downsampling the I_{k-1} image. For the pyramid representation example illustrated in Fig. 4.1, a dyadic multiscale analysis was assumed, in which I_k has double the resolution of I_{k+1} .

Recalling the most representative pyramid-decomposition-based fusion methods, which will be also used in the comparative analysis (§5.4.4):

- *The Gaussian pyramid*
- *The Laplacian pyramid*
- *The contrast pyramid*
- *The FSD pyramid*
- *The gradient pyramid*

4.4.2.2 Wavelet-based methods

An alternative to the “less” sophisticated pyramid transform decomposition methods is centered on the wavelet concept, and it was first introduced as a multiscale decomposition technique by Mallat in [Mal89]. The author argues that for efficiency reasons, successive layers of a pyramid decomposition should include only the additional details, which are not already available at preceding levels, this being the fundamental principle behind the wavelet decomposition. Moreover, since the wavelet decomposition amounts to a process of successive spatial filtering and sampling, the method has the property of simultaneously being a multiscale and a multiresolution technique.

⁴Fig. 4.1 – the original pyramid representation can be found in [Mit10]

Since both the wavelet transforms and the pyramid transforms are multiscale decomposition methods, the matter of choosing one family of transforms over the other amounts to analyzing which family possesses superior features for a given application field. In their use as an image fusion framework, wavelets have proven to deliver a richer directional information content, to be more robust to contrast inversions, to yield a superior fused result, in terms of SNR and visual perception [LMM95, LON⁺07].

The wavelet transforms share to some extent the pyramid transforms framework, begin subjected to the same decomposition-recomposition process with the same analysis stage. At each level, the wavelet function can be determined based on its *mother wavelet*. The most commonly used wavelet families in image processing were proposed and defined in [Dau92, CMW92].

The most important wavelet transforms employed in image fusion are the following:

- *The Discrete Wavelet Transform*
- *The Undecimated Discrete Wavelet Transform*
- *The Shift-Invariant Discrete Wavelet Transform*

Remark For the comparative analysis presented in §5.4.4 only fusion methods based on the DWT and the SIDWT are used.

4.4.2.3 Fusion criteria in multiscale image fusion

As discussed at the beginning of §4.4.2, image fusion techniques based on a multiscale decomposition are implemented using a three-stage approach, *i.e.*, a decomposition stage, a fusion stage and a recomposition stage. Since, the first and the last stages have been discussed so far, emphasis will be placed on analyzing the most widely used fusion criteria employed in the second stage of multiscale decomposition fusion methods.

This section is intended only as a synthesis of the most relevant decision criteria in multiscale-decomposition-based fusion, a more detailed perspective can be found in [ZB99, Pie03, PdlC04]. In multiscale image fusion, the input images are decomposed at each level of decomposition into a detail image and an approximation image, and further combined (fused) in order to generate a fused image $\tilde{I}^{(k)}$ at the k^{th} level of decomposition. Thus, the recomposition process will consist in creating a final fused result \tilde{I} from the previously obtained decompositions $\tilde{I}^{(k)}$.

The fusion criteria are usually divided into two types of processes: a selection process, of the multiscale representation, and the actual composition process, of the multiscale sub-images into a fused sub-image, at each level of decomposition. A commonly used fusion criterion, the *choose max* criterion, employs the two types of processes at different stages of decompositions, as follows: at the final decomposition level K , based on all the approximation input images at that level $I_s^{(K)}$, a mean value image $\tilde{I}^{(K)}$ is generated. For the remaining $K - 1$ levels, which contain the detail images $I_s^{(k)}$, $k = \{1, \dots, K - 1\}$, a selection criterion is applied. In its entirety, the *choose max* fusion criterion is mathematically expressed as:

$$\begin{aligned} \tilde{I}^{(K)}(p|0) &= \frac{1}{S} \sum_{s=1}^S I_s^{(K)}(p|0) \\ \tilde{I}^{(k)}(p|s) &= \arg \max (|I_s^{(k)}(p|g)|) \quad k = 1, \dots, K - 1; g = 1, \dots, G \end{aligned} \tag{4.5}$$

where S is the number of input images, K the last decomposition level, G the number of directional filters, i.e., $G = 4$ for a *gradient pyramid*, and p the current pixel's coordinates.

A more elaborate criterion – which resembles coefficient weighting based on a pertinence map – employing a *saliency* and *match* measure, is proposed by Burt and Kolczynski in [BK93] in order to differentiate between the selection process and the weighting process performed at each decomposition level. The *match* measure indicates the resemblance degree between images, at each decomposition level and can be interpreted as follows: if its value is high, the images are weighted, conversely, if its value is low, the image having the highest *saliency* value is selected. The measures are defined for a 1×1 , 3×3 or 5×5 neighborhood while the *saliency* measure can be either the energy or the variance, computed over the defined neighborhood. If the *saliency* measure is defined as an energy measure:

$$\text{sal}_s^{(k)}(p|g) = \sum_{\Delta p \in W^{(k)}} |I_s^{(k)}(p + \Delta n|g)|^2 \quad (4.6)$$

where $W^{(k)}$ is the defined neighborhood at level k . For the particular case of two input images (A and B), the *match* measure is defined as:

$$\text{mat}_{AB}^{(k)}(p|g) = \frac{2 \cdot \sum_{\Delta p \in W^{(k)}} I_A^{(k)}(p + \Delta p|g) I_B^{(k)}(p + \Delta p|g)}{\text{sal}_A^{(k)}(p|g) + \text{sal}_B^{(k)}(p|g)} \quad (4.7)$$

Based on (4.6) and (4.7) and using the two-input image scenario, the fusion process is described by:

$$\tilde{I}^{(k)}(p|g) = \alpha_A(p|g) I_A^{(k)}(p|g) + [1 - \alpha_A(p|g)] I_B^{(k)}(p|g) \quad (4.8)$$

where the $\alpha_A(p|g)$ weight is defined as:

$$\alpha_A(p|g) = \begin{cases} 1 & \text{if } \text{mat}_{AB}^{(k)}(p|g) \leq \tau \text{ and } \text{sal}_A^{(k)}(p|g) > \text{sal}_B^{(k)}(p|g) \\ 0 & \text{if } \text{mat}_{AB}^{(k)}(p|g) \leq \tau \text{ and } \text{sal}_A^{(k)}(p|g) \leq \text{sal}_B^{(k)}(p|g) \\ \frac{1}{2} + \frac{1}{2} \left(\frac{1 - \text{mat}_{AB}^{(k)}(p|g)}{1 - \tau} \right) & \text{if } \text{mat}_{AB}^{(k)}(p|g) > \tau \text{ and } \text{sal}_A^{(k)}(p|g) > \text{sal}_B^{(k)}(p|g) \\ \frac{1}{2} - \frac{1}{2} \left(\frac{1 - \text{mat}_{AB}^{(k)}(p|g)}{1 - \tau} \right) & \text{if } \text{mat}_{AB}^{(k)}(p|g) > \tau \text{ and } \text{sal}_A^{(k)}(p|g) \leq \text{sal}_B^{(k)}(p|g) \end{cases} \quad (4.9)$$

where τ is a threshold, above which the input images I_A and I_B are considered alike. This approach, and the similar *consistency check* approach, proposed by Li *et al.* in [LMM95], allow to overcome the problem of region-based fusion, i.e., contrast inversion.

As pointed out by Pop [Pop08], another important aspect of multiscale decomposition fusion is the selection of the appropriate number of decomposition levels for the multiscale transform. Although, an exact way to determine the minimum number of decomposition levels that would ensure a fused result of good quality does not exist, there exists a direct link between the size of the objects within the images to be fused and the number of decomposition levels. If this size is large, a higher number of decomposition levels is required in order to ensure a quality fused result. Moreover, Rockinger and Fechner [RF98] point out that, when using shift-variant multiscale methods the number of decomposition levels is directly influenced by the object's position and by the type of the filter used in the decomposition process.

4.5 Variational and PDE-based approaches to image fusion

Like any other current image processing formalism (§2.2), PDE-based and variational methods can be successfully employed as image fusion frameworks. Even more so, their use can provide a series of advantages, in the form of the inherent properties of PDE and variational techniques, discussed throughout this thesis. Since the two image processing approaches are closely related, from a theoretical point of view, it seems only natural to treat the subject of PDE-based and variational fusion techniques as a single entity.

A simple way of analyzing some of the most representative variational and PDE-based approaches to image fusion, is to make use of a chronological classification, which in turn can provide a parallel, intrinsic view of the evolution of such methods over the years.

4.5.1 Socolinsky’s variational image fusion model

The method proposed by Socolinsky in [Soc00a, SW02] is developed around multispectral and multisensor fusion applications in remote sensing, and its underlying principle states that the fused image should have the same gradient vector map as the contrast vector map measured across all input images I_s , where $s = \{1, \dots, S\}$.

For a single image, Socolinsky’s approach relies on obtaining the gradient vector ∇I from the structure tensor $\mathbf{J}(x, y)$ defined as:

$$\mathbf{J}(x, y) = \begin{pmatrix} \frac{\partial^2 I}{\partial x^2} & \frac{\partial I}{\partial x} \frac{\partial I}{\partial y} \\ \frac{\partial I}{\partial x} \frac{\partial I}{\partial y} & \frac{\partial^2 I}{\partial y^2} \end{pmatrix} \quad (4.10)$$

The gradient vector ∇I is determined from (4.10) as the eigenvector corresponding to largest eigenvalue of \mathbf{J} . For this particular structure tensor, the square root of the largest eigenvalue is equal to the gradient norm $|\nabla I|$, while the second eigenvalue is equal to 0.

Extending the computation of the gradient vector to a set of input images, as it is the case in a fusion scenario, is done by constructing the structure tensor according to the Di Zenzo [Zen86] definition:

$$\mathbf{J}^S(x, y) = \begin{pmatrix} \sum_{s=1}^S \frac{\partial^2 I_s}{\partial x^2} & \sum_{s=1}^S \frac{\partial I_s}{\partial x} \frac{\partial I_s}{\partial y} \\ \sum_{s=1}^S \frac{\partial I_s}{\partial x} \frac{\partial I_s}{\partial y} & \sum_{s=1}^S \frac{\partial^2 I_s}{\partial y^2} \end{pmatrix} \quad (4.11)$$

In (4.11) the combined structure tensor \mathbf{J}^S is constructed using equal contributions from all the input images I_s , a more complex approach being proposed in [Soc00b], where the weighting coefficients are determined using an entropy function. The combined gradient vector $\nabla \tilde{I}$ of the fused image \tilde{I} is equivalent to the first eigenvector V of \mathbf{J}^S , corresponding to the largest eigenvalue of \mathbf{J}^S , the square root of this eigenvalue being called by Socolinsky “multispectral contrast”.

In brief, the variational fusion model proposed by Socolinsky works by establishing the structure of the desired fused image: in every point of the fused image, the composite gradient $\nabla \tilde{I}$ should have a magnitude equal to the absolute value of the “multispectral contrast” and the direction of V ; and then formulating a minimization problem with a solution that best approximates the desired fused image.

Since based on the decomposition of the structure tensor \mathbf{J}^S into eigenvalues and eigenvectors only the orientation of V can be determined, the corresponding direction needs to be chosen so as to be consistent with the one of the composite gradient [Soc00a]. The dominant eigenvector⁵ V of \mathbf{J}^S is expressed as:

$$V(x, y) = \operatorname{sgn} \left(V(x, y) \cdot \nabla \left[\sum_{s=1}^S I_s(x, y) \right] \right) V(x, y) \quad (4.12)$$

Since the variational fusion process is expressed as the solution of a minimization problem, the functional that requires minimizing, as proposed by Socolinsky, has the following expression:

$$\int_{\Omega} \left| \nabla \tilde{I}(x, y) - V(x, y) \right|^2 dx dy \quad (4.13)$$

and its associated Euler–Lagrange equation:

$$\Delta \tilde{I} = \operatorname{div} V \quad (4.14)$$

with Neumann boundary conditions.

For the discretization of (4.13) Socolinsky employs an explicit numerical scheme, assuming an image defined on a finite grid of $[0, X] \times [0, Y]$ with an initial “guess” \tilde{I}^0 , of the form:

$$\tilde{I}_{i,j}^{n+1} = \tilde{I}_{i,j}^n + \frac{1}{4} \left[\Delta \tilde{I}_{i,j}^n - (\operatorname{div} V)_{i,j} \right] \quad (4.15)$$

with the Laplacian of \tilde{I} classically approximated as (2.77):

$$\Delta \tilde{I}_{i,j}^n = \frac{\partial^2 \tilde{I}_{i,j}^n}{\partial x^2} + \frac{\partial^2 \tilde{I}_{i,j}^n}{\partial y^2} = D_x^- [D_x^+ (\tilde{I}_{i,j}^n)] + D_y^- [D_y^+ (\tilde{I}_{i,j}^n)] \quad (4.16)$$

where $D_{x/y}^{\pm}$ is defined as (2.66).

The divergence operator is numerically expressed using a combination of forward and backward differences, *i.e.*, forward difference approximations in expressing the derivatives within \mathbf{J}^S and backward difference approximations for expressing the actual divergence of V .

Remark It is customary in image fusion problems, when an initialization of the fused image is required, to use an \tilde{I}^0 of the form (4.1).

Remark On the proposed variational fusion model: “convergence is guaranteed regardless of the initial guess, and all solutions agree up to an overall additive constant” [SW02].

⁵The *dominant eigenvector* of a matrix is an eigenvector corresponding to the eigenvalue of largest magnitude (for real numbers, largest absolute value) of that matrix.

In the interest of computational speed, the author proposes adding to (4.15) over- and under-relaxation, in order to speed convergence [SW02], thus the previous discretization model becomes:

$$\begin{cases} \tilde{I}_{i,j}^{n+\frac{1}{2}} = \tilde{I}_{i,j}^n + \frac{1}{4} \left(\Delta \tilde{I}^n - \operatorname{div} V \right)_{i,j} \\ \tilde{I}_{i,j}^{n+1} = (1 - \omega) \tilde{I}_{i,j}^n + \omega \tilde{I}_{i,j}^{n+\frac{1}{2}} \end{cases} \quad (4.17)$$

where $0 \leq \omega \leq 2$ is a relaxation parameter, defined as:

$$\omega = \frac{2}{1 + \sqrt{1 - \rho^2}}, \quad \text{for } \rho = \frac{\cos(\pi/X) + \cos(\pi/Y)}{2} \quad (4.18)$$

for a $[0, X] \times [0, Y]$ image.

Remark According to [SW02], since the usual input images have $X, Y > 100$, the relaxation parameter ω is very close to 2, resulting in large speed improvements due to over-relaxation.

Without trying to define a fusion model that implicitly yields a denoised fused image, Socolinsky tackles the noise issue by redefining the original fusion model (4.15) in order to exhibit an inherent noise robustness. This robustness is attained by constructing the structure tensor \mathbf{J}^S using low-pass versions of the input images I_s that lead to – using the newly defined \mathbf{J}^S – the low-pass version of the fused image \tilde{I} . In obtaining the final fused result \tilde{I} , the low-pass version of the fused image is added to the mean of the high-pass versions of the input images I_s .

Remark The averaging process of the high-pass versions of I_s leads – in theory, for $S \rightarrow \infty$ – to complete noise cancellation, if the noise is assumed to be of zero mean.

4.5.2 The John–Vorontsov variational fusion model

Representing the second major contribution in variational image fusion, the John–Vorontsov model [JV05] is derived from robust error estimation theory, and amounts to obtaining the fused image \tilde{I} from the input images I_s^0 by minimizing the following functional:

$$E(\tilde{I}) = \int_{\Omega} \rho \left((x, y), \tilde{I}(x, y), |\nabla \tilde{I}(x, y)| \right) dx dy \quad (4.19)$$

where $\rho(\cdot)$ is called the *error norm*.

The error norm ρ is defined according to the requirements of the application or the nature of the degradation, e.g., for filtering out AWGN from a degraded image, one suitable choice for ρ would be a least square error norm:

$$\rho [(x, y), |\nabla I(x, y)|] = \frac{1}{2} |\nabla I(x, y)|^2 \quad (4.20)$$

Solving the minimization problem (4.19) for the least square error norm (4.20) leads to the isotropic diffusion equation (2.7), expressed as:

$$\frac{\partial I(x, y, t)}{\partial t} = \Delta I(x, y, t) \quad (4.21)$$

In addition to being a fusion paradigm, the John–Vorontsov model also exhibits inherent edge enhancement characteristics, being defined for a single input image as:

$$\frac{\partial \tilde{I}(x, y, t)}{\partial t} = \alpha \Delta \tilde{I}(x, y, t) - \beta J_I(x, y) \left[\tilde{I}(x, y, t) - I(x, y) \right] \quad (4.22)$$

where J_I is a smoothed edge map of the form:

$$J_I(x, y) = \int |\nabla I(x', y')|^2 G(x - x', y - y', \sigma) dx' dy' \quad (4.23)$$

By suppressing the diffusion term ($\alpha = 0$) and setting $\beta = 1$, the generalized John–Vorontsov fusion model, for S input images, becomes:

$$\tau \frac{\partial \tilde{I}(x, y, t)}{\partial t} = -J_s(x, y, t) \Theta(J_s(x, y, t)) \left[\tilde{I}(x, y, t) - I_s(x, y) \right] \quad (4.24)$$

where

$$\Theta(J) \begin{cases} 1 & \text{if } J \geq 0 \\ 0 & \text{if } J < 0 \end{cases} \quad (4.25)$$

and

$$J_s(x, y, t) = J_{I_s}(x, y) - J_{\tilde{I}}(x, y, t) \quad \text{with } s \in [1, S] \quad (4.26)$$

The term $J_s(x, y, t) \Theta(J_s(x, y, t))$ ((4.25) and (4.26)) ensures that only salient information is transferred to \tilde{I} , i.e., the difference between the fused result \tilde{I} and the current input image I_s is “injected” into \tilde{I} as long as $|\nabla I_s| > |\nabla \tilde{I}|$, in other words, as long as I_s contains edge information that has not yet been incorporated into \tilde{I} .

As was the case with Socolinsky’s model, here too, the initial fused image \tilde{I}^0 is a “guess” that can either be a null image, a mean of the input images I_s or the first frame of a video sequence, when the frames of such a sequence are considered to be the inputs of the fusion process. The fusion process adds with each iteration the salient information from each input image I_s weighted by a factor of $1/\tau$. According to Pop [Pop08], $1/\tau$ can be considered as the time interval during which the input image I_s is used by the fusion process, thus τ is equivalent to the total number of input images S .

Remark For the sake of clarity, it should be noted that all input images I_s are only functions of (x, y) , being static in nature, from a time evolution point of view, $I_s(x, y, t) = I_s(x, y, 0) = I_s$, for $s = \{1, \dots, S\}$.

Remark As also noted by [Pop08], the discretization time step for the John–Vorontsov model needs to be sufficiently small so as to ensure that the fused result will be within the initial dynamic range (of the input images), since this discretization step strongly depends on the difference between the quadratic norms of \tilde{I} and I_s .

4.5.3 The Wang *et al.* variational fusion model

A continuation of Socolinsky’s variational fusion model, the Wang *et al.* approach [WYTY06, WY06] improves the initial model either by integrating into the computation (according to the Di Zenzo [Zen86] definition) of the structure tensor a pertinence map, as proposed

in [WYTY06] or by using a weighted approach, adapted to the HVS, in computing the same structure tensor, as proposed in [WY07].

As also mentioned in [Pop08], the second proposed improvement requires an “excessive” user supervision and is thus, limited in application and scope.

The first proposition, *i.e.*, the integration of a pertinence map into the computation of the structure tensor, is mathematically expressed as:

$$\mathbf{J}^S(x, y) = \begin{pmatrix} \sum_{s=1}^S \alpha_s^2(x, y) \frac{\partial^2 I_s}{\partial x^2} & \sum_{s=1}^S \alpha_s^2(x, y) \frac{\partial I_s}{\partial x} \frac{\partial I_s}{\partial y} \\ \sum_{s=1}^S \alpha_s^2(x, y) \frac{\partial I_s}{\partial x} \frac{\partial I_s}{\partial y} & \sum_{s=1}^S \alpha_s^2(x, y) \frac{\partial^2 I_s}{\partial y^2} \end{pmatrix} \quad (4.27)$$

The pertinence map $\alpha(x, y)$ from (4.27) is obtained starting from a distance measure computed over the (x, y) pixel’s neighborhood W :

$$D'_s(x, y) = \frac{1}{\text{card}(W)} \sum_{(x', y') \in W} e^{-\frac{[I_s(x, y) - I_s(x+x', y+y')]^2}{\sigma^2}} \quad (4.28)$$

Based on this distance, $D'_s(x, y)$, Wang *et al.* define the local contrast as:

$$D_s(x, y) = 1 - \frac{D'_s(x, y)}{\max_{(x, y) \in \Omega} [D'_s(x, y)]} \quad (4.29)$$

The pertinence map $\alpha(x, y)$ is readily computed after a normalization of $D_s(x, y)$ within the dynamic range $[0, 1]$:

$$\alpha_s(x, y) = \frac{D_s^r(x, y)}{\sqrt{\sum_{p=1}^P D_p^{2r}(x, y)}} \quad (4.30)$$

where r is a selectivity parameter, and the $\alpha_s(x, y)$ weights are further normalized with respect to the pertinence values computed for the rest of the input images.

The aim of this weighting process, using a pertinence map $\alpha_s(x, y)$, is to compute the dominant eigenvector V of \mathbf{J}^S only based on those input images that contain pertinent information. A further improvement consists in redefining the composite gradient vector V so as to eliminate the halo effect [WYTY06]:

$$V(x, y) = \left(\frac{\gamma}{|V(x, y)|} \right)^{1-\beta} \quad (4.31)$$

where γ is a percentage of the mean gradient norms of V computed in each point of the desired fused image \tilde{I} .

Remark For the generalized scenario of noise-contaminated input images, the authors propose adding a diffusion term to the initial Socolinsky model, the new functional, describing a variational fusion model with implicit noise filtering, being expressed as [WY07]:

$$\alpha \int_{\Omega} |\nabla \tilde{I}(x, y)| dx dy + \beta \int_{\Omega} |\nabla \tilde{I}(x, y) - V(x, y)|^2 dx dy \quad (4.32)$$

4.5.4 The Pop *et al.* variational fusion model

The Pop *et al.* PDE-based fusion model, first proposed in [PLTB07, PTB⁺07] is among the first complex fusion models that *a priori* assumes the input images to be closer to real-world images, *i.e.*, noise contamination being considered as part of the fusion problem's statement.

Although the proposed model is explicitly expressed within a discrete framework, it also possesses a continuous domain expression, complying with a discrete *min-max* principle:

$$\frac{\partial I_s}{\partial t} = -\beta \cdot \operatorname{div}(\nabla I_{max}) + \gamma \cdot \operatorname{div} [g_R(\nabla I_s, \nabla I_S^0) \nabla I_s] \quad (4.33)$$

with the constraint **C1**:

$$\min_{s=1,\dots,S} [I_s^0(x, y)] \leq I_s^n(x, y) \leq \max_{s=1,\dots,S} [I_s^0(x, y)] \quad (4.34)$$

and:

$$g_R[D_x^+(I_s), D_x^+(I_S^0)] = \begin{cases} \frac{D_x^+(I_s) - \min_{s=1,\dots,S} [D_x^+(I_s^0), 0]}{D_x^+(I_s)} & \text{if } D_x^+(I_s) < \min_{s=1,\dots,S} [D_x^+(I_s^0), 0] \\ \frac{D_x^+(I_s) - \max_{s=1,\dots,S} [D_x^+(I_s^0), 0]}{D_x^+(I_s)} & \text{if } D_x^+(I_s) > \max_{s=1,\dots,S} [D_x^+(I_s^0), 0] \\ 0 & \text{otherwise} \end{cases} \quad (4.35)$$

where D_x^+ is a forward finite difference approximation, defined according to (2.66) while β and γ are a fusion weighting parameter and a regularization weighting parameter, respectively.

The Pop *et al.* PDE-based fusion model is a fusion paradigm of the type S inputs (sources) – S outputs, with a theoretical convergence of all outputs to a unique solution, *i.e.*, the fused image \tilde{I} . This convergence is numerically proven for a sufficiently large number of iterations N , to this end Pop proposing in [Pop08] two alternative discretization schemes, one of them being specifically designed to increase the convergence speed.

Remark Although, for a sufficiently large number of time iterations (of the order of tens of thousands, depending on the input images), the Pop *et al.* image fusion model exhibits a discrete convergence of its outputs toward a unique fused result \tilde{I} , in practice such a large number of iterations is not necessary in ensuring a proper noise filtering. Thus, the Pop *et al.* method will deliver in practical use, S noise filtered outputs, but fusion quality-wise there still remains the issue of a user selected unique fused result, since the S outputs are not always convergent, given a fixed number of iterations.

4.5.5 The Piella variational fusion model

The Piella variational approach embodies an image fusion method for enhanced visualization, first proposed in [Pie08] and later detailed in [Pie09]. The Piella variational model performs the fusion of an arbitrary number of images while preserving the salient information and enhancing the contrast for visualization [Pie09].

The underlying principle of this model consists in the use of a structure tensor approach to simultaneously describe the geometry of all the inputs, the basic idea being that

the fused image should have a structure tensor which approximates the structure tensor obtained from the multiple inputs. At the same time, the fused image should be “natural” and “sharp” from a human interpreter perspective [Pie09].

The fusion paradigm combines the geometry merging of the inputs with perceptual enhancement and intensity correction, all of this being achieved through a functional minimization approach which implicitly takes into account a set of human vision characteristics [Pie09].

The proposed fusion model amounts to minimizing the following functional:

$$\begin{aligned} E(\tilde{I}) = & \eta \int_{\Omega} |\nabla I(x, y) - V(x, y)|^2 dx dy + \beta \int_{\Omega} \left(I(x, y) - \frac{1}{2} \right)^2 dx dy \\ & + \gamma \int_{\Omega} (I(x, y) - I_0(x, y))^2 dx dy \\ & - \int_{\Omega} \int_{\Omega} \omega(x, y | x', y') J(I(x, y) - I(x', y')) dx dy \cdot dx' dy' \end{aligned} \quad (4.36)$$

where the composite gradient vector V is computed as:

$$V(x, y) = \sqrt{\lambda^+} v^+ \operatorname{sgn} \left(v^+ \cdot \sum_{s=1}^S w_s(x, y) \nabla I_s(x, y) \right) \quad (4.37)$$

with a possible choice for w_s [Pie08]:

$$w_s(x, y) = \frac{|\nabla I_s(x, y)|}{\sqrt{\sum_{s=1}^S |\nabla I_s(x, y)|^2}} \quad (4.38)$$

$J(\cdot)$ represents the relative lightness appearance of the pixel and it is defined such that $J'(\cdot)$ is a sigmoid-type function, e.g.,

$$J'(r) = k \arctan(\alpha r) \quad k > 0, \alpha > 1.$$

v^+ and λ^+ are the dominant eigenvector and eigenvalue, respectively of the structure tensor \mathbf{J}^S defined using (4.38) as a weighting coefficient:

$$\mathbf{J}^S(x, y) = \begin{pmatrix} \sum_{s=1}^S w_s^2(x, y) \frac{\partial^2 I_s}{\partial x^2} & \sum_{s=1}^S w_s^2(x, y) \frac{\partial I_s}{\partial x} \frac{\partial I_s}{\partial y} \\ \sum_{s=1}^S w_s^2(x, y) \frac{\partial I_s}{\partial x} \frac{\partial I_s}{\partial y} & \sum_{s=1}^S w_s^2(x, y) \frac{\partial^2 I_s}{\partial y^2} \end{pmatrix} \quad (4.39)$$

For further insight about the model’s numerical discretization and parameter choice please refer to [Pie09].

4.5.6 Other variational or quasi-variational fusion models

This section, as indicated by its title will only briefly consider other existing variational or quasi-variational methods, *i.e.*, defined using a variational framework up to a point,

meaning that the complete fusion model is a mixture between a variational approach and some other image processing technique.

Chronologically, the first fusion model from this category is the Fischer–Modersitzki [FM06] variational approach for image fusion and registration. Since the two processing steps, *i.e.*, registration and fusion, are hierarchically interconnected (registration is usually a preprocessing step in image fusion), the authors propose handling the two processing tasks using the same framework, a variational one. The targeted application domain of the Fischer–Modersitzki variational approach is medical image processing, more precisely MRI mammography.

Another important contribution to image fusion, the variational approach proposed by Ballester *et al.* in [BCI+06], is a fusion method dedicated to multispectral image fusion for satellite imagery. Multispectral image fusion, usually employs the use of a high resolution, grayscale panchromatic image and several low resolution spectral channels, and since each type of image contains complementary information, the aim is to obtain a high resolution fused image that brings the complementary information from all sources into complete synergy.

The proposed fusion model is based on the assumption that, to a large extent, the geometry of the spectral channels is contained in the topographic map of its panchromatic image. This assumption, together with the relation between the panchromatic image and the spectral channels, and the ratio between the lowest resolution and the highest resolution available, constitute the elements for constructing an energy functional whose minima will give the reconstructed spectral images at higher resolution [BCI+06].

Having the John–Vorontsov variational model as a starting point, Wang, Shui and Feng, propose in [WSF08] a quasi-variational image fusion paradigm, based on robust error estimation, expressed as a TV minimization problem coupled with wavelet domain filtering. Thus, two distinct image processing formalisms are unified under a common framework, *i.e.*, image fusion, the proposed model being expressed as a variational representation in the wavelet domain, and its aim, to perform a joint fusion–denoising task in multifocus fusion scenarios.

In the pixel domain, the problem is expressed as a weighted energy functional minimization, where the TV is used as a regularity constraint for noise reduction. The authors propose a new family of weight fusion functions, based on the local average modulus of gradients and the power transform [WSF08]. In the wavelet domain, the problem is expressed as a shrinkage of the weighted wavelet coefficients of the source images, where the weight functions are based on the local average modulus of intra- and inter-scale wavelet coefficients and the power transform [WSF08].

Another representative example for the quasi-variational approach category is Mitianoudis and Stathaki’s [MS08] proposition, consisting of a variational framework, derived from error estimation theory (the John–Vorontsov approach), combined with a cost function approach for blind restoration. The Mitianoudis–Stathaki proposition represents a combined spatial-domain joint fusion–restoration method that works by identifying the common degraded areas within the fused image and uses a regularized restoration approach to enhance the content in those areas.

4.6 Quality assessment in image fusion

Assessing the quality of the output result in image fusion, requires a slightly different approach than the traditional one, where an “ideal” image is available, and thus the quality assessment is carried out using classic means (§3.6.1). The *a priori* existence of an “ideal” reference (ground truth) image is usually conceivable only in image restoration scenarios, since, according to the definition of image restoration (§2.2) the purpose of such a process is to restore the input image to its original, unaltered state.

Since image fusion is in essence an image enhancement paradigm, and according to the definition of enhancement (§2.2) it represents an increase or improvement in quality, value or extent, the existence of an “ideal” ground truth image would defeat the purpose of performing image fusion in the first place. Because every image fusion method emphasizes certain characteristics of its inputs into its output, it is very difficult to say which of the fused results, using several fusion methods, is the “best”, since the definition of *greater quality*, according to Wald [Wal98] will depend upon the application.

Nevertheless, image fusion results can be quantified in terms of quality using dedicated quality metrics and test scenarios. Since initially image fusion was intended, and in some cases still is, to be an additional confidence parameter in human-decision systems, it is only natural to subject its quality assessment to a human user as well. According to Petrovic [Pet01], in image fusion there exist two types of quality assessment methods, from a user involvement point of view:

- **subjective quality assessment:** where the degree of quality of the fused image is decided by a group of experts, with solid knowledge and understanding of how an “ideal” result (specific to a given application and subjected to the application’s requirements) should look like. In this case, the accuracy of the assessment depends on the number of evaluators, increasing with the increase of expert opinions.
- **objective quality assessment:** the quality of the fused result is measured in terms of a number of parameters derived from the input images as well as the fused image, this assessment being performed by means of a dedicated quality metric.

Additionally, a dedicated quality metric, for image fusion quality assessment should fulfil the following requirements [Pet01]:

- to properly and accurately identify and locate the visual information both within the input images as well as within the fused image,
- to be able to extract and estimate the importance of the aforementioned visual information,
- to accurately quantify the transfer of visual information from the input images to the fused image.

The existence of such quality metrics, *i.e.*, objective quality metrics, greatly improves the fusion process, since every fusion model requires a proper parameter adjusting, according to desired output characteristics. This parameter tweaking is possible, when an objective point of reference is available and the quality of the fused result is not influenced by any subjective factors.

The downside of objective quality metrics is that, due to the broad application spectrum of image fusion as an image processing tool and to the wide range of input

images/expected fused results, it is almost impossible to establish certain universally accepted features, that would constitute visual information cues across the whole application spectrum. Defining a universal notion of pertinence that would ensure the existence of an irrefutable, universally accepted, “ideal” fused result is close to impossible, when quality in image fusion means so many things and often those things are contradictory in nature.

Over the past decade, several authors have tackled with the task of defining fusion-specific quality metrics, making the qualitative evaluation process less biased and providing a proper, objective comparative analysis between fusion methods that share similar characteristics and application spectrum.

4.6.1 The Xydeas–Petrovic quality assessment metric

Among the first dedicated image fusion quality metrics, the Xydeas–Petrovic metric, was first proposed in [XP00, Pet01] and employs a per-pixel quality assessment approach in order to compute a global quality index. The quality metric works by measuring changes in the gradient norm and differences in pixel orientation between the two images, *i.e.*, the fused image (F) and the input image (A).

In practical use, as is the case of a minimal fusion scenario of two input images (A and B), the global Xydeas–Petrovic quality index is determined using a two-step approach: first, $Q^{AF}(i, j)$ and $Q^{BF}(i, j)$ are independently computed [XP00], and second, the global quality index $Q^{AB/F}(i, j)$ is obtained through a weighted summation of the two indices $Q^{AF}(i, j)$ and $Q^{BF}(i, j)$, using as weights the pertinence maps $s^A(i, j)$ and $s^B(i, j)$ corresponding to each input image:

$$Q^{AB/F}(i, j) = \frac{\sum_{i,j} [Q^{AF}(i, j) \cdot s^A(i, j) + Q^{BF}(i, j) \cdot s^B(i, j)]}{\sum_{i,j} [s^A(i, j) + s^B(i, j)]} \quad (4.40)$$

4.6.2 The Piella quality assessment metrics

Having as template the SSIM [WBSS04] and its earlier version the UQI⁶ [WB02], Piella [Pie04] proposes several quality metrics specifically designed for image fusion quality assessment.

Since, as previously mentioned, fusion scenarios do not benefit from the existence of a reference image for quality evaluation, Piella introduces the generic concept of *saliency* $s(I|w)$, representing a measure that quantifies the pertinence of visual information for a given image I within an analysis window w . The author indicates a few possible choices for $s(I|w)$, *e.g.*, contrast, variance, entropy or gradient norm, with the possibility of using other measures, such as the one proposed by Xydeas and Petrovic [XP00].

The first image fusion quality index proposed by Piella is expressed as follows:

$$Q(I_A, I_B, I_F) = \frac{1}{|W|} \sum_{w \in W} [\lambda_{I_A}(w) \cdot Q_0(I_A, I_F|w) + \lambda_{I_B}(w) \cdot Q_0(I_B, I_F|w)] \quad (4.41)$$

where Q_0 is the Wang and Bovik’s UQI [WB02], computed between each of the input images and the fused image, over a local analysis window w .

⁶Universal image Quality Index

The first term from (4.41) quantifies the overall quality $Q(I_A, I_B, I_F)$ for the regions of the fused image I_F where the information from I_A has a higher pertinence measure than the information from I_B . Conversely, the second term of (4.41) quantifies the quality from the second input image's (I_B) point of view.

In further improving the quality assessment, Piella redefines (4.41) so as to incorporate the properties of the HVS, particularly sensitive to regions of high pertinence. To this end, a new term is added to (4.41):

$$c(w) = \max [s(I_A|w), s(I_B|w)] \quad \text{or} \quad (4.42a)$$

$$c(w) = s(I_A|w) + s(I_B|w) \quad (4.42b)$$

The redefined quality metric, called *weighted fusion quality measure* is expressed as:

$$Q_W(I_A, I_B, I_F) = \frac{1}{|W|} \sum_{w \in W} c(w) [\lambda_{I_A}(w) \cdot Q_0(I_A, I_F|w) + \lambda_{I_B}(w) \cdot Q_0(I_B, I_F|w)] \quad (4.43)$$

Using (4.42a) or (4.42b), the redefined quality metric Q_W is also appropriate for fusion results classification, an additional reason that justifies the extensive use of this metric in image fusion analysis and comparative studies.

An alternative quality metric, derived from the *weighted fusion quality measure*, takes into account the HVS's sensitivity to contours and in order to assess the quality of a fusion method it additionally requires to apply the same fusion method for the contour images I'_A and I'_B . The *edge-dependent quality index* is mathematically expressed as:

$$Q_E(I_A, I_B, I_F) = Q_W(I_A, I_B, I_F)^{1-\alpha} Q_W(I'_A, I'_B, I'_F)^\alpha \quad (4.44)$$

where α expresses the importance of the contour images in relation to the input images, being defined on the interval $[0; 1]$.

4.6.3 The *rSFe* quality assessment metric

The *rSFe*⁷ metric, proposed by Zheng *et al.* [ZEHH07] provides a different perspective for image fusion quality assessment, since it indicates if a fused image is the result of an over- or under-fusion process. Thus, the *rSFe* behaves more as fusion fidelity indicator, its ideal value being $rSFe = 0$, which means that an ideal fusion process has taken place, while an $rSFe > 0$ translates into an over-fused image, with some distortion or noise introduced. Conversely, an $rSFe < 0$ indicates an under-fused image, with loss of meaningful information. Hence, the smaller the absolute value of the *rSFe*, the better the fused image, in terms of being the result of an "ideal" fusion process.

In defining the *rSFe*, Zheng *et al.* first define the notion of spatial frequency (*SF*) [EF95, LKW01], which estimates the overall activity level of an image, being expressed as follows for an $M \times N$ input image:

$$SF = \sqrt{RF^2 + CF^2 + MDF^2 + SDF^2} \quad (4.45)$$

where the four components used in computing the spatial frequency *SF* are the row frequency *RF*, column frequency *CF*, main diagonal frequency *MDF* and the secondary diagonal frequency *SDF*.

⁷ratio of Spatial Frequency error

The use of the $rSFe$ as an image fusion metric, requires computing the spatial frequency for the fused image SF_F and, since a ground truth image is not available, estimating a desired spatial frequency measure SF_R . The SF_R computation in each pixel (i, j) is performed on a 4- or 8-neighborhood, by approximating the first order derivatives corresponding to that neighborhood.

Remark Since the $rSFe$ metric behaves as a fusion fidelity indicator, its use can be extended to supervising iterative fusion processes and ensuring an objective stopping criterion, when the $rSFe$ approaches zero [ZEH04].

The image fusion quality metrics discussed so far represent only the most representative fusion metrics, with proven efficiency and extended use in the field of image fusion. Since image fusion is a very complex and diversified image processing task, researchers in the field are continuously trying to improve, expand and diversify the mathematical tools employed in addressing this task, as well as the means of objectively assessing the quality of the obtained results. To this end, other dedicated fusion metrics have been proposed by, e.g., Cvejic *et al.* [CLBC05], Chen and Varshney [CV07], Hossny *et al.* [HNC08] or Yang *et al.* [YZWL08].

4.7 Properly choosing a reference in image fusion quality assessment

As previously pointed out, image enhancement relies on the premise that the result is “greater than the sum of its parts”, hence the enhancement factor cannot always be correctly assessed by referencing it to the input data. Furthermore, an *a priori* existing ideal reference is only conceivable for testing and validating purposes, since in practice such an approach would contradict the need of image fusion in the first place. An even more complex scenario is when the fusion formalism is designed for concurrent image enhancement and restoration.

The two interdependent issues of properly assessing the quality in image fusion scenarios and of correctly establishing a result validation scenario for concurrent enhancement and restoration scenarios, will be the main topics of this section, the experimental analysis being carried out on a synthetic ground truth image. The reason for choosing a synthetic image for this analysis is obvious, since in a controlled test scenario the existence of an “ideal” fused image is possible and furthermore, allows the use of standard quality metrics (§3.6.1) in addition to the dedicated image fusion quality metrics.

4.7.1 Experimental setting

The experimental setting (*Fig. 4.2*) intended for analyzing the various facets of image fusion quality assessment has the following characteristics:

- The fusion inputs are obtained from a single synthetic image (*Fig. 4.2a*), which, for all intents and purposes, shall be also considered the *ground truth* image.
- The experimental paradigm consists in a minimal multifocus fusion scenario, comprising two input images (*Fig. 4.2b* and *Fig. 4.2c*) that are obtained using a rotationally symmetric Gaussian low-pass filter of size 15 with standard deviation $\sigma = 5$.

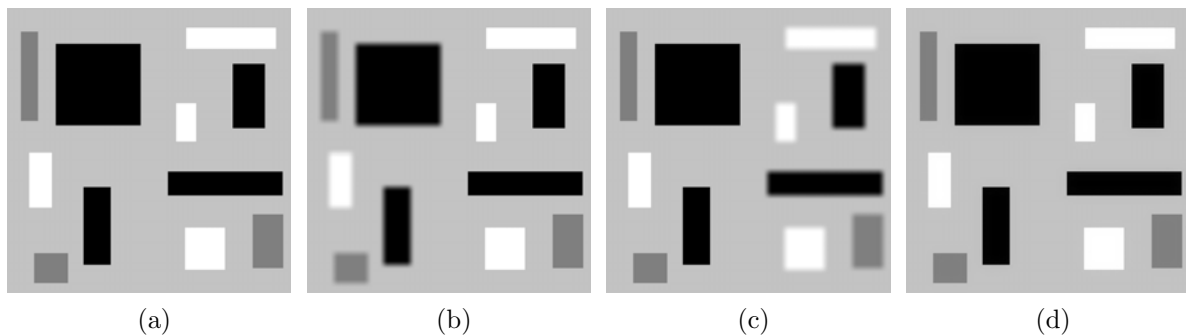


Fig. 4.2 – *Initial experimental setting: (a) Ground truth image; (b) I_1 input image; (c) I_2 input image; (d) \tilde{I} fused image.*

The input images, emulate a typical out-of-focus fusion paradigm, where the inputs describe complementary regions of the same scene in focus and out of focus, respectively.

- The fused reference (Fig. 4.2d) is obtained using Rockinger’s *fusetool* for MATLAB, available at [Roc99]. The chosen fusion method for this task is the Laplacian pyramid method (LAP) with the following input parameters: *decomposition level*=7, *high-pass combination*=saliency/match, *low-pass combination*=average(A,B) and *area* = 9.

The second part of the overall experimental setting is derived from the previous part (Fig. 4.2) and tackles the problem of concurrent image fusion and restoration, *i.e.*, denoising. The fusion inputs I_1 and I_2 are successively contaminated with an AWGN of $\sigma_n = \{0.5, 1, 2, 3, 4, 5, 10, 15, 20, 25\}$, yielding a total of ten input sets. Each set of input images, *i.e.*, $I_1^{\sigma_n}$ and $I_2^{\sigma_n}$, thus obtained, is fused using the same fusion method LAP, with the same set of input parameters, in order to ensure an unbiased fused result \tilde{I}^{σ_n} .

The experimental analysis and discussion based on the previously described experimental setting will be conducted in three-phase approach:

- Performing a standard quality evaluation of the fused results for $\sigma_n = \{0, \dots, 25\}$, using both the classic quality metrics described in §3.6.1 and the dedicated image fusion quality metrics, discussed in §4.6. The purpose of this first phase is to properly establish a fused result hierarchy, provided a ground truth image. This hierarchy will be further used as a reference for the other two phases of the analysis.
- Analyzing the importance of properly choosing the reference images when using image fusion metrics for assessing the quality of the fused result.
- Discussing how the standard fusion quality assessment is ill-posed in joint fusion–restoration scenarios.

4.7.2 Quality evaluation when a ground truth image is available

As repeatedly pointed out, the existence of a ground truth image I_{GT} in real-world image fusion scenarios is not feasible since it would contradict the principles and need of image fusion altogether. Such an assumption holds true only for synthetic images used in experimental analysis and method validation scenarios, where the ground truth (reference)

Table 4.1 – Standard qualitative analysis (when a reference image is available) results

Fused result $(I_1^{\sigma_n}, I_2^{\sigma_n}) \Rightarrow \tilde{I}^{\sigma_n}$	Quality metrics						
	RMSE	PSNR	SSIM	MSSIM	MI	VIF	VSNR
$\sigma_n = 0$	1.254	46.16	0.964	0.998	1.277	0.914	38.33
$\sigma_n = 0.5$	1.521	44.485	0.96	0.998	1.277	0.913	38.617
$\sigma_n = 1$	1.75	43.266	0.948	0.997	1.277	0.909	39.463
$\sigma_n = 2$	2.44	40.382	0.905	0.992	1.277	0.893	39.34
$\sigma_n = 3$	3.263	37.857	0.843	0.985	1.277	0.864	37.385
$\sigma_n = 4$	4.15	35.769	0.773	0.976	1.277	0.834	35.246
$\sigma_n = 5$	5.062	34.043	0.7	0.965	1.277	0.801	33.331
$\sigma_n = 10$	9.727	28.37	0.421	0.897	1.274	0.663	26.391
$\sigma_n = 15$	14.497	24.905	0.275	0.826	1.219	0.555	22.349
$\sigma_n = 20$	19.281	22.427	0.197	0.764	1.113	0.475	19.413
$\sigma_n = 25$	23.946	20.545	0.152	0.711	1.006	0.422	17.341
I_{GT}	0	∞	1	1	1.277	1	87.508

image is used in obtaining the fusion inputs, and the fused image represents an attempt to approximate as close as possible the initial, reference image.

Considering the first phase of the experimental setting described in §4.7.1, the results of the standard quality evaluation are summarized in *Table 4.1*. The overall result distribution is rather intuitive, since it is obvious that a fused result of a smaller σ_n fusion input set, will be closer to I_{GT} in terms of quality and similarity, than a fused result of a larger σ_n fusion input set.

Whenever a ground truth image is available, the quality assessment process is straightforward, the extent of this assessment depending only on the number of quality metrics used. As was the case with the experimental analysis from §3.6, the quality metrics used were part of the *MeTriX MuX Visual Quality Assessment Package* [Gau11], an extra measure in ensuring a bias-free evaluation.

Remark The I_{GT} vs. I_{GT} quality evaluation is performed in order to establish the base reference values in terms of best attainable results for each of the employed quality metrics.

4.7.3 Image fusion quality assessment in the presence of noise

When using dedicated metrics for assessing the quality of a fused image, it is important to understand the fusion process as well as its purpose. For example, the straightforward approach in defining an image fusion quality metric is to express that metric as a function of S variables, I_s , where $s = \{1, \dots, S\}$. This section will analyze when the “straightforward approach” is not well-posed, e.g., for concurrent fusion and denoising scenarios, and infer from the experimental analysis how to adapt the use of these metrics for a proper quality assessment.

Using the previously defined experimental setting, the fused results \tilde{I}^{σ_n} will be quantified in terms of quality by means of the metrics discussed in §4.7.3, employed “as is”, i.e., the quality evaluation for a given fused result \tilde{I}^{σ_n} is computed with respect to its corresponding fusion inputs $I_1^{\sigma_n}$ and $I_2^{\sigma_n}$, respectively. The quality assessment and its

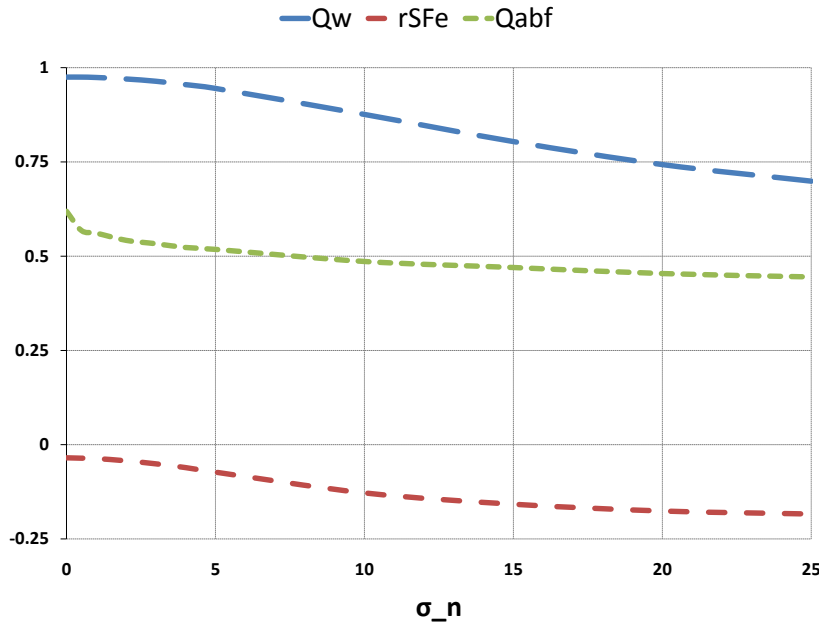


Fig. 4.3 – $(I_1^{\sigma_n}, I_2^{\sigma_n})|\tilde{I}^{\sigma_n}$ fusion quality assessment, using $Q^{AB/F}$, Q_W and $rSFe$.

evolution with respect to σ_n is illustrated in Fig. 4.3, while the measured quality metric results are summarized in Table 4.2.

Although the overall evolution, quality-wise, follows the same trend as the one indicated by the data from Table 4.1, the issue here is the improper use of the input images $I_1^{\sigma_n}$ and $I_2^{\sigma_n}$ as reference images. For noise-free fusion scenarios, a straightforward use of the image fusion quality metrics will usually suffice and, moreover, provide accurate data in terms of measured quality. For the more complex scenario of joint fusion–restoration paradigms, logic dictates that the proper reference images I_A and I_B , for all measured fused results \tilde{I}^{σ_n} , should be $I_1^{\sigma_n=0}$ and $I_2^{\sigma_n=0}$ since these input images are also noise-free and would provide a proper reference in terms of quality assessment, restoration-wise, in addition to fusion-wise. The quality assessment and its evolution with respect to σ_n , performed following the previously described line of reasoning, is illustrated in Fig. 4.4, while the measured quality metric results are summarized in Table 4.3.

Table 4.2 – Image fusion qualitative analysis results for the $(I_1^{\sigma_n}, I_2^{\sigma_n})|\tilde{I}^{\sigma_n}$ scenario

Quality metrics	Fused result for σ_n					
	0	0.5	1	2	3	4
Q_W	0.975	0.975	0.974	0.97	0.964	0.955
$rSFe$	-0.035	-0.036	-0.037	-0.043	-0.051	-0.061
$Q^{AB/F}$	0.619	0.568	0.561	0.542	0.533	0.523
	...continued σ_n					
	5	10	15	20	25	
Q_W	0.945	0.876	0.804	0.743	0.699	
$rSFe$	-0.073	-0.128	-0.158	-0.176	-0.184	
$Q^{AB/F}$	0.518	0.486	0.47	0.454	0.445	

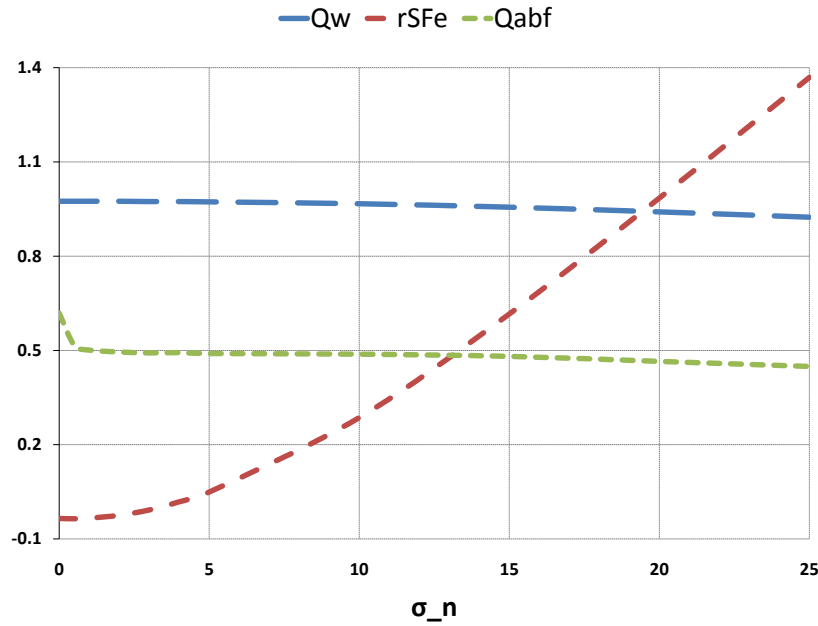


Fig. 4.4 – $(I_1^{\sigma_n=0}, I_2^{\sigma_n=0})|\tilde{I}^{\sigma_n}$ fusion quality assessment, using $Q^{AB/F}$, Q_W and $rSFe$.

The difference between the two approaches (Fig. 4.3 and Fig. 4.4) can be quantified in terms of *relative error* δx :

$$\delta x = \frac{x_0 - x}{x} \quad (4.46)$$

where x is the true value of a quantity and x_0 is the inferred or measured value. The relative error for the two quality assessments is illustrated in Fig. 4.5.

Upon analyzing the measured data from the two quality assessment scenarios (Table 4.2 and Table 4.3) and the evolution of the relative error (Fig. 4.5), the following conclusions can be formulated:

- The use of an improper set of reference images I_A and I_B can equally lead to an over- or under-assessment in terms of quality, especially when the fusion process is accompanied by a parallel restoration process.
- In terms of robustness, the Piella quality metric Q_W proves to possess a systematic

Table 4.3 – Image fusion qualitative analysis results for the $(I_1^{\sigma_n=0}, I_2^{\sigma_n=0})|\tilde{I}^{\sigma_n}$ scenario

Quality metrics	Fused result for σ_n					
	0	0.5	1	2	3	4
Q_W	0.975	0.975	0.975	0.975	0.974	0.974
$rSFe$	-0.035	-0.036	-0.034	-0.025	-0.008	0.018
$Q^{AB/F}$	0.619	0.517	0.501	0.495	0.492	0.493
	...continued σ_n					
	5	10	15	20	25	
Q_W	0.973	0.967	0.956	0.941	0.924	
$rSFe$	0.049	0.286	0.616	0.985	1.369	
$Q^{AB/F}$	0.49	0.488	0.481	0.465	0.449	

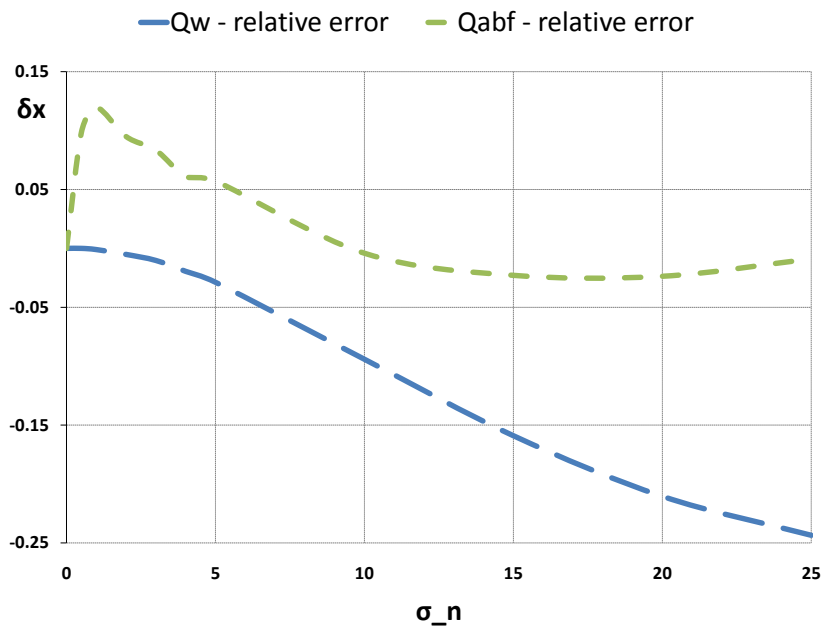


Fig. 4.5 – Q_W and $Q^{AB/F}$ relative error between assessing the image quality for $(I_1^{\sigma_n}, I_2^{\sigma_n}) | \tilde{I}^{\sigma_n}$ as opposed to assessing the quality for $(I_1^{\sigma_n=0}, I_2^{\sigma_n=0}) | \tilde{I}^{\sigma_n}$.

bias (Fig. 4.5) when improperly used. Nevertheless, this systematic bias follows the right evolution pattern and, in fact, when improperly used (Fig. 4.3) it proves detrimental to the true efficiency of the analyzed method, since it has the tendency to under-evaluate the fused result's quality. Conversely, the Xydeas–Petrovic quality metric $Q^{AB/F}$, does not possess the same systematic bias as Q_W , over-evaluating the fused result's quality for small values of σ_n and under-evaluating the fused result's quality for large values of σ_n , when improperly using the $(I_1^{\sigma_n}, I_2^{\sigma_n})$ input set as reference images.

Remark Usually, the $rSFe$ metric is less relevant in terms of fused result quality, especially when trying to assess a fused & restored image, since it evaluates a fused result from a fidelity point of view, this fidelity being expressed in terms of under- or over-fused results.

Remark The reason why the fused result of the proposed experimental setting scores so high on the Piella quality metric scale, even for high AWGN levels, can be explained from two perspectives:

1. The nature of the synthetic image: the synthetic image proposed in the initial experimental setting is very simple in terms of composition and geometry and the contamination (out-of-focus blurring or AWGN contamination) has not been taken to an extreme, since this was not the purpose of the experimental analysis.
2. The HVS is less sensitive to noise than is to other types of perturbations, such as blur. The Piella quality metric Q_W was specifically defined to emulate the responses of the HVS, being defined on the principles of the UQI [WB02], another quality metric designed to emulate the HVS and to place emphasis on structural visual information and overall image geometry when quantifying visual quality.

4.7.4 Image fusion quality assessment for joint fusion–restoration scenarios

The last point of this discussion on how to properly assess image fusion quality, is constructed on the following prerequisites: considering the same experimental setting (Fig. 4.2) it is assumed that $\tilde{I}^{\sigma_n=0}$ is the result of a concurrent fusion and denoising process, which has as inputs any of the image pairs $(I_1^{\sigma_n}, I_2^{\sigma_n})$, with $\sigma_n = \{0, \dots, 25\}$. For the sake of example, a particular instance of how the restoration process is emulated, assumes $\tilde{I}^{\sigma_n=0}$ to be the fused result of the image pair $(I_1^{\sigma_n=5}, I_2^{\sigma_n=5})$, where in this case the image pair in question is considered to be the only existing reference, not part of a gradual contamination process, like before. In other words, $I_1^{\sigma_n=5}$ and $I_2^{\sigma_n=5}$ are in this case $I_1^{\sigma_n=0}$ and $I_2^{\sigma_n=0}$ from an input reference point of view.

In practical use this is often the case, because seldom images are “ideal”, and even when they are assumed to be so, they may contain noise from various sources, e.g., acquisition, transmission, storage, compression, etc. For small values of σ_n the influence of noise on the quality evaluation is negligible, but even this aspect is open for debate, since there does not exist a universally accepted definition of how much or how little noise is negligible.

The purpose of the following analysis is to raise the still open question of how to correctly assess the quality of a joint fusion–restoration process using existing quality metrics, when neither an “ideal” fused image, nor the “ideal” inputs exist or are available.

Considering the latest experimental setting and the redefined relation between $\tilde{I}^{\sigma_n=0}$ and any of the $(I_1^{\sigma_n}, I_2^{\sigma_n})$ input sets, the quality assessment process will exhibit a gradually increasing evaluation bias, directly proportional to σ_n . This evaluation error is illustrated in Fig. 4.6 and quantitatively summarized in Table 4.4.

Assuming the $(I_1^{\sigma_n=0}, I_2^{\sigma_n=0})|\tilde{I}^{\sigma_n=0}$ scenario as the only well-posed joint fusion–restoration

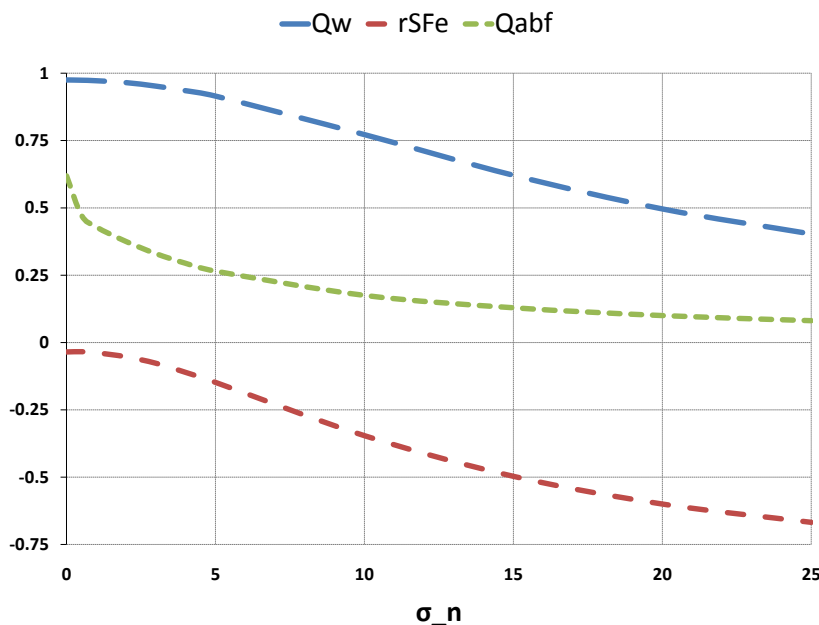


Fig. 4.6 – Quality assessment for a joint fusion–restoration process.

Table 4.4 – Quality assessment for a joint fusion–restoration process - experimental data

Quality metrics	Fused result for σ_n					
	0	0.5	1	2	3	4
Q_W	0.975	0.974	0.972	0.965	0.952	0.935
$rSFe$	-0.035	-0.034	-0.038	-0.053	-0.077	-0.111
$Q^{AB/F}$	0.619	0.473	0.429	0.375	0.33	0.294
		...continued σ_n				
		5	10	15	20	25
Q_W		0.915	0.772	0.621	0.496	0.403
$rSFe$		-0.148	-0.346	-0.497	-0.6	-0.668
$Q^{AB/F}$		0.265	0.175	0.129	0.1	0.081

situation, a relative error (4.46) can be expressed in terms of well-posed scenario vs. ill-posed ones.

Remark By analyzing the evolution of the relative error (Fig. 4.7), for Q_W and $Q^{AB/F}$, with respect to σ_n , the following conclusions are readily available:

- In a concurrent fusion–restoration process, if the input images are used as references in quality assessment, even when the noise contamination is otherwise considered negligible, the fused result will be under-evaluated by the Q_W and $Q^{AB/F}$ quality metrics.
- In this case, both metrics exhibit a systematic error, which leads to an under-evaluation irrespective of the noise level present in the input images.
- The relative error is substantially greater than the relative error present when using an improper set of reference images (Fig. 4.5).

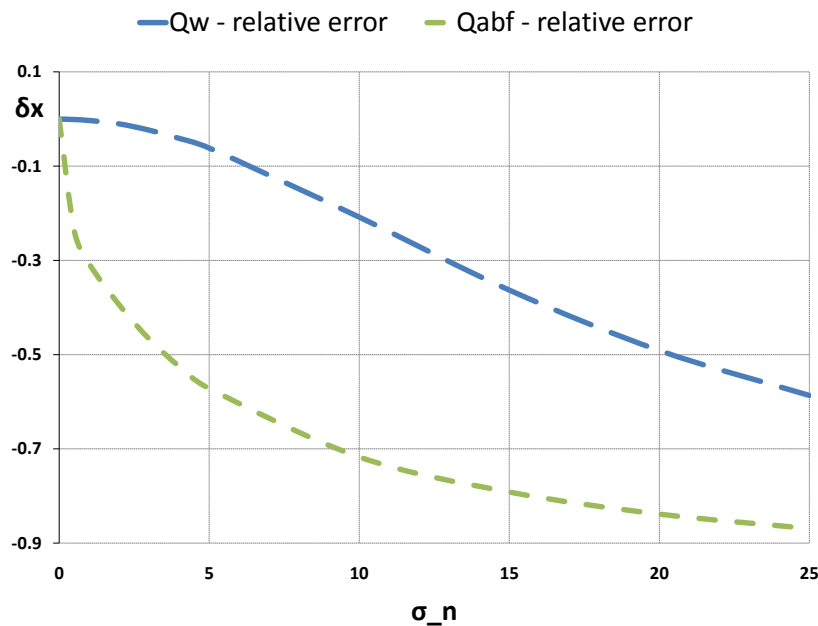


Fig. 4.7 – Q_W and $Q^{AB/F}$ relative error for a joint fusion–restoration scenario ($I_1^{\sigma_n=0}, I_2^{\sigma_n=0}$) | $\tilde{I}^{\sigma_n=0}$.

Remark Summing up all previous conclusions and based on the previously discussed test scenarios (§4.7) the following inference can be made: given a set of input images suited for an image fusion scenario and additionally contaminated by noise of a less than negligible σ_n , a concurrent fusion–restoration approach is required in order to further increase the quality of the resulting fused image. Assessing the quality of this fused image and implicitly of the concurrent fusion–restoration approach to the fullest extent of its performances is not always possible since the existing quality metrics under-evaluate the fused result in terms of quality, when the reference images are far from “ideal”. Nevertheless, an adequate approximation of the actual performances of such image processing paradigms is possible, provided an extensive quality assessment, employing a sufficiently large and varied number of quality metrics, coupled with the existence of “quasi-ideal” reference images.

4.8 Conclusion

As the chapter that bridges the two core concepts of image restoration and image enhancement, **Chapter 4** fulfils its intended purpose by providing a basic understanding of the field of image fusion, in terms of definitions, classifications, purpose and established methodology but at the same time it offers a functional insight into the family of variational and PDE-based approaches to image fusion. Without these fundamental notions, the following chapter, *i.e.*, **Chapter 5**, would be missing its theoretical and functional background, making its understanding cumbersome and out of proper context.

Moreover, the second part of this chapter, intended as an experimental analysis, raises the important questions of quality assessment in image fusion, and how well is this assessment suited for even more complex task, such as the combined task of fusion and denoising. Through a practical example it is shown just how much the entire quality assessment paradigm shifts when introducing noise in the “equation” and how, otherwise valid test scenarios, prove to be erroneous when employed in their default form to assess the quality for joint fusion–denoising image processing models.

Although, the discussion from §4.7, raises a few pertinent questions, complex both in form and in substance, it also provides the necessary guidelines on how to successfully overcome the obstacles of quality assessment in complex scenarios such as the joint fusion–denoising one. These questions alone would make the subject of at least another chapter, but since the main interest of this thesis is focused on image restoration and enhancement methods, the issue of proper quality assessment falls outside the scope of this thesis.

C 2 C

Image fusion: a short introduction – §4.2 – provided a necessary overview of the *fusion* in the context of image processing, more specifically image enhancement. As already pointed out, the main challenge in constructing this manuscript consisted, even from the beginning, was to bring together all the required prerequisites for the proper presentation and understanding of the work described within. Thus, the challenging part was to establish a balance between too much information and not enough information. Since this thesis covers both image restoration and image enhancement, it was difficult to present the necessary terminology within a single

chapter, comprising fundamental notions about *diffusion*, *deblurring* and *image fusion*, without creating confusion and forcing the reader to revisit this single chapter each time it moved on from one image processing paradigm to another.

Definitions and classifications – §4.3 – recalling on the last paragraphs of this section: the purpose of the presented definitions and classifications was to properly determine and position the proposed fusion method, detailed in **Chapter 5**, in order to correctly juxtapose it against the existing fusion methodology. This was an extremely important issue in the comparative analysis since comparing methods of different levels of complexity, e.g., pixel-level with decision-level, does not provide an adequate amount of relevancy, being like comparing apples and oranges.

Methodology in image fusion – §4.4 – provided a short presentation of the most commonly used techniques in image fusion, not being intended to cover the entire methodology from a theoretical understanding point of view. The purpose of this section was to provide an overview of the methods that will be further used in the comparative analysis from **Chapter 5** by briefly describing the main characteristics of the compared methodology. It is this author's belief that for the sake of thoroughness, any comparative analysis should contain a brief presentation of the compared methods (the existing ones) and not just to limit the discussion to the proposed method and then simply present the results of the comparative analysis, without placing the compared methodology into proper context.

Variational and PDE-based approaches to image fusion – §4.5 – the necessity and relevance of this section needs to be understood from the following perspectives:

- provided the theoretical prerequisites in understanding variational and PDE-based methodology in image fusion, serving as a starting point for the proposed fusion paradigm (**Chapter 5**).
- as for the previous section, it briefly discussed the existing methodology required for the comparative analysis.
- it tried to assemble into a short presentation all known (to this day and to the best of this author's knowledge) variational and PDE-based fusion techniques, since image fusion by means of variational and PDE-based methods is a rather new concept, with both interesting and promising results.

Quality assessment in image fusion – §4.6 – although image fusion results can be qualitatively assessed to some extent (depending on the initial fusion scenario) by standard objective image quality metrics (§3.6.1), more exactly quality metrics that require a reference image, there exist also dedicated quality metrics that use as reference the input images, being specifically designed for image fusion purposes. A proper understanding of these dedicated metrics was required, since for the proposed fusion model, even these quality metrics are not entirely adequate (the proposed fusion paradigm being design for concurrent fusion and denoising).

Properly choosing a reference in image fusion quality assessment – §4.7 – it provided a discussion using a practical example on how to properly choose the reference images in image fusion quality evaluation, with emphasis on the particular case of fusing noisy images. In this case, the customary way of choosing the references

as the initial, input images is no longer suitable, since the fused result will be theoretically an improved version of the inputs (noise-wise) and comparing a denoised result to a noisy, initial image, is not relevant in terms true method efficiency.

In a sense, this section can be viewed as a *secondary contribution of this thesis*, since it raised the question of properly assessing image fusion, when the fused result is also restored (denoised), via the fusion process. In the context of today's more complex image fusion methods, properly assessing the quality of the results is of paramount importance, since the traditional assessment will almost always underassess denoised results, as shown in §4.7.

CHAPTER 5

A variational approach for concurrent image fusion and denoising

Main Contents

5.1	Motivation	107
5.2	Theoretical prerequisites	108
5.3	Mathematical model	112
5.4	Experimental analysis	122
5.5	Potential application areas	143
5.6	Conclusion	148

5.1 Motivation

The fifth chapter of this thesis presents the second major contribution of the work carried out in partial fulfilment of the requirements for the degree of *Doctor of Philosophy*, unifying two extremely important areas of image processing, *i.e.*, image restoration and image enhancement.

This chapter represents the natural evolution in terms of addressed research topics, from image restoration (**Chapter 2**), via image restoration coupled with edge enhancement (**Chapter 3**) to concurrent image enhancement and restoration (**Chapter 4** and **Chapter 5**).

As discussed at length in the previous chapter, image fusion aims at extracting and synthesizing information from multiple sources, *e.g.*, multisensor, multifocus or multi-frame, in order to produce a more accurate, more reliable composite result.

The assumption that the input sources contain only useful information, pertinent to the desired fused output, does not hold true more often than not. A common contaminant in many image fusion scenarios is noise, originating from various sources such as data transmission, storage, compression or quantization. Preconditioning an image fusion application with the aforementioned assumption often leads to falling short of maximizing the output information of “greater quality”, as defined by Wald [[Wal98](#)]. In practice, input images are frequently subjected to noise contamination from various sources, and *a priori* considering noise-free inputs will fail to produce “the best” attainable results. Further discussion and analysis (§5.4.1) is required to stress why a sequential approach to denoising and fusion is not always possible nor does it lead to the best attainable fusion outcome.

In this chapter the image fusion issue is being addressed from a complex, joint fusion–denoising point of view, employing a fusion model for concurrent image fusion and denoising, defined using a variational framework and concepts derived from robust error estimation theory. The model’s desired behavior is attained through its implicit

anisotropic design, equally reflected in its edge enhancement and its denoising capabilities. Considering the criteria for discriminating between various types of image fusion paradigms (§4.3), the proposed image fusion model can be classified as a non-multiscale-decomposition-based, nonlinear fusion method. Complexity-wise the model falls between image-level and feature-level fusion, since fusing edge map-level information is considered to be a feature-level fusion process.

In recent years, several approaches, described in [Pha01, PLTB07, PTB⁺07, MS08, Pop08, WSF08], variational or non-variational, were proposed to tackle the intricate fusion–denoising problem, the majority of them employing a PDE-based framework to achieve this desideratum. Such a framework is ultimately a natural choice for the complex and intertwined task of concurrent image fusion and denoising, since the use of PDEs in image processing covers both image enhancement and image restoration, providing valuable tools for the two image processing tasks.

The proposed fusion model adds to the existing paradigms increased noise robustness (through anisotropic noise filtering) and edge enhancement, improving salient feature detection and preservation. All of this is accomplished using a variational PDE-based approach, numerically expressed by means of an approximation scheme that strengthens the implicit anisotropic filtering and edge-enhancing characteristics of the theoretical model.

The experimental analysis is aimed at thoroughly testing and proving the model’s robustness to noise, on the one hand, and performing a comparative evaluation of the proposed model employing some of the most representative, well-established image fusion models (variational or otherwise), on the other. The quality assessment is carried out using an extensive set of quality metrics (§4.7.3 and §4.6), both requiring and not requiring a ground truth (reference) image. Based on the measured results, conclusions are drawn, and potential applications and further work are presented.

5.2 Theoretical prerequisites

In order to facilitate the theoretical understanding of the proposed image fusion model certain theoretical concepts need to be *a priori* defined and discussed, with emphasis on two notions:

- *error estimation theory* and
- *vector orientation estimation*

The first notion is directly related to how the mathematical model describing the proposed joint fusion–denoising paradigm is formulated, sharing common elements with John and Vorontsov’s [JV05] model and all subsequent fusion models derived from it, *i.e.*, [MS08] and [WSF08]. The second theoretical concept is associated with the particular way in which the mathematical model is numerically expressed, representing one possible choice among the existing ones.

5.2.1 Error estimation theory: an overview

Following the guidelines established by John and Vorontsov in their seminal work on image fusion through TV minimization [JV05], the proposed model is formulated on the same

TV minimization principle of establishing a parallel between the fused image \tilde{I} and the recovered version I_r of an initial image I from error estimation theory. The fundamental difference between the original approach and the proposed one consists in the fact that the latter indirectly links \tilde{I} to I_r through fusion weights, ultimately describing the fusion process as a linear combination of the fusion inputs I_s , each having its own corresponding weight w_s [MS08].

Let $I: \Omega \rightarrow \mathbb{R}$ be a degraded observed image and $I_r(x, y)$ the recovered version of $I(x, y)$, where (x, y) refers to the pixel of coordinates (x, y) within the image space $\Omega \subset \mathbb{R}^2$. The recovered image $I_r(x, y)$ can be estimated, using error estimation theory, by means of an error functional $E(I_r)$ that expresses the difference between the original image and the estimated one, as a function of I_r :

$$E(I_r) = \int_{\Omega} \rho((x, y), I_r(x, y), |\nabla I_r(x, y)|) dx dy \quad (5.1)$$

where Ω is the image support and $\nabla I_r(x, y)$ is the image gradient vector in (x, y) . The error norm ρ is defined according to the requirements of the application or the nature of the degradation, e.g., for filtering out AWGN from a degraded image, one suitable choice for ρ would be a least square error norm.

The extremum of (5.1) is estimated using the Euler–Lagrange equation, satisfied by a function f of parameter u that extremizes the following functional:

$$E(f) = \int F(u, f(u), f'(u)) du \quad (5.2)$$

where F is a given function with continuous first order partial derivatives. The Euler–Lagrange equation can be described using an ODE¹ of variable u that extremizes $E(f)$:

$$\frac{\partial}{\partial f(u)} F(u, f(u), f'(u)) - \frac{d}{du} \frac{\partial}{\partial f'(u)} F(u, f(u), f'(u)) = 0 \quad (5.3)$$

Thus, using (5.3) the extremum of (5.1) can be analogously derived, leading to an Euler–Lagrange equation of the form:

$$\frac{\partial \rho}{\partial I_r} - \nabla \left(\frac{1}{|\nabla I_r|} \frac{\partial \rho}{\partial |\nabla I_r|} \nabla I_r(x, y) \right) = 0 \quad (5.4)$$

A closed-form solution $I_r(x, y)$ is obtainable from (5.4), but not in a straightforward manner, the estimation of I_r being performed using numerical optimization methods, such as gradient descent optimization. Hence, I_r can be iteratively estimated using the following update rule:

$$I_r(x, y, t + 1) \leftarrow I_r(x, y, t) - \tau \frac{\partial I_r(x, y, t)}{\partial t} \quad (5.5)$$

where t is the time evolution parameter, τ the optimization step size, and:

$$\frac{\partial I_r(x, y, t)}{\partial t} = -\frac{\partial \rho}{\partial I_r} + \nabla \left(\frac{1}{|\nabla I_r|} \frac{\partial \rho}{\partial |\nabla I_r|} \nabla I_r(x, y, t) \right) \quad (5.6)$$

with initial condition $I_r(x, y, 0) = I(x, y)$.

Remark The time evolution of (5.6), through the gradient descent optimization method, will iteratively continue until a given minimization criterion is satisfied. In practice, only a finite number of iterations are required for obtaining visually satisfactory results [JV05].

¹Ordinary Differential Equation

5.2.2 Vector orientation estimation using Principal Component Analysis

Let $I : \Omega \subset \mathbb{R}^2 \rightarrow \mathbb{R}$ be a real-valued image function and $\nabla I = (I_x, I_y)^T$ the gradient vector of I at pixel of coordinates (x, y) . In order to define the notion of orientation, the image function I is assumed to be continuous or piecewise continuous, thus differentiable. The orientation associated with any given pixel of coordinates (x, y) is defined *modulo* π as follows:

$$\begin{aligned} \theta(x, y) &= \left(\arg(\nabla I) + \frac{\pi}{2} \right) \bmod \pi \\ &= \left(\arctan \frac{I_y}{I_x} + \frac{\pi}{2} \right) \bmod \pi, \quad \theta(x, y) \in [0, \pi] \end{aligned} \quad (5.7)$$

Remark The orientation θ , as defined in (5.7), has meaning only for non-zero gradient vectors. For null gradient vectors, describing homogeneous regions of the image, a given value (by convention) will be associated with θ .

A more robust and reliable way of describing the orientation associated with a given vector, belonging to a vector field, is through PCA (Fig. 5.1), as thoroughly explained in [Don99]. In order to determine θ by means of PCA, a 2×2 symmetrical covariance matrix is constructed in each point of the vector field:

$$M = \begin{pmatrix} m_{11} & m_{12} \\ m_{12} & m_{22} \end{pmatrix} \quad (5.8)$$

and using its eigenvalues, the orientation of the first eigenvector (θ_η) can be computed as follows:

$$\theta_\eta = \arctan \left(\frac{m_{22} - m_{11} + \sqrt{(m_{11} - m_{22})^2 + 4m_{12}^2}}{2m_{12}} \right) \quad (5.9)$$

θ_η represents the orientation of the gradient vector ∇I , or more precisely of the η direction, but working in an anisotropic manner requires the use of the ξ direction, orthogonal to η , which describes the structure's (edge's) geometry. Since ξ is orthogonal to η , θ_ξ is expressed as:

$$\theta_\xi = \left(\theta_\eta + \frac{\pi}{2} \right) \bmod \pi \quad (5.10)$$

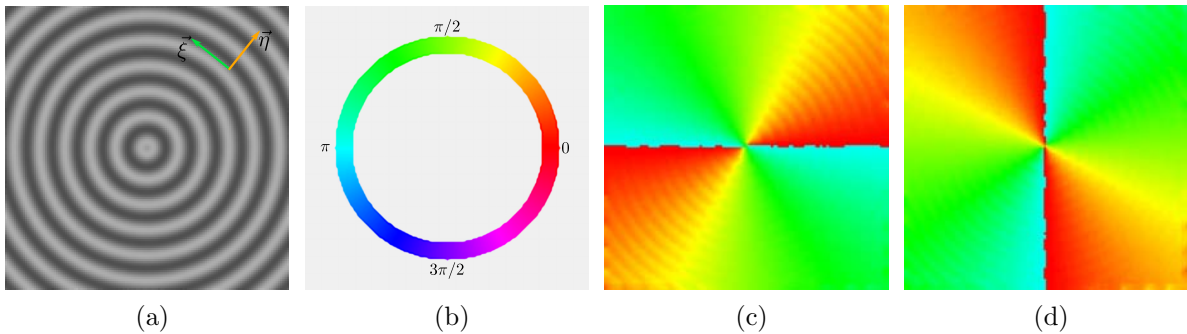


Fig. 5.1 – Vector orientation estimation using a PCA of rectangular support and fixed size $W_{PCA} = 5$: (a) Grayscale **concentric circles** synthetic image; (b) Orientation color map; (c) θ_η orientation map; (d) θ_ξ orientation map.

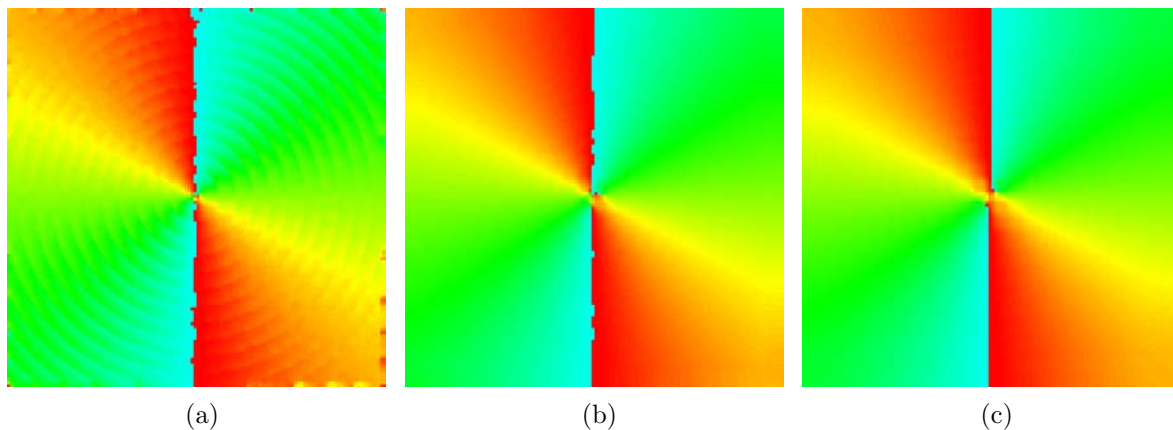


Fig. 5.2 – Vector orientation estimation using a PCA of rectangular support – multiscale characteristic example: θ_ξ orientation map for (a) $W_{PCA} = 3$, (b) $W_{PCA} = 11$ and (c) $W_{PCA} = 21$.

For specific details on how to construct the covariance matrix M (5.8) given the gradient vector field information, and other PCA-related issues in orientation estimation problems, please refer to [Don99].

In computing θ_η and consequently θ_ξ a PCA of rectangular support and fixed size W_{PCA} was performed in each pixel. Moreover, as pointed out by Terebes in [Ter04], the variable size of the PCA window behaves like a multiscale decomposition process, and hence the orientation estimation exhibits a multiscale characteristic as illustrated in Fig. 5.2.

Working with a PCA of rectangular support is only one of the available choices, a circular support that weights the pixels within the analysis window $W(x, y)$ according to their distance from the central pixel (x, y) is readily obtainable from (5.8) by applying a Gaussian smoothing, component-wise, to the original covariance matrix M . The resulting rotation-invariant circular support is defined as:

$$M^* = \begin{pmatrix} G_\rho * m_{11} & G_\rho * m_{12} \\ G_\rho * m_{12} & G_\rho * m_{22} \end{pmatrix} \quad (5.11)$$

Remark As noted by [Ter04], the choice between a PCA of rectangular support² and one of circular support involves a trade-off between noise robustness and improved estimation, respectively. That is, a circular support increases the accuracy of the orientation estimation, for noise-free images, while the rectangular support is better suited for noisy images, where the equal weights of the pixels within the analysis window $W(x, y)$ are more efficient at diminishing the influence of isolated noisy pixels.

A more computationally demanding approach would be to perform a variable-size PCA in each point of the vector field, thus making use of the PCA's multiscale property of better adapting the size of the analysis window $W(x, y)$ to the vector field's local geometry. Such an approach, *i.e.*, a multiscale PCA, requires a confidence measure that objectively quantifies the confidence level of an estimation and properly discriminates between all available estimations, in order to select the most appropriate of them with respect to the

²were all the pixels have the same contribution, *i.e.*, the same weight

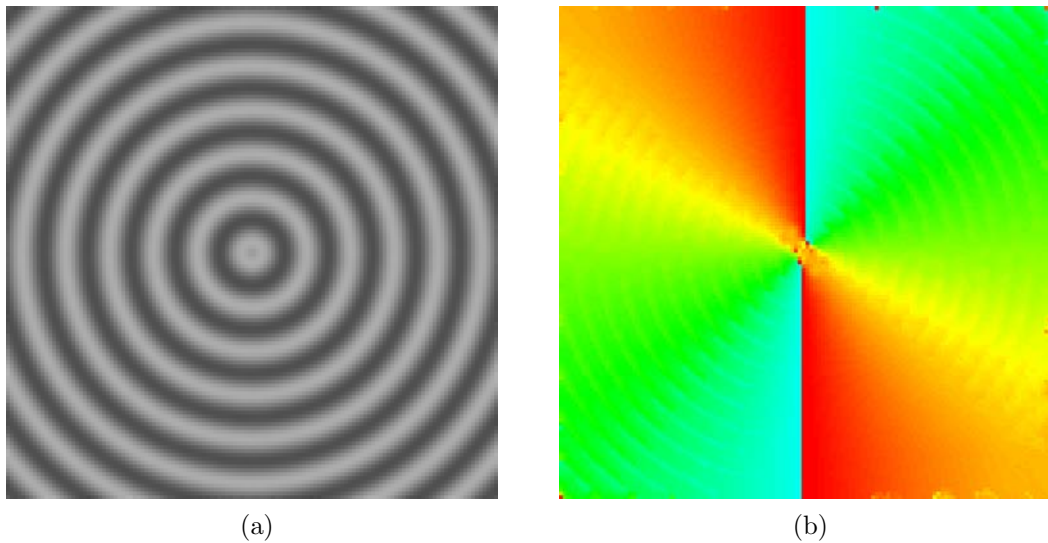


Fig. 5.3 – Vector orientation estimation using a multiscale PCA: (a) Grayscale *concentric circles* synthetic image; (b) θ_ξ – the result of a multiscale PCA.

local geometry within the analysis window $W(x, y)$. One possible choice for this coherence measure is Rao's coherence measure [RS89, Rao90, RS91]:

$$\text{coh}(\hat{\theta}(x, y)) = \frac{\sum_{(i,j) \in W(x,y)} |\nabla I(x_i, y_j)| \cdot \cos^2(\hat{\theta}(x_i, y_j) - \hat{\theta}(x, y))}{\sum_{(i,j) \in W(x,y)} |\nabla I(x_i, y_j)|} \quad (5.12)$$

where $\hat{\theta}(x, y)$ is the orientation estimate corresponding to the current pixel (x, y) , the center of the analysis window $W(x, y)$.

The multiscale PCA estimation (Fig. 5.3b) yields in each point (x, y) the orientation $\theta(x, y)$ for which $\text{coh}(\hat{\theta}(x, y))$ is maximum, thus ensuring a more accurate representation of the local geometry in terms of vector orientation.

5.3 Mathematical model

Having covered the necessary theoretical prerequisites in §5.2, this section focuses on the mathematical formalization of the proposed variational model for concurrent fusion and denoising from two complementary perspectives:

- *continuous domain definition* and
- *numerical discretization*

Although some image processing models are formalized directly within a discrete framework, the proposed model, being variational in nature, is described using a continuous framework, which, through proper numerical approximations, can be successfully expressed in discrete terms. In the present case, for this particular model, the numerical approximation is just as important as the actual theoretical definition, since it provides a considerable increase in performance by consolidating and enhancing the intrinsic anisotropic characteristic of the theoretical model.

5.3.1 Concurrent image fusion and denoising: a variational approach

Continuing the discussion about error estimation and error norms from §5.2.1, one possible choice for ρ from (5.1) is the *least square error norm*, expressed as:

$$\rho((x, y), |\nabla I_r(x, y)|) = \frac{1}{2} |\nabla I_r(x, y)|^2 \quad (5.13)$$

The above error norm provides a simple, straightforward way of filtering AWGN in an isotropic manner, being a function of $|\nabla I_r(x, y)|$, but not explicitly of the image itself.

From an image fusion point of view, a more suitable error norm would be one that combines AWGN filtering with edge enhancement, since the aim of a fusion process is to transfer salient features from the input images to the fused result.

In image fusion, as previously stated, saliency is defined as edge information, thus, the fusion process is aimed at enhancing and highlighting this type of information. Such an error norm, for noise filtering and edge enhancement, was proposed and used by [JV05, WSF08, MS08]:

$$\begin{aligned} \rho((x, y), I_r(x, y, t), |\nabla I_r(x, y, t)|) &= \frac{\alpha}{2} |\nabla I_r(x, y, t)|^2 \\ &+ \frac{\beta}{2} J_I(x, y) [I_r(x, y, t) - I(x, y)]^2 \end{aligned} \quad (5.14)$$

where α and β are constants that control the level of noise filtering and edge enhancement respectively, while J_I is a Gaussian smoothed edge map of the form (4.23):

$$J_I(x, y) = \int |\nabla I(x', y')|^2 G(x - x', y - y', \sigma) dx' dy' \quad (5.15)$$

where G is a zero-mean Gaussian function of standard deviation σ .

Application-wise, isotropic filtering is not suitable for practical use in image processing since it destroys salient information in the form of edges and structures [Ter04]. Conversely, anisotropic filtering has been for some time the method of choice in image processing, for various processing tasks, from image restoration to image enhancement, edge detection or image segmentation. The same desiderata apply for image fusion, since the end purpose is to properly detect and fuse salient features, in the form of edges and structures. This task can be best accomplished by anisotropically processing and filtering the input information, in this case the input images.

To this end, the proposed variational fusion model is defined using an anisotropic error norm that better responds to the needs of image fusion, both in terms of noise filtering and of edge enhancement:

$$\begin{aligned} \rho((x, y), I_r(x, y, t), |\nabla I_r(x, y, t)|) &= -\frac{\alpha}{2} \frac{|\nabla I_r(x, y, t)|^2}{\nabla I_r(x, y, t)} \nabla^{-1} [\mathfrak{D}_a(I_r(x, y, t))] \\ &- \frac{\beta}{2} J(x, y, t) [I_r(x, y, t) - I(x, y)]^2 \end{aligned} \quad (5.16)$$

where ∇^{-1} is the inverse *del* operator and $J(x, y, t) = J_I(x, y) - J_r(x, y, t)$ is the gain

function first introduced by [JV05], redefined in an anisotropic manner as follows:

$$\begin{aligned} J(x, y, t) = & \int |\dot{\nabla} I(x', y')| G(x - x', y - y', \sigma_{em}) dx' dy' \\ & - \int |\dot{\nabla} I_r(x', y', t)| G(x - x', y - y', \sigma_{em}) dx' dy' \end{aligned} \quad (5.17)$$

where $\dot{\nabla}$ is the gradient along the η direction, with $\vec{\eta} = \nabla I_r / |\nabla I_r|$, its numerical expression and computation being discussed in more detail in §5.3.2.

Substituting the anisotropic error norm from (5.16) into (5.6) leads to the following evolution equation:

$$\frac{\partial I_r(x, y, t)}{\partial t} = -\alpha \mathfrak{D}_a(I_r(x, y, t)) + \beta \Theta(J(x, y, t)) J(x, y, t) [I_r(x, y, t) - I(x, y)] \quad (5.18)$$

where

$$\mathfrak{D}_a(I_r) = c_\xi I_{r\xi\xi} + c_\eta I_{r\eta\eta} \quad (5.19)$$

is a diffusion differential operator computed in an anisotropic manner [TLBB02, TBB⁺04], while $\Theta(J)$ (4.25) is defined so as to allow only salient information to be transferred to I_r :

$$\Theta(J) = \begin{cases} 1, & \text{if } J \geq 0 \\ 0, & \text{if } J < 0 \end{cases} \quad (5.20)$$

Remark At first look, when comparing the proposed error norm (5.18) to the error norm employed by the John–Vorontsov fusion model (4.22), the proposed norm appears to be defined in a counterintuitive manner, since the diffusion term $\mathfrak{D}_a(I_r)$ describes a negative advection process, while the edge-enhancement term describes a positive advection process, the opposite of how a standard PDE-based *restoration with edge enhancement* process is normally described.

The fundamental difference between the two models lies in the fact that the John–Vorontsov model directly employs its error norm in defining a fusion paradigm, while the proposed model is constructed on the premise of describing a fusion process as a linear combination of weighted inputs. Thus, the variational framework is indirectly used to describe the time evolution of each independent weight function, a process that adds an additional overall sign inversion, ultimately leading to the standard PDE-based *restoration with edge enhancement* process description. The complete definition of the proposed fusion model is further explained and clarified in the following paragraphs.

$I_{r\xi\xi}$ and $I_{r\eta\eta}$ are the second order directional derivatives of I_r along the directions η and ξ ($\xi \perp \vec{\eta}$), where ξ describes the structure’s (edge’s) geometry. The detailed discussion regarding the expression of \mathfrak{D}_a and its discretization is provided in §5.3.2.

Mathematically, a fusion process can be described as comprising S input images, $I_1(x, y), \dots, I_S(x, y): \Omega \rightarrow \mathbb{R}$ representing the same scene, spatially or temporally. One way of classifying fusion techniques, according to [MS08] is into *spatial domain* and *transform domain* techniques. In the spatial domain, a fused image can be defined as:

$$\tilde{I}(x, y) = C(I_1(x, y), \dots, I_S(x, y)) \quad (5.21)$$

where C represents the fusion rule, describing how the relevant features from the input images are combined to yield the fused image \tilde{I} . Analogously, in the transform domain, described by a transform operator \mathcal{T} , the fusion process can be expressed as:

$$\tilde{I}(x, y) = \mathcal{T}^{-1}\{C(\mathcal{T}\{I_1(x, y)\}, \dots, \mathcal{T}\{I_S(x, y)\})\} \quad (5.22)$$

According to the classification of Mitianoudis and Stathaki [MS08], the proposed model is a spatial domain fusion technique based on error estimation theory, expressed using a variational framework.

Linking the two theoretical constructs of error estimation and variational fusion is unambiguously achieved by extending the notion of recovered image I_r , from error estimation theory, to image fusion theory in the form of the fused image \tilde{I} . Thus, every input image $I_s(x, y)$, $s = \{1, \dots, S\}$, of the fusion process is regarded as a degraded image I , recovered using the error estimation variational approach described by (5.18).

The fused image \tilde{I} can be constructed therefore, as a linear combination of S input images I_s , where the useful information is transferred to the fused result by means of weight functions $w_s(x, y, t)$, as part of the error estimation process [MS08]:

$$\tilde{I}(x, y, t) = \sum_{s=1}^S w_s(x, y, t) \cdot I_s(x, y) \quad (5.23)$$

The process of fusing multiple inputs into a single fused result requires, first and foremost, ensuring proper edge preservation. This cannot be achieved using a sequential approach to estimating the S fusion weight functions, since salient information belonging to one input could be lost if not correlated to all the other inputs. That is why concurrent fusion and denoising as a parallel, simultaneous process is not equivalent to a sequential denoising followed by a simple fusion process.

Simultaneously estimating the derivatives $\partial w_s / \partial t$, $s = \{1, \dots, S\}$ for all S input images can be accomplished by using the following simplifying mathematical construct:

$$\frac{\partial \tilde{I}}{\partial t} = \frac{\partial \tilde{I}}{\partial w_s} \frac{\partial w_s}{\partial t} = I_s \frac{\partial w_s}{\partial t} \quad (5.24)$$

Thus, all S weights w_s are simultaneously estimated based on their corresponding input I_s and correlated to the fused image \tilde{I} :

$$\frac{\partial w_s(x, y, t)}{\partial t} = \frac{1}{I_s(x, y)} \frac{\partial \tilde{I}(x, y, t)}{\partial t} \quad (5.25)$$

Each fusion weight function is iteratively estimated using an update rule of the form of:

$$w_s(x, y, t + 1) \leftarrow w_s(x, y, t) - \tau \frac{\partial w_s(x, y, t)}{\partial t} \quad (5.26)$$

where

$$\begin{aligned} \frac{\partial w_s(x, y, t)}{\partial t} = \frac{1}{I_s(x, y)} \left\{ -\alpha \mathfrak{D}_a(\tilde{I}(x, y, t)) \right. \\ \left. + \beta \Theta(J_s(x, y, t)) J_s(x, y, t) [\tilde{I}(x, y, t) - I_s(x, y)] \right\} \end{aligned} \quad (5.27)$$

$J_s(x, y, t)$ in this case is expressed as the difference:

$$\begin{aligned} J_s(x, y, t) &= \int |\dot{\nabla} I_s(x', y')| G(x - x', y - y', \sigma_{em}) dx' dy' \\ &\quad - \int |\dot{\nabla} \tilde{I}(x', y', t)| G(x - x', y - y', \sigma_{em}) dx' dy' \\ &= J_{I_s}(x, y, t) - J_{\tilde{I}}(x, y, t) \end{aligned} \quad (5.28)$$

The temporal evolution of each weight w_s , governed by the (5.26) update rule, leads to the fused result \tilde{I} described by (5.23).

At the beginning of the fusion process, at time $t = 0$, all fusion weights are initialized to $w_s(x, y, 0) = 1/S$; over time, the fusion weights $w_s(x, y, t)$ will adapt in order to emphasize the salient information found in their corresponding input images $I_s(x, y)$, correlated to the fused image $\tilde{I}(x, y, t)$ at that particular instant of time t .

Remark With regard to the previous remark, about the overall sign inversion, an explicit mathematical example can be given in order to emphasize the concurrent processes that are taking place as part of the general joint fusion–denoising model.

Assuming a typical fusion scenario of S input images I_1, \dots, I_S , the initial value of the fusion weight functions is set to $1/S$, for all $w_s(x, y, 0)$, and furthermore, in accordance with the (5.26) update rule:

$$w_s(x, y, t + 1) \leftarrow w_s(x, y, t) - \tau \frac{\partial w_s(x, y, t)}{\partial t} \quad (5.29)$$

with $\partial w_s(x, y, t)/\partial t$ expressed as (5.27). By integrating the computed $\partial w_s(x, y, t)/\partial t$ into (5.29), $w_s(x, y, t + 1)$ is now equal to:

$$\begin{aligned} w_s(x, y, t + 1) \leftarrow w_s(x, y, t) - \frac{\tau}{I_s(x, y)} \left\{ -\alpha \mathfrak{D}_a(\tilde{I}(x, y, t)) \right. \\ \left. + \beta \Theta(J_s(x, y, t)) J_s(x, y, t) [\tilde{I}(x, y, t) - I_s(x, y)] \right\} \end{aligned} \quad (5.30)$$

Finally, using (5.23), $\tilde{I}(x, y, t)$ is expressed as:

$$\begin{aligned} \tilde{I}(x, y, t + 1) &= \sum_{s=1}^S w_s(x, y, t + 1) \cdot I_s(x, y) \\ &= \sum_{s=1}^S \left\{ w_s(x, y, t) - \frac{\tau}{I_s(x, y)} \left\{ -\alpha \mathfrak{D}_a(\tilde{I}(x, y, t)) \right. \right. \\ &\quad \left. \left. + \beta \Theta(J_s(x, y, t)) J_s(x, y, t) [\tilde{I}(x, y, t) - I_s(x, y)] \right\} \right\} \cdot I_s(x, y) \\ &= \sum_{s=1}^S w_s(x, y, t) \cdot I_s(x, y) + \tau \sum_{s=1}^S \alpha \mathfrak{D}_a(\tilde{I}(x, y, t)) \\ &\quad - \tau \sum_{s=1}^S \beta \Theta(J_s(x, y, t)) J_s(x, y, t) [\tilde{I}(x, y, t) - I_s(x, y)] \end{aligned} \quad (5.31)$$

Recalling the general expression of a time-evolving PDE-based image processing paradigm:

$$I(x, y, t + 1) = I(x, y, t) + dt \cdot \frac{\partial I(x, y, t)}{\partial t} \quad (5.32)$$

(5.31) can be further simplified, by breaking it down into its constituent parts, i.e.,

$$\left\{ \begin{array}{l} \frac{\partial \tilde{I}}{\partial t} = \sum_{s=1}^S \alpha \mathfrak{D}_a(\tilde{I}(x, y, t)) \\ \quad - \sum_{s=1}^S \beta \Theta(J_s(x, y, t)) J_s(x, y, t) [\tilde{I}(x, y, t) - I_s(x, y)] \\ \tilde{I}(x, y, 0) = \sum_{s=1}^S w_s(x, y, 0) \cdot I_s(x, y) \end{array} \right. \quad (5.33)$$

where τ is equivalent to dt .

By analogy with the Kornprobst *et al.* [KDA97a] shock filter model (3.15), $\partial \tilde{I} / \partial t$ can be also formalized in terms of functional components, as follows:

$$\begin{aligned} \frac{\partial \tilde{I}}{\partial t} = & \underbrace{\sum_{s=1}^S \alpha \mathfrak{D}_a(\tilde{I}(x, y, t))}_{\text{Denoising}} \\ & - \underbrace{\sum_{s=1}^S \beta \Theta(J_s(x, y, t)) J_s(x, y, t)}_{\text{Deblurring}} \underbrace{[\tilde{I}(x, y, t) - I_s(x, y)]}_{\text{Coupling}} \end{aligned} \quad (5.34)$$

5.3.2 Fusion algorithm and model discretization

At the core of the proposed joint fusion–denoising variational model lies the anisotropic diffusion differential operator \mathfrak{D}_a generically expressed as:

$$\mathfrak{D}_a(I) = c_\xi I_{\xi\xi} + c_\eta I_{\eta\eta} \quad (5.35)$$

representing a curvature-dependent diffusion operator, driving the diffusion process along isolines, luminance-wise (§2.8).

In its generic form (5.35), the anisotropic diffusion differential operator \mathfrak{D}_a is equivalent to the compact form expression of the Alvarez *et al.* [ALM92] diffusion paradigm. The difference between the two expressions lies in their numerical approximation, the anisotropic diffusion differential operator \mathfrak{D}_a being numerically expressed using an explicit anisotropic numerical representation of sub-pixel accuracy, first employed by the Terebes *et al.* [TBB⁺04] anisotropic diffusion model, defined as follows³:

$$\left\{ \begin{array}{l} \mathfrak{D}_a(I) = c_\xi I_{\xi\xi} + c_\eta I_{\eta\eta} \\ c_\xi = \frac{\partial}{\partial \xi} [g^\xi(I_\xi) I_\xi] \quad \text{with } g^\xi(u) = \frac{1}{1 + (u/K_\xi)^2} \\ c_\eta = \frac{\partial}{\partial \eta} [g^\eta(I_\eta) I_\eta] \quad \text{with } g^\eta(u) = \frac{1}{1 + (u/K_\eta)^2} \end{array} \right. \quad (5.36)$$

³Fig. 5.4a, Fig. 5.5 and Fig. 5.6 – the original figures can be found in [Ter04]

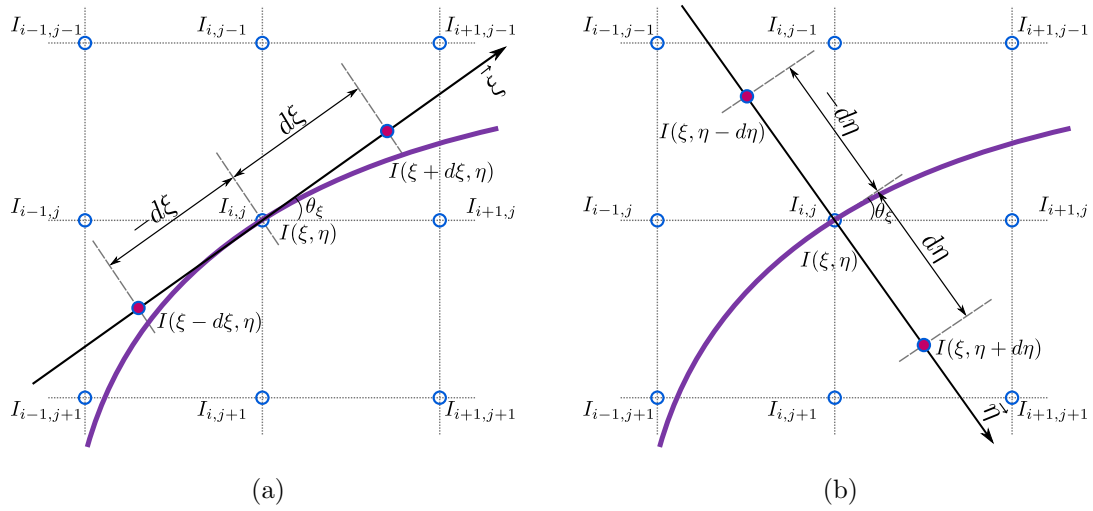


Fig. 5.4 – (ξ, η) frame of reference approximation example for a given contour, in pixel $I_{i,j}$: (a) [Ter04] – The $\vec{\xi}$ direction approximation frame; (b) The $\vec{\eta}$ direction approximation frame.

where K_ξ and K_η are threshold parameters, controlling the strength of the diffusion process along the ξ and η directions.

The use of the standard (i, j) frame of reference is not entirely suitable for anisotropic image processing, since it is fixed with respect to image structures, thus impeding their accurate description and representation. Hence, a variable, structure-dependent frame of reference is required to accurately approximate first and second order derivatives.

In selecting and constructing a structure-dependent frame of reference that best adapts to the local geometry, the (ξ, η) frame of reference is the natural choice since it best describes structures and gradients at a pixel level.

Moreover, properly describing salient features in an image often requires sub-pixel accuracy, therefore, a numerical interpolation scheme is needed for computing the finite difference approximations within the (ξ, η) frame of reference, as illustrated in Fig. 5.4. The computations performed in each pixel, require the following approximations: $I(\xi, \eta) = I(x, y)$, $I(\xi + d\xi, \eta)$, $I(\xi - d\xi, \eta)$, $I(\xi, \eta + d\eta)$ and $I(\xi, \eta - d\eta)$.

The interpolation points required for computing the previously mentioned approximations with a sub-pixel accuracy are determined using the θ_η and θ_ξ orientations, as defined by (5.9) and (5.10).

Computing $I(\xi + d\xi, \eta)$ requires three interpolation points, V_1 , V_2 and V_3 (Fig. 5.5a) expressed as:

$$\begin{cases} V_1 = I_{i,j-1} + 0.5 [I_{i+1,j-1} - I_{i-1,j-1}] d\xi \cos \theta_\xi \\ \quad + 0.5 [I_{i-1,j-1} - 2I_{i,j-1} + I_{i+1,j-1}] (d\xi \cos \theta_\xi)^2 \\ V_2 = I_{i,j} + 0.5 [I_{i+1,j} - I_{i-1,j}] d\xi \cos \theta_\xi \\ \quad + 0.5 [I_{i-1,j} - 2I_{i,j} + I_{i+1,j}] (d\xi \cos \theta_\xi)^2 \\ V_3 = I_{i,j+1} + 0.5 [I_{i+1,j+1} - I_{i-1,j+1}] d\xi \cos \theta_\xi \\ \quad + 0.5 [I_{i-1,j+1} - 2I_{i,j+1} + I_{i+1,j+1}] (d\xi \cos \theta_\xi)^2 \end{cases} \quad (5.37)$$

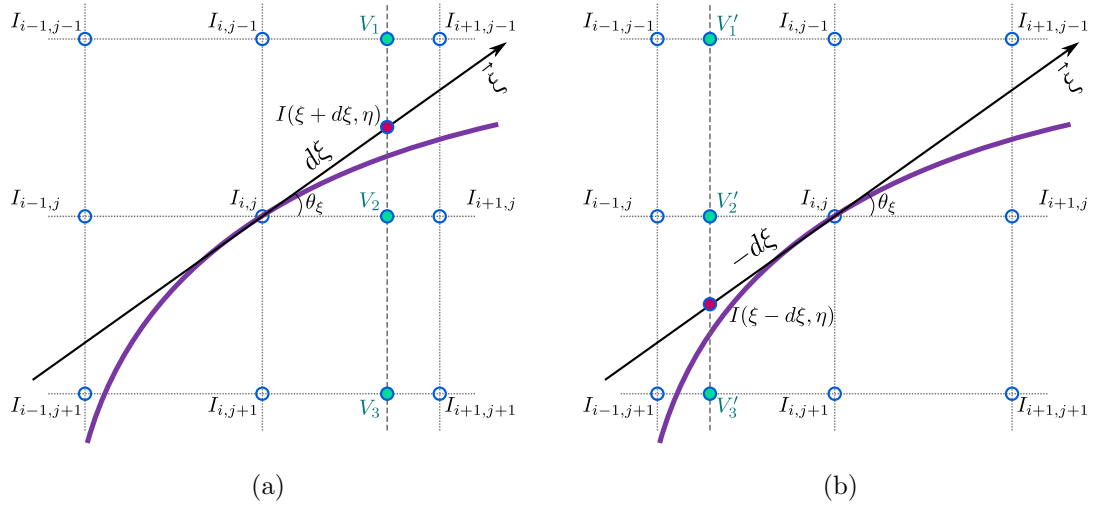


Fig. 5.5 – [Ter04] – $-\xi$ direction sub-pixel approximations: (a) V_1, V_2 and V_3 approximation points for computing $I(\xi + d\xi, \eta)$; (b) V'_1, V'_2 and V'_3 approximation points for computing $I(\xi - d\xi, \eta)$.

yielding:

$$I(\xi + d\xi, \eta) = V_2 + 0.5 (V_1 - V_3) d\xi \sin \theta_\xi + 0.5 (V_1 + V_3 - 2V_2) (d\xi \sin \theta_\xi)^2 \quad (5.38)$$

$I(\xi - d\xi, \eta)$ is computed in a similar manner, using another set of three interpolation points, V'_1, V'_2 and V'_3 (Fig. 5.5b) expressed as:

$$\begin{cases} V'_1 = I_{i,j-1} - 0.5 [I_{i+1,j-1} - I_{i-1,j-1}] d\xi \cos \theta_\xi \\ \quad + 0.5 [I_{i-1,j-1} - 2I_{i,j-1} + I_{i+1,j-1}] (d\xi \cos \theta_\xi)^2 \\ V'_2 = I_{i,j} - 0.5 [I_{i+1,j} - I_{i-1,j}] d\xi \cos \theta_\xi \\ \quad + 0.5 [I_{i-1,j} - 2I_{i,j} + I_{i+1,j}] (d\xi \cos \theta_\xi)^2 \\ V'_3 = I_{i,j+1} - 0.5 [I_{i+1,j+1} - I_{i-1,j+1}] d\xi \cos \theta_\xi \\ \quad + 0.5 [I_{i-1,j+1} - 2I_{i,j+1} + I_{i+1,j+1}] (d\xi \cos \theta_\xi)^2 \end{cases} \quad (5.39)$$

which in turn yields:

$$I(\xi - d\xi, \eta) = V'_2 - 0.5 (V'_1 - V'_3) d\xi \sin \theta_\xi + 0.5 (V'_1 + V'_3 - 2V'_2) (d\xi \sin \theta_\xi)^2 \quad (5.40)$$

$I(\xi, \eta + d\eta)$ and $I(\xi, \eta - d\eta)$ are analogously obtained, each requiring three interpolation points, as illustrated in Fig. 5.6:

$$\begin{cases} Z_1 = I_{i,j-1} + 0.5 [I_{i+1,j-1} - I_{i-1,j-1}] d\eta \sin |\theta_\xi| \\ \quad + 0.5 [I_{i-1,j-1} - 2I_{i,j-1} + I_{i+1,j-1}] (d\eta \sin \theta_\xi)^2 \\ Z_2 = I_{i,j} + 0.5 [I_{i+1,j} - I_{i-1,j}] d\eta \sin |\theta_\xi| \\ \quad + 0.5 [I_{i-1,j} - 2I_{i,j} + I_{i+1,j}] (d\eta \sin \theta_\xi)^2 \\ Z_3 = I_{i,j+1} + 0.5 [I_{i+1,j+1} - I_{i-1,j+1}] d\eta \sin |\theta_\xi| \\ \quad + 0.5 [I_{i-1,j+1} - 2I_{i,j+1} + I_{i+1,j+1}] (d\eta \sin \theta_\xi)^2 \end{cases} \quad (5.41)$$

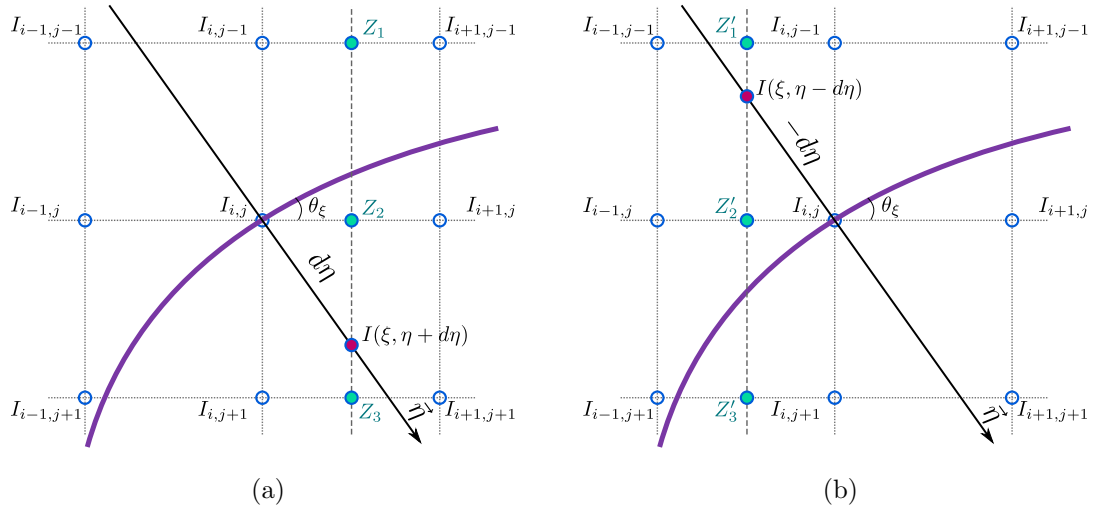


Fig. 5.6 – [Ter04] $-\vec{\eta}$ direction sub-pixel approximations: (a) Z_1, Z_2 and Z_3 approximation points for computing $I(\xi, \eta + d\eta)$; (b) Z'_1, Z'_2 and Z'_3 approximation points for computing $I(\xi, \eta - d\eta)$.

yielding a numerical approximation of $I(\xi, \eta + d\eta)$ of the form:

$$I(\xi, \eta + d\eta) = \begin{cases} Z_2 - 0.5 (Z_1 - Z_3) d\eta \cos \theta_\xi \\ \quad + 0.5 (Z_1 + Z_3 - 2Z_2) (d\eta \cos \theta_\xi)^2 & \theta_\xi > 0 \\ Z_2 + 0.5 (Z_1 - Z_3) d\eta \cos \theta_\xi \\ \quad + 0.5 (Z_1 + Z_3 - 2Z_2) (d\eta \cos \theta_\xi)^2 & \theta_\xi < 0 \end{cases} \quad (5.42)$$

and

$$\begin{cases} Z'_1 = I_{i,j-1} - 0.5 [I_{i+1,j-1} - I_{i-1,j-1}] d\eta \sin |\theta_\xi| \\ \quad + 0.5 [I_{i-1,j-1} - 2I_{i,j-1} + I_{i+1,j-1}] (d\eta \sin \theta_\xi)^2 \\ Z'_2 = I_{i,j} - 0.5 [I_{i+1,j} - I_{i-1,j}] d\eta \sin |\theta_\xi| \\ \quad + 0.5 [I_{i-1,j} - 2I_{i,j} + I_{i+1,j}] (d\eta \sin \theta_\xi)^2 \\ Z'_3 = I_{i,j+1} - 0.5 [I_{i+1,j+1} - I_{i-1,j+1}] d\eta \sin |\theta_\xi| \\ \quad + 0.5 [I_{i-1,j+1} - 2I_{i,j+1} + I_{i+1,j+1}] (d\eta \sin \theta_\xi)^2 \end{cases} \quad (5.43)$$

yielding an approximation of the form:

$$I(\xi, \eta - d\eta) = \begin{cases} Z'_2 + 0.5 (Z'_1 - Z'_3) d\eta \cos \theta_\xi \\ \quad + 0.5 (Z'_1 + Z'_3 - 2Z'_2) (d\eta \cos \theta_\xi)^2 & \theta_\xi > 0 \\ Z'_2 - 0.5 (Z'_1 - Z'_3) d\eta \cos \theta_\xi \\ \quad + 0.5 (Z'_1 + Z'_3 - 2Z'_2) (d\eta \cos \theta_\xi)^2 & \theta_\xi < 0 \end{cases} \quad (5.44)$$

The anisotropic diffusion differential operator \mathfrak{D}_a , defined as (5.36), is numerically expressed using forward and backward differences of the form (2.66) computed in: $I(\xi, \eta) =$

$I(x, y)$, $I(\xi + d\xi, \eta)$, $I(\xi - d\xi, \eta)$, $I(\xi, \eta + d\eta)$ and $I(\xi, \eta - d\eta)$, where the numerical values of these points are obtained through interpolation, i.e., (5.37) – (5.44).

$$\begin{aligned} \mathfrak{D}_a(I) = & g^\xi (D_\xi^+(I)) \cdot D_\xi^+(I) - g^\xi (D_\xi^-(I)) \cdot D_\xi^-(I) \\ & + g^\eta (D_\eta^+(I)) \cdot D_\eta^+(I) - g^\eta (D_\eta^-(I)) \cdot D_\eta^-(I) \end{aligned} \quad (5.45)$$

The model discretization is finalized by approximating the directional gradient vector $\dot{\nabla}I$ from (5.28) using only the η component of the (ξ, η) frame of reference. By choosing $\dot{\nabla}I = (I_\eta, 0)^T$ the anisotropic behavior of the *Deblurring* component of (5.34) is further strengthened and, as an observed side effect, this particular choice ensures the absence of fusion artifacts. $\dot{\nabla}I$ is numerically expressed using (5.42) and (5.44), by means of a central difference approximation scheme, and has the following norm:

$$|\dot{\nabla}I| = \sqrt{I_\eta^2} = \text{abs}(I_\eta) \quad (5.46)$$

With all the fusion model's elements properly computed and approximated, the fusion algorithm can be summarized as described in *Algorithm 5.1*.

Algorithm 5.1 Image fusion with concurrent denoising

```

input  $S$  input images
initialize  $w_s(x, y, 0) = \frac{1}{S}$ 
initialize  $\tilde{I}(x, y, 0) = \sum_{s=1}^S w_s(x, y, 0) \cdot I_s(x, y)$ 
for  $s = 1$  to  $S$  do
  compute  $\dot{\nabla}I_s(x, y)$ 
  compute  $J_{I_s}(x, y)$ 
end for
for  $t = 0$  to  $Time$  do
  compute  $\mathfrak{D}_a(\tilde{I}(x, y, t))$ 
  compute  $\dot{\nabla}\tilde{I}(x, y, t)$ 
  compute  $J_{\tilde{I}}(x, y, t)$ 
  for  $s = 1$  to  $S$  do
    compute  $J_s(x, y, t) = J_{I_s}(x, y) - J_{\tilde{I}}(x, y, t)$ 
    compute  $\partial w_s(x, y, t)/\partial t$ 
    compute  $w_s(x, y, t + 1) \leftarrow w_s(x, y, t) - \tau \cdot \partial w_s(x, y, t)/\partial t$ 
  end for
  compute  $\tilde{I}(x, y, t + 1) = \sum_{s=1}^S w_s(x, y, t + 1) \cdot I_s(x, y)$ 
end for
output fused image  $\tilde{I}(x, y, Time)$ 

```

5.4 Experimental analysis

The aim of the experimental analysis is to provide a thorough evaluation of the proposed fusion model from the following perspectives:

- underlining the difference between a sequential processing chain of denoising followed by fusion, and a concurrent fusion and denoising approach,
- experimentally validating the proposed fusion–denoising model and its robustness to noise,
- studying the model’s behavior in terms of parameter selection vs. fused image quality,
- performing a comparative analysis between the proposed model and a selection of existing fusion and fusion–diffusion approaches.

5.4.1 Sequential denoising and fusion vs. concurrent fusion and denoising

Before discussing any other experimental analysis-related issues, it is necessary to reiterate the statement from §5.3.1 that “concurrent fusion and denoising as a parallel, simultaneous process is not equivalent to a sequential denoising followed by a simple fusion process”.

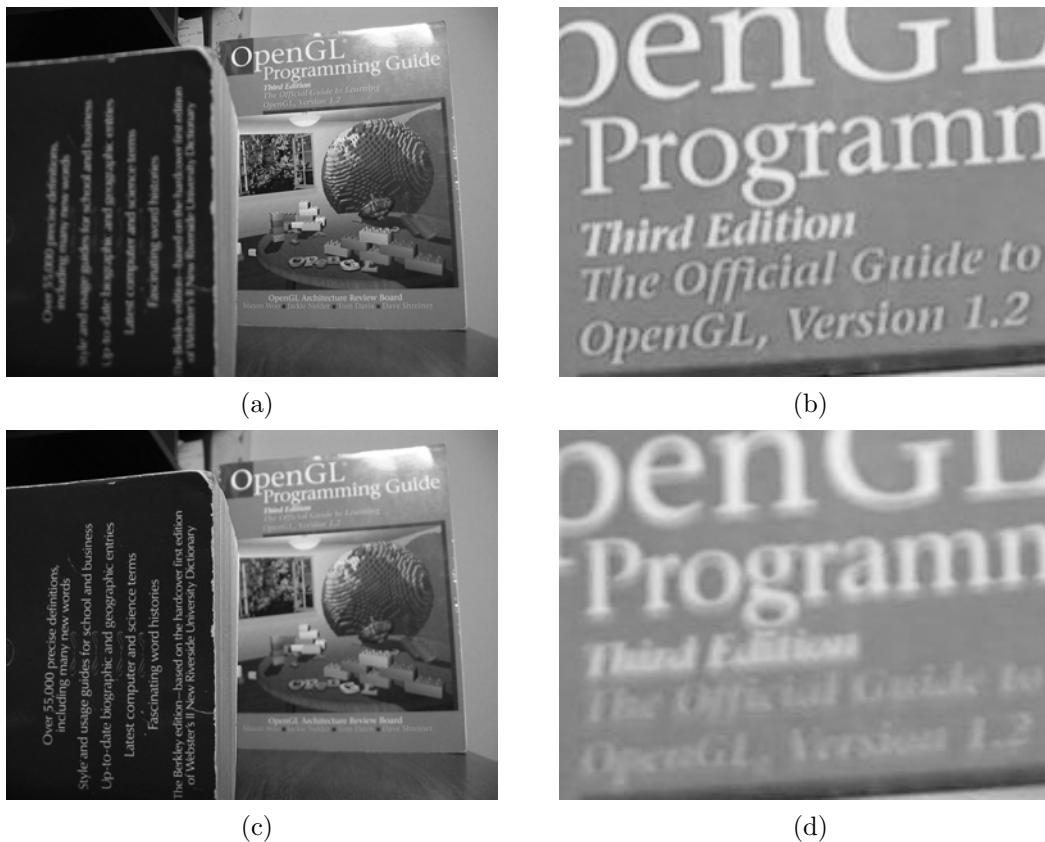


Fig. 5.7 – *Concurrent fusion and denoising – advantages. The **Book** image set test scenario: (a) **Book 1** original input image and detail (b); (c) **Book 2** original input image and detail (d).*



Fig. 5.7 – (continued): (e) SIDWT with Haar fusion method result and detail (f); (g) Anisotropic noise filtering of the inputs followed by SIDWT with Haar fusion result and detail (h); (i) Proposed fusion method result and detail (j).

This important difference ultimately being *la raison d'être* of the proposed fusion model.

To this end the following test scenario is constructed: given a real-world image set (*Book*), consisting of two grayscale input images, available at [Ima11a], with an estimated noise of $\sigma_n = 0.66$ and $\sigma_n = 0.65$ respectively, and of unknown distribution, three experimental settings are devised. The first experimental setting fuses the two input images using the *SIDWT with Haar* fusion method, part of Rockinger's image fusion toolbox, *fusetool* [Roc99], with the following parameter set: *Level=4*, *High-pass combination=choose max*, *Low-pass combination=average(A,B)*.

The second experimental setting is identical to the previous setting in every way,

except the input images. Since the original images are contaminated with a noise of unknown characteristics, the required processing steps in this case are a noise filtering followed by a fusion process. In order to maintain consistency between the experimental settings and to limit as much as possible method bias, the input images are anisotropically filtered prior to fusing them, with a filter based on the anisotropic diffusion differential operator \mathfrak{D}_a , also employed by the proposed fusion model. This limits any bias regarding the difference in denoising quality that would have arisen if different noise filtering methods had been employed. The parameter set for the noise prefiltering of the input images is the following: $t = 5s$, $\tau = 0.1$, $W_{PCA} = 3$, $K_\xi = 10$, $K_\eta = 5$. The thereby obtained experimental results are illustrated in *Fig. 5.7*.

The third, and final experimental setting fuses the two input images using the proposed fusion model with the following set of input parameters: $t = 1s$, $\tau = 0.1$, $W_{PCA} = 3$, $K_\xi = 10$, $K_\eta = 5$, $\sigma_{em} = 7$, $\alpha = 1.5$ and $\beta = 1$.

As it can be seen from the extracted details, visually, the best result from a definition point of view of greater quality [Wal98] is the fused result obtained with the proposed fusion method. This statement holds true if the requirements for a “greater quality” fused result are robust noise filtering with salient feature (edges, contours) preservation and enhancement. The former requirement is inherently fulfilled by the proposed fusion model, while the latter is satisfied by the combined effect of anisotropic fusion and the implicit complementary information contained in the input images.

From an informational point of view, according to [BXZ06], an image fusion process handles the following types of information: *redundant*, *complementary*, *more timely* and *less costly*. By attempting to fulfill the requirements for a “greater quality” fused result using sequential means, prefiltering followed by standard fusion, important information (complementary and redundant) may be lost. The noise filtering process in itself considers only the current input, disregarding all other inputs, regardless of their relevance to the current input and to the salient features contained within. The fusion process, by definition, allows simultaneously assessing all inputs and the salient information contained in each of them. Thus, it is only natural to integrate the denoising process into the overall fusion mechanism, allowing simultaneous feature assessment and noise filtering.

Remark It also needs to be stressed that the fused result yielded by the proposed model (*Fig. 5.7i*) falls within the category of expected results (quality-wise), but it is not the best, since the fusion model did not undergo any parameter optimization, nor it is the only possible result of acceptable quality (defined according to application).

5.4.2 Experimental validation and noise robustness assessment

In order to experimentally validate the proposed joint image fusion and denoising model [LL11b, LL11a], a multifocus image fusion scenario is chosen, comprising two input images (*Fig. 5.8a* and *Fig. 5.8b*) – the original images [ECE11] are real-world, registered images, describing the same scene in different focus points. The initial, estimated, AWGN of the original images is of $\sigma_{noise-bias} = 0.48$ and is considered as a noise bias when further adding AWGN.

For validating the fusion method’s denoising capabilities, the test scenario is constructed on the assumption of a *relative reference image*, since the desired output varies from application to application. In this case, the multifocus image fusion of noisy images

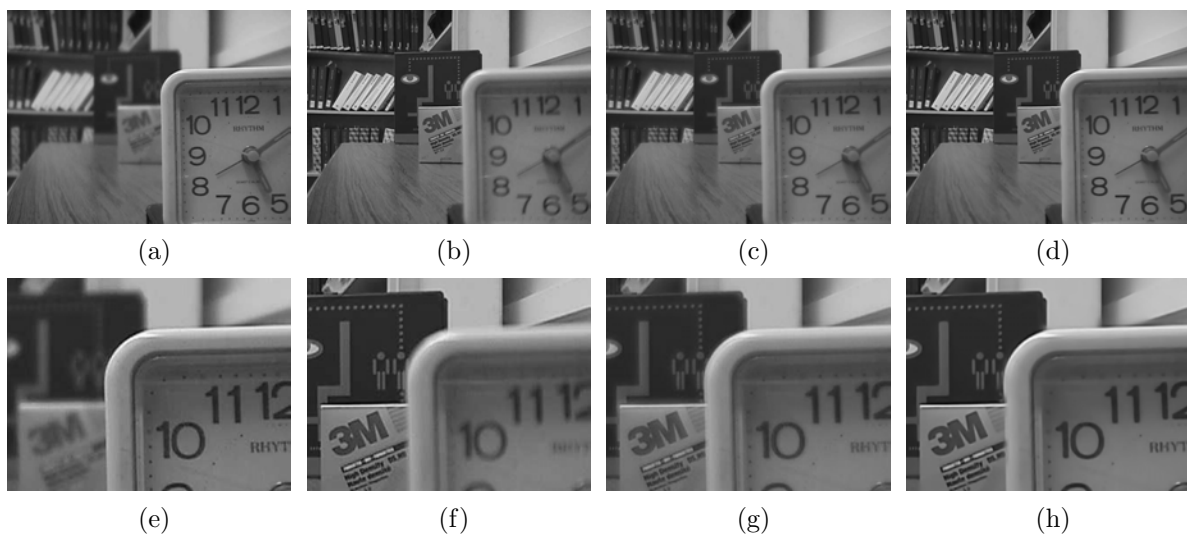


Fig. 5.8 – Multifocus image fusion test setting: (a) First input image I_1 ; (b) Second input image I_2 ; (c) Simple average reference image R_{avg} ; (d) Fusion reference image R_{fus} ; (e) I_1 – detail; (f) I_2 – detail; (g) R_{avg} – detail; (h) R_{fus} – detail.

is required to produce a fused result of the scene described by the input images (I_1 and I_2) that is both *in focus* and properly denoised.

To that end, the relative reference image is obtained using the fusion method itself, with an empirically chosen set of parameters that produce a fused image within desired quality specifications. This result is not necessarily the best, *per se*, since that would require *a priori* knowing the ideal outcome of the fusion process, thus contradicting the fundamental definition of information and making the image fusion redundant altogether.

In order to establish a somehow objective base of reference in relation with the fusion reference, a second relative reference is used, obtained by averaging the original input images, hence using to most basic fusion paradigm, also known as the *simple average* fusion rule (4.1), previously discussed in §4.4.1.1.

Thus, the two references are obtained as follows: the simple average reference R_{avg} , illustrated in Fig. 5.8c, is obtained by averaging the original input images (Fig. 5.8a and Fig. 5.8b). The fusion reference R_{fusion} , illustrated in Fig. 5.8d, is the result of the proposed fusion model, using (5.27) and (5.23) with an empirically chosen set of parameters (**ES1**⁴): *iterations* = 15, $\tau = 0.1$ – theoretical time $t = \tau \times \textit{iterations} = 1.5s$, $W_{PCA} = 3$, $K_\xi = 10$, $K_\eta = 5$, $\sigma_{em} = 7$, $\alpha = 1$ and $\beta = 0.6$.

Fig. 5.8e through Fig. 5.8h represent enlarged details of the input images, R_{avg} and R_{fusion} respectively, and illustrate the difference in visual quality and filtered noise between the original inputs, R_{avg} and R_{fusion} .

The joint fusion–denoising model can be analyzed in terms of noise filtering and edge enhancement using a set of *objective evaluation measures that require a reference image* [BXZ06], e.g., RMSE, PSNR, VIF and SSIM, topic previously covered in §4.6.

The test scenario is constructed on the idea of verifying the fusion method’s robustness to AWGN, while correctly performing multifocus image fusion, that is, yielding a fused result both *in focus* and denoised. The AWGN varies from no added noise,

⁴ES - Experimental Setting

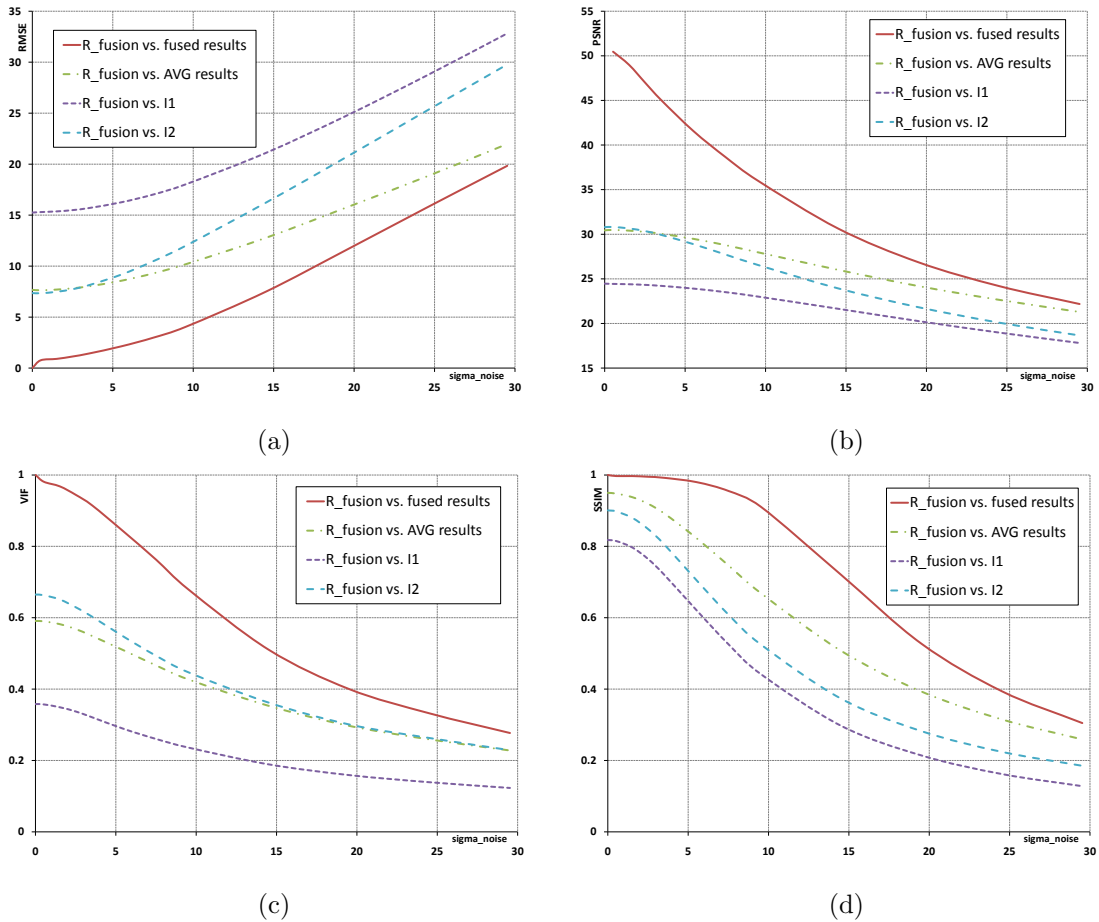


Fig. 5.9 – Multifocus image fusion test scenario (**ES1**) - quality metrics: (a) $RSME/\sigma_{noise}$ evolution; (b) $PSNR/\sigma_{noise}$ evolution; (c) VIF/σ_{noise} evolution; (d) $SSIM/\sigma_{noise}$ evolution.

($\sigma_n = \sigma_{noise-bias}$), to $\sigma_n = \sigma_{noise} + \sigma_{noise-bias} = 30$. For the first experimental setting (**ES1**), the quality metrics' evolution with respect to σ_{noise} is illustrated in Fig. 5.9.

Fig. 5.9 illustrates the evolution of the following test results:

- The fused result $\tilde{I}_{\sigma_{noise}}$ for all tested values of σ_{noise} , with respect to its relative reference R_{fusion} , where R_{fusion} falls within the category of “greater” quality results, fulfilling the two important criteria of being properly fused and denoised through a joint fusion–denoising approach.
- The averaged result $I_{avg}^{\sigma_{noise}}$ for all tested values of σ_{noise} , with respect to its relative reference R_{fusion} in order to qualitatively quantify the difference between the *simple average* fusion method and the proposed fusion–denoising model.
- The two inputs $I_{1,2}^{\sigma_{noise}}$ for all tested values of σ_{noise} , with respect to their relative reference R_{fusion} , to provide an extra point of reference, quality-wise.

Upon analyzing the experimental results illustrated in Fig. 5.9, the following immediate conclusions can be formulated:

- The proposed fusion model, with the parameter set **ES1**, suited for low to medium noise contamination, performs as intended even for high AWGN levels.

- As it can be seen from the quality metrics graphs (*Fig. 5.9*), the proposed fusion method yields promising results even when the method’s parameters are empirically chosen, without any prior parameter optimization.
- The proposed fusion process exhibits a robust salient information (*i.e.*, structure information, such as edges and contours) transfer and integration even for high AWGN levels, as indicated by the SSIM evolution in *Fig. 5.9d*.

The aim of defining additional experimental settings is to emulate a real-world scenario of adapting the image processing model to the conditions of the input data. Thus, two new experimental settings, **ES2** and **ES3**, are defined as instances of the proposed method, particularly adapted, parameter-wise, to tackle with medium and high noise contamination, respectively.

The three proposed experimental settings (*Table 5.1*) emulate a coarse optimization scenario (*Fig. 5.10*), where in order to maintain a high quality fused result regardless of the input images and the degree of their contamination, the model’s parameters are adjusted so as to compensate for any drop in quality, or at least limit this drop as much as possible. Thus, the resulting optimization is achieved by using the input parameters from one of the three experimental settings at each level of σ_{noise} , according to the best measured value, quality metric-wise.

All of the quality metrics used for the coarse optimization test scenario indicate that the increase in AWGN can be dynamically compensated by a proper selection of the fusion method’s input parameters. Hence, a proper parametrization ensures the robustness of the fusion method across the entire range of σ_{noise} values. The evolution of the SSIM quality metric (*Fig. 5.10d*) for the optimized experimental setting R_{fusion}/OPT underlines the implicit anisotropic characteristic of the fusion method, both for noise filtering and edge enhancement.

The same experimental settings can be evaluated using dedicated fusion quality metrics, like the $Q^{AB/F}$ or the Q_W (§4.6), having as reference the original input images $I_1^{\sigma_{noise-bias}}$ and $I_2^{\sigma_{noise-bias}}$ (*Fig. 5.8a* and *Fig. 5.8b*). Since there are no completely noise-free input images available, the quality assessment slightly under-evaluates the fused results, as discussed in §4.7.4, but within acceptable limits, providing an accurate enough evaluation.

Moreover, the same reasoning as for the test scenario illustrated in *Fig. 5.10* is used in assessing the quality of the fused results $\tilde{I}_{\sigma_{noise}}$ with dedicated fusion quality metrics, for the three experimental settings (*Table 5.1*). The resulting quality assessment and the corresponding fusion model’s coarse optimization are illustrated in *Fig. 5.11*, their interpretation leading to the following conclusions:

- The overall model behavior is consistent with the previous quality assessment and

Table 5.1 – Noise robustness assessment – experimental settings

Experimental setting	Proposed model parameters							
	t	τ	W_{PCA}	K_ξ	K_η	σ_{em}	α	β
ES1	1.5s	0.1	3	10	5	7	1	0.6
ES2	1.5s	0.1	5	10	5	7	1.6	0.3
ES3	4s	0.1	5	10	5	9	2.2	0.3

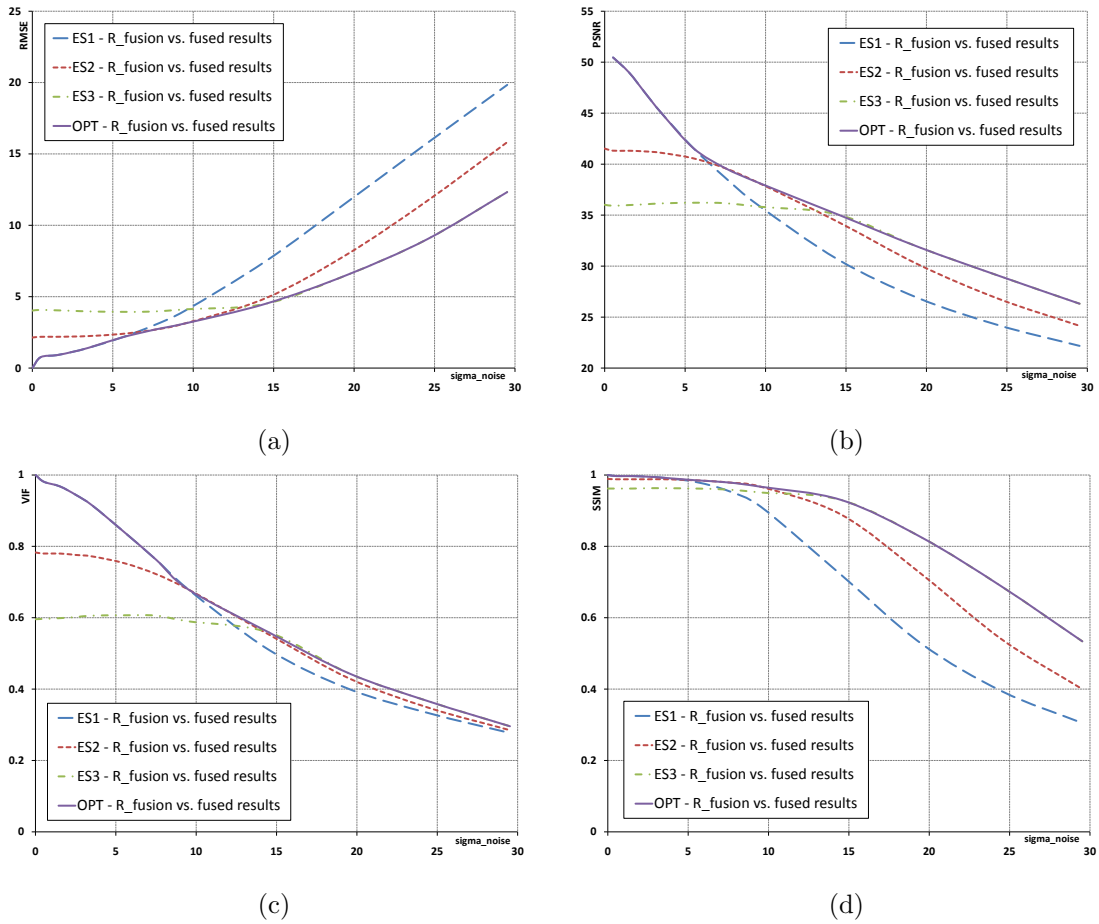


Fig. 5.10 – Noise robustness test scenario: (a) $RSME/\sigma_{noise}$ coarse optimization; (b) $PSNR/\sigma_{noise}$ coarse optimization; (c) VIF/σ_{noise} coarse optimization; (d) $SSIM/\sigma_{noise}$ coarse optimization.

coarse optimization scenario (Fig. 5.10), and confirms the validity of the proposed joint fusion–denoising model, as well as its robustness to noise, achieved by properly adjusting the model’s input parameters when required to compensate for the increase in AWGN contamination.

- The evolution of the Q_W fusion quality metric (Fig. 5.11b) for the three experimental settings not only supports the previous conclusions regarding the model’s noise robustness and how its parameters can be dynamically adjusted to compensate for the increase in AWGN, but also, through its values, underlines the model’s ability to transfer salient information from the inputs to the fused result, even for elevated noise levels. The quality assessment using the Q_W metric is all the more pertinent since, as concluded in §4.7, the Q_W fusion quality metric is more reliable in properly assessing the quality of the fused results than the other available dedicated fusion quality metrics.

Remark It needs to be reiterated that for the given initial test setting, illustrated in Fig. 5.8, the proposed method can yield even better results if thoroughly optimized in terms of *input parameters vs. input noise level*, a subject that will be discussed at length in §5.4.3.

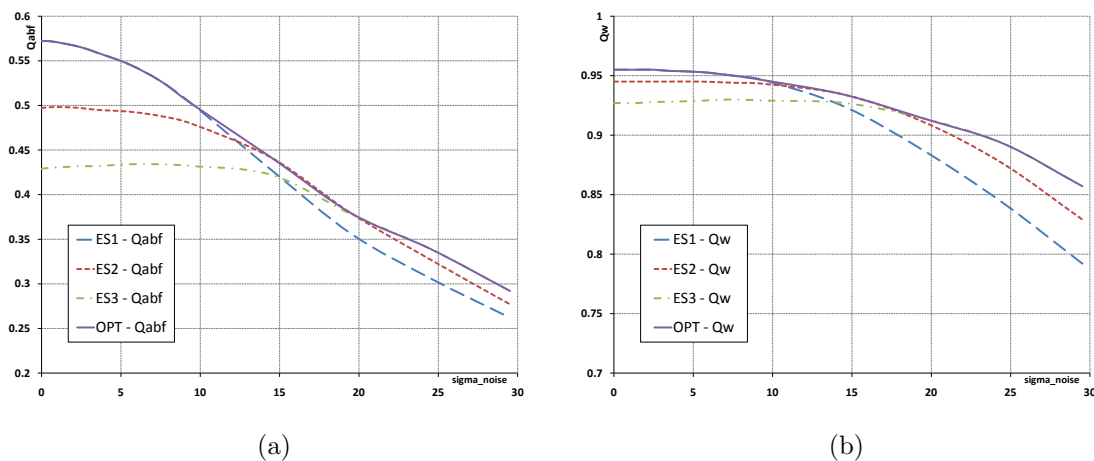


Fig. 5.11 – Noise robustness test scenario – dedicated fusion quality metrics evaluation: (a) $Q^{AB/F} / \sigma_{noise}$ coarse optimization; (b) Q_W / σ_{noise} coarse optimization.

The analysis of the proposed noise robustness scenario (Fig. 5.10 and Fig. 5.11), in terms of fused image quality vs. σ_{noise} , reveals another interesting fact: for high and very high noise levels the drop in quality is significant and partly due to external factors, such as:

- the limited number of input images – given a noise of zero mean, for a sufficiently large number of input images, the initialization process (input averaging) alone would act as an implicit denoising process. This theoretical property is employed as an additional denoising step by the Socolinsky fusion model [Soc00a], where the fusion process is always assumed as comprising a sufficiently large number of inputs.
- the entropy of the input images – usually filtering methods that employ a geometry-driven processing mechanism have difficulties in initially assessing the image geometry when the inputs are contaminated with high value noise, e.g., the Osher–Rudin [OR90] shock filter. A simple and efficient solution, employed by many denoising methods, is to integrate in the filtering model a pre-smoothing component that helps decrease the initial entropy and allows the model’s edge detector to properly describe the geometry of the input image. Thus, in the case of the proposed joint fusion–denoising model, an extra boost in output quality is available by integrating a pre-smoothing component in the overall model, the fusion inputs being thereby expressed as $G * I_s$, where G is a Gaussian PSF of σ_{ps} .

In order to illustrate the difference in output quality between the proposed fusion model without pre-smoothing and the proposed fusion model with pre-smoothing, the following experimental setting is constructed: for the input image set $I_{1,2}^{\sigma_n=30}$, the best quality scores for the proposed fusion model without a pre-smoothing component are obtained using the **ES3** parameter set; in order to assess the difference in quality for the proposed fusion model with pre-smoothing, the same set of parameters is kept, i.e., **ES3** (Table 5.1), with the additional parameter $\sigma_{ps} = 0.5$.

For the input image set $I_{1,2}^{\sigma_n=30}$ the initial entropies are $E_{I_1} = 7.639$ and $E_{I_2} = 7.657$, respectively and the fused result $\tilde{I}^{\sigma_n=30}$ (Fig. 5.12a) is obtained using the **ES3** input parameters set, as previously mentioned. For the pre-smoothing case, the input image

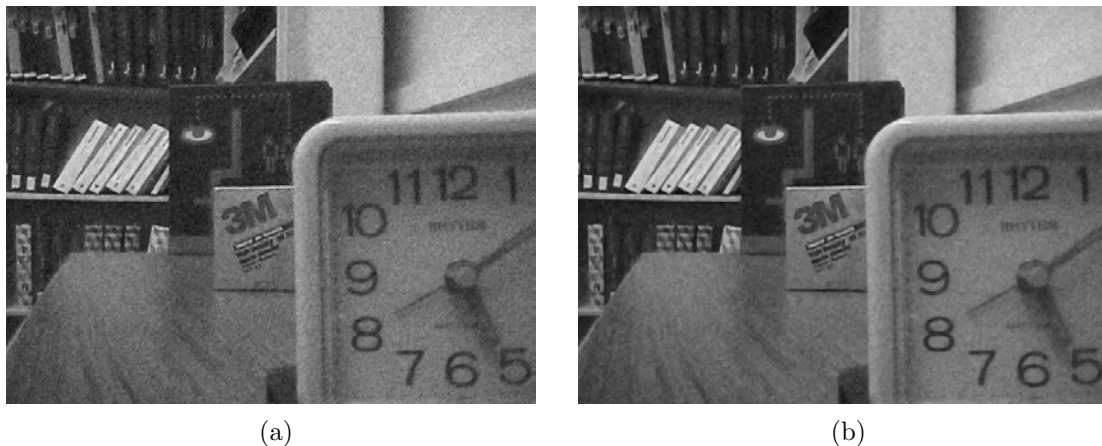


Fig. 5.12 – Noise robustness test scenario – pre-smoothing example: (a) $\tilde{I}^{\sigma_n=30}$ fused result; (b) $\tilde{I}_{\sigma_{ps}=0.5}^{\sigma_n=30}$ fused result.

set $G_{\sigma_{ps}=0.5} * I_{1,2}^{\sigma_n=30}$ has the following the initial entropies: $E_{I_1} = 7.525$ and $E_{I_2} = 7.579$, respectively, and the fused result $\tilde{I}_{\sigma_{ps}=0.5}^{\sigma_n=30}$ (Fig. 5.12b) is obtained using the **ES3** input parameters set and the additional input parameter $\sigma_{ps} = 0.5$.

The quality assessment for the proposed experimental setup is summarized in Table 5.2 from where it can be concluded that even a small decrease in the initial entropy of the input images, through a pre-smoothing process ($\sigma_{ps} = 0.5$), can provide a significant increase in quality of the output fused image \tilde{I} .

Remark The experimental setting summarized in Table 5.2 has a dual interpretation: on the one hand it supports the previous inference stating that a small pre-smoothing with the purpose of reducing the input images' entropy can provide an additional increase in fused output quality, as indicated by the image fusion quality metrics for the **ES3** w/ $\sigma_{ps} = 0.5$, while on the other hand it shows that by no means a sequential denoising followed by a classic fusion process is equivalent or superior in terms of output quality to the proposed concurrent fusion–denoising approach. Moreover, as the remaining experimental settings indicate (Table 5.2 – **ES3** w/ $\sigma_{ps} = 1.5, \dots, 3$) the fused result quality decreases if the pre-smoothing is anything other than minimal, just enough to slightly decrease the initial entropy.

The proposed method's joint fusion–denoising nature and its implicit noise robustness

Table 5.2 – Noise robustness assessment of the pre-smoothing example – quality evaluation

Experimental setting	Quality metrics						
	R_{fusion}/\tilde{I}	RMSE	PSNR	VIF	SSIM	$Q^{AB/F}$	Q_W
ES3		12.33	26.311	0.296	0.534	0.292	0.857
ES3 w/ $\sigma_{ps} = 0.5$		8.048	30.016	0.335	0.762	0.336	0.895
ES3 w/ $\sigma_{ps} = 1.5$		10.474	27.727	0.283	0.864	0.247	0.785
ES3 w/ $\sigma_{ps} = 2$		12.573	26.141	0.224	0.831	0.214	0.7
ES3 w/ $\sigma_{ps} = 3$		15.651	24.239	0.143	0.777	0.183	0.549

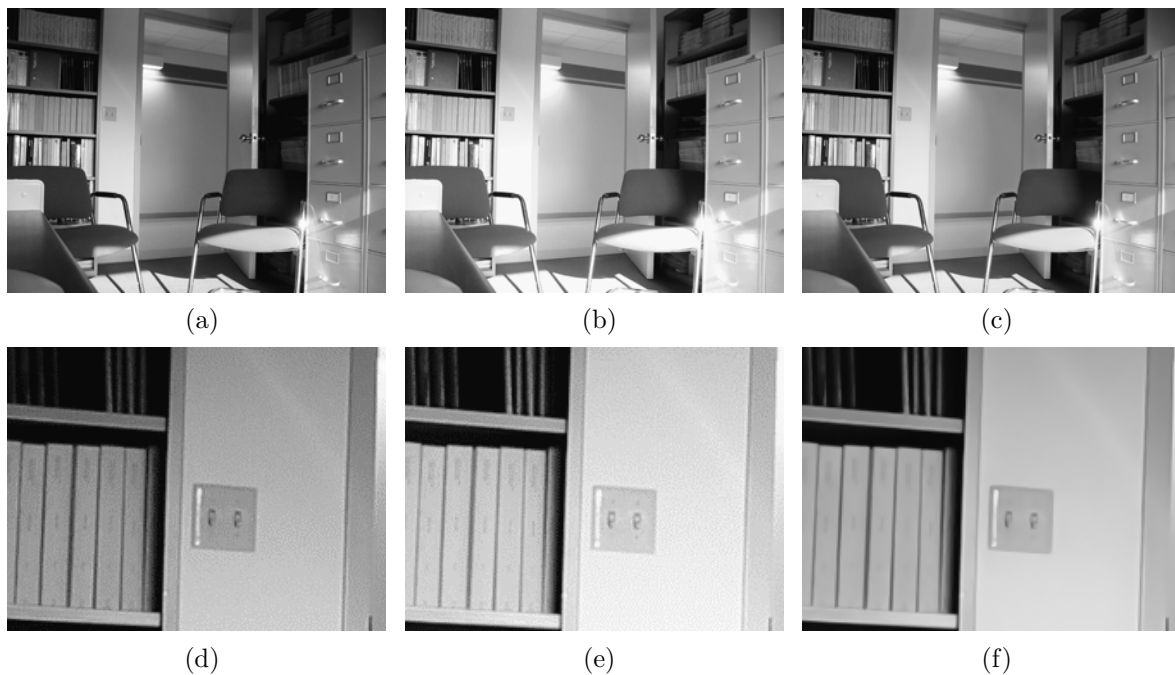


Fig. 5.13 – *Office image set – multi-exposure fusion scenario: (a) I_1 input image – with an estimated noise of $\sigma_{noise-bias} = 2.62$ and detail (d); (b) I_2 input image – with an estimated noise of $\sigma_{noise-bias} = 2.55$ and detail (e); (c) Proposed fusion model fused result \tilde{I} and detail (f).*

makes the quality assessment process more difficult, as previously discussed in §4.7.4, especially when the fused reference or the input references do not exist. As already discussed, seldom the input images are “ideal” in the sense that they contain only useful information. One such example of noise-corrupted input images is illustrated in *Fig. 5.13a* and *Fig. 5.13b*. The unknown noise contamination can originate from various sources, e.g., acquisition, transmission, storage, compression and should be either considered as a noise bias when evaluating the fused result or it should be filtered out to the extent of becoming a negligible contamination when using the original image set as reference for quality evaluation. *Fig. 5.8* has illustrated a standard multifocus image fusion scenario and its initial noise contamination problem. Another example of a similar noise contamination is illustrated in *Fig. 5.13* for a multi-exposure fusion scenario using the *Office* image set, available at [Ima11a].

As it can be seen from the detailed view in *Fig. 5.13d* and *Fig. 5.13e* the noise contamination in this case is not at all negligible and will strongly influence any quality evaluation, if the original input images are used as references. This is especially the case for dedicated fusion quality metrics (§4.6), where the input images are considered as references when evaluating the fused result.

In the case of concurrent fusion and denoising, when comparing a fused result that is both enhanced and restored with the initial noisy inputs, the evaluation is not based on sound, well-posed initial conditions. If using objective evaluation methods that require a reference image, such a reference usually needs to be constructed using a fusion method that can provide a result within the class of desired results. When dealing with noisy inputs, constructing the reference by means of a standard fusion method leads to a fused

result that shares the same shortcoming as its inputs, and renders the evaluation process ill-founded.

In order to overcome the initial noise problem in quality evaluation for the input references, one way is to use a slightly filtered version of the original image set, so much so that the reference images are visually and qualitatively acceptable from a “greater quality”-definition point of view. As for the fused reference, this can be obtained directly from the input references using a fusion process that provides a fused result of “greater quality”.

5.4.3 Model parametrization

Before performing a comparative analysis between the proposed fusion model and existing, variational and non-variational models, it is required to experimentally test the model’s response to its input parameters, and their influence on the quality of the fused output. To this end, a multifocus image fusion test scenario is constructed, using the *Clock* image set (available at [Ima11a]) progressively contaminated with an AWGN of $\sigma_n = 1, \dots, 50$. As discussed in §5.4.2, the original images from the *Clock* set are not entirely suitable for use as references since they contain an unknown noise contamination of estimated $\sigma_{noise-bias} = 0.53$ and $\sigma_{noise-bias} = 0.51$, respectively. Since the noise contamination in

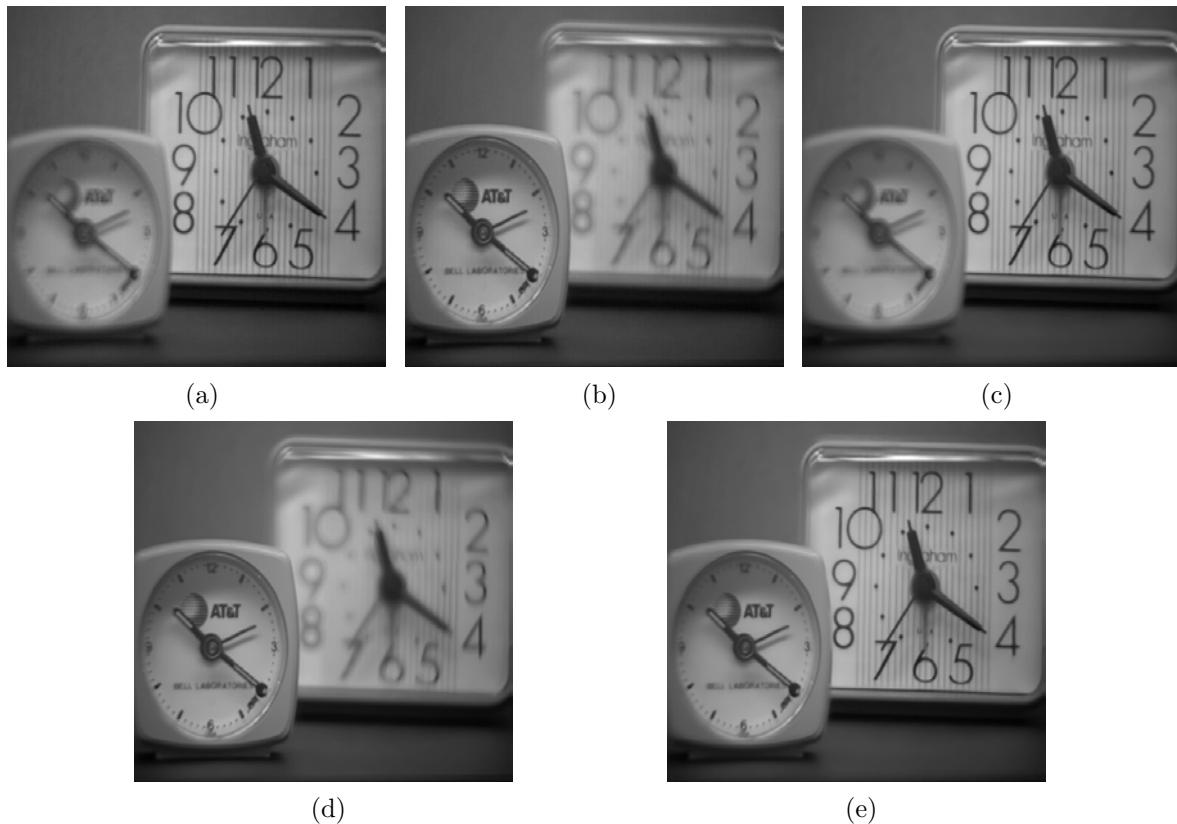


Fig. 5.14 – *Clock* image set – multifocus fusion scenario: (a) *Clock 1* original image – with an estimated noise of $\sigma_{noise-bias} = 0.53$; (b) *Clock 2* original image – with an estimated noise of $\sigma_{noise-bias} = 0.51$; (c) I_1 reference input image; (d) I_2 reference input image; (e) Reference fused image – used in the noise stress analysis.

this case is weak, an acceptable approximation of the “ideal” input images can be obtained by performing an anisotropic filtering of the original images.

In order to establish a fused reference image, needed for the noise behavioral analysis, the quasi-“ideal” image set is fused using the proposed method with the following parameter set: $t = 0.5s$, $\tau = 0.1$, $W_{PCA} = 3$, $K_\xi = 10$, $K_\eta = 5$, $\sigma_{em} = 1$, $\alpha = 1$ and $\beta = 1$. The original *Clock* set, along with the reference inputs and the reference fused image are illustrated in *Fig. 5.14*.

For the following experimental analysis, the reference input images (*Fig. 5.14c* and *Fig. 5.14d*) will be progressively contaminated with an AWGN of up to $\sigma_n = 50$. The envisaged noise stress scenario is designed as follows: each input parameter at a time varies within specified limits and the output fused result is assessed using three quality metrics, *i.e.*, RMSE, PSNR and SSIM. The evolution of the quality metrics will indicate in what way the fusion model is influenced by any given input parameter and how should the model be parameterized for any given σ_n so as to yield the best obtainable results.

As a first optimization assessment, α and β are varied between 0 and 2.5 in increments of 0.1, in order to ascertain how they influence the fusion model’s behavior with the

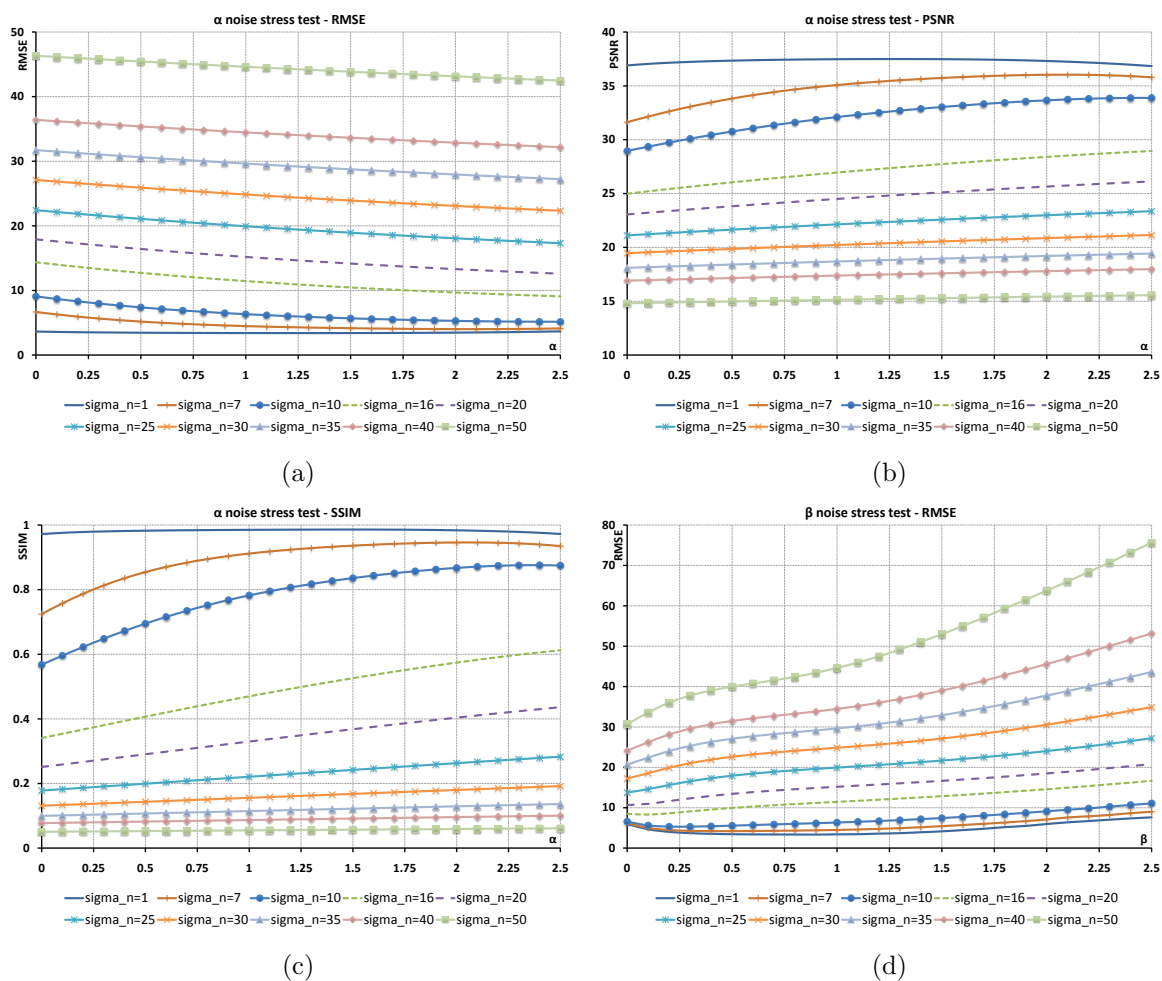


Fig. 5.15 – Proposed fusion method – noise stress behavior: (a) RMSE/noise evolution – α ; (b) PSNR/noise evolution – α ; (c) SSIM/noise evolution – α ; (d) RMSE/noise evolution – β .

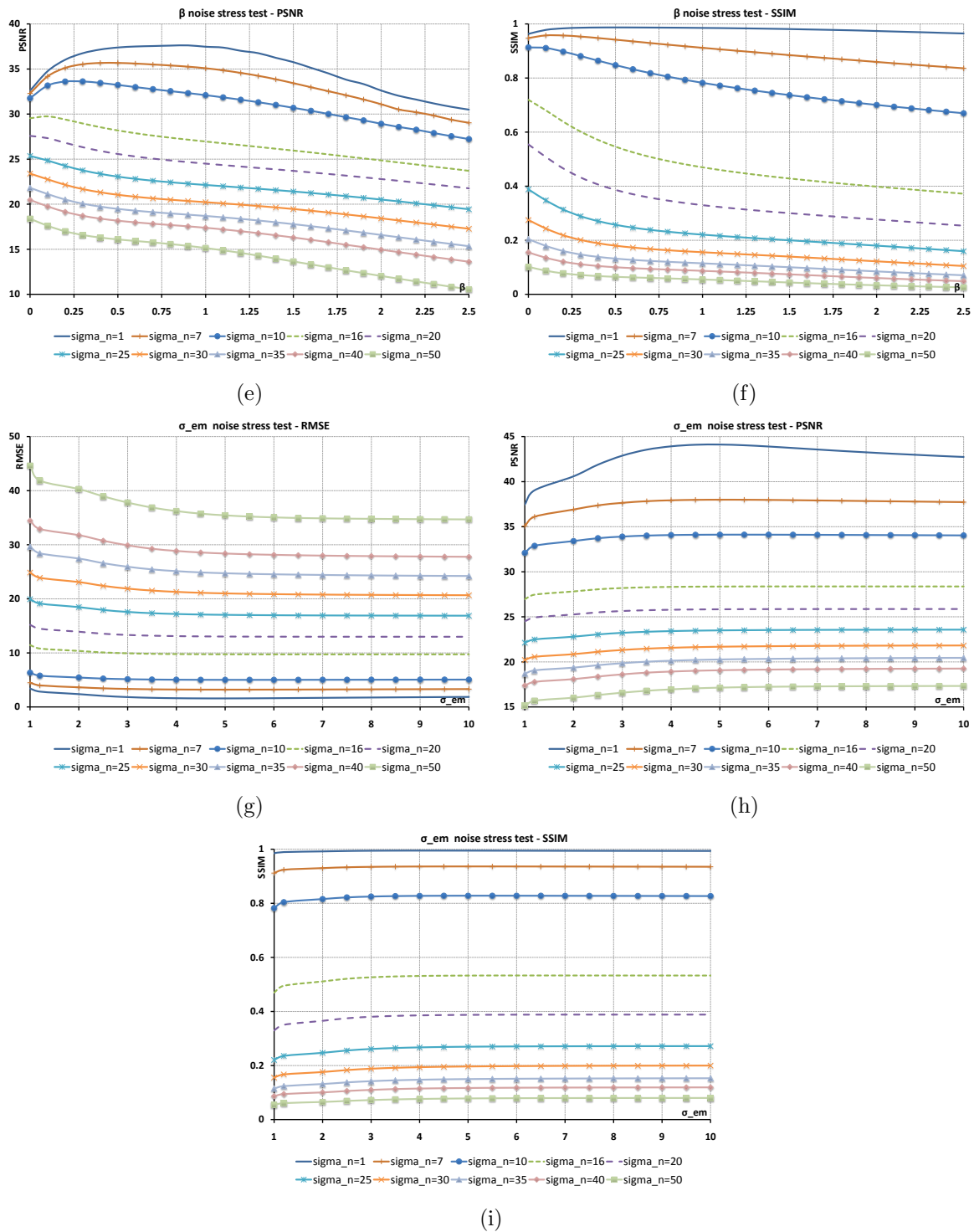


Fig. 5.15 – (continued): (e) PSNR/noise evolution – β ; (f) SSIM/noise evolution – β ; (g) RMSE/noise evolution – σ_{em} ; (h) PSNR/noise evolution – σ_{em} ; (i) SSIM/noise evolution – σ_{em} .

increase in AWGN. The two input parameters control the amount of denoising (α) and edge enhancement (β) the fusion method performs on the combined information supplied from its inputs.

Another important input parameter of the proposed model is σ_{em} which controls the degree of dispersion within the employed edge maps, of singular values that usually appear because of noise contamination. Hence are avoided false gradient responses that lead to false structures which propagate through edge enhancement into the final fused result. σ_{em} is varied between 1 and 10 in increments of 0.5, to properly evaluate the influence of this input parameter on the overall behavior of the fusion model.

For illustrative purposes, only the evolutions of α , β and σ_{em} are shown in *Fig. 5.15*, analyzed using the RMSE, PSNR and SSIM quality metrics. In a similar manner, the PCA window size W_{PCA} and the number of time iterations were analyzed using the same noise stress test setting and the same quality metrics. It should be also noted that the orientation estimation can be performed independently for the denoising and deblurring terms of (5.34), using different W_{PCA} window sizes. By doing so, the orientation is determined separately, allowing for more flexibility in the fusion mechanism, since the denoising process would require a larger PCA window to benefit from an overall view of local geometry, while the edge enhancement component should be restricted to a smaller window size in order to preserve details. But not too small, as to not be able to distinguish singularities (due to noise) from small salient features. With the increase of AWGN, distinguishing between localized variations in signal intensity and small structures, comparative in size with the former, becomes even harder and some details can be lost in the denoising process. That is why the denoising PCA window size should not be too large as to filter out the smaller details. Conventionally, as empirically determined in other works related to PCA-based image filtering, the acceptable maximum window size is set to 21×21 .

Based on the noise stress analysis, partially illustrated in *Fig. 5.15*, the overall optimal behavior of the proposed fusion method can be attained as follows:

- *for weak noise contamination* the α and β input parameters should have similar values, close to 1, the σ_{em} parameter should be between 1.5 and 5, and a value of 3 for the W_{PCA} parameter should suffice. Last but not least, $K_\xi \geq 10$ and $K_\eta/K_\xi \leq 0.5$, configuration used for any σ_n .
- *for moderate noise contamination* the α and β input parameters should be: $\alpha \geq 1.5$ and $\beta \leq 0.5$, while the σ_{em} parameter should be between 5 and 7, and a value of up to 5 for the W_{PCA} parameter should be used.
- *for strong noise contamination* the α and β input parameters should be $\alpha \geq 2$ and $\beta \leq 0.3$, respectively, the σ_{em} parameter should be between 7 and 11, and a value of 7 for the W_{PCA} parameter should be enough. For high noise values, the fused result can be further enhanced by working on $G_{\sigma_{ps}} * I_s$ inputs, an approach commonly used in image processing. In this case, the input parameters require adjusting to the new inputs.

5.4.4 Concurrent fusion and denoising: a comparative analysis

In this section [LL11c], the analysis of the proposed fusion model focuses on its effectiveness with respect to other existing methods, in terms of concurrent fusion and denoising, using a comparative test scenario based on the *Clock* image set with the fusion inputs *Fig. 5.14c* and *Fig. 5.14d*, and employing for comparison purposes, several existing fusion models, variational and non-variational, summarized in *Table 5.3*.

For the comparative analysis, the tested fusion methods are evaluated using three levels of AWGN: $\sigma_n = 0$, $\sigma_n = 13$ and $\sigma_n = 30$. The first noise level, more accurately the absence of AWGN, tests the proposed model's effectiveness when employed like any other fusion method, for fusion purposes only. This will also help in establishing the best fusion reference for quality metrics that require a reference image (§4.7.3), used to better assess noise filtering performance for higher AWGN levels.

Table 5.3 – Compared fusion methods and their input parameters

#	Fusion method	Input parameters
1	Average (AVG) - [Roc99]	
2	Principal Component Analysis (PCA) - [Roc99]	
3	Laplacian Pyramid (LAP) - [Roc99]	L - decomposition level H - high-pass combination: - choose-max - max - saliency/match - sm w - area (for sm)
4	Filter-Subtract-Decimate Pyramid (FSD) - [Roc99]	L - decomposition level H - high-pass combination: - choose-max - max - saliency/match - sm w - area (for sm)
5	Ratio Pyramid (RAT) - [Roc99]	L - decomposition level H - high-pass combination: - choose-max - max - saliency/match - sm w - area (for sm)
6	Contrast Pyramid (CON) - [Roc99]	L - decomposition level H - high-pass combination: - choose-max - max - saliency/match - sm w - area (for sm)
7	Gradient Pyramid (GRA) - [Roc99]	L - decomposition level H - high-pass combination: - choose-max - max - saliency/match - sm w - area (for sm)
8	Discrete Wavelet Transform - Daubechies Spline DBSS(2,2) (DWT) - [Roc99]	L - decomposition level H - high-pass combination: - choose-max - max - saliency/match - sm w - area (for sm)
9	Shift Invariant Discrete Wavelet Transform with Haar (SIDWT) - [Roc99]	L - decomposition level H - high-pass combination: - choose-max - max - saliency/match - sm w - area (for sm)
Variational approaches		
10	Socolinsky (Soc) - [Soc00a]	IT - number of iterations dt - optimization step
11	Wang-Ye (WaY) - [WY07]	IT - number of iterations dt - optimization step w - neighborhood (similar to area) n - selectivity σ - standard deviation
12	John-Vorontsov (JoV) - [JV05]	IT - number of iterations dt - optimization step σ - standard deviation
13	Pop (Pop) - [Pop08]	IT - number of iterations dt - optimization step β - fusion weight γ - regularization weight
14	Proposed fusion model (Proposed)	IT - number of iterations dt - optimization step (τ) α - noise filtering weight β - fusion weight W_{PCA} - PCA window size K_ξ - anisotropic barrier K_η - anisotropic barrier σ_{em} - standard deviation (edge map)

As not all fusion methods were designed for simultaneous noise filtering, only the most relevant (or their adapted versions) are used for comparison when the AWGN is different from 0 ($\sigma_n = 13$ and $\sigma_n = 30$). In order to properly compare the performances of the fusion methods listed in *Table 5.3*, an optimization process must be carried out prior to comparing the fused results. Since a similar comparative analysis, using the *Clock* image set, was conducted in [Pop08], the optimized parameter sets for the existing fusion methods are used as determined in [Pop08]. Based on the model parametrization described in §5.4.3, the proposed fusion model is coarsely optimized so as to provide results within its best attainable performances.

For the first comparative analysis, when no AWGN is present and the input image set is assumed quasi-“ideal”, the comparative quality assessment can be performed only using quality metrics that do not require a reference image (§4.6), since no ideal fused result exists.

By analyzing the particularities of each fusion quality metric, the best suited for parameter optimization proves to be the Q_W [Pie04] metric, because it weights discriminately the different regions of the fused image, based on their relevance, in terms of visual acuity, as also concluded by Pop [Pop08]. Its definition is inspired from the human visual system (HVS) and has a dynamic range between $[-1;1]$, analogous in interpretation to the SSIM and MSSIM.

On the other hand, the $rSFe$ fusion quality metric behaves more as fusion fidelity indicator, since its ideal value is $rSFe = 0$, meaning that an ideal fusion process has taken place, while $rSFe > 0$ translates into an over-fused image, with some distortion or noise introduced. Finally, $rSFe < 0$ indicates an under-fused image, with lost of meaningful information. Hence, the smaller the $rSFe$'s absolute value, the better the fused image. Although, the $Q^{AB/F}$ fusion metric is useful in evaluating a fusion process from several points of view (artifacts, information loss, etc.), it presents a multitude of parameters that require tweaking, and are often application-dependent, characteristic that further complicates the quality evaluation and parameter optimization process.

The fusion performances, objectively assessed using the Q_W , $rSFe$ and $Q^{AB/F}$ fusion quality metrics are presented in *Table 5.4* along with the list of optimized parameters associated with each fusion method.

The fusion quality metrics were parameterized as follows: for the Q_W a 9×9 estimation window was used with a *max* selection criterion. The saliency reference information in this case, is the variance map of each reference input image obtained using a 5×5 sliding window, illustrated for both inputs in *Fig. 5.16*.

In computing the $rSFe$ a 9×9 window was used, while the $Q^{AB/F}$ metric was employed with the following set of parameters: $L = 1$, $\Gamma_g = 0.9994$, $\kappa_g = -15$, $\sigma_g = 0.5$ and $\Gamma_\alpha = 0.9879$, $\kappa_\alpha = -22$, $\sigma_\alpha = 0.8$.

As it can be seen from the experimental setting, qualitatively described in *Table 5.4*, the proposed fusion method (**Proposed- Q_W**) result scores the highest score measured by the Q_W fusion metric along with the SIDWT fusion method result. The optimization of the fusion methods was done, as already mentioned, with the purpose of attaining the highest possible value of the Q_W , since from a fusion point of view, this metric is the most relevant. The **Proposed- $rSFe$** result is shown in *Table 5.4* with the purpose of illustrating just how close to an ideal fusion, from an $rSFe$ point of view, the fused result can be, when the fusion model is properly parameterized. Even when optimized for the

Table 5.4 – Comparative analysis – AWGN of $\sigma_n = 0$

Fusion method	Optimal parameter set	Quality metrics		
		Q_W	$rSFe$	$Q^{AB/F}$
AVG		0.907	-0.39	0.656
PCA		0.909	-0.385	0.664
LAP	L=6 H= <i>sm</i> w=3×3	0.957	-0.037	0.751
FSD	L=3 H= <i>max</i>	0.92	-0.291	0.7
RAT	L=4 H= <i>sm</i> w=9×9	0.912	-0.377	0.667
CON	L=6 H= <i>sm</i> w=3×3	0.956	-0.028	0.752
GRA	L=3 H= <i>max</i>	0.921	-0.293	0.702
DWT	L=7 H= <i>sm</i> w=9×9	0.951	-0.033	0.73
SIDWT	L=4 H= <i>sm</i> w=3×3	0.958	-0.062	0.751
Soc	IT=26 dt=0.25	0.953	-0.05	0.735
WaY	IT=114 dt=0.25 w=5×5 n=1 $\sigma=10$	0.953	-0.147	0.747
JoV	IT=55 dt=0.0003 $\sigma=5$	0.956	-0.088	0.761
Pop-out1	IT=4032 dt=0.1 $\beta=0.01$ $\gamma=2.49$	0.949	-0.056	0.739
Pop-out2		0.955	-0.038	0.75
Proposed- Q_W	IT=6 dt=0.1 $\alpha=0.1$ $\beta=1.2$ $W_{PCA}=3\times 3$ $K_\xi=2$ $K_\eta=0.4$ $\sigma_{em}=5$	0.958	-0.105	0.761
Proposed- $rSFe$	IT=5 dt=0.1 $\alpha=0.2$ $\beta=1$ $W_{PCA}=3\times 3$ $K_\xi=10$ $K_\eta=5$ $\sigma_{em}=3$	0.95	0.0004	0.752

$rSFe$ fusion metric, the fused result scores well on the other two fusion metric scales. From a $Q^{AB/F}$ metric point of view, the proposed method scores the second best score at a negligible difference of 0.0004 from the highest score.

Remark As previously mentioned in §4.5.4, the **Pop** variational fusion method has two outputs, since it is an “ S inputs – S outputs” method with theoretical converging outputs toward a single solution, for a very large number of iterations, theoretically infinite. That is why there exist two output results, *i.e.*, **Pop-out1** and **Pop-out2**.

The fused results pertaining to the experimental setting described in Table 5.4 are illustrated in Fig. 5.17.

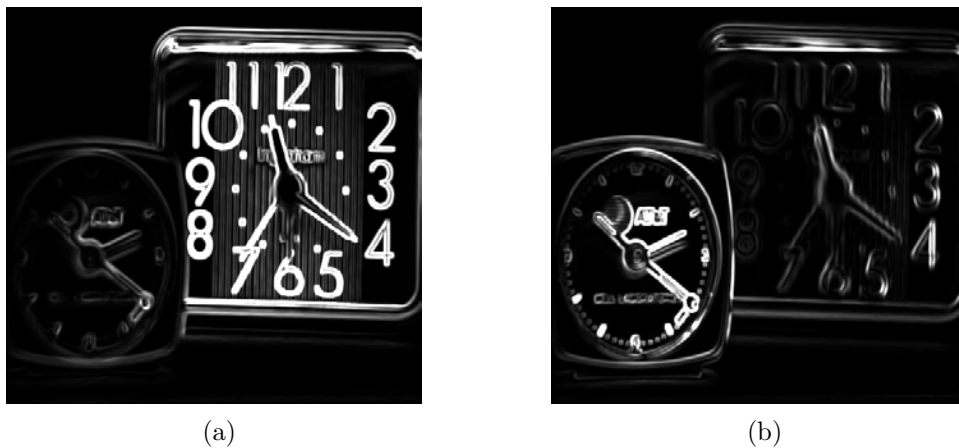


Fig. 5.16 – I_1 and I_2 's variance maps – used in computing the Q_W fusion quality metric: (a) I_1 's variance map; (b) I_2 's variance map.

In the following, the analysis is focused on the selected fusion models' behavior for medium AWGN ($\sigma_n = 13$) contamination and strong AWGN ($\sigma_n = 30$) contamination, respectively. As previously mentioned not all the fusion methods compared in *Table 5.4* are implicitly suited for concurrent fusion and denoising, thus only the more robust are retained for the following comparative analyses. Furthermore, the **AVG** method serves as a control reference point since it is the most basic form of fusion.

The **JoV** method can employ a TV minimization approach for fusing noisy images, as suggested but not tested in [JV05]. A similar adaptation is used by the **Pop** method, where a diffusion and regularization term is added, linked to the general fusion model

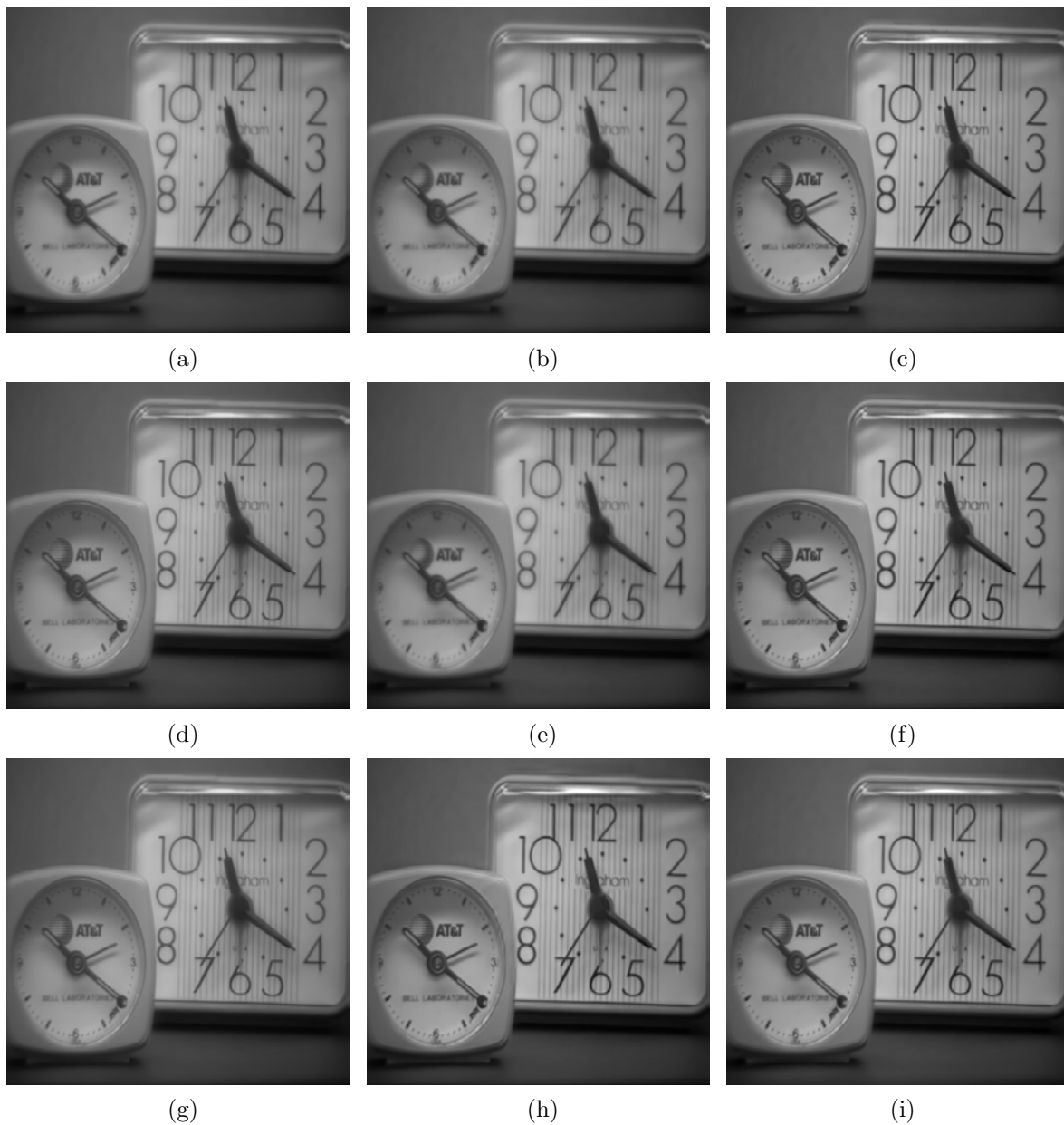


Fig. 5.17 – *Comparative analysis – Table 5.4: (a) AVG fused result; (b) PCA fused result; (c) LAP fused result; (d) FSD fused result; (e) RAT fused result; (f) CON fused result; (g) GRA fused result; (h) DWT fused result; (i) SIDWT fused result.*

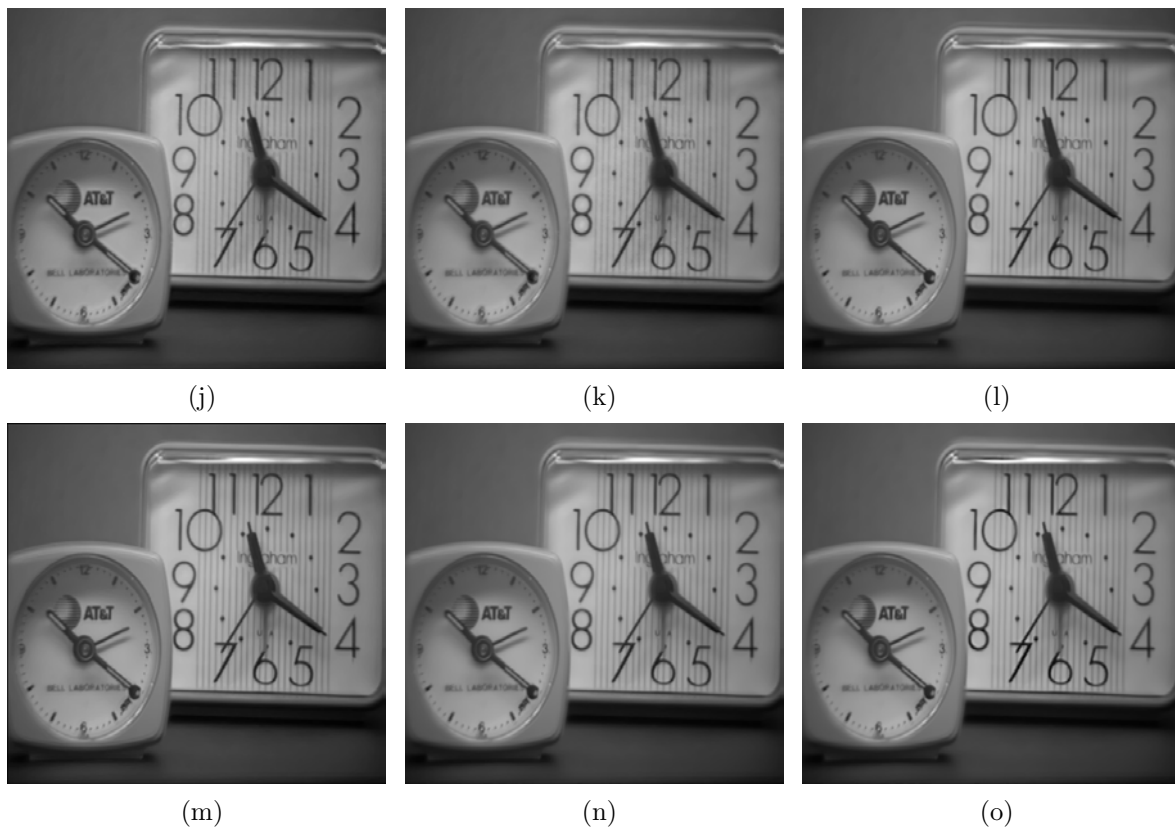


Fig. 5.17 – (continued): (j) *Soc* fused result; (k) *WaY* fused result; (l) *JoV* fused result; (m) *Pop-out2* fused result; (n) *Proposed- Q_W* fused result; (o) *Proposed-rSFe* fused result.

[Pop08]. As for the **DWT** and **SIDWT** fusion models, their adaptation to noisy inputs follows the lines of the approach suggested in [PX03], where the DWT coefficients are denoised prior to being used in the fusion process. In order to maintain consistency with the general formalism employed by the two methods, the *VisuShrink* approach is used, the denoising being performed by means of a noise estimation step (MAD⁵) to properly separate the wavelet coefficients in: noise coefficients and information coefficients.

The comparative analysis is carried out using the previously established guidelines, following a Q_W optimization approach (*Appendix A*), using the existing methods' optimization performed in [Pop08]. The previous experimental results, described in *Table 5.4*, help in selecting a fused reference in order to thoroughly assess the combined fusion–denoising performances of the tested methods. Based on the quality metrics scores from *Table 5.4* and aiming to maintain objectivity and a bias-free assessment, the **LAP** fused result (*Fig. 5.17d*) is selected as the fused reference. Thus, the fused reference is among the results having the highest scores, quality-wise, while the **LAP** method used in obtaining the reference result is not further used in the noise comparative analysis, hence providing a bias-free assessment.

The results from the previous test scenarios, *i.e.*, for an AWGN of $\sigma_n = 13$ and $\sigma_n = 30$, are summarized in *Table 5.5* and *Table 5.6*, respectively. The reference-based quality metrics used to assess the performance of the compared fusion models are part

⁵Median Absolute Deviation

Table 5.5 – Comparative analysis – AWGN of $\sigma_n = 13$

Fusion method	Optimal parameter set	Fusion quality metrics			Reference quality metrics						
		Q_W	$rSFe$	$Q^{AB/F}$	RMSE	PSNR	SSIM	MSSIM	VSNR	VIF	MI
AVG		0.833	0.726	0.295	10.913	27.371	0.557	0.904	21.485	0.354	1.981
DWT	L=7 H= <i>max</i>	0.79	2.103	0.257	17.427	23.305	0.358	0.823	19.276	0.336	1.502
SIDWT	L=5 H= <i>max</i>	0.821	1.854	0.292	15.461	24.345	0.395	0.861	21.852	0.383	1.618
DWT- <i>soft</i>	L=7 L _n =1 H= <i>max</i>	0.885	0.439	0.335	10.112	28.033	0.637	0.89	19.568	0.352	2.209
DWT- <i>hard</i>	L=7 L _n =2 H= <i>max</i>	0.877	0.503	0.356	9.948	28.175	0.674	0.892	19.853	0.333	2.284
SIDWT- <i>soft</i>	L=5 L _n =1 H= <i>max</i>	0.929	0.021	0.425	6.837	31.433	0.798	0.932	21.448	0.432	2.726
SIDWT- <i>hard</i>	L=5 L _n =2 H= <i>max</i>	0.931	-0.082	0.477	5.771	32.905	0.911	0.965	23.275	0.455	3.055
JoV	IT=339 dt=0.0001 $\sigma=5$ $\alpha=2500$ $\beta=0.9$	0.855	1.197	0.328	11.585	26.852	0.524	0.906	24.569	0.418	1.961
Pop-out1	IT=35 dt=0.1 $\alpha=0.7$ $\beta=0.3$ $\gamma=1.5$ $K_\xi=5$ $K_\eta=2$	0.864	-0.25	0.424	9.557	28.523	0.878	0.94	18.489	0.391	2.657
Pop-out2		0.925	-0.161	0.485	7.904	30.173	0.902	0.959	21.517	0.436	2.976
Proposed- Q_W	IT=18 dt=0.1 $\alpha=1.6$ $\beta=0.3$ $W_{PCA}=5 \times 5$ $K_\xi=15$ $K_\eta=1.5$ $\sigma_{em}=5$	0.936	-0.046	0.524	5.162	33.874	0.879	0.965	26.029	0.482	3.027
Proposed	IT=16 dt=0.1 $\alpha=1.7$ $\beta=0.4$ $W_{PCA}=5 \times 5$ $K_\xi=10$ $K_\eta=5$ $\sigma_{em}=5$	0.932	-0.048	0.478	5.219	33.777	0.885	0.965	25.993	0.48	3.04

of the *MeTriX MuX Visual Quality Assessment Package* [Gau11], an additional step in eliminating any quality metrics implementation bias.

Based on the analysis of the experimental data from Table 5.4 – 5.6 it can be inferred that the proposed method has achieved its expected goals by providing good quality results through image fusion, even in less than ideal conditions, such as AWGN contamination. The quality metric scores clearly underline the proposed method’s ability to simultaneously fuse and denoise input images, affected by AWGN, ranging from a mild distortion up to a strong interference, not at all negligible. Fig. 5.18 selectively illustrates the fused results from the test scenarios summarized in Table 5.5 and Table 5.6.

Remark Optimizing the proposed fusion method using the Q_W quality metric by decreasing the K_η/K_ξ ratio can lead to unwanted artifacts, as illustrated in Fig. 5.18d. By providing a second test result in the form of **Proposed** for each experimental setting,

Table 5.6 – Comparative analysis – AWGN of $\sigma_n = 30$

Fusion method	Optimal parameter set	Fusion quality metrics			Reference quality metrics						
		Q_W	$rSFe$	$Q^{AB/F}$	RMSE	PSNR	SSIM	MSSIM	VSNR	VIF	MI
AVG		0.656	2.741	0.172	21.706	21.398	0.247	0.766	17.385	0.212	1.18
DWT	L=6 H= <i>max</i>	0.519	5.691	0.117	38.071	16.518	0.132	0.614	11.86	0.18	0.719
SIDWT	L=5 H= <i>max</i>	0.56	5.2	0.14	34.479	17.379	0.149	0.669	13.866	0.212	0.786
DWT- <i>ps</i>	L=6 H= <i>max</i> $\sigma_{ps}=1$	0.855	0.247	0.28	11.925	26.601	0.59	0.806	15.298	0.251	1.945
SIDWT- <i>ps</i>	L=5 H= <i>max</i> $\sigma_{ps}=1$	0.876	0.159	0.308	13.207	25.714	0.592	0.78	13.96	0.205	1.845
DWT- <i>soft</i>	L=6 L _n =2 H= <i>max</i>	0.811	0.152	0.258	19.516	22.322	0.382	0.719	13.911	0.182	1.467
DWT- <i>hard</i>	L=6 L _n =2 H= <i>max</i>	0.729	1.818	0.214	10.519	27.69	0.625	0.835	16.442	0.271	2.092
SIDWT- <i>soft</i>	L=5 L _n =2 H= <i>max</i>	0.876	-0.328	0.345	8.766	29.274	0.801	0.894	17.367	0.289	2.391
SIDWT- <i>hard</i>	L=5 L _n =2 H= <i>max</i>	0.884	-0.048	0.342	8.808	29.233	0.775	0.894	18.576	0.293	2.369
JoV	IT=179 dt=0.0001 $\sigma=5$ $\alpha=2500$ $\beta=0.07$	0.641	3.525	0.172	25.491	20.002	0.217	0.74	16.383	0.221	1.046
Pop-out1	IT=26 dt=0.1 $\alpha=0.8$ $\beta=0.2$ $\gamma=1.5$ $K_\xi=18$ $K_\eta=6$	0.774	-0.264	0.28	11.978	26.562	0.748	0.863	15.166	0.242	2.077
Pop-out2		0.881	-0.146	0.35	9.991	28.138	0.787	0.895	17.785	0.286	2.305
Proposed- Q_W	IT=20 dt=0.1 $\alpha=1$ $\beta=1.2$ $W_{PCA}=5 \times 5$ $K_\xi=10$ $K_\eta=2$ $\sigma_{em}=7$ $\sigma_{ps}=1$	0.904	-0.151	0.4	7.474	30.659	0.806	0.911	19.692	0.33	2.376
Proposed	IT=20 dt=0.1 $\alpha=1$ $\beta=1.2$ $W_{PCA}=5 \times 5$ $K_\xi=10$ $K_\eta=5$ $\sigma_{em}=7$ $\sigma_{ps}=1$	0.902	-0.171	0.38	7.406	30.738	0.816	0.915	19.771	0.328	2.385

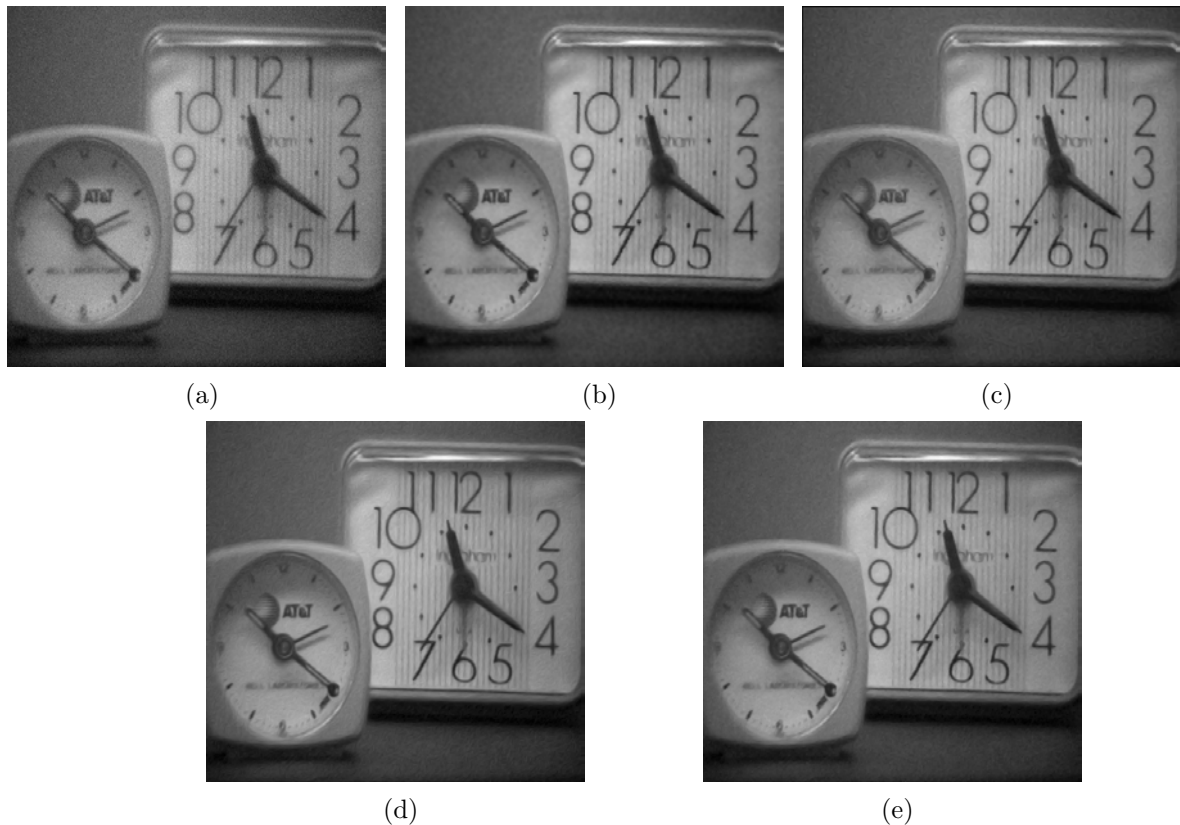


Fig. 5.18 – Comparative analysis – Table 5.5: AWGN of $\sigma_n = 13$ – (a) **AVG** fused result; (b) **SIDWT-hard** fused result; (c) **Pop-out2** fused result; (d) **Proposed- Q_W** fused result; (e) **Proposed** fused result.

it can be shown that by making a small tradeoff between the Q_W quality score and the absence of unwanted artifacts, the proposed fusion method can still yield superior results (see Table 5.5 and Table 5.6). This is especially the case of the test scenario described in Table 5.6, where the tradeoff is in fact the better result when compared to the reference fused result – **LAP** for $\sigma_n = 0$ (Fig. 5.17c).

Moreover, this proves that, although the Q_W quality metric is inspired by the HVS and adapted to discriminately assess different regions of an image based on their pertinence and salient information content, it is not entirely suited for simultaneously assessing salient information fusion and denoising.

Another important remark concerns the use of the additional parameter σ_{ps} for high AWGN levels. It is a common practice in image processing to stabilize an input or to simply preprocess it by means of a Gaussian pre-smoothing. In the present case, for high AWGN levels, the fusion process can be performed on $I_s^{\sigma_{ps}}$ inputs in order to reduce the initial image entropy, thus increasing the quality of the final result, as shown in §5.4.2.

This preprocessing step is similar to the *VisuShrink* approach used in conjunction with the DWT fusion methods. To illustrate this fact the **DWT- ps** and **SIDWT- ps** fusion results are obtained by replacing the *VisuShrink* with a simple Gaussian pre-smoothing (Table 5.6). The **DWT- ps** result demonstrates that sometimes simpler is better, and can increase noise robustness while providing acceptable results. Combining this pre-smoothing stage with the proposed method produces superior results to any of

the compared fusion methods, as it can be seen in *Table 5.6*. This is due to the model’s inherent anisotropic behavior combined with the stabilized input entropy obtained through pre-smoothing.

After analyzing the reference-based quality metric scores of the proposed method in both AWGN test scenarios, it can be concluded that the method performs well in filtering, preserving and enhancing the salient features extracted from its inputs. On a related note, the SSIM–MSSIM discrepancy from *Table 5.5* is, to some extent, the consequence of the small artifacts introduced by the strong anisotropic behavior of the method, when decreasing too much the K_η/K_ξ ratio.

One simple way of counteracting this effect when optimizing the method using Q_W as a reference metric, thus using a small anisotropic barrier ratio, is to use the previously mentioned pre-smoothing technique with a very small σ_{ps} . Since the SSIM measures the response to structured information, the artifacts register as false information when compared to the reference image.

In themselves, due to their size, the artifacts are not qualitatively significant when properly measured by the MSSIM, since a multiscale assessment is closer to the behavior of the HVS. The MSSIM is in this case more relevant, and supersedes the SSIM since it “supplies more flexibility than previous single-scale methods in incorporating the variations of viewing conditions”, as underlined by Wang *et al.* in [WSB03].

5.5 Potential application areas

So far, application-wise, section §5.4 has discussed and experimentally analyzed two types of fusion scenarios, *i.e.*, multi-exposure image fusion (*Fig. 5.13*) and multifocus image fusion (*Fig. 5.7*, *Fig. 5.8* and *Fig. 5.14*). Two of these fusion scenarios (*Fig. 5.8* and *Fig. 5.14*) were tested using simulated AWGN of known σ_n , with the initial noise, estimated and considered either as a noise bias, or as being of negligible intensity and filtered out using an anisotropic diffusion filter, while the other two (*Fig. 5.7* and *Fig. 5.13*) were tested “as is”, with an unknown noise contamination, in this case due to color-to-grayscale conversion.

The proposed method does not claim to be universally applicable, and to this end, this section is dedicated to presenting several potential application areas, image fusion-wise, where the use of the proposed method can prove useful, and where its particular characteristics can ensure superior results to other fusion techniques, both for noise filtering as well as for salient feature detection, transfer and enhancement.

The potential applications areas tested and discussed in this section include, but are not limited to:

- multifocus image fusion
- multi-exposure image fusion
- medical imaging
- remote sensing image fusion
- enhanced vision

The first two examples (*Fig. 5.19* and *Fig. 5.20*) illustrate the joint fusion–denoising capabilities of the proposed method in multifocus image fusion scenarios, with emphasis in the first example, *i.e.*, *Fig. 5.19*, on the actual denoising (*Fig. 5.19f*). The second example

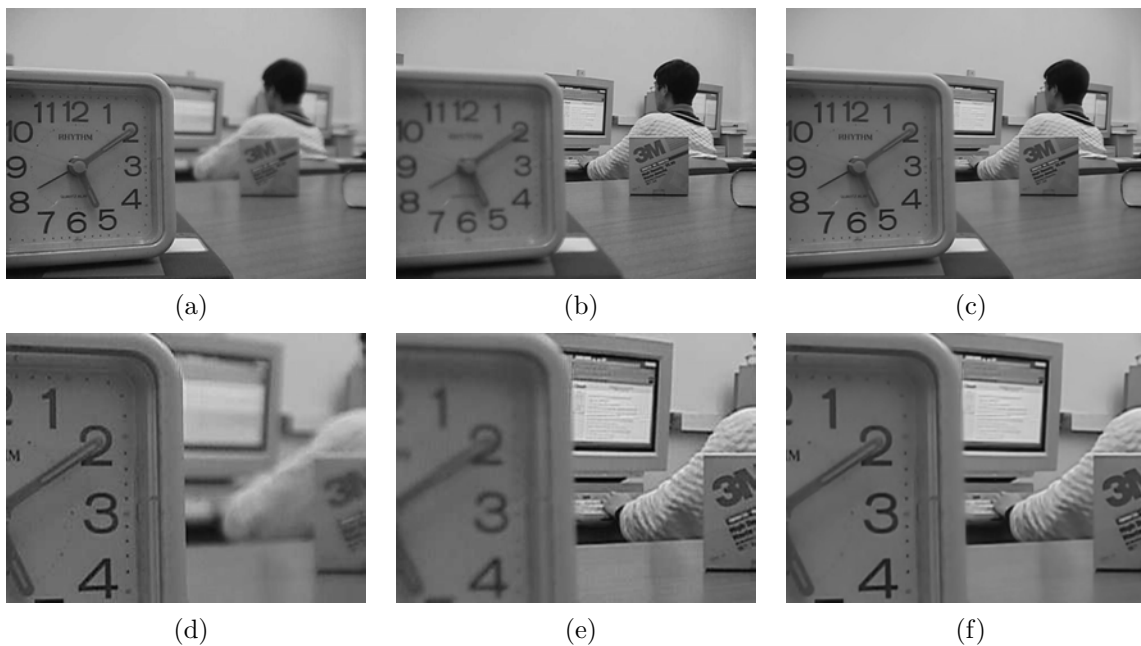


Fig. 5.19 – Multifocus image fusion application example: *Lab* image set – (a) I_1 and detail (d); (b) I_2 and detail (e); (c) \tilde{I} fused result and detail (f).

illustrates an even more complex situation, when the input images are contaminated with a quasi-structured interference, where the noise layout resembles a textured surface (Fig. 5.20d and Fig. 5.20e).

In this case, i.e., Fig. 5.20, the fused result not only successfully filters out the unwanted noise, but moreover, eliminates the texture-like interference, thus underlining the advantages of its anisotropic design (Fig. 5.20f).

The third example (Fig. 5.21) illustrates a multi-exposure fusion scenario, where the original input images are severely affected by a noise contaminant of unknown distribution (Fig. 5.21d and Fig. 5.21e). Once again the duality of the proposed joint fusion–denoising model is highlighted by the fused result (Fig. 5.21f) both in terms of fusion efficiency and

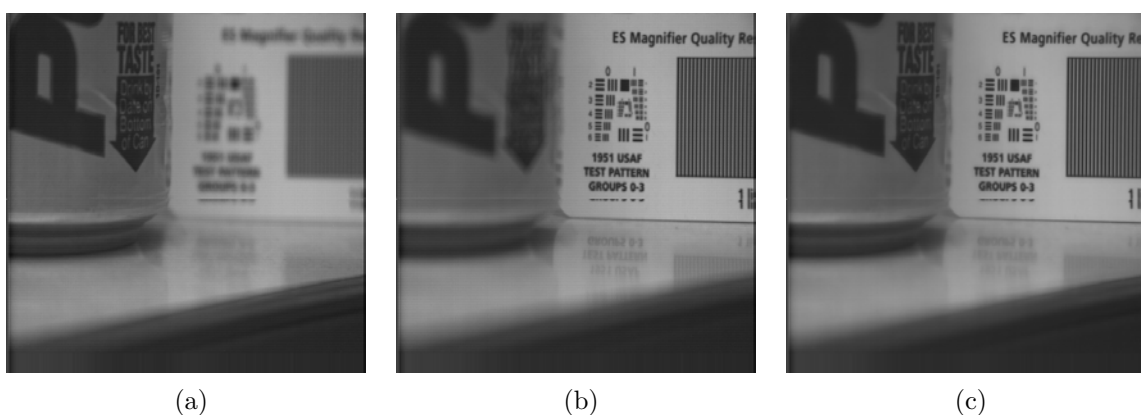


Fig. 5.20 – Multifocus image fusion application example: *Pepsi* image set – (a) I_1 ; (b) I_2 ; (c) \tilde{I} fused result.

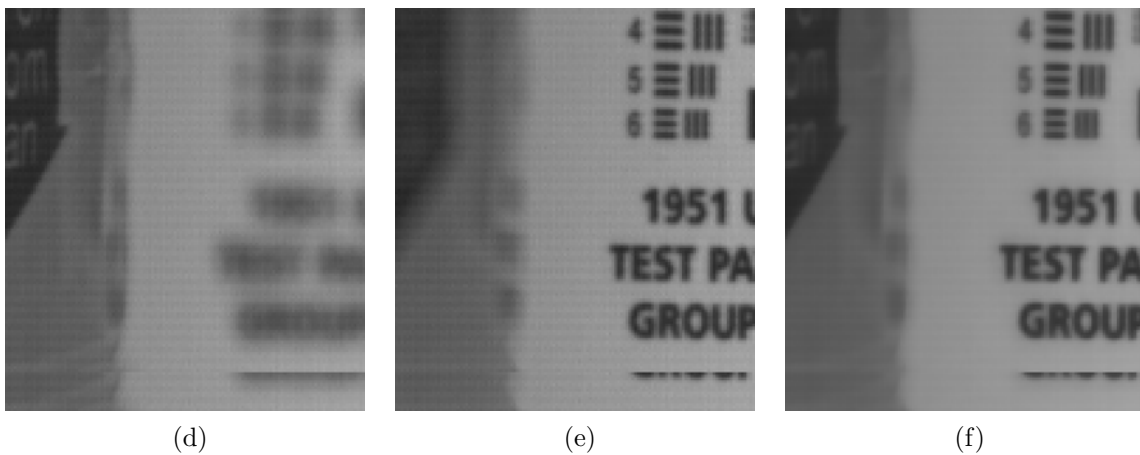


Fig. 5.20 – (continued): (d) I_1 detail; (e) I_2 detail; (f) \tilde{I} fused result detail.

in terms of denoising performance.

Remark All previous examples used the original image sets, i.e., *Lab*, *Pepsi* and *Battlefield*, as they are available at [ECE11]. Since all these original image sets are contaminated versions of the “ideal” image set, and since this set is either not available or it does not exist altogether, the quality assessment proves difficult, especially if using dedicated fusion quality metrics, since their use would under-assess the quality of the fused result, as previously discussed in §4.7.4.

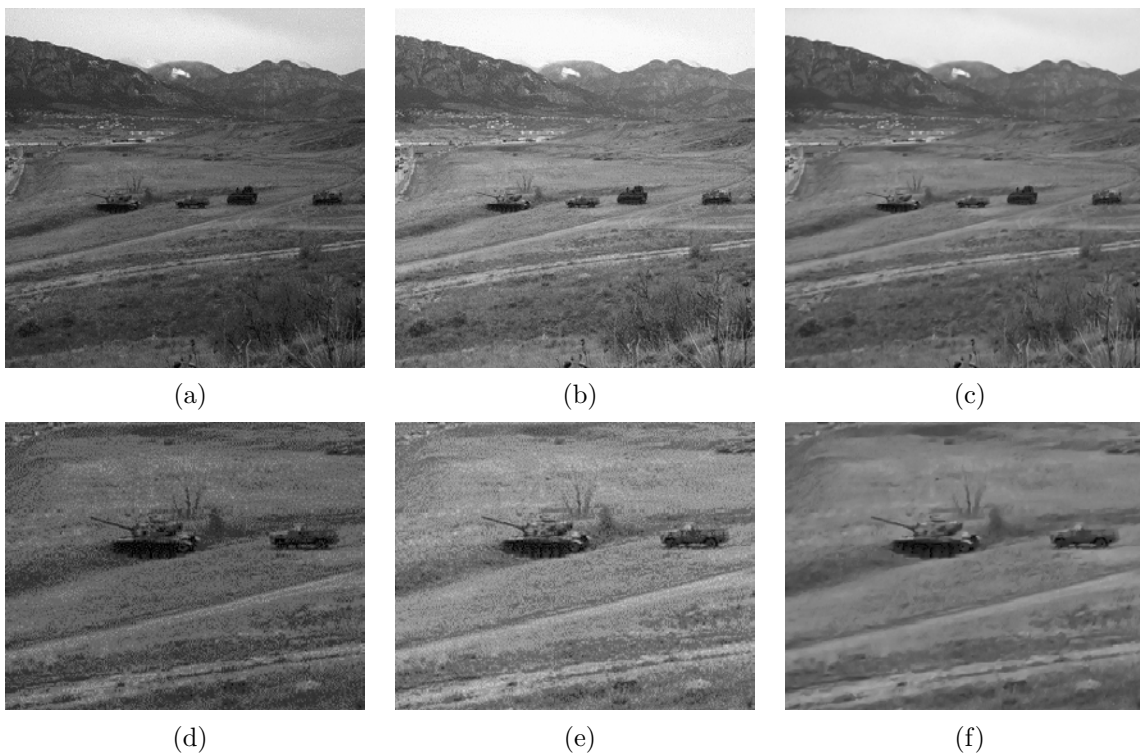


Fig. 5.21 – Multi-exposure image fusion application example: *Battlefield* image set – (a) I_1 and detail (d); (b) I_2 and detail (e); (c) \tilde{I} fused result and detail (f).

The next example illustrates the use of the proposed fusion model in medical imaging, fusing a CT⁶ image (Fig. 5.22a) and an MRI image (Fig. 5.22b), available at [Ima11a], in order to improve diagnostic accuracy and integrate the two complementary medical imaging techniques.

Remark Properly assessing the quality of the fused result is somehow subjective in this case, since for this type of images a human expert opinion is of paramount importance, being the decisive factor in making a final diagnostic based on the medical imaging data. Nevertheless, as it can be seen from visually comparing Fig. 5.22e with Fig. 5.22f, the proposed fusion model successfully integrates the salient information from the two input images, while ensuring a noise-free output.

Fig. 5.23 illustrates a standard remote sensing multi-resolution image fusion scenario where the aim is to produce a fused result of both higher resolution and increased chromatic detail. In this case the proposed methods adds an extra dimension to the expected result, by producing a fused result that not only provides the required higher resolution and increased chromatic detail, but at the same time produces a coherent, noise-free result ensuring salient information preservation.

Another example of a potential application for the proposed joint fusion–denoising model is represented by enhanced vision applications, in essence a multisensor fusion process, where the specific characteristics of each sensor is combined to produce an enhanced

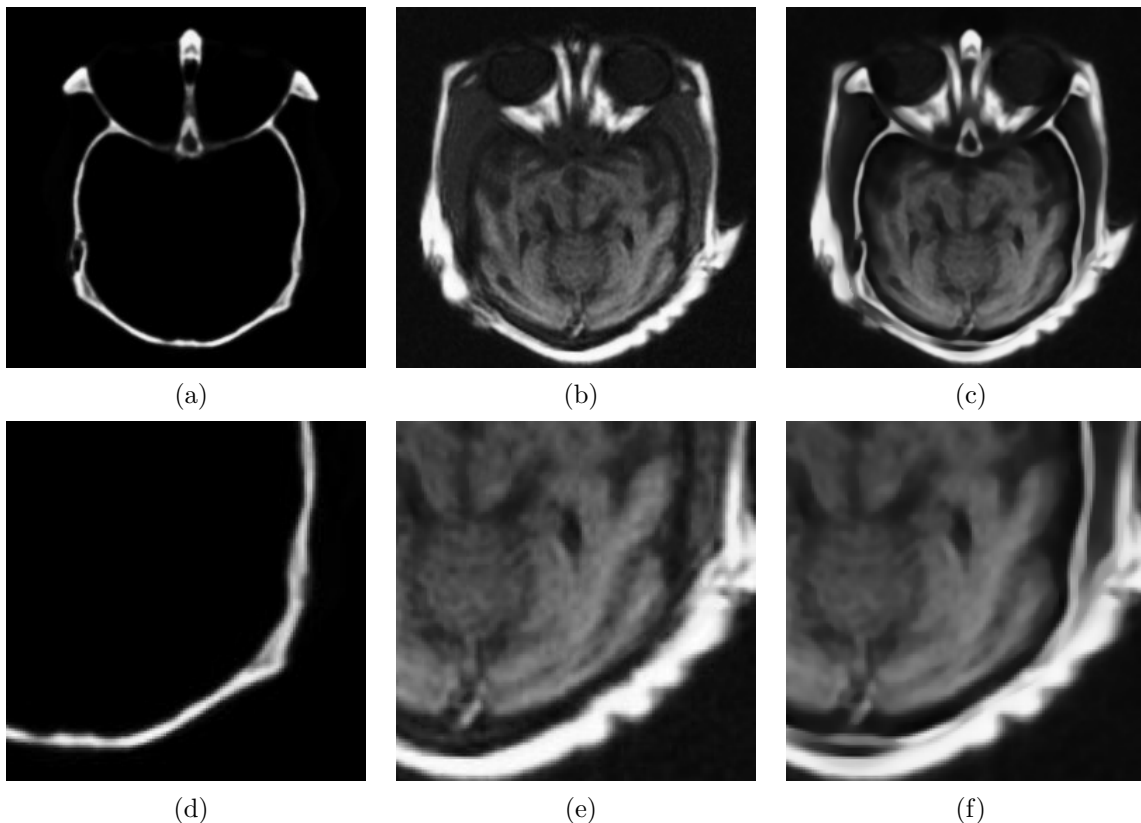


Fig. 5.22 – Medical image fusion application example: (a) I_1 CT image and detail (d); (b) I_2 MRI image and detail (e); (c) \tilde{I} fused result and detail (f).

⁶X-ray Computed Tomography

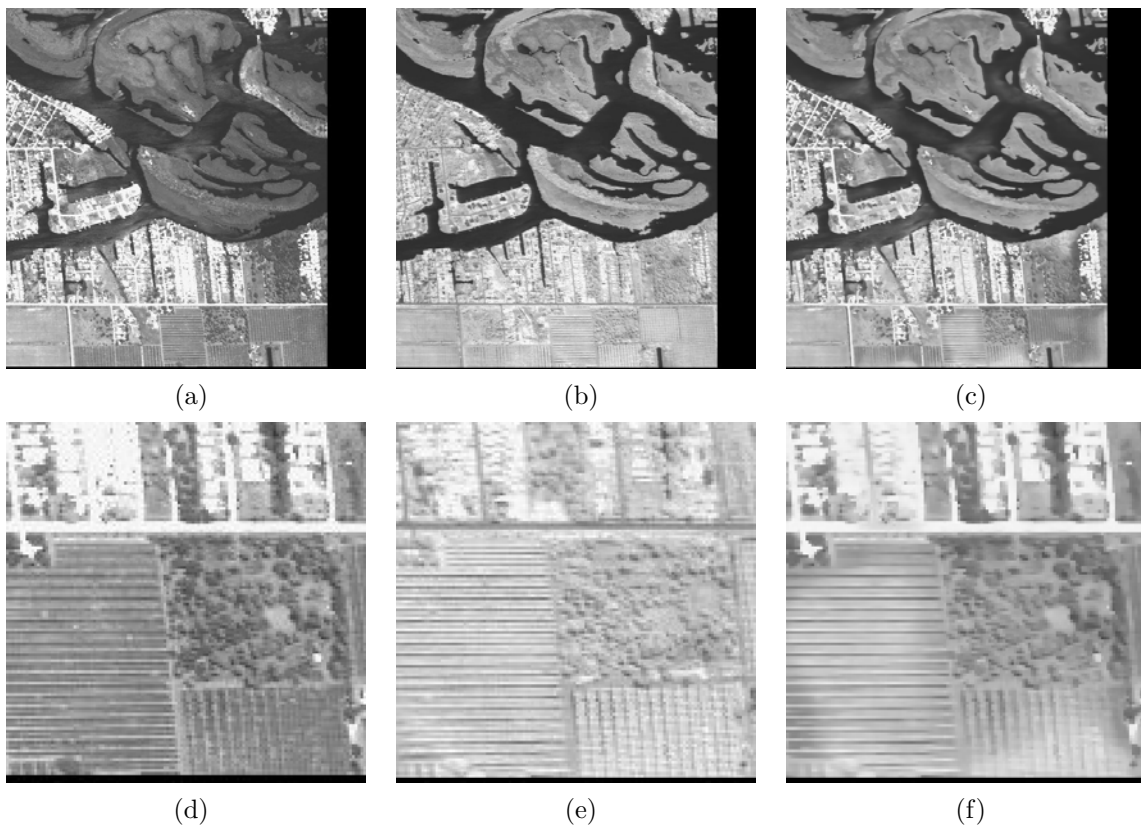


Fig. 5.23 – Remote sensing fusion application example: (a) I_1 and detail (d); (b) I_2 and detail (e); (c) \tilde{I} fused result and detail (f).

fused result. In the example illustrated in Fig. 5.24, the images from two different sensors, *i.e.*, LLTV⁷ and FLIR⁸, are combined in order to provide an enhanced view of the scene.

Table 5.7 summarizes the model parametrization for each of the discussed potential application areas, with the remark that no explicit parameter optimization was carried

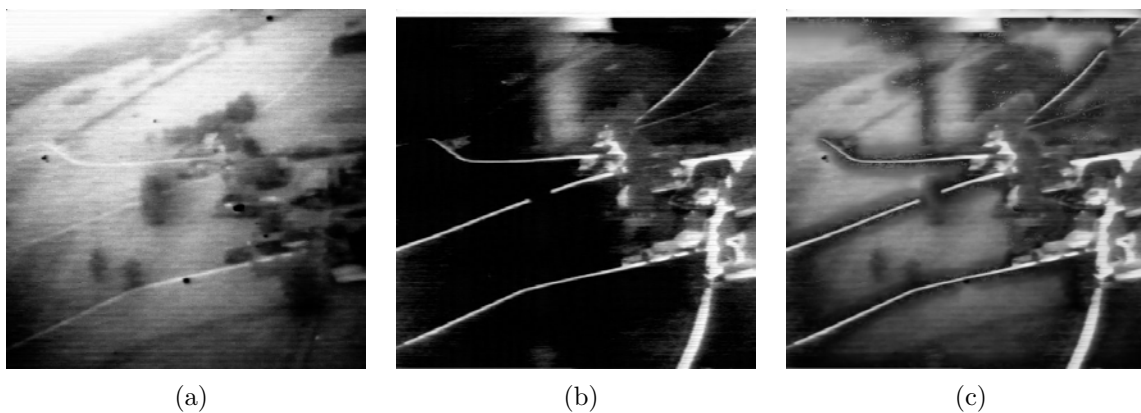


Fig. 5.24 – Enhanced vision application example: (a) I_1 LLTV image; (b) I_2 FLIR image; (c) \tilde{I} fused result.

⁷Low-light Level TV

⁸Forward Looking Infrared

Table 5.7 – Potential application areas – model parametrization

Experimental setting	Proposed model parameters							
	t	τ	W_{PCA}	K_ξ	K_η	σ_{em}	α	β
<i>Fig. 5.19</i>	1s	0.1	5	10	5	11	0.7	1
<i>Fig. 5.20</i>	0.5s	0.1	5	15	3	7	0.7	1
<i>Fig. 5.21</i>	2s	0.1	5	10	5	9	1.6	0.4
<i>Fig. 5.22</i>	3s	0.1	5	15	3	9	0.5	1
<i>Fig. 5.23</i>	1s	0.1	5	15	3	9	1	1
<i>Fig. 5.24</i>	1s	0.1	5	15	3	9	1	0.5

out in order to obtain the fused results. This also means that, if employed by any specific application, the model can be optimized and adapted to best respond to the application's requirements and consequently the quality of its output can be further increased.

Remark This section serves only as a practical example, in the sense that the use of the proposed joint fusion–denoising model is not restricted to the applications presented in §5.5, other usage areas being easily conceivable.

5.6 Conclusion

After discussing the mathematical formalization and experimentally validating the numerical model of the proposed variational model for concurrent fusion and denoising, the following conclusions can be formulated regarding its main characteristics:

- The proposed fusion model (5.31) is fundamentally different from the original proposition of John and Vorontsov [JV05], described by (4.22), in the following ways:
 - it employs an “intelligent” diffusion component in the form of the geometry-driven anisotropic diffusion term (5.35) as opposed to a Total Variation-based isotropic diffusion that was not explicitly designed for denoising (the original model has limited denoising capabilities),
 - its edge-enhancing component (5.28) is also defined anisotropically, as opposed to the original formalism that is based on a classic Gaussian-smoothed gradient map.

With these two important changes, the proposed joint fusion–denoising model possesses anisotropic fusion characteristics as well as anisotropic denoising ones, making it a fully anisotropic image processing model (the importance of anisotropy in image processing being detailed in **Chapter 2**).

- The anisotropic characteristic of the proposed fusion model is also reinforced by its numerical approximation §5.3.2 which provides an inherent anisotropic behavior for all model's components (the numerical approximation applying for all discretized quantities).
- The proposed model integrates an anisotropic denoising element together with the classic fusion component, defined with the use of a unifying variational framework.

- The intrinsic anisotropic behavior of the theoretical model is consolidated by the use of a PCA-based orientation estimation for anisotropically characterizing salient features and of a discrete interpolation scheme for the model’s numerical approximation, in order to provide sub-pixel accuracy.
- The fusion process is defined as a linear combination of its weighted inputs and its time evolution is indirectly described by the evolution of the fusion weights themselves, defined using robust error estimation theory and expressed as a TV minimization problem.
- It addresses a complex image processing paradigm, closer to real-world scenarios, *i.e.*, fusion of “imperfect” images, where “imperfect” refers to noise contamination, apart from the usual contamination factors that are normally removed through classic image fusion.

The results obtained thus far, as described in §5.4.2 and §5.4.3, show that the fusion method efficiently filters AWGN (even for high values of σ_n) while properly enhancing edges and contours, delivering a fused result of desired quality, both *in focus* and denoised.

The comparative analysis conducted in §5.4.4 underlines the proposed method’s capabilities of delivering high quality results, even for high AWGN levels. The noise filtering is performed in an anisotropic manner, hence no compromise is needed when choosing between properly denoising the input images and efficiently transferring salient information to the fused output.

The experimental analysis of the proposed model, carried out throughout **Chapter 5** also helped highlight a series of potential improvements that would further enhance the model’s performances both in terms of noise filtering and image fusion:

- The fusion process can be further improved by adding a measure of confidence (coherence) when computing the orientation θ_ξ by means of PCA.
- The edge enhancement behavior can be further strengthen in order to amend contrast preservation within the fused image.
- On the same note, an immediate improvement would also be reconsidering the initialization phase of the fusion weight functions. Currently, initializing them with $1/S$, where S represents the number of fusion inputs, provides a simple and sometimes efficient way of reducing the initial entropy, but this is entirely effective only when having a very large number of inputs. In real-world scenarios, often the number of inputs is restricted to a minimum of two or more, but not enough to completely solve the initial entropy problem. To this end, a better suited solution for initializing the weights would be through an adaptive weight process, either image-dependent or even pixel-dependent. Of course, such an approach would add to the overall processing time and should be employed only when processing time is not a stringent issue.
- Another improvement that would considerably influence the total processing time is the use of a multiscale PCA in determining θ_ξ . In this case as in the previous, careful consideration should be given to choosing the more complex solution, and a cost–benefit analysis is required in order to determine the best course of action.

C 2 C

Theoretical prerequisites – §5.2 – provided an overview of required notions, such as *error estimation theory* (viewed as a TV minimization problem) and *PCA* in vector field orientation estimation, both, theoretical concepts that directly relate to the proposed fusion model, expressed within a variational framework.

Mathematical model – §5.3 – represented an in-depth discussion of the proposed fusion model (the second major contribution of this thesis) from a theoretical perspective, comprising:

- model description,
- parameter analysis,
- model discretization,
- algorithmic description.

Experimental analysis – §5.4 – this section was dedicated to experimentally testing and validating the proposed fusion model, carried out on the following directions:

- practical comparison between sequential and concurrent processing in combined scenarios of fusion and denoising, underlying the differences between the two approaches and also the inherent advantages of the latter,
- stand-alone experimental validation and noise robustness assessment,
- model parametrization and parameter behavior analysis,
- comparative analysis using existing fusion models, previously described in **Chapter 4**

Potential application areas – §5.5 – given the fact that the proposed fusion model, in its current form, serves a general purpose, without being adapted for a specific image processing task, this section briefly discussed some of the potential application areas of the model, in its current form. For each application area, a real-world, non-artificially altered set of input images is used further proving the method's efficiency in properly filtering noise while simultaneously fusing the input images. The noise characteristic of the input images is unknown, thus the quality of the fused results also underlines the wide applicability of the proposed model, *i.e.*, the proposed fusion model is not limited to filtering AWGN.

Conclusion – §5.6 – presented the conclusions derived from the experimental analysis for the proposed *variational approach for concurrent image fusion and denoising* as well as offers several pointers in the direction of further improving and extending the proposed model.

CHAPTER 6

Conclusions, remarks, perspectives

Main Contents

6.1	Conclusions	151
6.2	Remarks	154
6.3	Perspectives	155

6.1 Conclusions

Without reiterating the closing section of each of the previous chapters, this section intends to synthesize the overall conclusions derived from this thesis as a whole, *i.e.*, starting from the general problem statement and finishing with how each requirement has been fulfilled and to what extent.

The underlying purpose of this thesis has been to analyze the possibility and feasibility of employing combined processing models for image restoration and enhancement, thus replacing the classic sequential processing chain. Moreover, the analysis was also intended to assess the flexibility of PDEs in defining image processing paradigms and their versatility in expressing a wide range of image processing problems, sometimes even diametrical in nature.

All these desiderata were addressed in a progressive manner, employing a step-by-step approach, starting with the initial theoretical analysis of PDEs in image restoration (**Chapter 2**), with the intent of establishing the fundamental prerequisites for attaining the final goal, *i.e.*, defining a functional unifying framework for image restoration and enhancement and highlighting its advantages over the classic sequential approaches. **Chapter 2** helped establish the theoretical fundamentals of PDE-based image restoration by analyzing the seminal contributions to this area of research and, based on this analysis, formulating conclusions that were subsequently used in defining the sought-after concurrent restoration–enhancement models.

Chapter 2 is concluded by discussing the appropriate way of approximating the continuous domain PDE-based models as discrete domain image processing algorithms, since these approximations schemes were further used throughout this manuscript to describe PDE-based paradigms, irrespective of their processing purpose, *i.e.*, image restoration or enhancement.

Chapter 3 introduced the first proposition for a compound image processing model in the form of the *hybrid shock filter*, a joint deblurring–denoising PDE-based model, representing the first step in defining a unified PDE-based image restoration and enhancement approach. This desideratum was brought one step closer to fulfilment by extending the initial *hybrid shock filter* capabilities to coherence enhancement (§3.5.4), which according to its definition is an image enhancement attribute.

Thus the first step, albeit partial, toward bridging these two core components of image processing is represented by the proposed *hybrid shock filter*, proving the feasibility

of combined approaches and moreover, experimentally showing their intrinsic advantages in terms of filtered quality (§3.6.3). The proposed shock filter model also proves that the two counteracting processes of deblurring and denoising, especially when expressed by means of a PDE-based framework, can be brought into synergy if certain continuous domain conditions are fulfilled and the mathematical model is properly discretized.

The success of proving the feasibility of a joint deblurring–denoising image processing model paved the way for the final stage of this thesis, *i.e.*, defining and analyzing a functional and efficient concurrent image restoration and enhancement model. The proposed model is defined as a joint fusion–denoising model, where the fusion process represents the image enhancement component while the denoising process embodies the image restoration part of the overall model.

Prior to experimentally validating and comparing the proposed fusion–denoising model, it was necessary to study and understand how the classic, as well as the fusion-specific quality metrics behave in complex test scenarios, where the notion of quality is defined in complex terms, covering robust noise filtering and proper edge preservation and in some cases edge enhancement. The difficulty of correctly assessing the model’s output result in terms of quality and ensuring that the fused result is not under-evaluated arose from the fact that the result is usually superior in terms of quality to the fusion inputs, used by the fusion-specific quality metrics as references.

The second part of **Chapter 4** addressed this quality assessment issue and experimentally analyzed the phenomena of over- and under-evaluation, showing that special consideration is required when selecting the fusion references and furthermore, that a proper reference image is not always available when evaluating image fusion models, even more so in the case of a joint fusion–denoising model. Investigating the particularities of quality assessment in joint image fusion and denoising scenarios, also raised several interesting questions regarding the gaps in the existing image fusion quality assessment methodology, which currently lacks the necessary tools for properly evaluating complex fusion models, like the proposed concurrent fusion and denoising model.

The second proposition, *i.e.*, the concurrent image fusion and denoising model, was discussed at length in **Chapter 5**, both from a theoretical and an experimental point of view, the proposed model, as previously mentioned, representing the end goal of this thesis. By defining a functional and, as the comparative analysis (§5.4.4) has proved, superior¹ fusion model the following goals were attained:

- To unequivocally prove the feasibility of concurrent approaches in image processing, as opposed to sequential processing chains.
- To provide an alternative fusion model that can provide high quality results in classic fusion scenarios as well as in fusion–denoising situations.
- Through the significant improvement in quality between the fused result and the initial fusion inputs, in fusion–denoising situations to underline the shortcomings of the existing dedicated fusion quality metrics.

As a final, overall conclusion, it needs to be stressed that through the theoretical analysis and proposed models, the most important accomplishment of this thesis is that it contributed to what is hoped to be a better and thorough understanding of the core concepts of image restoration and enhancement, to comprehending the importance and

¹in terms of quality, related to the set of compared fusion models and to the discussed test scenarios

versatility of PDEs in image processing, and last but not least to pave the way for compound image processing paradigms while underlining the key role played by the variational and PDE-based framework in modeling such models.

In terms of contribution, this thesis could be summarized as follows:

Direct contributions

- *Primary contributions:*
 - ***the hybrid shock filter*** – an original proposition derived from existing methodology, for concurrent deblurring and denoising. The proposed shock filter model is further extended to also provide coherence enhancement, an image enhancement characteristic.
 - ***the variational approach for concurrent image fusion and denoising*** – again, an original proposition that brings into synergy image restoration and image enhancement under a common framework. The proposed model is formalized using error estimation theory expressed as a TV minimization problem and anisotropic diffusion, thus obtaining a fusion model that perfectly adapts to the recent trends in image fusion, *i.e.*, combining the main fusion process with additional image processing tasks for better handling correlated visual data.
- *Secondary contribution:* through the second proposition of this thesis, *i.e.*, the variational approach for concurrent image fusion and denoising, raises the problem and at the same time the question of how to objectively assess the fused result quality in complex image fusion scenarios, where denoising is also involved as part of the fusion mechanism. Furthermore, it experimentally exemplifies how existing quality assessment methods, be they classic quality metrics or fusion-dedicated ones, have the tendency to under-evaluate fused results when those results are also denoised, and implicitly the input images (the image fusion inputs) are noisy.

Indirect contributions

- provides a proper and thorough theoretical background for all discussed notions² in order to facilitate the understanding of this thesis on the one hand, and to provide a starting point for researchers interested in further advancing image restoration and enhancement, using the PDE formalism, on the other.
- continues the work of Terebes and Pop as part of the research team's³ overall desideratum of advancing the study and methodology of PDE-based image processing by: proposing new processing paradigms, expanding the application area of existing ones and integrating the team's work in order to provide a complete spectrum of PDE-based processing solutions for image restoration and enhancement.

²while keeping the discussed topics within the thesis' area of interest and directly relating to the original contributions presented within, as clearly explained in the C2C section at the end of each chapter

³*Signal and Image research group – IMS - CNRS UMR5218*

6.2 Remarks

As a first remark, it should be reiterated the particularity of this manuscript, *i.e.*, that it is constructed on a functional framework rather than a classic approach, where the opening chapter covers the *state of the art*, while the rest of the chapters explore the theoretical proposition(s) of the thesis from various points of view.

It was this author's belief that the thesis' topics would be better addressed and presented in a functional manner, progressively, from basic to complex, to best emulate the way in which the research carried out in fulfilment of the requirements for the degree of *Doctor of Philosophy* progressed, providing thus a logically structured presentation of the addressed research topics.

Regarding the first proposed model, *i.e.*, the *hybrid shock filter*, the following remarks are in order:

- A first, immediate, remark regarding the *hybrid shock filter* is that from a theoretical point of view it represents an exercise in studying the possibility and subsequently proving the feasibility of compound image restoration and enhancement constructs.
- Although it represents a versatile and efficient image processing tool for deblurring and denoising, successfully addressing the shortcomings of the previous shock filters⁴, its current definition still leaves room for improvements.
- One future improvement would be to further increase the deblurring capabilities of the model, by addressing the filtering process in a more anisotropic manner, to ensure edge preservation and robust structure enhancement.
- In its current form, the proposed filter is semi-independent since its control functions require an initial input parameter set. A step toward decreasing this user-dependency would be to redefine the control functions so as to describe a dynamic, image-dependent behavior.

On the other hand, concerning the second proposition, *i.e.*, the concurrent fusion and denoising model, based on its experimental analysis the following remarks can be formulated:

- In its current form, the proposed fusion–denoising model is somehow bounded in terms of output performance by its initialization phase, *i.e.*, \tilde{I}_0 , since this initial value is computed using a simple averaging process.
- The edge enhancement component of the model supports further improvement, an enhancement component with an even more pronounced anisotropic characteristic would additionally increase the overall quality of fused result.
- Since the joint fusion–denoising model was initially defined as a general purpose image processing method, adapting the method's functionality to the input images' particular characteristics (adapting the method to behave in an application-specific manner) can provide a further increase in quality.

⁴to a certain degree

6.3 Perspectives

One of the main goals of this thesis, *i.e.*, bringing together image restoration and enhancement under a common, synergistic framework, can be also regarded as an incentive for continuing the study and development of new and improved compound processing models that elegantly address complex image processing problems.

Since the current trend in image processing research is to address more and more complex issues, often with immediate application value, it is this author's belief that further emphasis should be placed on continuing the study and research into developing and improving the general joint fusion–denoising model since it represents a versatile and efficient image processing tool, with an extended practical application range.

The current joint image fusion and denoising model can be further improved and extended by:

- increasing the existing edge-enhancing capabilities by redefining the model's edge enhancement component,
- defining an additional, dedicated contrast enhancement term and integrating this term into the overall joint fusion–denoising model,
- analyzing the proper way of extending the joint fusion–denoising model to 3D and color image fusion,
- further increasing the model's upper-end ($\sigma_n > 25$) noise robustness by consolidating and improving the initial image geometry descriptor for the edge-enhancing component, currently expressed as (5.28).

As an overall remark, another possible extension of the joint fusion–denoising model would be to bridge the two proposed models, *i.e.*, the *hybrid shock filter* and the joint fusion–denoising model, that is to integrate the complex domain approach of the *hybrid shock filter* into the fusion–denoising model. The benefits of such an approach remain to be determined and its overall feasibility experimentally analyzed and validated.

From a more general perspective, the underlying concept behind concurrent image restoration and enhancement can be also addressed using different methodologies and fusion approaches, *e.g.*, feature-level fusion or even decision-level fusion, numerically expressed using estimation theory or artificial neural networks.

On a related note, based on the discussion and experimental analysis carried out in §4.6, another important issue that requires addressing is the absence of a fully adequate means of assessing fusion quality in compound scenarios from today's image quality evaluation methodology. As seen from the experimental data, the current quality metrics have difficulties in simultaneously assessing denoising and deblurring and hence, one or both of these image processing tasks is under-evaluated, resulting in an overall under-evaluation of the fused result.

APPENDIX A

Concurrent fusion and denoising – model optimization

Table A.1 – Q_W optimization – concurrent fusion and denoising: comparative analysis for an AWGN of $\sigma_n = 13$ – Table 5.5

Proposed model parameters								Quality metric
t	τ	W_{PCA}	K_ξ	K_η	σ_{em}	α	β	Q_W
1.5s	0.1	3	10	5	5	2	0.3	0.928
1s	0.1	3	10	5	5	2	0.3	0.928
1s	0.1	3	10	5	7	2	0.3	0.928
1s	0.1	3	10	5	5	1.5	0.3	0.929
1s	0.1	3	10	5	5	1.5	0.5	0.929
1s	0.1	3	10	5	5	1.2	0.3	0.928
1s	0.1	3	10	5	5	1.6	0.3	0.93
1.2s	0.1	3	10	5	5	1.6	0.3	0.9306
1.2s	0.1	3	10	5	5	1.7	0.3	0.9304
1.4s	0.1	3	10	5	5	1.6	0.3	0.9309
1.6s	0.1	3	10	5	5	1.6	0.3	0.931
2s	0.1	3	10	5	5	1.6	0.3	0.9309
1.8s	0.1	3	10	5	5	1.6	0.3	0.931
1.6s	0.1	5	10	5	5	1.6	0.3	0.9313
1.6s	0.1	7	10	5	5	1.6	0.3	0.9312
1.6s	0.1	5	10	2	5	1.6	0.3	0.9355
1.6s	0.1	5	15	1.5	5	1.6	0.3	0.93602
1.6s	0.1	5	15	3	5	1.6	0.3	0.9349
1.6s	0.1	5	20	2	5	1.6	0.3	0.9355
1.6s	0.1	5	10	1	5	1.6	0.3	0.9354
1.6s	0.1	5	15	1	5	1.6	0.3	0.9358
1.7s	0.1	5	15	1.5	5	1.6	0.3	0.93608
1.5s	0.1	5	15	1.5	5	1.6	0.3	0.9359
1.8s	0.1	5	15	1.5	5	1.6	0.3	0.9361 ¹

¹ Proposed- Q_W

Table A.1 – (continued) Q_W optimization – concurrent fusion and denoising: comparative analysis for an AWGN of $\sigma_n = 13$ – Table 5.5

Proposed model parameters								Quality metric
t	τ	W_{PCA}	K_ξ	K_η	σ_{em}	α	β	Q_W
2.5s	0.1	5	15	1.5	5	1.6	0.3	0.9356
1.6s	0.1	5	10	5	5	1.6	0.4	0.9322
1.6s	0.1	5	10	5	5	1.6	0.2	0.926
1.6s	0.1	5	10	5	5	1.5	0.35	0.932
1.6s	0.1	5	10	5	5	1.6	0.35	0.932
1.6s	0.1	5	10	2	5	1.6	0.35	0.9353
1.6s	0.1	5	10	5	5	1.7	0.4	0.9321 ²
1.6s	0.1	5	10	5	5	1.6	0.5	0.9319
1.6s	0.1	5	10	5	5	1.5	0.4	0.9322
1.6s	0.1	5	10	5	5	1.3	0.4	0.9317
2s	0.1	5	10	5	5	1.5	0.4	0.9322
1.4s	0.1	5	10	5	5	1.5	0.4	0.9321

Table A.2 – Q_W optimization – concurrent fusion and denoising: comparative analysis for an AWGN of $\sigma_n = 30$ – Table 5.6

Proposed model parameters								Quality metric	
t	τ	W_{PCA}	K_ξ	K_η	σ_{em}	α	β	σ_{ps}	Q_W
2s	0.1	7	20	2	11	3	0.1	0	0.852
2s	0.1	7	15	1.5	13	3	0.1	0	0.851
1.5s	0.1	7	15	1.5	11	3	0.1	0	0.851
2.5s	0.1	7	15	1.5	11	3	0.1	0	0.854
3s	0.1	7	15	1.5	11	3	0.1	0	0.855
5s	0.1	7	15	1.5	11	3	0.1	0	0.855
2s	0.1	7	15	1.5	7	2	0.1	0.5	0.89
2s	0.1	5	10	5	7	2	0.1	0.5	0.877
2s	0.1	5	10	2	7	2	0.1	0.5	0.886
2s	0.1	5	10	1	7	2	0.1	1	0.876
2s	0.1	5	10	5	7	2	0.3	1	0.885
2s	0.1	5	10	5	7	2	0.5	1	0.895
2s	0.1	5	10	5	7	2	0.7	1	0.898

² Proposed

Table A.2 – (continued) Q_W optimization – concurrent fusion and denoising: comparative analysis for an AWGN of $\sigma_n = 30$ – Table 5.6

t	Proposed model parameters								Quality metric
	τ	W_{PCA}	K_ξ	K_η	σ_{em}	α	β	σ_{ps}	Q_W
2s	0.1	5	10	5	7	2	0.9	1	0.9
2s	0.1	5	10	5	7	2	1	1	0.9
2s	0.1	5	10	5	7	1.5	1	1	0.902
2s	0.1	5	10	5	7	1	1	1	0.902
2s	0.1	5	10	5	5	1	1	1	0.901
2s	0.1	5	10	5	7	0.5	1	1	0.9
2s	0.1	5	10	5	7	1	1.2	1	0.9021
2s	0.1	5	10	5	7	1	1.5	1	0.9017
3s	0.1	5	10	5	7	1	1.2	1	0.9021
2s	0.1	5	10	2	7	1	1.2	1	0.9045
2s	0.1	5	10	1	7	1	1.2	1	0.9045
2s	0.1	5	15	1.5	7	1	1.2	1	0.9045

Bibliography

- [AGLM93] L. Alvarez, F. Guichard, P.-L. Lions, and J.-M. Morel. Axioms and Fundamental Equations of Image Processing. *Arch. Rational Mech. Anal.*, 123(3):199–257, September 1993. 12, 30, 31
- [AK06] G. Aubert and P. Kornprobst. *Mathematical Problems in Image Processing: Partial Differential Equations and the Calculus of Variations*, volume 147 of *Applied Mathematical Sciences*. Springer-Verlag, 2nd edition, 2006. 8, 10, 13, 17, 32, 45, 46, 47
- [ALM92] L. Alvarez, P.-L. Lions, and J.-M. Morel. Image Selective Smoothing and Edge Detection by Nonlinear Diffusion. II. *SIAM J. Numer. Anal.*, 29(3):845–866, June 1992. 12, 23, 29, 117
- [AM94] L. Alvarez and L. Mazorra. Signal and image restoration using shock filters and anisotropic diffusion. *SIAM J. Numer. Anal.*, 31:590–605, April 1994. 44, 48, 55, 66
- [AV97] G. Aubert and L. Vese. A Variational Method in Image Recovery. *SIAM J. Numer. Anal.*, 34(5):1948–1979, October 1997. 21
- [Bar01] D. Barash. One-Step Deblurring and Denoising Color Images Using Partial Differential Equations. HP Laboratories Israel, January 2001. 55
- [BBSK07] L. Bar, A. Brook, N.A. Sochen, and N. Kiryati. Deblurring of Color Images Corrupted by Impulsive Noise. *IEEE Trans. Image Process.*, 16(4):1101–1111, 2007. 55
- [BCI⁺06] C. Ballester, V. Caselles, L. Igual, J. Verdera, and B. Rougé. A Variational Model for P+XS Image Fusion. *Int. J. Comput. Vision*, 69(1):43–58, August 2006. 92
- [BCRS03] M. Bertalmio, V. Caselles, B. Rougé, and A. Solé. TV Based Image Restoration with Local Constraints. *J. Sci. Comput.*, 19(1-3):95–122, December 2003. 21
- [BDFO06] J.M. Bioucas-Dias, M.A.T. Figueiredo, and J.P. Oliveira. Total Variation-Based Image Deconvolution: a Majorization–Minimization Approach. In *Proceedings of the 2006 IEEE International Conference on Acoustics, Speech, and Signal Processing*, ICASSP '06, pages II–II, 2006. 55
- [BDH06] P. Blanchard, R.L. Devaney, and G.R. Hall. *Differential equations*. Thomson Brooks/Cole, 3rd edition, 2006. 32
- [Bio11] Biometric Systems Lab – University of Bologna. FVC2000 fingerprint database. <http://bias.csr.unibo.it/fvc2000/>, 2011. xvi, 53, 54, 61

- [BK93] P.J. Burt and R.J. Kolczynski. Enhanced image capture through fusion. In *Proceedings of the 4th International Conference on Computer Vision, ICCV '93*, pages 173–182, 1993. 84
- [BKS06] L. Bar, N. Kiryati, and N.A. Sochen. Image deblurring in the presence of impulsive noise. *Int. J. Comput. Vision*, 70(3):279–298, December 2006. 55
- [BM08] I. Bloch and H. Maître. *Information Fusion in Signal and Image Processing: Major Probabilistic and Non-probabilistic Numerical Approaches*, chapter Fusion in Image Processing, pages 47–56. ISTE Ltd – John Wiley and Sons, Inc., London, UK – Hoboken, NJ, USA, 1st edition, 2008. 76
- [BS08] S. Bettahar and A.B. Stambouli. Shock filter coupled to curvature diffusion for image denoising and sharpening. *Image Vision Comput.*, 26(11):1481–1489, November 2008. 55
- [BW06] M. Breuß and M. Welk. A conservative shock filter model for the numerical approximation of conservation laws. *Appl. Math. Lett.*, 19(9):954–959, 2006. 55
- [BXZ06] R.S. Blum, Z. Xue, and Z. Zhang. *Multi-Sensor Image Fusion and Its Applications*, chapter An Overview of Image Fusion, pages 1–36. CRC Press Taylor and Francis Group, Boca Raton, FL, USA, 1st edition, 2006. 78, 79, 124, 125
- [CBFAB94] P. Charbonnier, L. Blanc-Feraud, G. Aubert, and M. Barlaud. Two deterministic half-quadratic regularization algorithms for computed imaging. In *Proceedings of the 1994 IEEE International Conference on Image Processing*, volume 2 of *ICIP '94*, pages 168–172, November 1994. 26
- [CH07] D.M. Chandler and S.S. Hemami. VSNR: A Wavelet-Based Visual Signal-to-Noise Ratio for Natural Images. *IEEE Trans. Image Process.*, 16(9):2284–2298, September 2007. 63
- [Cha87] D. Chandler. *Introduction to Modern Statistical Mechanics*. Oxford University Press, USA, 1 edition, September 1987. 9
- [Che03] M. Cheriet. Shock Filters for Character Image Enhancement and Peeling. In *Proceedings of the 7th International Conference on Document Analysis and Recognition*, volume 2 of *ICDAR '03*, pages 1247–1251, Washington, DC, USA, 2003. IEEE Computer Society. 55
- [Chi08] M. Chipot, editor. *Handbook of differential equations: stationary partial differential equations*, volume 6. Elsevier, 1st edition, 2008. 32
- [CKS01] T.F. Chan, S.H. Kang, and J. Shen. Total Variation Denoising and Enhancement of Color Images Based on the CB and HSV Color Models. *J. Visual Commun. Image Represent.*, 12(4):422–435, 2001. 21
- [CL97] A. Chambolle and P.-L. Lions. Image Recovery via Total Variation Minimization and Related Problems. *Numer. Math.*, 76:167–188, 1997. 21

- [CLBC05] N. Cvejic, A. Loza, D. Bull, and N. Canagarajah. A novel metric for performance evaluation of image fusion algorithms. *Trans. Eng. Comp. Tech.*, 7:80–85, 2005. 96
- [CLMC92] F. Catté, P.-L. Lions, J.-M. Morel, and T. Coll. Image Selective Smoothing and Edge Detection by Nonlinear Diffusion. *SIAM J. Numer. Anal.*, 29(1):182–193, February 1992. 12, 19, 36
- [CM99] T.F. Chan and P. Mulet. On the Convergence of the Lagged Diffusivity Fixed Point Method in Total Variation Image Restoration. *SIAM J. Numer. Anal.*, 36(2):354–367, February 1999. 21
- [CMST98] V. Caselles, J.-M. Morel, G. Sapiro, and A. Tannenbaum. Introduction To The Special Issue On Partial Differential Equations And Geometry-driven Diffusion In Image Processing And Analysis. *IEEE Trans. Image Process.*, 7(3):269–273, March 1998. 10
- [CMW92] R.R. Coifman, Y. Meyer, and V. Wickerhauser. Wavelet Analysis and Signal Processing. In *Wavelets And Their Applications*, pages 153–178, 1992. 83
- [Com11] Computational Vision Group, California Institute of Technology. Caltech image database. <http://www.vision.caltech.edu/html-files/archive.html>, 2011. 18
- [COS01] T.F. Chan, S. Osher, and J. Shen. The Digital TV Filter and Nonlinear Denoising. *IEEE Trans. Image Process.*, 10(2):231–241, 2001. 23
- [CS00] T.F. Chan and J. Shen. Variational restoration of nonflat image features: Models and algorithms. *SIAM J. Numer. Anal.*, 61(4):1338–1361, 2000. 21
- [CS02] T.F. Chan and J. Shen. Mathematical models for local nontexture inpaintings. *SIAM J. Numer. Anal.*, 62(3):1019–1043, 2002. 21
- [CS03] T.F. Chan and J. Shen. *Recent Advances in Scientific Computing and Partial Differential Equations*, volume 330 of *Contemp. Math.*, chapter On the role of the BV image model in image restoration, pages 25–41. American Mathematical Society, Providence, RI, USA, 2003. 21
- [CS05] T.F. Chan and J. Shen. *Image Processing and Analysis: variational, PDE, wavelet, and stochastic methods*. Society for Industrial and Applied Mathematics, Philadelphia, PA, USA, 2005. 8, 9, 10, 43
- [CV07] H. Chen and P.K. Varshney. A human perception inspired quality metric for image fusion based on regional information. *Inform. Fusion*, 8(2):193–207, April 2007. 96
- [CW98] T.F. Chan and C.-K. Wong. Total variation blind deconvolution. *IEEE Trans. Image Process.*, 7(3):370–375, 1998. 55
- [Dau92] I. Daubechies. *Ten lectures on wavelets*. Society for Industrial and Applied Mathematics, Philadelphia, PA, USA, 1992. 83

- [DF95] R. Deriche and O. Faugeras. Les EDP en traitement des images et vision par ordinateur (in French). *Traitement du Signal*, 5(2697):136–146, 1995. xx, 21, 25, 26
- [Don99] M. Donias. *Caractérisation de Champs d’Orientations par Analyse en Composantes Principales et Estimation de la Curbure (in French)*. PhD thesis, L’Université Bordeaux I - École Doctorale des Sciences Physiques et de L’Ingénieur, 1999. 110, 111
- [Dzy95] V.K. Dzyadyk. *Approximation methods for solutions of differential and integral equations*. VSP, 1995. 32
- [ECE11] ECE – Lehigh University. Investigations of image fusion. <http://www.ece.lehigh.edu/SPCRL/IF/disk.htm>, 2011. 124, 145
- [EF95] A.M. Eskicioglu and P.S. Fisher. Image quality measures and their performance. *IEEE Trans. Commun.*, 43(12):2959–2965, December 1995. 95
- [Eva10] L.C. Evans. *Partial Differential Equations*, volume 19 of *Graduate Studies in Mathematics*. American Mathematical Society, Providence, RI, USA, 2nd edition, March 2010. 32
- [FM06] B. Fischer and J. Modersitzki. Image fusion and registration - a variational approach. In E. Krause, Y. Shokin, M. Resch, and N. Shokina, editors, *Computational Science and High Performance Computing II*, volume 91 of *Notes on Numerical Fluid Mechanics and Multidisciplinary Design*, pages 193–203. Springer Berlin–Heidelberg, 2006. 92
- [Fun92] D. Funaro. *Polynomial approximation of differential equations*. Lecture Notes in Physics. Springer-Verlag, 1992. 32
- [Gau11] M. Gaubatz. MeTriX MuX Visual Quality Assessment Package. http://foulard.ece.cornell.edu/gaubatz/metrix_mux/, 2011. 63, 98, 141
- [GCTO00] P. Gonsalves, R. Cunningham, N. Ton, and D. Okon. Intelligent threat assessment processor (ITAP) using genetic algorithms and fuzzy logic. In *Proceedings of the 3rd International Conference on Information Fusion*, volume 2 of *FUSION ’00*, pages 18–24, July 2000. 77
- [GH86] M. Gage and R.S. Hamilton. The heat equation shrinking convex plane curves. *J. Differential Geom.*, 23(1):69–96, 1986. 31
- [Gib02] J.W. Gibbs. *Elementary Principles of Statistical Mechanics*. Yale University Press, USA, 1902. 9
- [Gil04] Guy Gilboa. *Super-resolution Algorithms Based on Inverse Diffusion-type Processes*. PhD thesis, Technion-Israel Institute of Technology, Haifa, Israel, 2004. 42, 58
- [Gra87] M.A. Grayson. The Heat Equation Shrinks Embedded Plane Curves to Round Points. *J. Differential Geom.*, 26(2):285–314, 1987. 31

- [Gre90] P.J. Green. Bayesian reconstructions from emission tomography data using a modified EM algorithm. *IEEE Trans. Med. Imaging*, 9(1):84–93, 1990. 26
- [GSZ02a] G. Gilboa, N.A. Sochen, and Y.Y. Zeevi. Forward-and-backward diffusion processes for adaptive image enhancement and denoising. *IEEE Trans. Image Process.*, 11(7):689–703, 2002. 20, 21
- [GSZ02b] G. Gilboa, N.A. Sochen, and Y.Y. Zeevi. Regularized Shock Filters and Complex Diffusion. In *Proceedings of the 7th European Conference on Computer Vision-Part I*, Lecture Notes in Computer Science, pages 399–413. Springer-Verlag, May 2002. 44, 54, 55, 56, 57, 58, 65, 66
- [GW06] R.C. Gonzalez and R.E. Woods. *Digital Image Processing*. Prentice-Hall, Inc., Upper Saddle River, NJ, USA, 3rd edition, 2006. 24
- [GZS00] G. Gilboa, Y.Y. Zeevi, and N.A. Sochen. Signal and Image Enhancement by a Generalized Forward-and-Backward Adaptive Diffusion Process. In *10th European Signal Processing Conference, EUSIPCO '00*. European Association for Signal Processing (EURASIP), September 2000. 20, 21
- [GZS01] G. Gilboa, Y.Y. Zeevi, and N.A. Sochen. Complex Diffusion Processes for Image Filtering. In *Proceedings of the 3rd International Conference on Scale-Space and Morphology in Computer Vision, SCALE-SPACE '01*, pages 299–307. Springer-Verlag, July 2001. 54, 57, 58
- [Hal92] D.L. Hall. *Mathematical Techniques in Multisensor Data Fusion*. Artech House, Inc., Norwood, MA, USA, 1992. 77
- [HNC08] M. Hossny, S. Nahavandi, and D. Crieghton. Feature-Based Image Fusion Quality Metrics. In *Proceedings of the 1st International Conference on Intelligent Robotics and Applications: Part I, ICIRA '08*, pages 469–478. Springer-Verlag, 2008. 96
- [Ima11a] ImageFusion.org. 2-D Image Collections. <http://www.imagefusion.org/>, 2011. 123, 131, 132, 146
- [Ima11b] ImageProcessingPlace.com. Image databases. http://www.imageprocessingplace.com/root_files_V3/image_databases.htm, 2011. 24
- [JV05] S. John and M.A. Vorontsov. Multiframe selective information fusion from robust error estimation theory. *IEEE Trans. Image Process.*, 14(5):577–584, May 2005. 87, 108, 109, 113, 114, 136, 139, 148
- [KDA96] P. Kornprobst, R. Deriche, and G. Aubert. Image restoration via PDE. In *Proceedings of the First Annual Symposium on Enabling Technologies for Law Enforcement and Security*, SPIE Conference 2942: Investigative Image Processing, pages 22–33, November 1996. 26, 27

- [KDA97a] P. Kornprobst, R. Deriche, and G. Aubert. Image coupling, restoration and enhancement via PDE's. In *Proceedings of the 1997 IEEE International Conference on Image Processing*, volume 2 of *ICIP '97*, pages 458–461, Washington, DC, USA, October 1997. IEEE Computer Society. 44, 48, 50, 55, 66, 117
- [KDA97b] P. Kornprobst, R. Deriche, and G. Aubert. Non-linear operators in image restoration. In *Proceedings of the 1997 IEEE Conference on Computer Vision and Pattern Recognition, CVPR '97*, pages 325–330, Washington, DC, USA, 1997. IEEE Computer Society. 26, 27
- [KDA99] P. Kornprobst, R. Deriche, and G. Aubert. Image sequence analysis via partial differential equations. *J. Math. Imaging Vis.*, 11(1):5–26, September 1999. 26, 27
- [Kod11] Kodak. Kodak Lossless True Color Image Suite. <http://r0k.us/graphics/kodak/index.html>, 2011. xv, xvi, 49, 57
- [Koe84] J.J. Koenderink. The structure of images. *Biol. Cybern.*, 50(5):363–370, 1984. 11, 13
- [Kor98] P. Kornprobst. *Contribution à la restauration d'images et à l'analyse de séquences: Approches Variationnelles et Solutions de Viscosité. (in French)*. PhD thesis, Université de Nice Sophia-Antipolis, November 1998. 36
- [KS96] B.B. Kimia and K. Siddiqi. Geometric heat equation and nonlinear diffusion of shapes and images. *Comput. Vis. Image Underst.*, 64(3):305–322, November 1996. 30, 31
- [KSZ05] R. Kaftory, N.A. Sochen, and Y.Y. Zeevi. Variational blind deconvolution of multi-channel images. *Int. J. Imaging Syst. Technol.*, 15(1):56–63, 2005. 55
- [KW87] M. Kass and A. Witkin. Analyzing oriented patterns. *Comput. Vision Graph. Image Process.*, 37(3):362–385, March 1987. 28, 52
- [Lab11] Laboratory for Image and Video Engineering. Image and Video Quality Assessment at LIVE. <http://live.ece.utexas.edu/research/quality/>, 2011. 63
- [LKW01] S. Li, J.T. Kwok, and Y. Wang. Combination of images with diverse focuses using the spatial frequency. *Inform. Fusion*, 2(3):169–176, September 2001. 95
- [LL11a] **C. Ludusan** and O. Laviaille. Approche variationnelle pour la fusion d'images multifocus bruitées (in French). In *XXIIIe Colloque GRETSI, GRETSI Symposium on Signal and Image Processing*, September 2011. 124
- [LL11b] **C. Ludusan** and O. Laviaille. Multifocus image fusion and denoising: a variational approach. *Pattern Recognit. Lett.*, 2011. Considered for publication – under revision. 124

- [LL11c] **C. Ludusan** and O. Laviaille. A variational approach for concurrent image fusion and denoising. *Pattern Recognit.*, 2011. Considered for publication – under revision. 135
- [LLBT11] **C. Ludusan**, O. Laviaille, M. Borda, and R. Terebes. Filtre de choc hybride pour la restauration d’images (in French). In *XXIIIe Colloque GRETSI, GRETSI Symposium on Signal and Image Processing*, September 2011. 72
- [LLT⁺10] **C. Ludusan**, O. Laviaille, R. Terebes, M. Borda, and S. Pop. Image enhancement using hybrid shock filters. In *Proceedings of the 2010 IEEE International Conference on Automation Quality and Testing Robotics*, volume 3 of *AQTR ’10*, pages 111–116, May 2010. 63
- [LLTB10a] **C. Ludusan**, O. Laviaille, R. Terebes, and M. Borda. Coherence enhancing image sharpening and denoising using a novel shock filter model. In *Proceedings of the 9th IEEE International Symposium on Electronics and Telecommunications*, ISETC ’10, pages 333–336, November 2010. 72
- [LLTB10b] **C. Ludusan**, O. Laviaille, R. Terebes, and M. Borda. Morphological sharpening and denoising using a novel shock filter model. In *Proceedings of the 4th International Conference on Image and Signal Processing*, volume 6134 of *ICISP’10*, pages 19–27, Berlin, Heidelberg, June 2010. Springer-Verlag. 65
- [LMM95] H. Li, B.S. Manjunath, and S.K. Mitra. Multisensor image fusion using the wavelet transform. *Graph. Models Image Process.*, 57(3):235–245, May 1995. 83, 84
- [LON⁺07] J.J. Lewis, R.J. O’Callaghan, S.G. Nikolov, D.R. Bull, and N. Canagarajah. Pixel- and region-based image fusion with complex wavelets. *Inf. Fusion*, 8(2):119–130, April 2007. 83
- [LW09] D. Laidlaw and J. Weickert, editors. *Visualization and Processing of Tensor Fields: Advances and Perspectives*. Springer-Verlag Berlin Heidelberg, 2009. 29
- [Mal89] S.G. Mallat. A Theory for Multiresolution Signal Decomposition: The Wavelet Representation. *IEEE Trans. Pattern Anal. Mach. Intell.*, 11(7):674–693, July 1989. 82
- [Mar06] P. Markowich. *Applied Partial Differential Equations: A Visual Approach*. Springer-Verlag, 1st edition, 2006. 32
- [MB98] J. Monteil and A. Beghdadi. A new adaptive nonlinear anisotropic diffusion for noise smoothing. In *Proceedings of the 1998 IEEE International Conference on Image Processing*, volume 3 of *ICIP ’98*, pages 254–258, October 1998. 18
- [MB99] J. Monteil and A. Beghdadi. A new interpretation and improvement of the nonlinear anisotropic diffusion for image enhancement. *IEEE Trans. Pattern Anal. Mach. Intell.*, 21(9):940–946, September 1999. 18

- [MH80] D. Marr and E. Hildreth. Theory of edge detection. *Proceedings of the Royal Society of London. Series B, Containing papers of a Biological character. Royal Society (Great Britain)*, 207(1167):187–217, February 1980. 11
- [Mit10] H. B. Mitchell. *Image Fusion - Theories, Techniques and Applications*. Springer-Verlag Berlin Heidelberg, 2010. xvii, 76, 79, 80, 82
- [MS89] D. Mumford and J. Shah. Optimal approximations by piecewise smooth functions and associated variational problems. *Commun. Pure Appl. Math.*, 42(5):577–685, 1989. 21
- [MS95] J.-M. Morel and S. Solimini. *Variational methods in image segmentation*. Birkhauser Boston Inc., Cambridge, MA, USA, 1995. 11, 21
- [MS08] N. Mitianoudis and T. Stathaki. *Image Fusion: Algorithms and Applications*, chapter Enhancement of multiple sensor images using joint image fusion and blind restoration, pages 299–326. Academic Press, Amsterdam, The Netherlands, 1st edition, July 2008. 92, 108, 109, 113, 114, 115
- [OBDF09] J.P. Oliveira, J.M. Bioucas-Dias, and M.A.T. Figueiredo. Review: Adaptive total variation image deblurring: A majorization-minimization approach. *Signal Process.*, 89(9):1683–1693, September 2009. 55
- [OR90] S. Osher and L.I. Rudin. Feature-oriented image enhancement using shock filters. *SIAM J. Numer. Anal.*, 27(4):919–940, August 1990. 15, 43, 44, 45, 47, 48, 56, 57, 66, 129
- [Ort87] E.L. Ortiz, editor. *Numerical approximation of partial differential equations*, volume 133 of *Mathematics Studies*. Elsevier Science Publishers, 1987. 32
- [PdIC04] G. Pajares and J.M. de la Cruz. A wavelet-based image fusion tutorial. *Pattern Recognit.*, 37(9):1855–1872, 2004. 83
- [Pet01] V.S. Petrovic. *Multisensor Pixel-level Image Fusion*. PhD thesis, University of Manchester, 2001. 93, 94
- [Pha01] T.D. Pham. An image restoration by fusion. *Pattern Recognit.*, 34(12):2403–2411, 2001. 108
- [Pie03] G. Piella. *Adaptive Wavelets and their Applications to Image Fusion and Compression*. PhD thesis, University of Amsterdam, 2003. 81, 83
- [Pie04] G. Piella. New quality measures for image fusion. In *Proceedings of the 7th International Conference on Information Fusion, FUSION '04*, pages 542–546, June 2004. 94, 137
- [Pie08] G. Piella. A variational approach for image fusion visualization. In *16th European Signal Processing Conference (EUSIPCO)*, August 2008. 90, 91
- [Pie09] G. Piella. Image fusion for enhanced visualization: A variational approach. *Int. J. Comput. Vision*, 83:1–11, June 2009. 90, 91

- [PLTB07] S. Pop, O. Laviaille, R. Terebes, and M. Borda. Low-level fusion: a PDE-based approach. In *Proceedings of the 10th International Conference on Information Fusion*, FUSION '07, pages 1–8, July 2007. 90, 108
- [PM90] P. Perona and J. Malik. Scale-space and edge detection using anisotropic diffusion. *IEEE Trans. Pattern Anal. Mach. Intell.*, 12(7):629–639, July 1990. 12, 15, 16, 17, 18
- [Pop08] S. Pop. *Modèles de Fusion et Diffusion par Équations aux Dérivées Partielles: Application à la Sismique Azimutale (in French)*. PhD thesis, L'Université Bordeaux I - École Doctorale des Sciences Physiques et de L'Ingénieur en cotutelle avec L'Université Technique de Cluj-Napoca (Roumanie), November 2008. 81, 84, 88, 89, 90, 108, 136, 137, 140
- [PTB⁺07] S. Pop, R. Terebes, M. Borda, S. Guillon, N. Keskes, P. Baylou, and O. Laviaille. 3D Seismic Data Fusion and Filtering using a PDE-Based Approach. In *Proceedings of the 2007 IEEE International Conference on Image Processing*, volume 4 of *ICIP '07*, pages 117–120, October 2007. 90, 108
- [PX03] V. Petrovic and C.S. Xydeas. Sensor noise effects on signal-level image fusion performance. *Inform. Fusion*, 4(3):167–183, 2003. 140
- [QV08] A. Quarteroni and A. Valli. *Numerical Approximation of Partial Differential Equations*, volume 23 of *Computational Mathematics*. Springer-Verlag, 2008. 32
- [Rao90] A.R. Rao. *A taxonomy for texture description and identification*. Springer-Verlag New York, Inc., New York, NY, USA, 1990. 28, 52, 112
- [RC03] L. Remaki and M. Cheriet. Numerical Schemes of Shock Filter Models for Image Enhancement and Restoration. *J. Math. Imaging Vis.*, 18:129–143, March 2003. 44, 50, 51, 66
- [RC08] P.D. Romero and V.F. Candela. Blind Deconvolution Models Regularized by Fractional Powers of the Laplacian. *J. Math. Imaging Vis.*, 32(2):181–191, October 2008. 55
- [RF98] O. Rockinger and T. Fechner. Pixel-level image fusion: the case of image sequences. In *Proceedings SPIE*, SPIE Conference 3374: Signal Processing, Sensor Fusion, and Target Recognition VII, pages 378–388, July 1998. 84
- [RO94] L.I. Rudin and S. Osher. Total variation based image restoration with free local constraints. In *Proceedings of the 1994 IEEE International Conference on Image Processing*, volume 1 of *ICIP '94*, pages 31–35, November 1994. 21
- [Roc99] O. Rockinger. image fusion toolbox. <http://www.metapix.de/toolbox.htm>, 1999. 97, 123, 136
- [ROF92] L.I. Rudin, S. Osher, and E. Fatemi. Nonlinear total variation based noise removal algorithms. *Phys. D*, 60(1-4):259–268, November 1992. 21, 22

- [RS89] A.R. Rao and B.G. Schunck. Computing oriented texture fields. In *Proceedings of the 1989 IEEE Conference on Computer Vision and Pattern Recognition*, CVPR '89, pages 61–68, June 1989. 112
- [RS91] A.R. Rao and B.G. Schunck. Computing oriented texture fields. *CVGIP: Graph. Models Image Process.*, 53(2):157–185, March 1991. 28, 52, 112
- [Rud87] L.I. Rudin. *Images, numerical analysis of singularities and shock filters*. PhD thesis, California Institute of Technology, Pasadena, CA, USA, 1987. UMI Order No. GAX87-19699. 15, 48
- [Sam03] F. Samadzadegan. Fusion techniques in remote sensing. In *Challenges in Geospatial Analysis, Integration and Visualization II, ISPRS Commission IV Joint Workshop*. ISPRS, Int. Arch. Photogram. Rem. Sens. Spatial Inform. Sci., September 2003. 77
- [Sam04] F. Samadzadegan. Data Integration Related To Sensors, Data And Models. In *Proceedings of the XXth ISPRS Congress, Commission IV*, volume XXXV of *ISPRS '04*, pages 569–574, July 2004. 77
- [Sap01] G. Sapiro. *Geometric Partial Differential Equations and Image Analysis*. Cambridge University Press, 1st edition, 2001. 30, 31
- [SB06] H.R. Sheikh and A.C. Bovik. Image information and visual quality. *IEEE Trans. Image Process.*, 15(2):430–444, February 2006. 63
- [SBW99] A.N. Steinberg, C.L. Bowman, and F.E. White. Revisions to the JDL data fusion model. In Belur V. Dasarathy, editor, *Sensor Fusion: Architectures, Algorithms, and Applications III*, volume 3719, pages 430–441. SPIE, 1999. 77
- [Soc00a] D.A. Socolinsky. *A Variational Approach To Image Fusion*. PhD thesis, The Johns Hopkins University, April 2000. 85, 86, 129, 136
- [Soc00b] D.A. Socolinsky. A locally-adaptive metric for contrast-fusion of noisy multimodal imagery. Technical report, Equinox Corporation, New York, NY, USA, 2000. 85
- [ST94] G. Sapiro and A. Tannenbaum. On Affine Plane Curve Evolution. *J. Funct. Anal.*, 119(1):79–120, January 1994. 12, 31
- [Str05] G. Strang. *Linear Algebra and Its Applications*. Brooks Cole, 4th edition, 2005. 27
- [SW00] H. Scharr and J. Weickert. An anisotropic diffusion algorithm with optimized rotation invariance. In *DAGM-Symposium*, Informatik Aktuell, pages 460–467. Springer, 2000. 33
- [SW02] D.A. Socolinsky and L.B. Wolff. Multispectral image visualization through first-order fusion. *IEEE Trans. Image Process.*, 11(8):923–931, August 2002. 85, 86, 87

- [TBB⁺04] R. Terebes, M. Borda, Y. Baozong, O. Laviaille, and P. Baylou. A new PDE based approach for image restoration and enhancement using robust diffusion directions and directional derivatives based diffusivities. In *Proceedings of the 7th International Conference on Signal Processing*, volume 1 of *ICSP '04*, pages 707–712, August 2004. 114, 117
- [TD01] D. Tschumperlé and R. Deriche. Diffusion Tensor Regularization with Constraints Preservation. In *Proceedings of the 2001 IEEE Computer Society Conference on Computer Vision and Pattern Recognition*, volume 1 of *CVPR '01*, pages 948–953, Los Alamitos, CA, USA, December 2001. IEEE Computer Society. 21
- [TD02] D. Tschumperlé and R. Deriche. Orthonormal Vector Sets Regularization with PDE's and Applications. *Int. J. Comput. Vision*, 50(3):237–252, December 2002. 21
- [Ter04] R. Terebes. *Diffusion Directionnelle. Applications à la Restauration et à l'Amélioration d'Images de Documents Anciens (in French)*. PhD thesis, L'Université Bordeaux I - École Doctorale des Sciences Physiques et de L'Ingénieur en cotutelle avec L'Université Technique de Cluj-Napoca (Roumanie), May 2004. xvii, 11, 12, 15, 28, 30, 31, 32, 35, 36, 48, 111, 113, 117, 118, 119, 120
- [Tho95] J.W. Thomas. *Numerical partial differential equations: finite difference methods*, volume 22 of *Texts in Applied Mathematics*. Springer-Verlag, 1995. 32
- [TLBB02] R. Terebes, O. Laviaille, P. Baylou, and M. Borda. Mixed Anisotropic Diffusion. In *Proceedings of the 16th International Conference on Pattern Recognition*, volume 3 of *ICPR '02*, pages 760–763, Washington, DC, USA, 2002. IEEE Computer Society. 114
- [TLCO07] X.-C. Tai, K.-A. Lie, T.F. Chan, and S. Osher, editors. *Image Processing Based on Partial Differential Equations*. Springer-Verlag, 2007. 32
- [Uni11] University of Southern California. The USC-SIPI image database. <http://sipi.usc.edu/database/index.php>, 2011. xv, 48, 67, 68
- [Ves01] L. Vese. A Study in the BV Space of a Denoising-Deblurring Variational Problem. *Appl. Math. Optim.*, 44(2):131–161, December 2001. 21
- [VO02] L. Vese and S. Osher. Modeling textures with total variation minimization and oscillating patterns in image processing. Cam tech. report, UCLA, 2002. 21
- [Wal98] L. Wald. A european proposal for terms of reference in data fusion. *Int. Arch. Photogram. Rem. Sens. Spatial Inform. Sci.*, XXXII(7):651–654, 1998. 77, 93, 107, 124
- [WB02] Z. Wang and A.C. Bovik. A universal image quality index. *IEEE Signal Process. Lett.*, 9(3):81–84, March 2002. 63, 94, 101

- [WB09] Z. Wang and A.C. Bovik. Mean squared error: Love it or leave it? A new look at signal fidelity measures. *IEEE Signal Process. Mag.*, 26(1):98–117, 2009. 63
- [WBSS04] Z. Wang, A.C. Bovik, H.R. Sheikh, and E.P. Simoncelli. Image Quality Assessment: From Error Visibility to Structural Similarity. *IEEE Trans. Image Process.*, 13(4):600–612, 2004. 63, 94
- [Wei94] J. Weickert. Scale-Space Properties of Nonlinear Diffusion Filtering with a Diffusion Tensor. Report 110, Laboratory of Technomathematics, University of Kaiserslautern, October 1994. 12, 16, 27
- [Wei95] J. Weickert. Multiscale Texture Enhancement. In *Proceedings of the 6th International Conference on Computer Analysis of Images and Patterns, CAIP '95*, pages 230–237. Springer-Verlag, 1995. 27, 28, 29, 37, 52
- [Wei97a] J. Weickert. A Review of Nonlinear Diffusion Filtering. In *Proceedings of the 1st International Conference on Scale-Space Theory in Computer Vision, SCALE-SPACE '97*, pages 3–28. Springer-Verlag, 1997. 16
- [Wei97b] J. Weickert. Coherence-Enhancing Diffusion of Colour Images. In *Proceedings of the 7th National Symposium on Pattern Recognition and Image Analysis*, volume 1 of *NSPRIA '97*, pages 239–224, April 1997. 27, 28
- [Wei99] J. Weickert. Coherence-Enhancing Diffusion Filtering. *Int. J. Comput. Vision*, 31(2-3):111–127, April 1999. 27, 28, 52
- [Wei03] J. Weickert. Coherence-enhancing shock filters. In *Lecture Notes in Computer Science*, volume 2781 of *Pattern Recognit.*, pages 1–8. Springer, 2003. 41, 44, 52, 53, 60, 71
- [WH06] J. Weickert and H. Hagen, editors. *Visualization and Processing of Tensor Fields*. Springer-Verlag Berlin Heidelberg, 2006. 29
- [Wit84] A. Witkin. Scale-space filtering: A new approach to multi-scale description. In *Proceedings of the 1984 IEEE International Conference on Acoustics, Speech, and Signal Processing*, volume 9 of *ICASSP '84*, pages 150–153, 1984. 11
- [WP93] R. Whitaker and S. Pizer. A multi-scale approach to nonuniform diffusion. *CVGIP: Image Underst.*, 57(1):99–110, January 1993. 18
- [WSB03] Z. Wang, E.P. Simoncelli, and A.C. Bovik. Multiscale structural similarity for image quality assessment. In *Conference Record of the Thirty-Seventh Asilomar Conference on Signals, Systems and Computers*, volume 2, pages 1398–1402, November 2003. 63, 143
- [WSF08] W.-W. Wang, P.-L. Shui, and X.-C. Feng. Variational models for fusion and denoising of multifocus images. *IEEE Signal Process. Lett.*, 15:65–68, January 2008. 92, 108, 113

- [WTBW05] M. Welk, D. Theis, T. Brox, and J. Weickert. PDE-Based Deconvolution with Forward-Backward Diffusivities and Diffusion Tensors. In *Proceedings of the 3rd International Conference on Scale-Space and Morphology in Computer Vision*, SCALE-SPACE '05, pages 585–597. Springer-Verlag, April 2005. 55
- [WtHRV96] J. Weickert, B.M. ter Haar Romeny, and M.A. Viergever. Conservative image transformations with restoration and scale-space properties. In *Proceedings of the 1996 IEEE International Conference on Image Processing*, volume 1 of *ICIP '96*, pages 465–468, September 1996. 16, 27
- [WtHRV98] J. Weickert, B.M. ter Haar Romeny, and M.A. Viergever. Efficient and reliable schemes for nonlinear diffusion filtering. *IEEE Trans. Image Process.*, 7(3):398–410, March 1998. 16, 36, 38
- [WWG07] M. Welk, J. Weickert, and I. Galić. Theoretical foundations for spatially discrete 1-D shock filtering. *Image Vision Comput.*, 25(4):455–463, April 2007. 55
- [WY06] C. Wang and Z. Ye. First-order fusion of volumetric medical imagery. *IEE Proceedings - Vision, Image and Signal Processing*, 153(2):191–198, April 2006. 88
- [WY07] C. Wang and Z. Ye. Perceptual Contrast-Based Image Fusion: A Variational Approach. *Acta Autom. Sin.*, 33(2):132–137, February 2007. 89, 136
- [WYTY06] C. Wang, Q. Yang, X. Tang, and Z. Ye. Saliency Preserving Image Fusion with Dynamic Range Compression. In *Proceedings of the 2006 IEEE International Conference on Image Processing*, ICIP '06, pages 989–992, October 2006. 88, 89
- [XP00] C.S. Xydeas and V. Petrovic. Objective image fusion performance measure. *Electron. Lett.*, 36(4):308–309, February 2000. 94
- [YZWL08] C. Yang, J.-Q. Zhang, X.-R. Wang, and X. Liu. A novel similarity based quality metric for image fusion. *Inform. Fusion*, 9(2):156–160, April 2008. 96
- [ZB99] Z. Zhang and R.S. Blum. A categorization of multiscale-decomposition-based image fusion schemes with a performance study for a digital camera application. In *Proceedings of the IEEE*, volume 87, pages 1315–1326, August 1999. 83
- [ZEH04] Y. Zheng, E.A. Essock, and B.C. Hansen. An advanced image fusion algorithm based on wavelet transform-incorporation with PCA and morphological processing. In *Image Processing: Algorithms and Systems III*, volume 5298, pages 177–187. SPIE, 2004. 96
- [ZEHH07] Y. Zheng, E.A. Essock, B.C. Hansen, and A.M. Haun. A new metric based on extended spatial frequency and its application to DWT based fusion algorithms. *Inform. Fusion*, 8(2):177–192, April 2007. 95

- [Zen86] S. Di Zenzo. A note on the gradient of a multi-image. *Comput. Vision Graph. Image Process.*, 33(1):116–125, January 1986. 85, 88

List of Publications

Refereed Journal Publications

- [TBP⁺10a] R. Terebes, M. Borda, S. Pop, O. Laviaille, C. Germain, and **C. Ludusan**. A novel diffusion filter for image restoration and enhancement. *Revue roumaine des sciences techniques*, 55(3):310–319, 2010.
- [TBP⁺10b] R. Terebes, M. Borda, S. Pop, **C. Ludusan**, and O. Laviaille. Asymmetric Diffusion and Fusion Techniques for Image Restoration. *Acta Technica Napocensis, Electronics and Telecommunications*, 51(1):21–26, 2010.
- [LLP⁺09] **C. Ludusan**, O. Laviaille, S. Pop, R. Terebes, and M. Borda. Image enhancement using a new shock filter formalism. *Acta Technica Napocensis, Electronics and Telecommunications*, 50(3):27–30, 2009.
- [TBLP08] R. Terebes, M. Borda, **C. Ludusan**, and S. Pop. A combined fusion-diffusion approach for image filtering and enhancement. *Scientific Bulletin of “Politehnica” University of Timisoara, Transactions on Electronics and Communications*, 53(2):103–108, 2008.
- [LLTB07] **C. Ludusan**, O. Laviaille, R. Terebes, and M. Borda. An approach to image fusion implementing feature level fusion on seismic attributes. *Scientific Bulletin of “Politehnica” University of Timisoara, Transactions on Electronics and Communications*, 52(1):9–14, 2007.

Submitted Refereed Journal Publications

- [LLa] **C. Ludusan** and O. Laviaille. Multifocus image fusion and denoising: a variational approach. *Pattern Recognit. Lett.* 2011. **Considered for publication – under revision.**
- [LLb] **C. Ludusan** and O. Laviaille. A variational approach for concurrent image fusion and denoising. *Pattern Recognit.* 2011. **Considered for publication – under revision.**

Refereed Conference Publications

- [LL11a] **C. Ludusan** and O. Laviaille. Approche Variationnelle pour la fusion d’images multifocus bruitées (in French). In *XXIIIe Colloque GRETSI, GRETSI Symposium on Signal and Image Processing*, September 2011.
- [LLBT11a] **C. Ludusan**, O. Laviaille, M. Borda, and R. Terebes. Filtre de choc hybride pour la restauration d’images (in French). In *XXIIIe Colloque GRETSI, GRETSI Symposium on Signal and Image Processing*, September 2011.

- [LLTB10a] **C. Ludusan**, O. Laviaille, R. Terebes, and M. Borda. Coherence enhancing image sharpening and denoising using a novel shock filter model. In *Proceedings of the 9th IEEE International Symposium on Electronics and Telecommunications*, ISETC '10, pages 333–336, November 2010.
- [TPB⁺10] R. Terebes, S. Pop, M. Borda, **C. Ludusan**, and O. Laviaille. 3D image restoration using diffusion and fusion techniques. In *Proceedings of the 52nd IEEE International Symposium*, ELMAR '10, pages 37–40, September 2010.
- [LLTB10b] **C. Ludusan**, O. Laviaille, R. Terebes, and M. Borda. Morphological sharpening and denoising using a novel shock filter model. In *Proceedings of the 4th International Conference on Image and Signal Processing*, volume 6134 of ICISP '10, pages 19–27, Berlin, Heidelberg, June 2010. Springer-Verlag.
- [LLT⁺10] **C. Ludusan**, O. Laviaille, R. Terebes, M. Borda, and S. Pop. Image enhancement using hybrid shock filters. In *Proceedings of the IEEE International Conference on Automation Quality and Testing Robotics*, volume 3 of AQTR '10, pages 111–116, May 2010.
- [PTdC⁺10] S. Pop, R. Terebes, J. da Costa, C. Germain, M. Borda, **C. Ludusan**, and O. Laviaille. A novel 3D anisotropic diffusion filter. In *(3DIP), SPIE 3D Image Processing and Applications*, volume 7526 of Society of Photo-Optical Instrumentation Engineers (SPIE) Conference Series, January 2010.
- [LPT⁺09] O. Laviaille, S. Pop, R. Terebes, **C. Ludusan**, and M. Borda. Approches EDP pour la fusion d'images bruitées (in French). In *XXIIe Colloque GRETSI, GRETSI Symposium on Signal and Image Processing*, September 2009.
- [LLP⁺08] **C. Ludusan**, O. Laviaille, S. Pop, R. Terebes, and M. Borda. An improved method for directional image smoothing based on structure tensors and vector field visualization techniques. In *Proceedings of the 8th International Symposium on Electronics and Telecommunications*, ISETC '08, September 2008.

Non-Refereed Publications

- [TBPL10] R. Terebes, M. Borda, S. Pop, and **C. Ludusan**. Tehnici de difuzie și de fuziune pentru restaurarea și îmbunătățirea imaginilor (in Romanian, Fusion-diffusion techniques for image restoration and enhancement): 60 pages, Technical University of Cluj-Napoca, Technical report research grant CNCSIS-UEFISCSU project number PNII-IDEI code ID 908/2007 (6), 2010.
- [Lud10] **C. Ludusan**. Metode de fuziune de imagini bazate pe formalismul ecuațiilor cu derivate parțiale (in Romanian, PDE-based image fusion

- methods): 34 pages, Technical University of Cluj-Napoca, Doctoral School - Ph.D. program - scientific research report (3), 2010.
- [TBPL09] R. Terebes, M. Borda, S. Pop, and **C. Ludusan**. Tehnici de difuzie și de fuziune pentru restaurarea și îmbunătățirea imaginilor (in Romanian, Fusion-diffusion techniques for image restoration and enhancement): 76 pages, Technical University of Cluj-Napoca, Technical report research grant CNCSIS-UEFISCSU project number PNII-IDEI code ID 908/2007 (5), 2009.
- [Lud09a] **C. Ludusan**. Studiul operatorilor de estimare a orientării în problema filtrării de imagini (in Romanian, The study of orientation estimation operators in image filtering): 58 pages, Technical University of Cluj-Napoca, Doctoral School - Ph.D. program - scientific research report (1), 2009.
- [Lud09b] **C. Ludusan**. Studiul filtrelor de șoc în problema filtrării de imagini prin formalismul ecuațiilor cu derivate parțiale (in Romanian, The study of shock filters in image filtering using the PDE formalism): 28 pages, Technical University of Cluj-Napoca, Doctoral School - Ph.D. program - scientific research report (2), 2009.
- [TBPL08a] R. Terebes, M. Borda, S. Pop, and **C. Ludusan**. Defnirea de metrici pentru implementarea de reguli de fuziune la nivel de pixel și nivel de attribute a rezultatelor filtrelor de tip EDP (in Romanian, Defining new metrics of implementing pixel and feature-level fusion rules for PDE-type filter results): 50 pages, Technical University of Cluj-Napoca, Technical report research grant CNCSIS-UEFISCSU project number PNII-IDEI code ID 908/2007 (3), 2008.
- [TBPL08b] R. Terebes, M. Borda, S. Pop, and **C. Ludusan**. Elaborarea de noi modele teoretice de EDP bazate pe geometria locală a imaginilor cuantificată prin intermediul unor operatori de estimare a orientării (in Romanian, Developing new theoretical PDE models based on local image geometry quantified using orientation estimation operators): 45 pages, Technical University of Cluj-Napoca, Technical report research grant CNCSIS-UEFISCSU project number PNII-IDEI code ID 908/2007 (4), 2008.
- [TBPL07a] R. Terebes, M. Borda, S. Pop, and **C. Ludusan**. Studii de caz cu privire la principalele tipuri de filtre de tip EDP susceptibile a fi utilizate în procesul de fuziune funcție de principalele modele de degradări de imagini (in Romanian, Case studies concerning the main types of PDE filters susceptible to use in image fusion according to the main image degradation models): 45 pages, Technical University of Cluj-Napoca, Technical report research grant CNCSIS-UEFISCSU project number PNII-IDEI code ID 908/2007 (1), 2007.
- [TBPL07b] R. Terebes, M. Borda, S. Pop, and **C. Ludusan**. Studiu comparativ al metodelor de estimare a orientării (in Romanian, Orientation estimation methods - a comparative study): 40 pages, Technical Univer-

sity of Cluj-Napoca, Technical report research grant CNCSIS-UEFISCSU project number PNII-IDEI code ID 908/2007 (2), 2007.

[Lud07]

C. Ludusan. Feature-Level Image Fusion: 124 pages, Technical University of Cluj-Napoca, B.S. diploma project paper, 2007.

